Design and Fabrication of Autoclavable Modular Microfluidics for Plant Research

Zur Erlangung des akademischen Grades einer

Doktorin der Ingenieurwissenschaften (Dr.-Ing.)

von der KIT-Fakultät für Maschinenbau des
Karlsruher Instituts für Technologie (KIT)

angenommene

Dissertation

von

M.Sc. Leona M. Speicher

Tag der mündlichen Prüfung:	17.12.2025
Hauptreferent:	Prof. Dr. Jan G. Korvink
Korreferenten:	Prof. Dr. Andreas E. Guber
	Prof. Dr. Peter Nick

Kurzfassung

Da der Klimawandel die landwirtschaftlichen Systeme verstärkt belastet, gewinnt die Entwicklung nachhaltiger Pflanzenschutzstrategien, wie z.B. dem Eingriff in die Kommunikation zwischen Pflanzen und ihren Aggresoren, zunehmend an Bedeutung. Mikrofluidik bietet hierbei neue Ansätze zur Analyse der Interaktion von Pflanzen und ihren Schädlingen sowohl auf mikroskopischer Ebene und in der chemischen Analyse. Ziel dieser Dissertation ist die Entwicklung, Optimierung und Herstellung zweier mikrofluidischer Systeme: des mikrofluidischen Bioreaktors (MBR) und des Wurzelchips (RC). Beide Systeme dienen der Langzeitkultivierung biologischer Proben sowie ihrer chemischen und optischen Analyse. Der MBR wurde basierend auf am Institut für Mikrostrukturtechnik (IMT) bestehenden Designs weiterentwickelt und für die Kultivierung von Pilzen angepasst. Er erlaubt die optische Überwachung sowie die Probenentnahme während der Kultivierung und kann modular über den Versorgungsstrom mit weiteren Reaktoren verbunden werden, um gerichtete interspezifische Kommunikation zu untersuchen. Der RC wurde in Anlehnung an publizierte Konzepte konzipiert und zunächst in Polydimethylsiloxan (PDMS) hergestellt. Um den RC auch per Autoklavieren sterilisieren zu können, wurde der erfolgreich getestete PDMS Chip auch aus Polykarbonat (PC) hergestellt. Der RC erlaubt die Kultivierung von Keimlingen über eine Woche unter mikroskopischer Beobachtung und mit der Möglichkeit zur Analyse des abfließenden Mediums. Die Entwicklung dieser Systeme erforderte auch die Erforschung und Anpassung geeigneter Fertigungsverfahren. Für den MBR wurde eine Methode zur falten- und beschädigungsfreien Integration ultra-dünner poröser Membranen unter Verwendung von Ultraschallschweißen (USS) entwickelt. Dazu wurde ein neuartiges Design mit zehn Energierichtungsgebern (Pin-und-Nut-Geometrie) und umlaufender Dichtung eingeführt, bei dem die Membran wie bei einem Trommelfell aufgespannt wird. Im Fall des RCs wurden systematisch die Parameter für das absorberfreie Laserdurchstrahlschweißen (LDSS) von PC im Allgemeinen und für ungleich dicke PC-Schweißpartner im Speziellen untersucht und dadurch eine Lücke in der Literatur geschlossen. Ein besonderes Augenmerk lag auf der Analyse des Fokusabstands des Lasers, der Bauteilkonfiguration und der Oberflächenvorbehandlung, um geeignete Parameter für das Schweißen dünner PC-Folien auf dickere Substrate zu ermitteln. Die vier Schwerpunkte dieser Arbeit – die Weiterentwicklung des MBR, das Design des RCs sowie die Erforschung der Prozesse USS und absorberfreies LDSS – wurden systematisch untersucht. Dies umfasste Literaturrecherchen, die Identifikation und Bewertung prozessrelevanter Einflussgrößen, experimentelle Untersuchungen sowie eine umfassende Auswertung der Ergebnisse. Beide Systeme wurden von Projektpartnern des DialogProTec Projekts erfolgreich eingesetzt. Am Joseph Gottlieb Kölreuter Institut für Pflanzenwissenschaften (JKIP) gelang die Kultivierung des Pilzes *Neofusicoccum parvum* im MBR, während das Institut de Biologie Moléculaire des Plantes (IBMP) das Wachstumsverhalten von *Arabidopsis thaliana* Wurzeln im RC analysierte. Die in dieser Arbeit entwickelten mikrofluidischen Systeme bieten eine gute Grundlage sowohl für die direkte Erforschung nachhaltiger Pflanzenschutzstrategien als auch für die technische Weiterentwicklung solcher Plattformen. Überdies leisten sie einen Beitrag zur Schließung bestehender Forschungslücken im Bereich des USS und des absorberfreien LDSS und sind damit über den hier dargelegten Kontext hinaus weiter nutzbar.

Abstract

As climate change places increasing strain on agricultural systems, the development of effective and sustainable crop protection tools becomes even more critical. Microfluidic technologies provide novel opportunities to investigate interactions between plants and their aggressors with high spatial and temporal resolution, enabling the design of targeted and environmentally friendly protection strategies. Within the scope of this thesis, two microfluidic chips (MFCs) were designed, refined, and manufactured: the Microfluidic Bioreactor (MBR), intended for the cultivation and analysis of plant cells and fungi; and the Root Chip (RC), developed to observe root growth behaviour *in planta* under controlled environmental conditions. The MBR supports microscopic observation, direct sampling, and run-off analysis of cultivated cells, building on the work of previous dissertations conducted at the Institute for Microstructure Technology (IMT). Moreover, it can be connected modularly with other MBRs via a unidirectional flow, thus enabling the dissection of local chemical communication between intra- or inter-kingdom cell populations. The RC, a new design at the IMT was based on previously published root observation platforms. It facilitates the controlled cultivation and microscopic analysis of seedling root systems initially within polydimethylsiloxane (PDMS) RCs. This thesis also addresses key technological research gaps in the manufacturing of microfluidic devices. For MBRs, the challenge was to install ultra-thin porous membranes while bonding the chip halves using ultrasonic welding (USW). As there were no detailed publicly available protocols, initial tests evaluated parameter variations, but ultimately a redesign of the energy director (ED) system was required. A shift from a continuous weld line to ten discrete pillar-and-groove EDs enabled the membrane to be stretched taut over a sealing ring, preventing wrinkling and damage during welding. For the RC, the challenge was to replace PDMS with the autoclavable material Polycarbonate (PC) as the RC's material and to bond the chip halves using absorber-free laser transmission welding (LTW). This process was underexplored in literature, particularly for uneven welding partners such as a thin foil welded to a bulk substrate. Therefore, a systematic investigation was carried out that evaluated parameters such as focal plane alignment, surface preparation, and weld interface geometry. A viable parameter set was established that enabled the manufacturing of functional PC RCs. Each of the four primary research areas, the design and optimisation of the MBR and RC, as well as the advancement of USW-based membrane integration and absorber-free LTW of PC, was addressed through a structured process of literature review, analytical design, experimental implementation, and evaluation. Application experiments performed in collaboration with the Joseph Gottlieb Kölreuter Institut für Pflanzenwissenschaften (JKIP) and the Institut de Biologie Moléculaire des Plantes (IBMP) demonstrated the usability and value of both MFCs. Fungal cultivation in the MBR was achieved successfully and the revised RC design was manufactured in PC for the first time. In conclusion, the devices and manufacturing strategies developed in this thesis provide robust platforms for biological studies in the context of sustainable plant protection, while laying essential groundwork for future research in microfluidic device design and manufacturing.

Acknowledgements

As I bring this dissertation to completion, I am reminded of the many people whose guidance, encouragement, and kindness made this journey possible.

First and foremost, I am thankful to Prof. Andreas E. Guber – my doctoral supervisor – for granting me the opportunity to pursue my research at the Institute of Microstructure Technology (IMT). The flexibility he afforded me and his sustained encouragement enabled me to focus on my work and to bring it to completion.

I also wish to acknowledge Prof. Jan G. Korvink, who kindly assumed the day-to-day supervision of my thesis after Prof. Guber retired from the IMT. Taking over a student and research topic is neither straightforward nor self-evident, and his patience and commitment proved essential for the completion of this dissertation.

During my time on this research I benefitted from the direct supervision of Dr. Ralf Ahrens and Dr. Dario Mager. I am grateful to both of them for the many insightful discussions, their thoughtful advice, and their willingness to offer support when difficulties arose along the path to finishing a dissertation.

I am obliged to Prof. Peter Nick for serving as the third examiner of this thesis and for the stimulating discussions within the DialogProTec project. Collaborating with him and his former PhD student Dr. Christian Metzger provided this research with numerous opportunities to test the Microfluidic Bioreactor (MBR) in laboratory conditions, resulting in insights that substantially improved its design.

Furthermore, I am grateful to Prof. Zanger for chairing the examination committee for this dissertation.

This thesis was carried out in the context of the DialogProTec project, and I wish to acknowledge my colleagues and collaborators in biology: Dr. Christian Metzger (Joseph Gottlieb Kölreuter Institut für Pflanzenwissenschaften (JKIP)), Prof. Etienne Herzog (Institut de biologie moléculaire des plantes (IBMP), Centre national de la recherche scientifique (CNRS)), Prof. Marie-Edith Chabouté (IBMP, CNRS), and Prof. Anne-Catherine Schmit (IBMP, CNRS). Working together on the development of the MBR and the Root Chip (RC) was both rewarding and inspiring. Your constructive feedback and laboratory expertise helped to shape the MBR and RC into more mature and effective designs.

The IMT and all its staff provided a nurturing environment for both research and writing. I owe a particular debt to the workshop, headed by Alexandra Moritz and her team André Wolfschläger, Reiner Heidt, and Andreas Bühler, for their practical assistance and unfailing readiness to help during this work. I am equally appreciative of Marc Schneider for his expertise in hot embossing and Richard Thelen for his meticulous measurements of structures too large for conventional microscopy yet too fine for simple photography. I am indebted to Dr. Uwe Köhler and the cleanroom team, as well as Jürgen Benz and Stefan Vietmeyer, for maintaining a safe and well-equipped workspace where advanced

fabrication could be carried out. I also extend my appreciation to Ida Humbert, Siegfried Roth, Marie Nowotny, Manuel Giraud, and Dr. Arndt Last, who assisted in many ways, from administration to laboratory matters. I am thankful to Dr. Kerstin Länge for trusting me, early in my time at the IMT, with the opportunity to co-author a review. Moreover, I am glad to the members of the Aktivpause for making Thursday mornings more dynamic and enjoyable. Finally, I wish to acknowledge my students Timo, Fabian, Zita, Eugenia, Tobias, Benjamin, Laura, and Yannick, whose efforts and questions constantly challenged me to refine the MBR and RC. Without all these contributions, this research would have been far more arduous and time-consuming.

I am particularly appreciative of the spontaneous help of Heino Besser (IAM-AWP), Konradin Kaiser (Microworks GmbH), Lars Riedel (IAM-WK), and Michaela Nagel (IAM-WK) in preparing the laser welding samples during the final months of my thesis. Your expertise and willing assistance yielded valuable insights into absorber-free laser transmission welding of polycarbonate. I further acknowledge the state of Baden-Württemberg for providing computational resources through bwHPC, which enabled the simulations presented in this work.

I am grateful to Dr. Christof Megnin (memetis GmbH) for giving me access to laboratory facilities to analyse samples efficiently at a crucial point of the project. I also appreciate the collaboration with Andreas Tegel and PreSens Precision GmbH, who supplied the optical pH measuring device employed in this thesis.

Beyond research, I am thankful to have found many friends during my time at the IMT. Sharing countless lunches, coffees, and cupcakes with Dr. Luisa Borgmann, Andrea Christina Hurtado Rivera, Dr. Markus Guttmann, Dr. Arzu Ergene, and Shraddha Singhal enriched my everyday life.

A special note of appreciation goes to my careful proof-readers – Dr. Luisa Borgmann, Dr. Jonas Zarzalis, Dr. Johanna Naumann, Thilo Hartleif, Dr. Christian Metzger, Prof. Etienne Herzog, Max Rödelsperger, Augustin Vestner, and Dr. Harshad Inamdar – whose meticulous feedback elevated this thesis.

Finally, it all begins and ends with family. I consider myself profoundly fortunate to have such a wonderful one. I owe my parents, Dr. Ursula and Karl-Heinz Schmidt-Speicher, the curiosity that inspired this research and the perseverance that carried it forward through all obstacles. I am deeply thankful to my sisters, Dr. Valerie Schmid and Dr. Alida Euler, for the many conversations in which they listened and thought things through with me. And most of all, I am grateful to Johannes Speicher, my husband, my partner in everything life presents, for his encouragement and for being my anchor whenever I needed one.

Contents

List of Abbreviations

A. thaliana	*Arabidopsis thaliana*
ABS	Acrylonitrile-Butadiene-Styrene
AM	additive manufacturing
BY-2	*Nicotiana tabacum* Bright Yellow 2
cb	Carbon Black
CMD	coverslip based microfluidic device
CNRS	Centre national de la recherche scientifique
CW	contour welding
DI water	deionised water
DMD	digital micromirror device
ED	energy director
EIP	electrolytic iron powder
ER	endoplasmic reticulum
ESR	Elegoo Standard LCD UV-Curing Photopolymer Rapid Resin
FEM	finite element model
FFF	fused filament fabrication
HAZ	heat-affected zone
HE	hot embossing
HEK-293	human embryonic kidney cells
IBMP	Institut de biologie moléculaire des plantes
IMT	Institute of Microstructure Technology
JKIP	Joseph Gottlieb Kölreuter Institut für Pflanzenwissenschaften
KIT	Karlsruhe Institute of Technology
LCM	laser-capture microdissection
LOM	Prusa UV Sensitive Resin Super Low Odor Magenta
LTW	laser transmission welding
MBR	Microfluidic Bioreactor
MFC	microfluidic chip
MS	Murashige- and Skoog
MW	mask welding
N. crassa	*Neurospora crassa*
N. parvum	*Neofusicoccum parvum*
N. tabacum	*Nicotiana tabacum*
nanoPOTS	nanodroplet processing in one pot for trace samples
O. sativa	*Oryza sativa*
PAR	Phrozon Aqua Resin
PASF	polyarylsulfone
PC	polycarbonate
PCW	primary cell wall
PDMS	Polydimethylsiloxane

PE	polyethylene
PET	polyethylene terephthalate
PFOTCS	trichloro(1H,1H,2H,2H-perfluorooctyl)silane
PI	polyimide
PLA	polylactic acid
PMMA	polymethyl methacrylate
PP	polypropylene
PRGM-Chip	Petaloid root-growth microfluidic chip
PS	polystyrene
QSW	quasi-simultaneous welding
RC	Root Chip
ROS	reactive oxygen species
RPN	Reference Point Numeric
RRB	NOVA3D LCD UV Resin 405nm Rapid Resin Black
RRC	NOVA3D LCD UV Resin 405nm Rapid Resin Cyan
SE	standard error
SLA	stereolithography
SoI	substance of interest
SW	simultaneous welding
tds	transport of diluted species
TWIST®	Transmission Welding by an Incremental Scanning Technique
USW	ultrasonic welding
WUM	Wärmeumformmaschine

1. Introduction

Crop protection is always key, not only, but especially, when preparing for a future with a changed climate. Although there are many forms of it, sustainable plant protection has been shown to offer significant economic, environmental, social, and health benefits [1]–[4]. There are several approaches to sustainable plant protection, such as biological, chemical, mechanical, and physical controls, as well as cultural practices. The DialogProTec project – within which this thesis was initiated – seeks to dissect, analyse, and ultimately functionalise communication between plants and their aggressors (e.g., fungi and pests). This places the project at the intersection of biological and chemical control. It combines aspects of biological crop protection, as its mechanisms resemble allelopathy, the biochemical interaction between plants, fungi, or pests [5], [6], with aspects of chemical crop protection, as it aims to develop targeted compounds or formulations [7]–[12].

In this context, two microfluidic chips (MFCs)[1] were designed, refined and manufactured within the scope of this thesis: the MBR for the cultivation and analysis of plant cells and fungi, and the RC for the *in planta* analysis of seedling root behaviour. These microfluidic chips offer valuable platforms for investigating fundamental processes relevant to sustainable crop protection, such as local and chemical communication pathways between distinct biological entities, or phenotype expression in response to specific stimuli. The MBR allows for controlled aqueous cultivation, either as a stand-alone device or in modular configurations where multiple MBRs are interconnected and perfused by a unidirectional flow, allowing communication analysis between separate cultivation chambers. The RC is designed for the cultivation and analysis of the roots of seedlings. In this way, the root growth behaviour can be directly analysed microscopically *in planta*.

Although this thesis is embedded in a biological research framework, it is by nature a technological study. Its main objective is to address the technological research gaps in MFC manufacturing – both in terms of design and process development. For instance, the MBR required a novel approach – and thus design – for installing ultra-thin membranes using ultrasonic welding (USW), avoiding membrane wrinkling or rupture of the membrane while ensuring leak tightness. In the case of the RC, a key challenge was to realise a chip from polycarbonate (PC) so that it could withstand autoclaving (contrary to its Polydimethylsiloxane (PDMS)-predecessor). Once it was determined that USW would distort the microchannel geometry, and glueing or mechanical fastening were not viable alternatives, absorber-free laser transmission welding (LTW) emerged as a potential solution, a method with very limited precedent in the literature, particularly for unevenly thick welding partners such as a foil welded to a bulk part.

This thesis is structured in several thematic layers. It begins with an overview of the design constraints and requirements for both MFCs in the following section. Next, the

[1] Microfluidic setups are generally referred to as MFCs. They can be used for but are not limited to a use in biological experiments. The Microfluidic Bioreactor (MBR) and the Root Chip (RC) are therefore specific types of MFCs with specialised characteristics and for a restricted use-case.

state of the art on the MBR (section 2.1) and RC (section 2.2) are discussed, highlighting the research gaps justifying further development of these MFCs. This is followed by an analysis of the manufacturing techniques involved. For the MBR, this includes a review of available literature on the installation of ultra-thin membranes using USW, which revealed a scarcity of data (section 2.4). For the RC, the choice of PC as chip material necessitated the exploration of absorber-free LTW, again addressing a largely unexplored topic in the literature (section 2.5).

Building on these insights, a detailed description of the development, refinement, and research on the necessary manufacturing techniques for each MFCs individually is given. Since the context of this thesis is still a biological one, the order of the MFCs is inspired by the size of the sample for which it is designed. The MBR is discussed first (in chapter 3), as it is created to house the basic building blocks of plants: plant cells. Next, the evolution of the RC is outlined (in chapter 4), which is created to cultivate whole seedlings and analyse their growth behaviour. The chapter of each device first describes the manufacturing of the initial design of the MFCs (sections 3.1 and 4.1), followed by describing the design adaptations and optimisations to the MFCs (3.2.1 and 3.2.3.3 and sections 4.2 to 4.4). The subsequent sections present dedicated investigations of the associated manufacturing techniques: wrinkle-free membrane installation in USW-bonded MBRs (3.2.3), and absorber-free LTW of PC with unevenly thick welding partners in the case of the RC (4.4.3.4).

In chapter 5, both MFCs and their respective applications are discussed. This includes experiments conducted in the collaborating biological laboratories of the DialogProTec project: The Joseph Gottlieb Kölreuter Institut für Pflanzenwissenschaften (JKIP) at Karlsruhe Institute of Technology (KIT), Karlsruhe, Germany, for the MBR, and the Institut de biologie moléculaire des plantes (IBMP) at Centre national de la recherche scientifique (CNRS), Strasbourg, France, for the RC. The thesis concludes with a summary in chapter 6. Additional technical details on materials, methods, or design considerations are provided in appendix A.

1.1 Requirements and general layout of MBR and RC

Both microfluidic chips presented in this thesis share a number of fundamental requirements. Requirements specific to each MFC are discussed in the sections following their respective design descriptions.

Since both MFCs are intended for the cultivation of plants or plant cells, they must be manufactured from biocompatible materials. A monomaterial design would be ideal. Furthermore, since optical observation of biological specimens is a standard analytical tool for biologists, the material must also be transparent. To avoid biohazards, the MFCs must be leak tight and be capable of sustaining cultivation for several days.

Furthermore, the MFCs must be sterilisable, preferably by autoclaving, according to the preferences of the collaborating biologists. The setups should be user-friendly and facilitate the introduction and extraction of samples for further analysis. From an engineering perspective, the MFCs should be relatively quick to fabricate – ideally within a couple of days for a batch of at least three devices. Lastly, the systems should be robust to minimise breakages and avoid the risk of sharp fragments in laboratory environments.

1.1.1 Microfluidic Bioreactor

Based on the work of Kreppenhofer [13] and Finkbeiner [14], the Microfluidic Bioreactor consists of two oval-shaped chambers stacked vertically (figure 1.1A). The lower chamber, termed the supply chamber, is perfused with nutrient medium. The upper chamber,

known as the cultivation chamber, contains the plant cells during experiments. These chambers are separated by a porous membrane fabricated by track etching. Depending on the experimental setup, the membrane pores have diameters of 5 µm, 3 µm, or 1 µm, effectively preventing plant cells from entering the supply chamber and thus avoiding cross-contamination between different MBRs.

Multiple MBRs can be connected via microfluidic inlets. Perfusion with a pump enables unidirectional flow through a series of MBRs, each containing different plant cell or fungal cultures. Figure 1.1B illustrates the general design of an MBR as well as a visualisation of the modular cultivation system.

For successful and reproducible experiments, it is crucial that uniform flow conditions are maintained within the chambers. To this end, the membrane must be installed without wrinkles to prevent disruption of the fluid flow. In addition, plant cells are highly sensitive to shear stress, which may be induced by fluid motion. To avoid cellular damage or stress, the device is designed for very low flow rates, typically up to 100 µL/min.

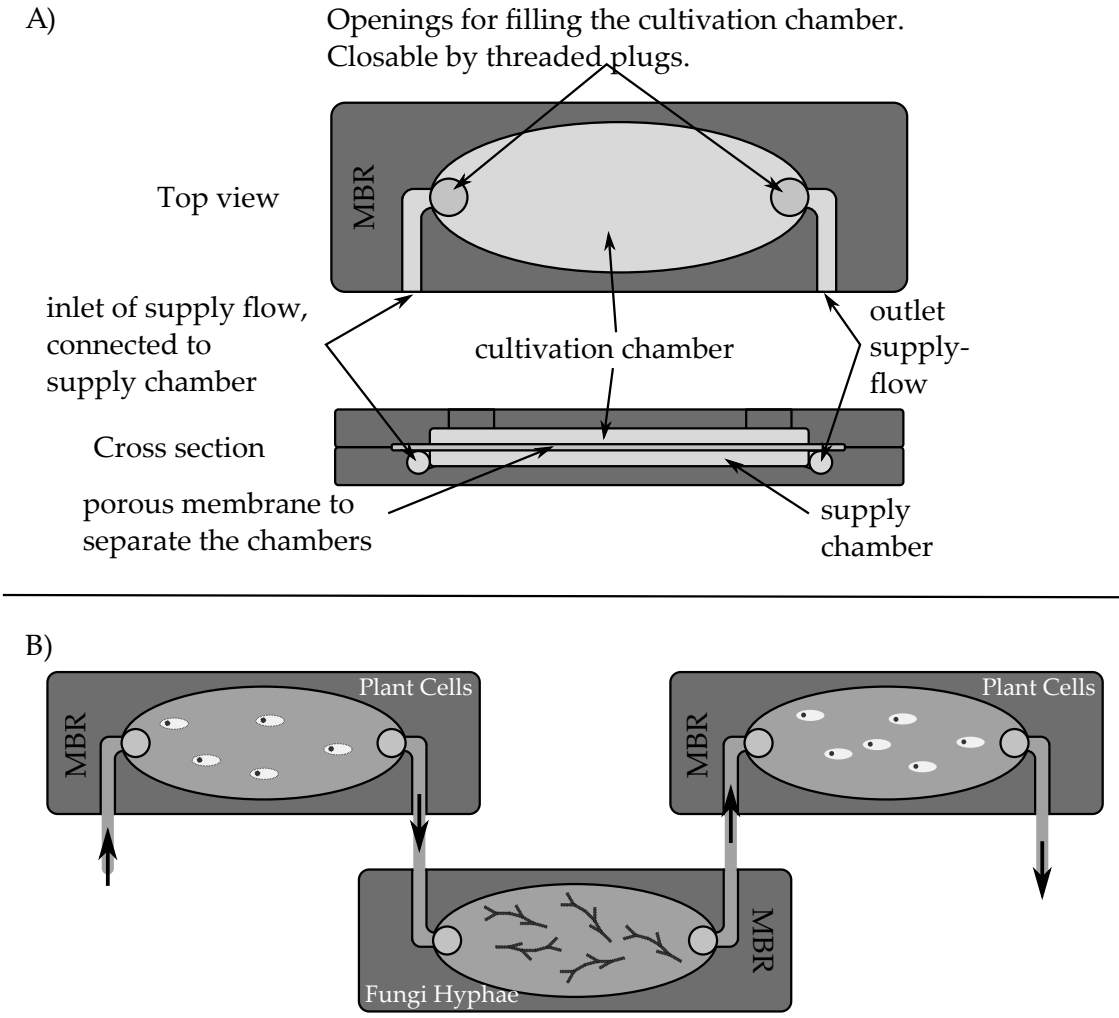

Figure 1.1: A) Conceptual sketch of the Microfluidic Bioreactor illustrating its basic design. Two oval chambers are separated by a porous membrane, allowing nutrient media to flow into and metabolites to exit the cultivation chamber, while retaining the plant cells. **B)** Visualisation of a modular cultivation setup with unidirectional flow through three individual MBRs.

1.1.2 Root Chip

The general setup of a Root Chip based on previously published literature (section 2.2) is described in the following. Each chip contains three individual compartments, each accommodating a single seedling for analysis. Seedlings are pre-germinated in shortened pipette tips and subsequently transferred to a seedling inlet angled at 45°. The root then grows from the transfer tip into the analysis channel.

The analysis channel begins at the point where the root enters the perfused section of the RC and continues to the outlet. Throughout this work, the channel has a square cross section of 200 µm in width and height. The total length of the channel depends on the chip design and varies between 28 mm, 35 mm, and 39 mm for the PDMS RC, the 9-channel RC, and the PC-RC, respectively. This allows for root growth over a period of at least 4 d. Continuous perfusion with nutrient or analytical solutions via inlet and outlet tubing supports root development while enabling experimental manipulation and observation of growth behaviour. Figure 1.2 presents a schematic overview of the general RC design.

Because many biological laboratories lack high field depth microscopes, the transparent wall that covers the analysis channel should be as thin as possible. This maximises the usable optical range for imaging root cells at different distances from the lens. In addition, the collaborating biologists had access only to inverted microscopes in their laboratory. Consequently, the RC was specifically designed to accommodate such optical analysis setups. Finally, since analytical compounds and substance of interests (SoIs) can be costly or difficult to obtain, it is a critical requirement for a well-designed RC to minimise the dead volume between the inlet and the entry of the seedling. This reduces unnecessary material waste and improves the efficiency of experiments.

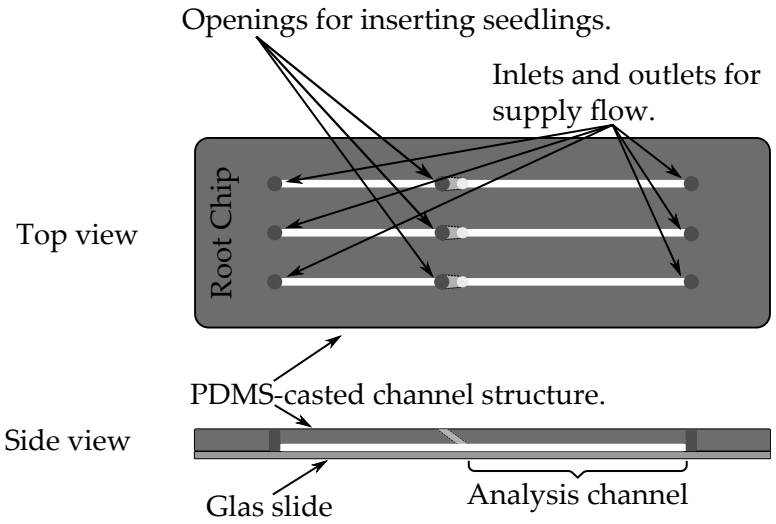

Figure 1.2: Sketch of the general design of the RCs. The analysis channel can be perfused with nutrient solution through the inlets and outlets. Seedlings are pre-germinated outside the chip in transfer tips, which are then inserted into the RC such that the root can grow along the channel.

2. State of the Art

The current public knowledge in research and industry underpins the development of the MFCs covered in this thesis and is accordingly summarised in the following subsections. Both microfluidic chips described here enable the controlled cultivation of specimen – plant cells, fungi, or seedlings – within a microfluidic setup. Compared with conventional macro-scale assays, the MFCs allow a more controlled cultivation and thus, produced biological responses that more closely match *in planta* outcomes under similar environmental impacts. To root the MFCs in the scientific landscape, first, scientific publications on similar setups for plant cell cultivation (section 2.1) and root analysis (section 2.2) are examined to further establish the necessity and potential of research on the MBR and RC. Next, to include not only the scientific but economical interest in the MFCs covered here, an analysis of the commercial potential – which was assessed through an online questionnaire (section 2.3) – is presented. The chapter concludes with discussing challenges in manufacturing such MFCs, focusing on issues and current solutions related to ultra-thin polymer film installation (section 2.4) and the LTW of polymers (section 2.5).

2.1 Plant cell cultivation using microfluidics

As established, the MBR enables monitored cultivation of plant cells. By exchanging the installed membrane, it can be adapted for fungal cultivation. It also permits straightforward downstream interconnection of multiple MBRs, facilitating studies of communication between individual cultivations. When two or more MBRs are connected in series with unidirectional perfusion, soluble factors produced upstream causally and directionally modulate outcomes in a downstream MBR, while reverse modulation is absent under identical conditions. An externally sterilisable sensor screw enables integration of optical sensors in close proximity ($< 1\,\mathrm{mm}$) of the cultivated specimen while maintaining a sterile, leak-tight seal of the cultivation chamber after insertion of the plant cells to be analysed. Together, these features constitute novel approaches to plant cell experimentation, laying the foundation for further advances in sustainable plant protection research. The concept has neither been extensively explored nor widely studied. To contextualise the development of the MBR, the following paragraphs introduce research and advances in plant cell cultivation within microfluidic devices. The discussion begins with an overview of manufacturing techniques and sensing setups employed in such systems, followed by an examination of the key research areas that have emerged in MFC applications in plant-related studies.[1] For a chronological review of research publications on microfluidic devices for plant cell or protoplast[2] cultivation, further details can be found in appendix B. Research on MFCs for

[1] A detailed distinction between MFCs and the MBR is provided in chapter 1. In short, microfluidic setups are generally referred to as MFCs, while the MBR is a specific type of MFC with specialised characteristics.

[2] A protoplast is a plant cell with its cell wall enzymatically removed, leaving the plasma membrane intact. Without the rigid wall, it is softer and more deformable, making it easier to handle and trap in microfluidic setups than intact plant cells [6].

plant root analysis is addressed separately in section 2.2 and appendix C due to its greater relevance to this thesis and the advancement of the RC (more details on its development in chapter 4).

MFCs for plant-related research are predominantly manufactured using PDMS-cast channel structures bonded onto a glass slide [15]–[31]. Alternative manufacturing approaches include additive manufacturing (AM) [32], the assembly of multiple patterned or functionalised glass slides [33]–[36], shear-spun scaffolds from polyethylene terephthalate (PET) or polylactic acid (PLA) [37], and the use of materials such as PC and PET, fabricated through techniques such as micromilling, thermoforming, and welding [14], [38], [39]. These latter manufacturing techniques are particularly relevant to one of the core topics of this thesis – the design and fabrication of the MBR. Among publications employing PC or PET, only one is not a direct predecessor of the current MBR and originates from a different research group: Comtet *et al.* [39] describe an MFC constructed by stacking multiple layers of PET, PC, and polyvinyl chloride, sandwiched between aluminium sheets and secured with screws. Their microfluidic setup withstands pressures of up to 1.07 MPa, a requirement for studying passive phloem loading. However, this system differs significantly from the low-flow cultivation design of the MBR, both in function and assembly techniques, and therefore does not provide relevant insights for the latter's development and refinement. In contrast, two other publications are directly linked to the MBR, having been developed under the same supervisor as this thesis, Andreas E. Guber [14], [38].

Aside from [14], [38], nearly all literature on MFCs for plant-related research presents stand-alone setups that are not designed for interconnection [15], [16], [18], [21], [24], [26], [29], [30], [32]–[37], [39], [40]. Few platforms in plant-related research are designed for sample preparation, with subsequent analysis performed on MFCs down the line [17], [19], [20], [23], [25]. The MBR is unique in presenting a fully modular setup. Initially, it was created to model the metabolism of a single plant through connecting several individually cultivated cell types of the plant [14]. In this work, this approach has been expanded for the controlled dissection of intra- but as well interkingdom communication between individual cultivations.

The third aspect relevant to this thesis is sensor implementation. In plant-related research, most on-chip analysis relies on electric fields, controlled via electrodes deposited onto the base substrate, such as a glass slide. These electrode-based setups have been developed by [17], [19], [27], [28], [31]. Another, less common approach is the integration of a force sensor on a PCB [40]. Standard optical microscopy is also widely used, and in this overview, it is considered only when applied for extended periods to measure experimental parameters [15], [16], [18], [21], [24]–[26], [29], [30]. Additionally, some authors analyse fluid samples after they have passed through the chip [14], [38]. Overall, MFCs for plant-related research are typically designed to accommodate specific measurement techniques that are fixed onto the chip and not interchangeable. The MBR, however, introduces an adaptable and exchangeable sensor-screw (3.3.1), a concept that has not been explored in such detail before.

The available publications can be broadly categorised into *baseline papers* and *application papers*. The former introduce new microfluidic setups, examining aspects such as the viability of cultivations, optimal channel designs, and experimental accuracy, often concluding with a proof-of-concept experiment. The latter are typically follow-up studies involving the original researchers, in which previously established setups are applied to biological experiments. While minor design or parameter adjustments may occur, the focus remains on experimental application. A notable example is the nanodroplet processing in one pot for trace samples (nanoPOTS) platform: Zhu *et al.* [33] presented the baseline paper, while

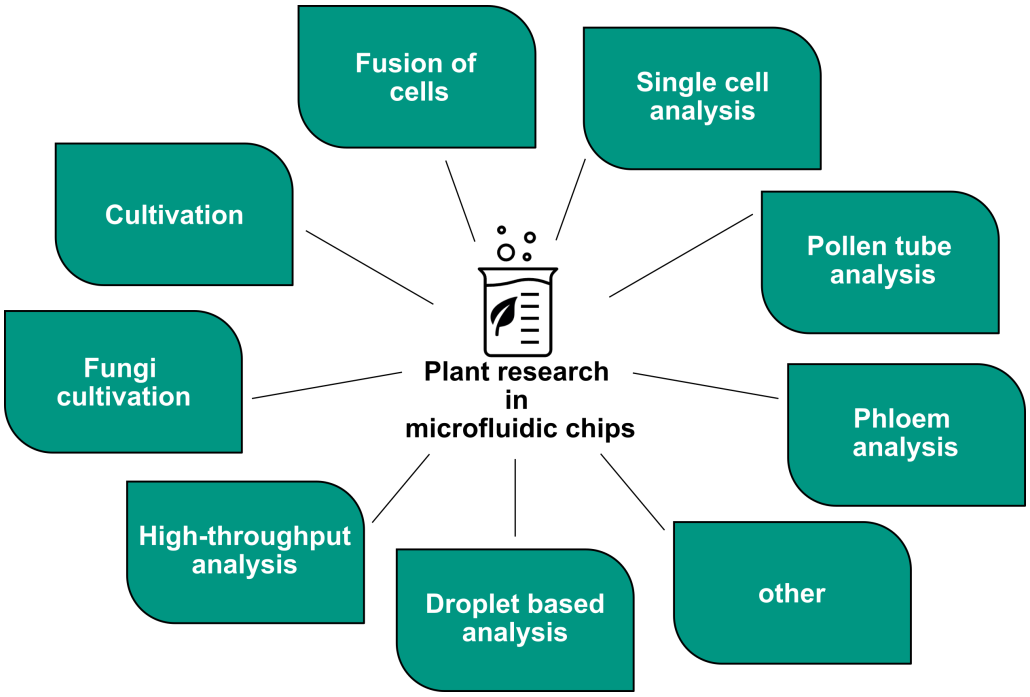

Figure 2.1: Overview of research topics explored in publications on plant studies using MFCs. Literature on plant root analysis with MFCs is addressed separately in section 2.2 and is therefore not included in this overview

Liang *et al.*, Zhu *et al.*, Balasubramanian *et al.* [34]–[36] subsequently applied the system in biological studies.

Compared to other fields, there are relatively few publications on MFCs for plant-related research, with published studies spanning only two decades. These microfluidic setups have been applied across various research topics with many designs, manufacturing techniques, and approaches overlapping between subfields. To fully contextualise the MBR, it is necessary to consider the entire spectrum of MFCs for plant-related research, rather than focusing solely on cultivation setups. To maintain conciseness, overlaps with microfluidic devices for bacterial or mammalian cell research are not discussed.

The field of plant-related research using MFCs can be broadly categorised into seven subtopics: straightforward cultivation setups, cell fusion, single-cell analysis, pollen tube analysis, phloem analysis, droplet-based analysis, and fungal cultivation (see figure 2.1). The following paragraphs provide a brief introduction to each of these areas. Further chronological details on key publications can be found in appendix B.

The first publication in this field was a proof-of-concept study demonstrating the feasibility of cultivating plant protoplasts within an MFC [15]. Following this approach, this text begins with the topic of straightforward cultivation setups. Publications in this area primarily consist of baseline studies aimed at determining whether specific plant cells, protoplasts, mosses, or fungi can be cultivated within a given MFC without affecting the specimen's response to treatments or compromising its viability [15], [16], [22], [25], [26], [30], [37]. To achieve this, studies have investigated variations in channel height and width, comparing them to standard cultivation methods such as Petri dish or coverslip cultures [26]. Additionally, novel material combinations for cultivation have been explored [37], and proof-of-concept experiments have been conducted to demonstrate cell viability within these setups [15], [16], [22], [25], [26], [30], [37].

Building on the work of Ko *et al.* [15], Cao *et al.* [17] introduced a microfluidic approach for protoplast fusion in 2008 [17]. The fusion of different cells is relevant because it enables the generation of hybrid cells tailored to specific research applications. This technique is widely used in fields such as cloning, cancer immunotherapy, and antibody production, but it also plays a role in plant research, particularly in the development of novel pharmacological compounds. The process involves bringing two cells into close proximity, disrupting their membranes, allowing them to merge, and subsequently enabling them to regenerate a unified cell wall. Membrane disruption can be achieved through chemical treatment, pulsed electric fields, or precise laser manipulation. Microfluidic setups are particularly suitable for cell fusion, as they allow for precise cell positioning, thereby improving the efficiency of the initial contact step. A major focus in the development of these systems has been increasing fusion efficiency: The proportion of successfully fused cells that remain viable for subsequent experiments [17], [19], [20], [25], [31]. Early chemically induced fusion methods outside MFCs reported fusion efficiencies as low as 1 % [17], whereas electrofusion techniques within microfluidic setups have since achieved efficiencies exceeding 80 % [30].

Single cell analysis has been a field of interest in microfluidic setups for over two decades. However, it covered only bacteria and mammalian cell related research. Since 2020 two research alliances have formed that apply single cell analysis in plant-related research as well [27]–[29], [41], [42]. One was formed around Jiehua Wang and Xuexin Duan and design MFCs that analyse properties of many individual cells instead of getting a unified readout from a larger mass of cells (like from a Petri dish cultivation) [27], [28], [42]. The researchers around Kazunori Shimizu create their MFCs to be able to monitor specific plant cells – which have to be cultivated in aqueous suspension, thus not-fixed – over longer periods, thus finding a way to anchor plant cells (or strands of cells) in place without influencing the outcome of the experiments [29], [41].

Pollen tube analysis investigates how pollen tubes navigate towards ovules. Before the introduction of microfluidic setups for this purpose in 2011, monitoring pollen tube growth was highly challenging. Studies either relied on in situ observations within plant tissues, where visibility was limited, or on Petri dish cultures, which provided an unnatural environment and altered growth behaviour. While microfluidic setups do not fully replicate natural conditions, they offer more controlled environments with minimal external interference while allowing continuous optical monitoring [18], [21], [40], [43], [44].

As outlined in appendix A.5.2, phloem is a critical plant tissue responsible for bidirectional transport of sugars and nutrients produced during photosynthesis. Its counterpart, xylem, carries water and dissolved minerals from the roots upward through passive flow. While the fundamental functions of these tissues are well understood, current research focuses on topics such as plant responses to stress (e.g., drought or disease) and the transport of signalling molecules such as hormones [32], [39], [45]–[47]. Microfluidic setups can be adapted to meet the specific requirements of phloem and xylem research, though these setups differ significantly from those used in plant cell culture. Consequently, they are only briefly covered in this thesis. Unlike low-flow plant cell cultivation setups, these systems must withstand pressures of several MPa [39]. Additionally, high 3D structural complexity is often required to replicate fluid dynamics within plant vasculature [32].

The use of droplet-based microfluidics has gained traction across multiple research fields. Common approaches include digital microfluidics, where droplets are manipulated via electric fields, and carrier oil droplet encapsulation, which isolates small sample volumes in an aqueous flow. A key advantage of droplet-based microfluidics is the minimal sample volume required, which is particularly beneficial in plant research where some compounds are difficult to extract in large quantities [33]–[36], [48]. These systems also facilitate single-cell studies by preventing cells from being lost within suspension cultures [23], [29].

An objective of this dissertation is to adapt the MBR to fungi-cultivation (3.2.1). Despite extensive research on fungal biology and interactions, microfluidic-based fungi studies remain rare. The only reported studies are those by Held et al. [16], [24], which utilised PDMS-based chips produced via soft lithography (cf. appendix A.1.2). These studies demonstrated the successful cultivation of *Neurospora crassa (N. crassa)*, revealing strong directional memory in fungal hyphae [16] and linking this behaviour to the Spitzenkörper, a vesicle-organising structure at the hyphal tip [24].

In conclusion, research on modular MFCs remains limited. As shown, only a few published setups are designed for interconnection rather than stand-alone operation, and none address intercellular communication within a modular system. Reports of fungal cultivation in an MFC are scarce, and none employ a PC-based setup. Adaptable and interchangeable sensor implementations – such as the sensor screw in the MBR (3.3.1) – have not yet been investigated in detail. Moreover, nearly all MFCs in the literature rely on PDMS-based designs, which pose challenges for sterilisation, leakage, and unintended interactions between cultivated cells and material compounds (cf. appendices A.1.2 and A.3.1). These gaps underscore the need for further research and development of the MBR.

2.2 Root analysis using microfluidics

The RC described in chapter 4 answers several necessities. It provides a simple yet efficient platform to study the development of a seedling's root *in planta*. Furthermore, adapted designs of the RC provide the option to easily, yet variably administer different compounds to the seedling's root in the analysis channel. Finally, in section 4.4 an RC made from PC is presented, which can be sterilised through autoclaving. Although several publications on Root Chips have emerged since 2010, this remains an often overlooked research area in plant studies, with relatively few contributions compared to conventional biological research on root growth and behaviour. This may be due to the interdisciplinary nature of the field, which often requires collaboration between research groups in Microsystems Engineering and Plant Root Biology. Before detailing its development in chapter 4, this text provides an overview of microfluidic approaches in plant root research. It begins by covering key aspects of plant root studies, followed by a description of the general design of MFCs used for cultivating and analysing plant roots. For additional information, a chronological summary of relevant publications can be found in appendix C.

Root analysis is generally conducted using one of two approaches: roots are either grown in soil or within a (micro-)fluidic setup.

When cultivated in soil, roots develop a natural rhizosphere (see appendix A.5.2). However, analysing roots in this environment is challenging. One approach is to extract the root for measurement and microscopic examination, but this always carries the risk of damaging vital structures [49], [50]. Another method involves growing the root in a specialised *Rhizotron*, a narrow box with transparent glass or polymer windows, allowing researchers to observe interactions between the root and its surroundings, such as soil and microorganisms [51]–[53].

Over the past decade, non-invasive techniques such as magnetic resonance imaging and X-ray computed tomography have also been applied to root analysis, enabling the generation of virtual 3D models of root systems [54]–[56]. However, these methods still face challenges, particularly in achieving sufficient resolution. Consequently, much of the research in this area has focused on improving and automating image processing, as demonstrated by Van Dusschoten *et al.* [55] and Selzner *et al.* [54].

This thesis focuses on microfluidic devices for root analysis. One of the key advantages of these systems lies in their scale: the microfluidic environment requires only minimal

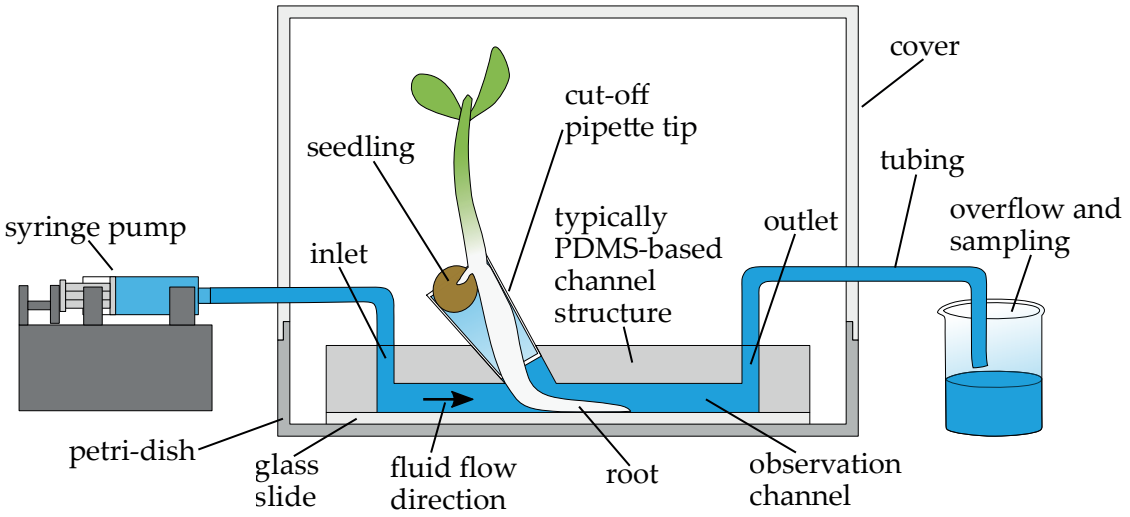

Figure 2.2: Schematic sketch of the general underlying setup of MFCs for root analysis. Publications typically contain the majority of the depicted elements, but – of course – are not limited to this setup. Often, the root is analysed microscopically from underneath using an inverted microscope. Sampling the overflow and testing it for certain chemical compounds has been reported, too. Instead of a single analysis channel – as depicted in this cross-section – usually three or more channels are manufactured onto one chip setup to allow the growth of several roots simultaneously. This sketch is based on [59]–[62], [64], [65], [68], [69].

amounts of substances, reducing the cost of often expensive reagents. Additionally, analysis can be conducted more efficiently, as small reaction volumes lead to faster experimental processes and lower energy consumption. This makes microfluidic approaches highly cost-effective for plant research [57]–[59]. So far, microfluidic Root Chips have primarily been used to study root tip regions involved in growth [59]–[67] or root hair formation [68]–[71]. Consequently, these setups are frequently employed for cell- or subcellular-level analyses. In recent years, a small number of systems have been developed to investigate rhizosphere interactions, focusing on root-bacteria relationships and the influence of surrounding chemical environments [72]–[75]. However, publications on MFCs for root analysis remain significantly less frequent compared to comparable lab-on-a-chip devices designed for human cell or bacterial research.

The general design of MFCs for root analysis follows a standard pattern, as illustrated in figure 2.2. These chips feature inlet and outlet ports connected to a tubing system, which facilitates the delivery of nutrients and other substances, such as bacteria or chemicals simulating stress conditions like drought. The root itself is introduced through a separate inlet and typically grows along a downstream channel, following the direction of flow. To transfer pre-germinated seedlings into the MFC, researchers often use cut-off pipette tips or funnel-shaped pipes. The entire setup is commonly housed within a closed Petri dish or a polymer-based enclosure to maintain stable growth conditions, such as controlled humidity, while minimising external influences.

Seeds selected for examination are typically germinated outside the chip in media such as agar. This approach ensures that only properly oriented seedlings are used, while excluding those that have germinated upside down or exhibit developmental abnormalities [59], [60], [62], [64], [67]–[70], [73]–[75]. However, some studies have explored in-chip germination methods [61], [63], [65], [66], [76], [77]. Once transferred to the MFC, seedlings are typically nourished using liquid media such as Murashige- and Skoog (MS)-media or the Hoagland solution.

Microfluidic Root Chips are generally fabricated by bonding a PDMS-cast containing the required channels and cavities to a glass slide, which serves as the bottom plate [59], [61], [62], [64]–[69], [71], [73]–[75], [78], [79]. The transparency of the glass slide allows microscopic analysis of the root using both optical and fluorescence microscopy. One publication by Busch *et al.* [60] introduced a stereolithographically printed chip as an alternative approach. However, no work has been published on replication techniques such as injection moulding or hot embossing, which could facilitate large-scale production of MFCs, a crucial requirement for high-throughput screening applications.

As with research on MBRs, the published approaches to MFCs for plant-root analysis leave substantial under-explored ground. Few studies propose RCs that are sterilisable by autoclaving, since most rely on a PDMS-cast device sealed with a glass slide or a second PDMS-cast, which cannot be sterilised in this way. In addition, only a small number of set-ups enable the controlled yet variable delivery of different compounds within an MFC for root analysis. These gaps motivate the development and refinement of the RC, with further details provided in chapter 4.

2.3 Commercial potential of the MBR and Root Chip

When designing a new microfluidic setup, it is sensible to consider not only its necessity in research but instead examine the possibilities for manufacturing it and the interest of the according industry as well. Therefore, in collaboration with Eugenia Pawlenko, a study was conducted among commercial MFC manufacturers and research institutions to enquire about the interest in research cooperations and the willingness for a wider production of the MBR developed at the Institute of Microstructure Technology (IMT). The following paragraphs summarise the findings. Further details are available in E. Pawlenko's Master's thesis [80].

This expands the previous commercial analysis on an earlier version of the MBR carried out by [14], which focused solely on the manufacturing cost: There, a comparison between the manufacturing techniques hot embossing and injection moulding as well as the bonding methods laser transmission welding and ultrasonic welding was conducted. For research purposes – meaning lower production volumes – the combination of hot embossing and ultrasonic welding was recommended, considering only the manufacturing cost and time [14] but not the industries interest in the MBR.

In contrast, in the current questionnaire, participants were specifically asked about their interest and potential application of the MBR. For the survey, 34 manufacturers and research institutions focusing on microfluidic setups for plant and mammalian cell analysis with potential interest in manufacturing or working with the MBR in Germany, France, Switzerland, the Netherlands, and Austria, were contacted. Out of these, eight completed the online questionnaire on what materials they frequently worked with, which methods for part replication and bonding of chip parts they applied, what ways of sterilizing they used for a completed product, and, in particular, if they were interested in working together to make the MBR available to a wider audience.

It was found that polymers – such as polymethyl methacrylate (PMMA), PC, and cyclic olefin copolymer – or glass are predominantly used in the production of microfluidic chips. The chip components are mostly manufactured using injection moulding or 3D printing and are then bonded together either by glueing or through thermal or plasma bonding.

Additionally, seven participants use coatings to optimise the base materials. For example, the Fraunhofer Institut für Biomedizinische Technik utilises collagen and Matrigel to promote cell adhesion or as a foundation for cell culture growth. Only two participants,

Fraunhofer Institut für Biomedizinische Technik and microTEC, produce membranes themselves, whereas seven confirm processing purchased membranes. Two participants stated the ability to sterilize products thermally or chemically in-house, while five manufacturers prefer to collaborate with external service providers for this.

Overall, the manufacturers generally appeared interested in the MBR and MFCs discussed in the questionnaire. However, an emphasis was put on that many pieces of information fall under trade secrecy. Consequently, they should be contacted with concrete proposals for possible collaboration.

2.4 Installation of ultra-thin polymer films

Dissecting plant-aggressor communication, e.g. between plants and fungi, is central to achieve sustainable plant protection and requires adapting the Microfluidic Bioreactor for fungal cultivation. This warrants replacing the membrane that separates the cultivation and supply chambers. Membranes with sufficiently smaller pore sizes to retain fungal hyphae, which were available to this work, are significantly thinner, which complicates installation. Before discussing approaches for installing such membranes in the MBR (3.2.1 and 3.2.3), the following sections review previous research on installing polymer films and membranes. Three main installation processes are discussed: Heat welding (see 2.4.1); an overview of the industry's standard polymer-processing technique, ultrasonic welding (2.4.2); and, concluding the overview, a more flexible bonding method, laser transmission welding (2.4.3).

Before proceeding, it is necessary to define the terms *foil*, *thin film*, and *membrane*. Focke *et al.* [81] define a foil as a semi-finished part of any material that is thinner than 500 µm and of flexible character [81]. In the literature, a *thin film* is generally considered to have a thickness of several hundred micrometres [82]–[86]. Of course, this classification generally depends on the material in question. A film is called *ultra-thin* when its thickness ranges from several hundred nanometres to a maximum of 100 µm [87]–[89]. This last definition will be applied for this work.

Membranes can be regarded as a subcategory of films, specifically ultra-thin functionalised films [81], [90]. In this thesis, a membrane is further defined as a porous film with a controlled permeability.

2.4.1 Heat welding approaches

The simplest method for bonding two thermoplastic polymers without using adhesives is to heat the materials above their glass transition temperature T_G, press them together to form a bond, and then allow them to cool so that the bond solidifies. This process – known as heat welding or hot plate welding when two heated plates are used to apply heat and pressure – has been widely employed in the polymer industry for several years [81], [91]–[93]. However, depending on the material, this process can have a significant impact on the films and membranes being installed. Iwasiro *et al.* [93] reported that a PET film could not be securely bonded to a PMMA flask body to create a waterproof seal, as it detached easily. Similarly, Scheffler and Leao [92] observed severe wrinkling and geometric deviations when producing air mattress-like heat transfer elements due to the pronounced thermal expansion and contraction of polypropylene (PP). A related issue was noted by Kreppenhofer [13], who found that thin PC-, PET-, and PI-membranes sagged to the bottom of the chamber during sealing when the microfluidic chip halves were closed.

Due to these challenges, an alternative bonding process – ultrasonic welding – was utilised for membrane installation in the MBR, (cf. 3.2.1 and 3.2.3).

2.4.2 Ultrasonic welding approaches

Ultrasonic welding has been a well-established method for bonding thermoplastic polymers since the 1960s (appendix A.3.2 provides further information of its working principle, machine setup, process controls, etc.). It is particularly suited for applications requiring a more focused and controlled energy input than general heat welding (see 2.4.1). USW is widely used for polymer bonding, particularly in packaging applications such as food packaging and blister packaging for medical pills, which are well documented in the research community [81]. However, sample images presented in studies such as Dobrotă and Lazăr [84] indicate that films are often installed with wrinkles, and concerns have been raised regarding potential damage to electronic components due to vibrations induced by USW, as reported by Dahlstrand [94].

Despite its widespread application, there is limited literature addressing the *diaphragming effect* or *oil-canning effect* – a core challenge for adapting the MBR for fungal growth. This phenomenon refers to the strong oscillation of a thin membrane or film welded across a larger cavity or opening due to vibrations introduced by USW. This oscillation can lead to film wrinkling caused by stretching, tearing, improper adhesion, or complete detachment [94], [95].

Dukane Intelligent Assembly Solutions [95], a manufacturer of USW equipment, has suggested that this effect may result from excessive vibration amplitude and recommends either damping the welding area to absorb the high amplitude or increasing the welding system's frequency – an approach that typically requires the acquisition of new equipment [95]. However, no further studies on this issue have been identified, which is unexpected given that wrinkled films and membranes can cause system malfunctions like unwanted voltage fluctuations in batteries or uneven flow conditions in microfluidic chips.

2.4.3 Laser welding approaches

In terms of contour flexibility, ultrasonic welding has a significant disadvantage: modifying the welding contour requires a complete redesign and precise manufacturing of either the welding components or the sonotrode, making quick adjustments impossible. In contrast, this is one of the major advantages of laser transmission welding [86], [96]–[98]. As detailed in appendix A.3.3, LTW enables a remote and highly localised introduction of energy through the absorption of focused laser light in small polymer areas.

Several publications have explored laser welding of polymers, though most focus on bulk materials, similar to the available literature on USW. Relevant studies concerning the bonding of RC chip halves are reviewed in section 2.5. Research on welding thinner films or membranes primarily addresses applications in the (food) packaging industry [86], [99]–[101], as well as in microfluidics [102], micro electro mechanical system-scale devices [96], and the joining of dissimilar polymer films [103]. Most of these applications employ either an absorber layer in the lower welding partner [101], the introduction of an absorber dye [100], or a sputtered absorber layer positioned between the polymers to be joined [96], [102], [103]. Very few reports discuss absorber-free LTW (see appendix D.1 and 2.5.1 for further details).

One of the key advantages of LTW – its ability to concentrate high energy into small areas – simultaneously poses a major challenge, as it can easily lead to polymer degradation [101]. Additional challenges include ensuring proper clamping of the components to prevent misalignment or air entrapment, which could lead to ignition [96], [99]. Furthermore, rapid and intense temperature fluctuations in the polymer can cause severe distortions or film sagging [96], [99], [102]. Achieving high weld quality without defects presents another difficulty, with potential issues including humping, excessive bubble formation within the

weld seam, a burnt inner zone, or an unbalanced seam structure due to an excessively offset heat-affected zone [86], [100]–[104].

Limited information is available on laser welding of PC, which is particularly relevant for bonding the PC chip halves of the RC, as discussed in 4.4.3, specifically 4.4.3.6. Notably, no studies were found that investigated absorber-free LTW of PC in the context of bonding a thin film to a bulk substrate in either a contour or quasi-simultaneous welding setup, as performed in the aforementioned subsection.

This concludes the overview on the research on installing thin or ultra-thin foils and membranes using either heat welding, ultrasonic welding, or laser transmission welding. Few publications dealt with it and none provide a sufficiently wrinkle-free installation approach. However, despite the absence of prior success, ultra-thin membranes can be installed wrinkle-free and leak-tight in the Microfluidic Bioreactor as shown in 3.2.1 and 3.2.3.

2.5 Laser transmission welding of bulk PC parts

Refining the MFCs for DialogProTec to be sterilisable by autoclaving is a key objective. Because the setups must also be biocompatible, transparent, and shatter-resistant, PC was selected for the MFCs. The chip halves are bonded by either USW or LTW. Absorber-free laser welding of PC is relatively recent (about 10 yr old), and little information is available. The following sections review publications on absorber-free laser welding of PC and on welding partners of uneven thickness where at least one is PC. The overall objective is to yield hermetic PC-bonds suitable for application in an MFC using absorber-free LTW.

Beyond the requirement for optical transparency – which already excludes any absorber-based LTW method that relies on absorbers altering the colour of the absorbing part – the material for the microfluidic chips should be as pure as possible. This minimises the presence of additives that could interact with cultivated specimens. For this reason, even colourless dyes such as ClearWeld™ [105] were not considered a viable option for an absorber-based approach, leaving absorber-free LTW as the only possibility.

The following paragraphs first present literature on absorber-free laser transmission welding of PC in 2.5.1, as it is most relevant for bonding the chip halves of the RC in 4.4.3.6. This is followed by a discussion of contributions on laser welding of components with uneven thicknesses, such as bonding a 2 mm PC sheet to a 4 mm polystyrene (PS) substrate, in 2.5.2. This topic is particularly relevant because the laser transmission welded microfluidic chip examined in 4.4.3.6 consists of a 3 mm substrate covered with a 300 µm film. An overview of further key publications from the past 20 years that have contributed directly or indirectly to the field of absorber-free LTW is provided in appendix D, where they are categorised into absorber-free and absorber-based LTW.

2.5.1 Absorber-free LTW of PC

In absorber-free LTW (cf. appendix A.3.3), the laser energy is absorbed across the entire thickness of both welding partners. Wherever the absorbed energy exceeds the welding temperature, a heat-affected zone is formed. In absorber-based LTW, a clear distinction can be made between the weld core, the weld seam, and the heat-affected zone (HAZ). In contrast, in absorber-free LTW, only the heat-affected zone is distinctly visible in cross-sections, and therefore no further differentiation is made between the weld seam and the HAZ. Figure 2.3 presents a conceptual illustration of the principle of absorber-free laser transmission welding.

The most recent publication on absorber-free laser transmission welding of polymers – specifically PC and PP – is the 2023 dissertation by Nguyen [106]. His research examines

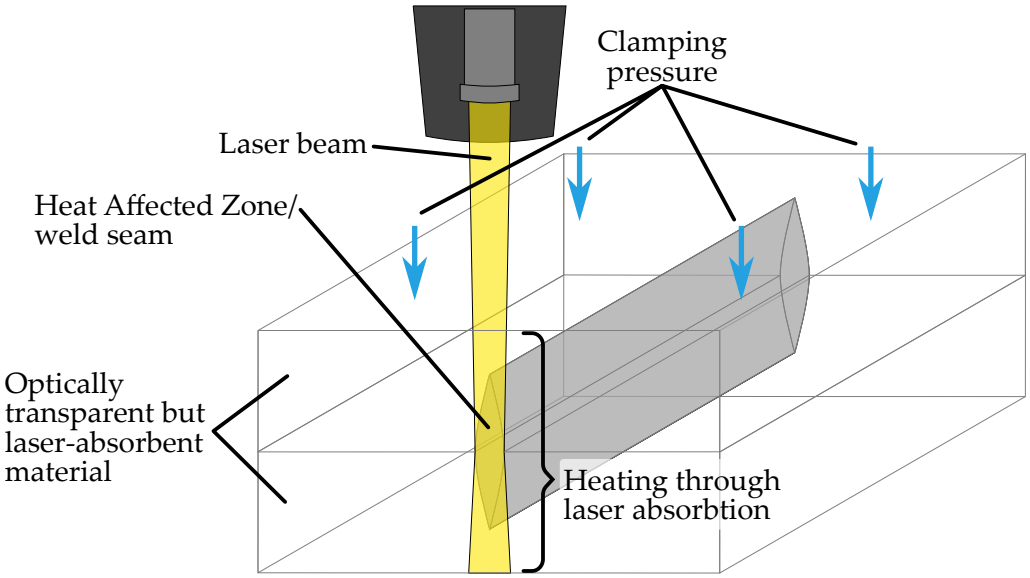

Figure 2.3: Working principle of absorber-free laser welding. The laser light is absorbed by both welding partners throughout the entire stack. Wherever the absorbed energy exceeds the melting temperature of the welding partners, an HAZ/weld seam is formed. The workpieces are pressed together, which facilitates the formation of the weld.

how irradiation can be locally confined to the welding interface, how material structure influences the HAZ, and how weld seam quality can be assessed non-destructively. The most relevant findings for the research in 4.4.3 include:

1. Using contour welding (CW), energy deposition during welding can be controlled to some extent in the z-direction by adjusting the focal plane. This is particularly useful for welding materials of uneven thickness, such as bonding a covering foil to a substrate, as done in this thesis. Figure 2.4 illustrates how the HAZ position in PC can be adjusted in the z-direction. The more gradual energy deposition of quasi-simultaneous welding (QSW) consistently results in the HAZ forming at the centre of the overall material thickness due to heat accumulation. This eliminates the need for fine focal plane adjustments, simplifying the process setup. However, when using QSW, similar material thicknesses are recommended for a successful weld.

2. Finer weld seam widths between 50 µm and 150 µm can be achieved in PC using CW, whereas QSW produces a preferable relative ratio of weld width to height. A higher ratio indicates a broader weld seam in relation to the heat-affected height, which is advantageous, as weld width contributes more significantly to mechanical strength than seam height.

3. Closely spaced weld seams influence each other in both width and height. Nguyen [106] identified appropriate cooling times for adjacent welds, examined the effects of neighbouring seams, and tested weld seam segmentation. Without cooling time, heat accumulation from neighbouring welds increases the substrate temperature, leading to greater seam height and width. To maintain consistent weld dimensions, segmenting the weld path was found to be beneficial, allowing sufficient cooling between passes [106].

Due to the recent publication of his dissertation, only the first two findings could be incorporated into this thesis.

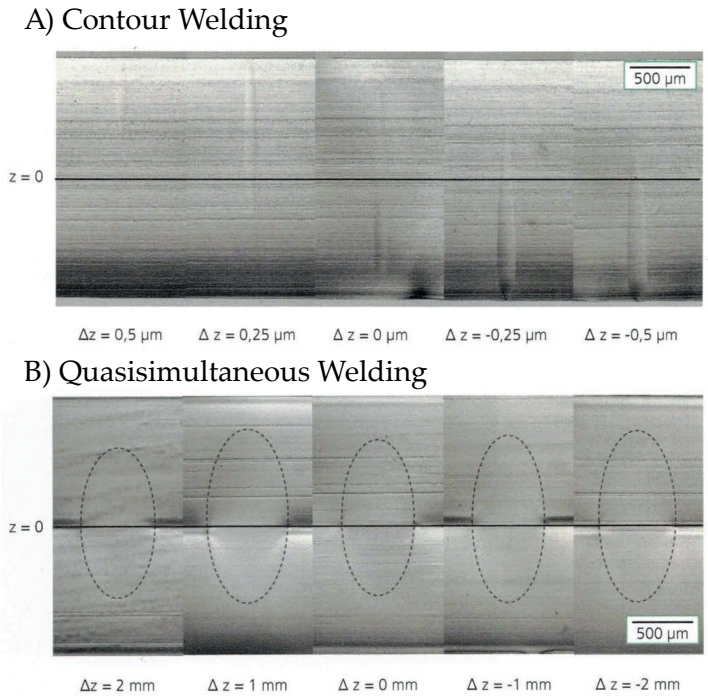

Figure 2.4: Cross sections of heat-affected zones at different welding parameters for two PC-plates with similar thickness. **A)** HAZ positions when CW is applied. The centre of the HAZ adjusts with the focus plane of the laser. **B)** HAZ positions at different focus planes when QSW is applied. As evident from the images, adjusting the focus plane does not influence the position of the HAZ centre. Adapted from [106].

Earlier journal publications by Nam-Phong Nguyen also provided valuable insights into the LTW of PC. In 2019, Nguyen *et al.* [107] examined the influence of various parameters on HAZ development during QSW using a thulium fibre laser. This study is particularly relevant as it involves welding PC with a laser similar to the setup applied in 4.4.3. Nguyen *et al.* [107] investigated how the number of passes over a contour affects the height and width of the HAZ while maintaining a constant line energy of 2.5 J/mm and a fixed laser power of 22 W. The results showed that increasing the number of passes reduces both HAZ height and width. Additionally, the study examined seam distance and cooling times, demonstrating that a cooling time of at least 15 s prevents width expansion in seams spaced 450 µm apart. It was also found that closely spaced seams, welded in quick succession, are affected by residual heat from the preceding weld. Segmentation of the weld seam mitigated this issue, ensuring consistent seam width and height. Furthermore, the focal plane position was varied to assess its impact on HAZ placement. The findings confirmed that in QSW, heat accumulation always results in the HAZ forming at the centre of the welding partners [107].

Further publications by Nam-Phong Nguyen are discussed in appendix D.1, as they address absorber-free LTW of materials other than PC.

In 2015, Mamuschkin *et al.* [108] explored methods for restricting the size of the HAZ, which in absorber-free LTW typically spans the entire cross-section of the welding partners. The authors achieved this by using a ring mirror irradiated by a fibre laser ($\lambda = 1940$ nm) in a circular motion at 1000 Hz to dynamically modulate the laser beam. This approach allowed the laser beams to intersect at the weld interface, heating this region while reducing radiation intensity in the surrounding material. As a result, heat generation was confined to the weld interface, preventing excessive thermal spread – contrary to the behaviour observed in QSW, where the HAZ typically extends across the full cross-section of the

welding partners [108]. However, this setup was not feasible at the IMT and could not be applied in this work.

In 2016, Mamuschkin, Engelmann and Olowinsky [109] published an additional parameter study on absorber-free LTW of PC. This study investigated the effect of increasing the number of passes using QSW at a set line energy of 2.5 J/mm. Since weld seam width contributes most to mechanical strength, while excessive vertical heat distribution is undesirable, a weld seam with a wider profile and lower vertical spread is considered optimal. Mamuschkin, Engelmann and Olowinsky [109] demonstrated that QSW produces such favourable weld profiles compared to CW, even when achieving similar weld widths. The improved heat transport in QSW was identified as the underlying reason. Additionally, this study was among the few to mention frequent surface burning of PC during preliminary weld tests when the focal plane was positioned directly at the weld interface. This was attributed to high radiation intensity at the surface, where impurities burn more easily. To mitigate this, the focal point was adjusted to 5 mm below the weld interface, reducing surface radiation intensity [109].

Overall, this review highlights that absorber-free LTW of PC remains a relatively new research area, likely due to the recent commercial availability of suitable laser welding systems for polymer welding (see appendix A.3.3 for details on these lasers). Furthermore, the optimal parameters for welding PC are still under investigation, as evidenced by the shift in preferred irradiation strategies – from CW to QSW and back to CW – over the past 15 yr and partly by the same authors. 4.4.3.6 (particularly table 4.10) details the parameters that were successfully applied for bonding the RC.

2.5.2 Unevenly thick welding partners

The only publication analysing welding partners of different thicknesses and providing an evaluation of parameters for improving weld seam quality as well as the HAZ is a 2023 study by Kumar Goyal and Kant [110]. In contrast to the approach detailed in 4.4.3.6, where a 300 µm thin film is welded onto a 3 mm substrate, Kumar Goyal and Kant investigated the bonding of a 4 mm thick PS piece to a 2 mm thick PC sheet. However, their approach relied on an absorber-based weld, incorporating electrolytic iron powder (EIP) (500 mesh size) applied to the PC in the weld seam area, which makes it unsuitable for application in this thesis. Additionally, instead of analysing the weld seam cross-sections through slicing and imaging, their assessment was limited to top-view microscopy. The authors observed that small bubbles within the weld seam enhanced weld strength due to well-intermixed molecular chains, whereas larger bubbles and thermal degradation weakened the bond [110].

In summary, it can be stated that there is few information published on absorber-free LTW of PC. However, as already noted in the beginning of these sections, the material used for the MFCs should be as pure as possible to avoid unmonitored interactions between additives and the future cultivations. Therefore, the standard procedure for laser welding PC using absorbers is not suitable for bonding the MFC chip halves. Instead, absorber-free LTW of PC will be researched further in this work to create a hermetic bond between PC chip halves.

3. The Microfluidic Bioreactor for plant cell cultivation

The MBR allows the controlled cultivation of plant cells – and later fungus hyphae – as well as the modular combination of several individual MBRs to assist in the understanding of communication pathways. First the manufacturing of the initial MBR (section 3.1) is described, followed by the refinement of its design (section 3.2), as well as the adaptation of a sensor screw (section 3.3). This chapter builds on the previous work conducted at the IMT for the MBR and identifies areas of necessary adjustment in it as well as closes research gaps identified in sections 2.1 and 2.4.

3.1 Manufacturing of the Microfluidic Bioreactor for plant cell analysis

The order of the sections reflects the chronological sequence of the fabrication steps: First, the chip halves of the MBR are fabricated via hot embossing. Subsequently, the membrane separating the cultivation and supply chambers is preinstalled through an imprinting procedure using an ultrasonic welding machine (3.1.2.1). The MBR chip halves are then sealed together in a second USW step (3.1.2.2). Then, the connector openings are milled into the material (3.1.3). Finally, each MBR is tested to verify that it is leak-tight (3.1.4).

3.1.1 Hot-embossing chip halves

The chip halves of the MBR were fabricated by hot embossing from PC (specifically, 3 mm thick Makrolon® GP clear 099 sheets, manufactured by Covestro Deutschland AG, Leverkusen, Germany [111][1]). Sections of raw blank were cut from Makrolon® sheets to dimensions of 22 mm by 66 mm. To minimise overflow during embossing, two corners of each piece were trimmed at a 45° angle (see figure 3.1).

Throughout this work, the term *raw blank* refers to these pre-cut pieces, while *chip halves* denotes the final hot-embossed PC parts. The *upper chip half*, which later contains the cultivation chamber, is characterised by two threaded openings leading into the chamber cavity. The *lower chip half*, by contrast, features a continuous inlet channel and houses the supply chamber.

Hot embossing was conducted using the Wärmeumformmaschine (WUM) 02 (Jenoptik Mikrotechnik, Germany; see figure 3.2). This system heats the base-, and mouldplate via oil circulation (cf. appendix A.2.3), enabling slower but more precise heating to the forming temperature T_p than systems with electrical heating. Cooling is performed through water circulation. Although Finkbeiner [14] reported that the WUM 01 – equipped with electrical heating – yielded chip halves of comparable quality, Fedder [112] demonstrated

[1] In January 2020, Covestro sold its polycarbonate sheet business to the Serafin Group, which subsequently established the Exolon Group. Since then, Makrolon® sheets have been marketed under the brand name Exolon®. However, the material used in this thesis was purchased before 01/2020 and is thus still referred to as Makrolon®.

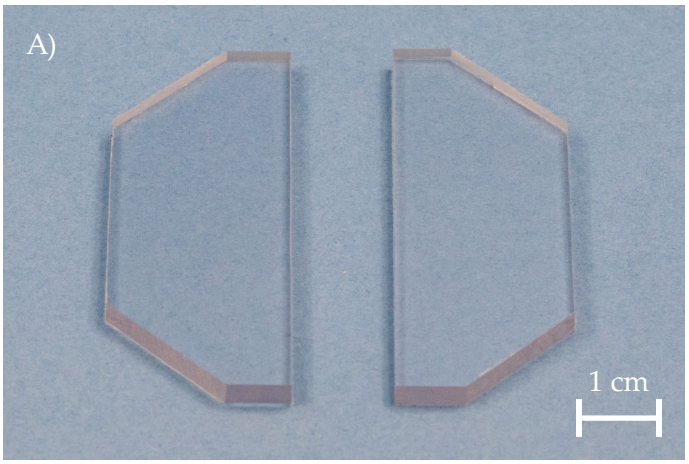

Figure 3.1: Prepared raw blank for hot embossing the MBR, cut from Makrolon® sheets (Covestro Deutschland AG, Leverkusen, Germany). The pieces are sized 22 mm by 66 mm to minimise overflow of molten material during thermoforming. Two corners are cut at a 45° angle to accommodate the rounded geometry of the base and mould plates.

that parts produced on the WUM 01 exhibited significantly greater deformation. This resulted in a higher incidence of failed welds in downstream processing steps. Accordingly, all chip halves in this thesis were hot embossed using the WUM 02, despite its process time being approximately 10 min longer.

Prior to use, both the baseplate and the mould plate were cleaned in an ultrasonic bath – first in 2-propanol, then in deionised water (DI water) – and subsequently dried with compressed air. The machine was then assembled with a polished chrome-coated plate as the baseplate to ensure optical clarity of the embossed chip halves, which is essential for enabling the dual function of the MBR as both cultivation and analytical platform. The mould was mounted on the upper half of the machine, facing downward. Figure 3.3A depicts the mould used for hot embossing the chip halves, while figure 3.3B shows the polished chrome-coated baseplate used during this step. Technical drawings for both – the initial and revised – MBR designs are provided in appendices F and G, respectively.

The actual hot embossing process begins by removing the protective film from the raw blank immediately before embossing, and clearing any dust particles from mould and raw blank by using compressed air. The raw blank was then positioned on the polished chrome-coated plate in alignment with the moulding posts. Forming parameters for the embossing process are listed in table 3.1.

Parameter	Value
Embossing temperature [°C]	167
Contact pressure [kN]	125
Embossing path [mm]	3.0
Embossing velocity [mm/s]	0.5
Demoulding temperature [°C]	85
Demoulding velocitiy [mm/s]	1
Cycle period [min]	40

Table 3.1: Parameters for hot embossing of MBR chip halves.

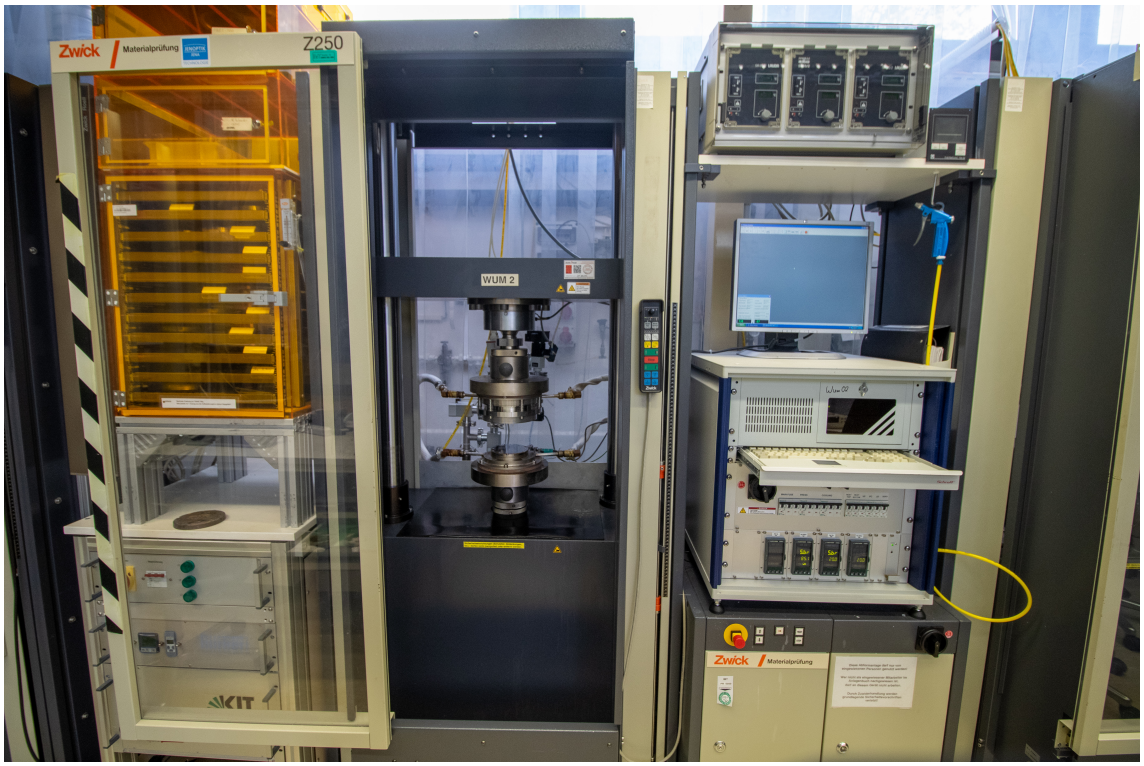

Figure 3.2: The Wärmeumformmaschine 02 (WUM 02) by Jenoptik Mikrotechnik, Germany was used for hot embossing the chip halves of the MBR.

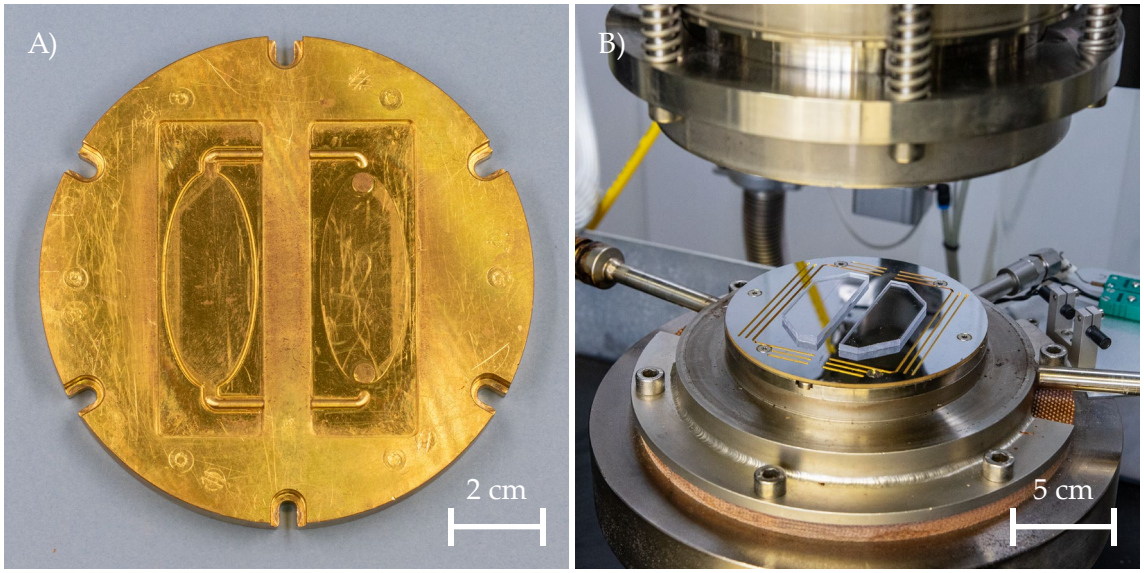

Figure 3.3: **A)** Mould for hot embossing the initial MBR chip halves. **B)** Polished chrome-coated plate for casting the chip halves transparently, installed as the baseplate in the WUM 02.

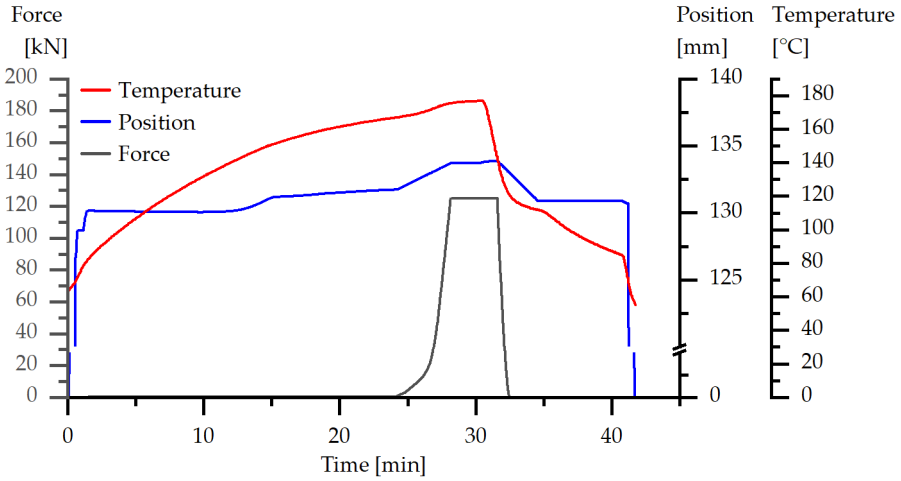

Figure 3.4: Diagram showing the progression of three essential parameters during hot embossing: temperature (red), applied force (black), and travelled path (blue). These curves illustrate the process control strategy used to cast the chip halves for the initial MBR.

The hot embossing process begins with the machine closing and initiating a vacuum. Once the vacuum is established, the system pauses for 20 s to allow conditions to stabilise. Subsequently, the force sensor is zeroed, and the press moves upwards until a small contact force of 250 N is achieved. The substrate is then heated to above 167 °C, surpassing the glass transition temperature of the PC raw blank, which is 148 °C. Once the material is sufficiently plasticised, it is pressed into the mould posts at a rate of 0.5 mm/min until a maximum embossing force of 125 kN is reached. A holding period of 120 s follows, allowing the molten polymer to completely fill the mould cavities and settle into its new geometry.

After this forming phase, the setup is cooled to 145 °C, just below the glass transition temperature of PC. The press then opens at a rate of 1.0 mm/min over a distance of 3 mm, intended to disengage the embossed chip halves from the mould. The system continues cooling until the temperature reaches 85 °C, after which the vacuum chamber is vented and the press opens fully.

Figure 3.4 illustrates the process via three measured parameters: the applied force (black), travelled path (blue), and substrate temperature (red). The path curve reveals the initial closing of the chamber and the final opening step. A slight increase in the travelled path during forming indicates the pressing of the softened material into the mould cavities, coinciding with the sharp rise in the applied force. The holding period is represented by a plateau in the force curve, indicating constant pressure as the material settles.

The baseplate temperature, shown in red, increases steadily in the initial phase. Notably, even after exceeding the target forming temperature of 167 °C, heating continues during the forming and holding phases, peaking at around 176 °C. Only after the holding phase is completed, active cooling is initiated. The initial cooling rate is steep due to efficient heat transfer while the mould remains closed. Once the chip halves are released from the mould, the reduced thermal conductivity under vacuum conditions leads to a noticeably slower temperature decline (cf. the steeper decrease in figure 3.4).

After thermoforming, the chip halves are either demoulded or separated from the polished chrome-coated plate. Excess material is trimmed, and edges are cleaned. The finished parts are shown in figure 3.5 and are subsequently stored in clear PS containers in a clean room until further use. The total duration of the hot embossing cycle takes on average 40 min.

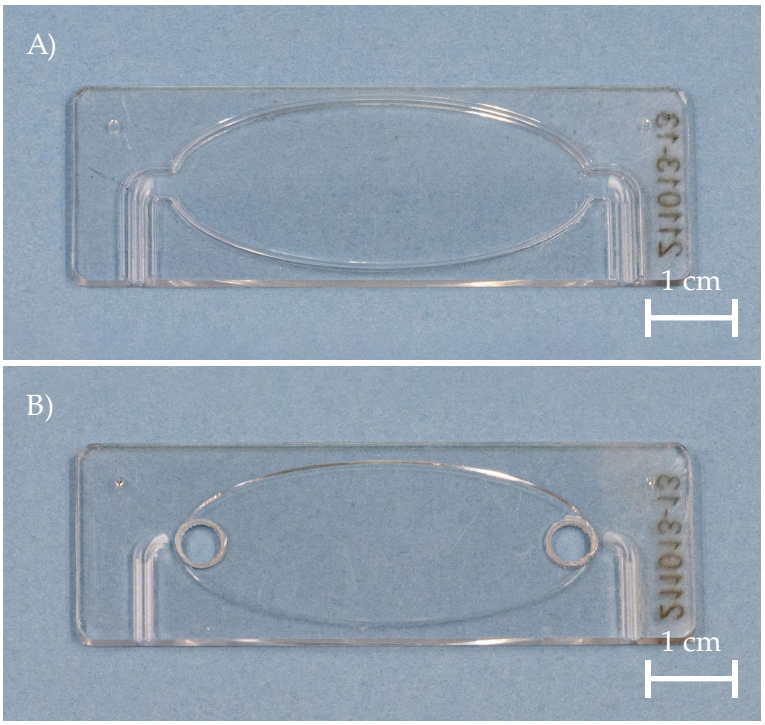

Figure 3.5: Hot-embossed and trimmed MBR chip halves after demoulding. The upper chip half (**A**) features two drilled and M6-threaded inlets to the cultivation chamber. In contrast, the lower chip half (**B**) lacks these openings; instead, the supply channels continue through to the chamber, enabling direct flow entry and exit (contrary to the upper chip halves were the channels run out before they reach the actual chamber).

As outlined in appendix A.2.3, the standard configuration for hot embossing involves a sandblasted baseplate, which offers improved adhesion for demoulding. However, for the fabrication of the transparent chip halves required in this thesis, a polished chrome-coated plate was used instead. Although this setup enabled optical transparency, the lack of surface roughness often failed to provide adequate traction, preventing reliable release of the chip halves from the mould posts. As a result, demoulding had to be carried out by extracting the parts from above, which occasionally introduced warping or even damage.

To mitigate this, a new chrome-coated plate was developed featuring shallow milled grooves. During embossing, the molten polymer partially flowed into these grooves. Upon cooling, the grooves offered sufficient and uniform traction to pull the parts from the mould with reduced deformation. Crucially, the plate surface directly opposite the mould posts remained polished, ensuring that the chip halves retained their optical transparency. This new chrome-coated plate is shown in figure 3.6 and has improved the demoulding step significantly.

3.1.2 Ultrasonic welding of chip halves

Here the procedure used to close the standard version of the MBR is outlined, which served as the basis for this thesis. This design builds on previous work by Finkbeiner [14], but required further modification before a stable and reproducible process could be established.

USW is used for bonding the chip halves of the MBR and integrating the chamber separating membrane. This process is carried out in two consecutive steps: First, the membrane is imprinted onto the upper chip half; subsequently, this membrane-laminated upper assembly is welded onto the lower chip half.

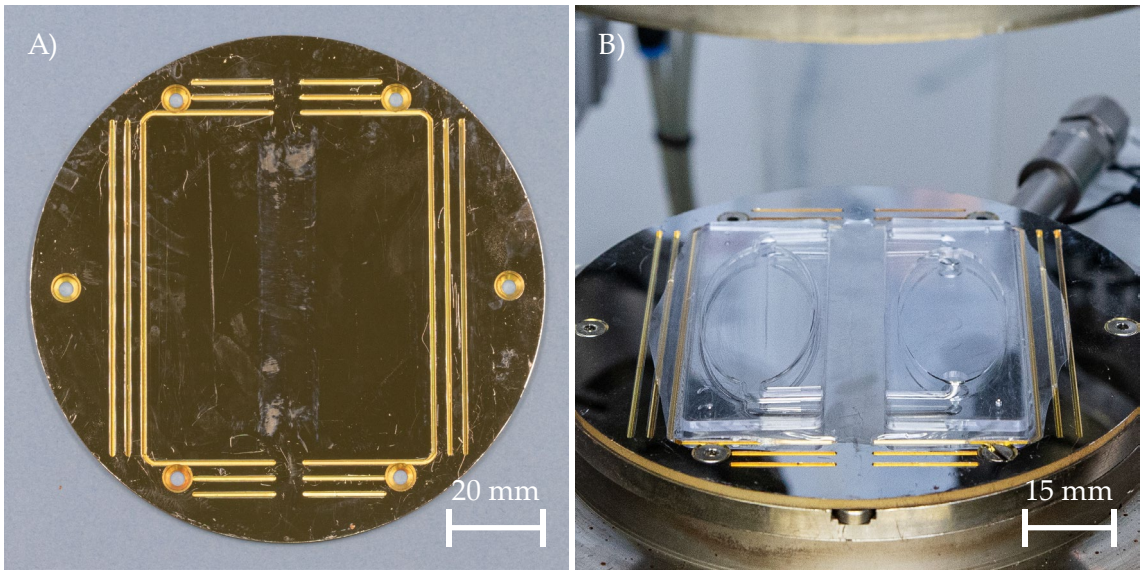

Figure 3.6: A) Structured chrome-coated plate featuring milled grooves designed to facilitate demoulding. **B)** When installed in the WUM 02, the structured plate enabled more uniform removal of the MBR chip halves from the overhead mould. The molten PC visibly interlocked with the grooves, improving grip during demoulding.

The key criteria for a reliable ultrasonic weld were discussed in detail in appendix A.3.2. In brief, the resulting seam should be clear and free of air bubbles, which could compromise the integrity or transparency of the weld. Furthermore, the weld seam must be continuous and uniform, exhibiting consistent clarity and width along the full perimeter of the chamber interface. For the MBR, an additional requirement applies: the membrane must be incorporated with minimal wrinkling to ensure homogeneous flow and even nutrient distribution throughout the cultivation area.

3.1.2.1 Imprinting the membrane

The materials used for the MBR include PC for the chip halves and a PET membrane. As outlined in 3.1.1, the chip halves are fabricated via hot embossing from PC, a polymer that exhibits lower absorption of ultrasonic energy compared to PET. While it is generally preferable to use a single material for both the membrane and the bulk structure when manufacturing, this was not feasible in the present case. Available PC membranes were opaque, which is unsuitable for optical monitoring. Moreover, the use of a PET membrane facilitates imprinting onto the PC substrate without damaging the bulk structure, owing to the lower glass transition temperature of PET (ranging between 67 °C and 81 °C).

The standard membrane employed in the MBR is a laser-cut PET membrane filter (Sterlitech no. 130008) featuring 5 µm pores produced via track etching (see figure 3.7B). The material has been previously characterised in detail by Finkbeiner [14], and those tests are not repeated in this thesis. The membrane follows the elliptical contour of the MBR chambers, with precise dimensions provided in appendix E. A tongue-shaped extension with an opening on the upper left and right side of the membrane allows it to be aligned using positioning pins on the MBR. This feature ensures accurate placement and fixation during the welding process.

To shield the structurally weaker membrane material from absorbing excessive energy during the imprinting and welding steps, a woven PET fabric (SEFAR PETEX® 07-105/52, Sefar AG, Switzerland) was placed on top of the membrane (see figure 3.7A). The cutout followed the elliptical perimeter of the MBR chambers on the inside, and its width was determined by the width of the imprinting structure.

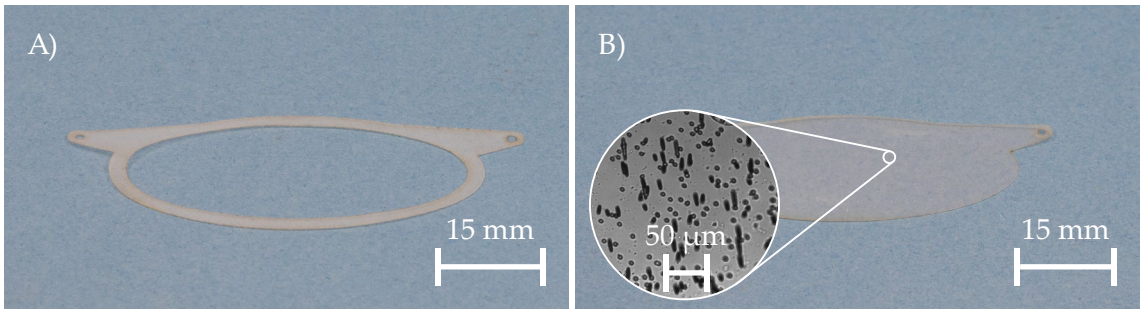

Figure 3.7: A) Woven fabric (SEFAR PETEX® 07-105/52, Sefar AG, Switzerland) placed on top of the PET membrane during imprinting to absorb part of the induced ultrasonic energy. This prevents tearing of the membrane during the welding processes. **B)** Track etched PET membrane filter (Sterlitech PET5020030), used to separate the upper and lower chambers of the MBR. The membrane has been laser-cut to match the elliptical outline of the chamber.

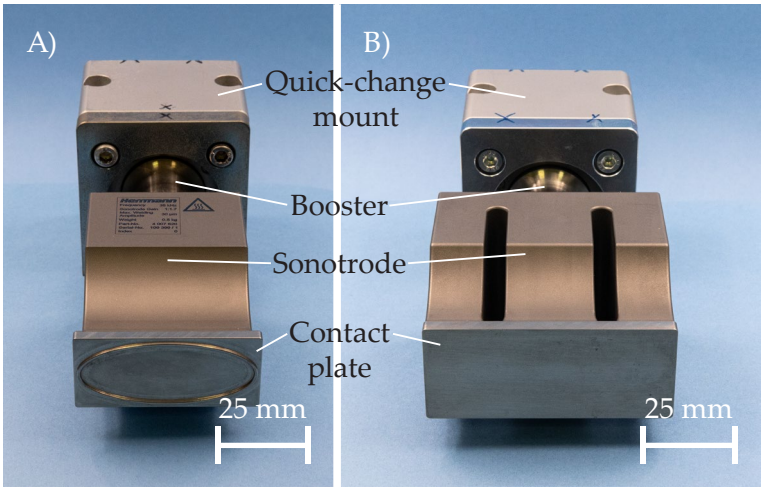

Figure 3.8: A) Structured sonotrode for imprinting the membrane onto the upper chip half of the MBR. **B)** Unstructed sonotrode for assembling the chip halves of the MBR. In both cases, the booster is mostly covered by the sonotrodes, because their structured or unstructured underside should be shown here. The sketch of an ultrasonic welding machine in figure A.3 displays the stack setup from the side, displaying the booster more visibly.

Prior to the fundamental redesign of the MBR (cf. 3.2.3), the bonding process was conducted in two sequential steps: First, the membrane was imprinted onto the upper chip half using a structured sonotrode to carry out the USW process (see figure 3.8A). Subsequently, the upper chip half was bonded to the lower assembly using an unstructured sonotrode (see figure 3.8B).

The use of two distinct sonotrodes was introduced by Finkbeiner [14] and demonstrated to be effective for this initial MBR design. As discussed in appendix A.3.2, the energy director can be integrated either into the component or onto the sonotrode surface. For bonding a thin PET membrane to a PC substrate, a structured sonotrode proved more suitable. The membrane itself lacked sufficient material volume to accommodate an energy director (ED), and in this step, the objective was to attach the membrane without inducing excessive melting of the bulk structure. Integrating the ED onto the sonotrode enabled a more controlled and less aggressive weld.

The oval-shaped ED on the sonotrode, shown in figure 3.8A, has a width of 1.65 mm. The welding parameters for this imprinting step are summarised in table 3.2. The process is

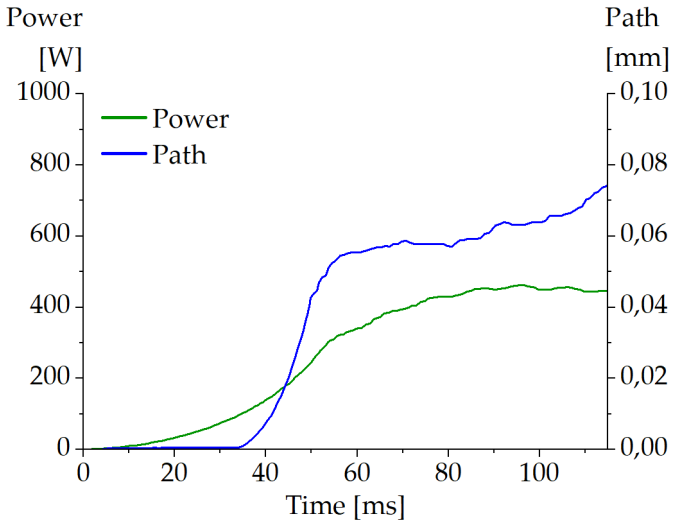

Figure 3.9: Diagram depicting the ultrasonic imprinting process of the membrane onto the upper chip half.

carried out in energy-controlled mode, with the cut-off set at 35 J. Both the triggering and welding forces are defined as 240 N, and the holding time is set to 1 s. The vibration amplitude introduced during the weld is 15.47 µm.

Parameters	Imprinting standard membrane
Membrane thickness [µm]	19
Welding mode	Energy-controlled
Induced welding energy [J]	35
Welding force [N]	240
Holding period [s]	1
Amplitude [µm]	15.47

Table 3.2: Parameters for the ultrasonic imprinting of the standard membrane onto the lower chip half of the MBR. The amplitude of the introduced vibrations was calculated using equation (A.1) from the initial converter amplitude of the USW machine ($A_{Converter}$ = 6.5 µm) limited to 70 % of its capacity ($\%_{Amplitude}$), the booster gain ($G_{Booster}$ = 1:1.7), and the gain of the structured sonotrode ($G_{Sonotrode}$ = 1:2).

Figure 3.9 displays the progression of the individual parameters during the weld. It clearly shows that, after the initial trigger force is reached, the power induced through the sonotrode's vibrations (green) increases until the cut-off energy is reached, at which point the welding process terminates. The programmed displacement of the sonotrode is shown in blue and visualises the plasticisation and compression of the material. Following a smooth initial approach, the curve exhibits a characteristic wavy pattern resulting from the ultrasonic vibrations.

Figure 3.10A presents the imprinted membrane and figure 3.10B shows a close up of such a successfully formed imprint seams. The membrane and woven fabric are ideally firmly imprinted and partly welded to the bulk material of the upper chip half. Furthermore, the imprint should be centred evenly around the chamber rim and the membrane should display minimal wrinkle formation. By contrast, figure 3.10B-E highlight common defects that may occur during this process. Once an appropriate parameter set was established, the imprinting step achieved a reproducibility rate of 89 %.

Defects during processing could result in membrane rupture (see figure 3.10D), detachment either during or after imprinting (figure 3.10E), or misalignment of chamber and sonotrode (figure 3.10C). These issues were particularly prevalent with ultra-thin membranes (thickness approx. 10 µm), for which achieving a consistent imprint without tearing proved especially difficult. Following extensive experimentation, an optimised parameter set for imprinting such membranes was developed and will be presented in 3.2.1. Furthermore, the initial MBR design and imprinting procedure often led to notable membrane wrinkling. To mitigate this, a redesigned MBR structure was introduced, as described in 3.2.3.

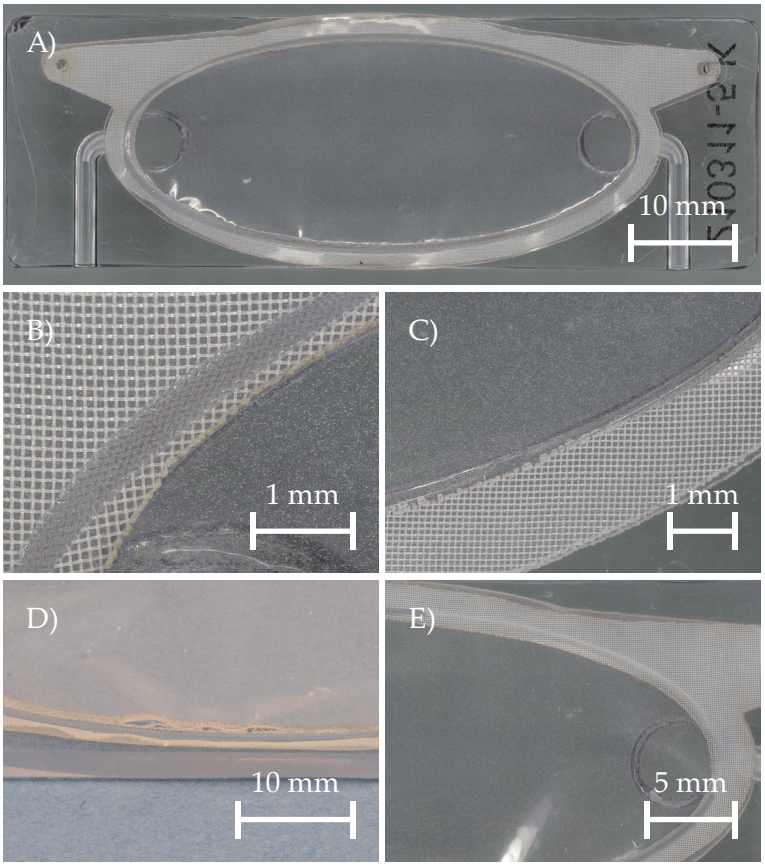

Figure 3.10: A) Successfully imprinted membrane on the upper MBR chip half. The imprint is well-centred and evenly distributed around the chamber perimeter, forming a continuous, clean attachment of the membrane. **B)** Close-up view of a successful imprint. Membrane and woven fabric are firmly embedded into the bulk material without overly welding the ultra-thin materials, thus weakening them prior to the final welding step of the MBR. **C)** Result of a misaligned sonotrode. The membrane and woven fabric are only minimally welded, with slight imprinting visible at the chamber rim. Most of the ultra-thin foils remain unattached, which results in wrinkling during the subsequent processing step. **D)** Imprinting with excessive parameters caused rupture of the membrane. Such chip halves are unsuitable for further manufacturing of the MBR. **E)** Detachment of membrane and woven fabric from the chip surface following imprinting. This failure is evident by the white, opaque appearance of the imprint (c.f. clear imprint in A and B).

3.1.2.2 Closing the MBR

In a second welding step, the top half of the MBR was bonded ultrasonically to the previously imprinted lower half (cf. 3.1.2.1). As with the imprinting process, the key criteria for a successful weld were the formation of a uniform and robust weld seam, the avoidance of membrane wrinkling or tearing, and the prevention of bulk material being displaced into the chambers. A uniform weld is characterised by a continuous seam along

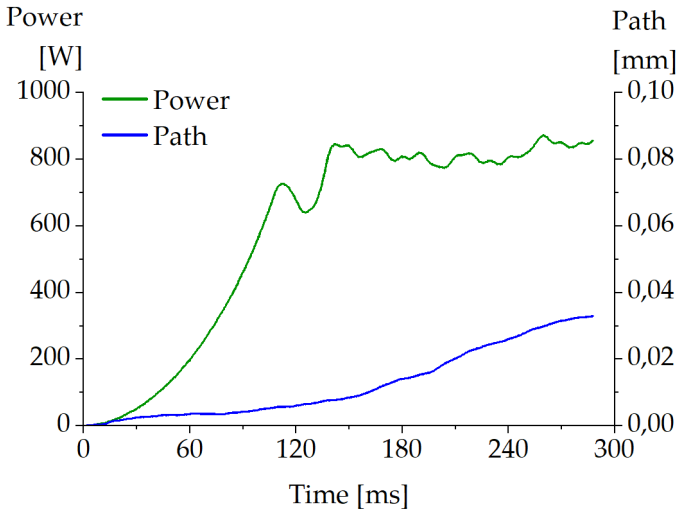

Figure 3.11: Diagram depicting the USW process to combine the MBR and seal it.

the ED integrated into the lower chip half. A robust weld is optically clear, free from gaps, detachments, or excessive bubble formation.

This second welding step was performed by placing the lower chip half onto the upper unit, which had been pre-assembled with the membrane and woven fabric. The parts were then joined using an unstructured sonotrode (see figure 3.8B). As discussed in appendix A.3.2, the ED guiding the USW process can either be incorporated into the sonotrode or into one of the welding partners. In this case, embedding the ED into the lower chip half was favourable, as it provided additional material required for the weld and allowed access to the weld area, which could not be reached by a structured sonotrode.

The parameter set for this weld is presented in table 3.3. The process was energy-controlled, because this allows for a more careful weld process. The ED height is 400 µm. The cap out energy was set to 180 J. The ultrasonic vibrations were applied with an amplitude of 24.38 µm, and a welding force of 275 N was selected to support this slower and more controlled weld process. After a holding time of 1 s, the process was terminated.

Parameters	Closing the MBR
Welding mode	energy-controlled
Induced welding energy [J]	180
Welding force [N]	275
Holding period [s]	1
Amplitude [µm]	24.38

Table 3.3: Parameters for the ultrasonic welding of MBR chip halves. The amplitude of the introduced vibrations was determined from equation (A.1) with the initial converter amplitude ($A_{Converter}$ = 6.5 µm) at a 100 % of its capacity ($\%_{Amplitude}$), the booster gain ($G_{Booster}$ = 1:1.5), and the gain of the unstructured sonotrode ($G_{Sonotrode}$ = 1:2.5).

With this parameter set, the MBR could be reliably sealed with a reproducibility of approximately 85 %. Figure 3.11 depicts the progression of the individual parameters during the welding process. Once the trigger force of 275 N is reached, the generator activates ultrasonic vibrations within the stack, which are transmitted to the welding partners, initiating the actual weld. At this point, the power input to the welding partners begins to rise (green).

As the membrane imprinting step, this process is governed by the energy transferred to the welding partners. The set path initially increases slowly but accelerates as the weld progresses due to the improved transmission of ultrasonic vibrations through the molten material compared to solid PC, which further accelerates the melting of the remaining solid polymer. Once a maximum total input energy of 180 J is reached, the welding process is terminated. A holding time of 1 s follows to stabilise and resolidify the molten material before the sonotrode is retracted, completing the weld. The final set path after welding typically reached 370 µm, ensuring a reliable seal of the MBR while utilising nearly the entire height of the ED.

Examples of resulting weld seams are shown in figure 3.12. A solid weld seam fulfils several criteria which are visualised in the figure: The weld seam runs evenly welded along the perimeter of the chamber as well as the in- and outlet channels. The width of the generated weld seam should be approximately the same everywhere and no area should be over-welded. Furthermore, a clear and transparent weld provides the best quality seam. The energy director should be molten entirely to ensure a snug fit of the bonded parts. Good – even though not ideal – weld seams show some but not intense bubble formation.

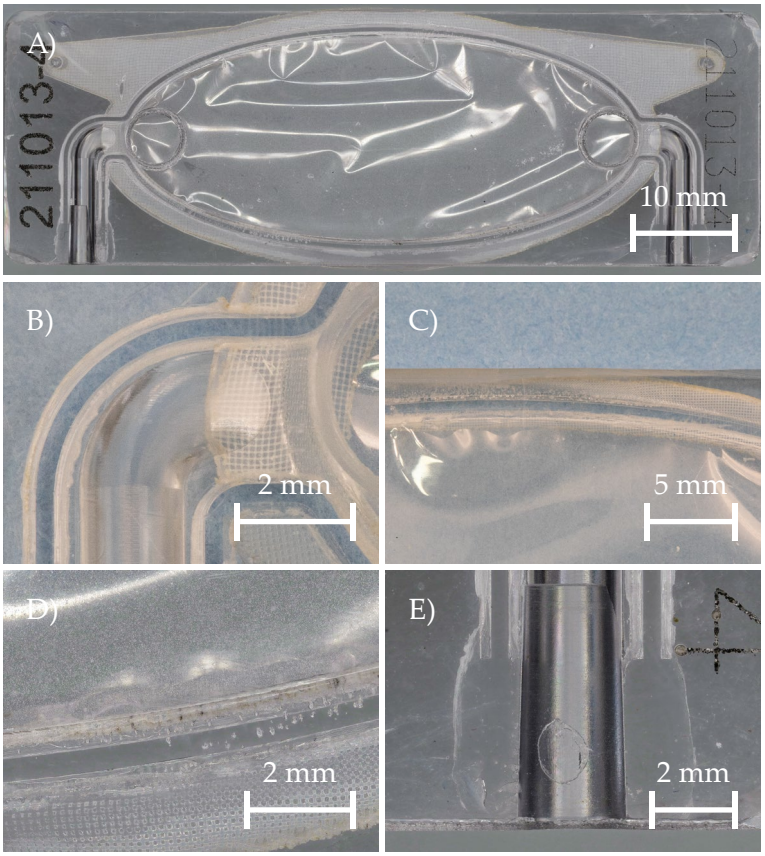

Figure 3.12: Examples of good seam quality when sealing the MBR. **A)** Overview of a fully sealed MBR. A clear weld seam is visible along the entire perimeter of the chamber and around the in- and outlet channels, indicating a continuous and leak-proof bond. **B)** Detailed view of a clear weld seam at the inlet channel. The displaced molten material is pushed laterally towards the channel but is retained by a groove. **C)** A clear weld seam along the upper perimeter of the oval chamber. **D)** Although a clear seam is preferred, a weld seam containing a few small air bubbles – like in this case – may still form a leak-tight seal. **E)** At the in- and outlet, the molten material should be pushed into a broad surrounding area, as shown here. This ensures that sufficient material remains to mill the fit for the Mini Luer connector without compromising the seal. Here the opening has already been milled.

In the area of the in- and outlet the molten material should be squeezed between the chip halves in an extensive area in order to provide ample material into which the fit for the fluidic connectors can be milled. The membrane and woven material – imprinted onto the upper chip half in the previous weld step – are welded in place through the ED on the lower chip half. A solid and leak-proof weld seam is clear and continuous and does not overly wrinkle or even rip the foils.

Defective – thus leaking – weld seams were also observed, although only in 24 % of bonded MBRs using this parameter set. Figure 3.13 depicts examples of such faulty weld seams that led to leakages.

As this work builds upon the process proposed by Finkbeiner [14], it is worth noting that, in his approach, the fluidic connectors were installed during this welding step. While this reduced the number of manufacturing steps, it posed significant challenges. Specifically, the

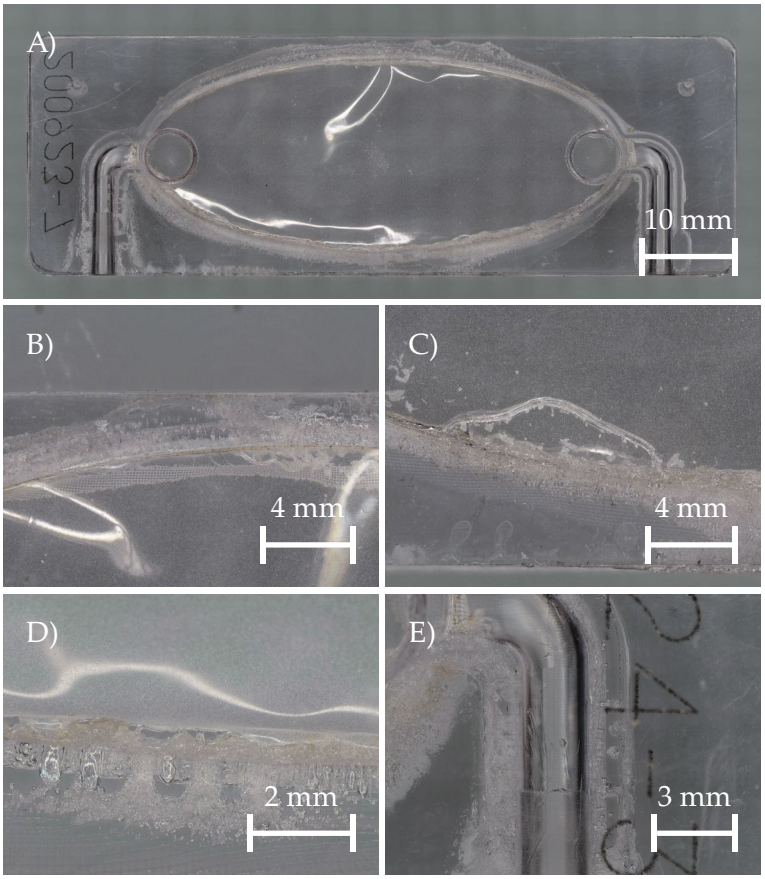

Figure 3.13: Examples of poor seam quality resulting from USW during the sealing of the MBR. **A)** Example of a leaking MBR, where multiple regions around the inlet and outlet channels, as well as the oval chambers, exhibit bubbly weld seams. These irregularities typically indicate overheating or insufficient alignment during welding. **B)** In this case, the woven fabric was torn during the welding process and displaced into the cultivation chamber. Such an obstruction may interfere with subsequent experimental procedures. **C)** Excessive flash material was forced into both the cultivation and supply chambers, likely due to an overly aggressive weld. This intrusion can disrupt fluid flow and compromise experimental consistency. **D)** Clearly visible leakage resulting from a bubbly – and thus excessively strong – weld seam. In many cases, additional surface bubbles can obscure underlying defects, complicating quality inspection. **E)** Weld seams surrounding the inlet and outlet channels can also suffer from excessive welding. Frequently, only one side is affected, which may indicate an uneven distribution of pressure or a misaligned baseplate during welding.

presence of the connectors tilted the upper chip half backward, complicating the welding process and resulting in a low number of fully sealed and leak-proof MBRs. Consequently, a design modification was implemented, which is described in detail in the following subsection.

In addition, the requirement to install the membrane without pronounced wrinkling or, more critically, tearing was not met consistently. This issue prompted a redesign of the membrane installation process, presented in 3.2.3.

3.1.3 Installing fluidic connector plugs

Initially, the fluidic connector plugs were welded into the MBR during the second ultrasonic welding step, i.e. while sealing the device. Finkbeiner [14] proposed this approach to simplify the process by combining two steps and argued that a single weld would be more economical and still allow for a leak-proof seal. However, Finkbeiner's study already identified two major challenges with this approach. First, the top chip half was significantly tilted backwards prior to welding due to the placement of the two fluidic connectors at the front. This misalignment led to uneven contact between the chip halves, resulting in irregular weld initiation points and frequent leakages. Second, generating a complete weld required high energy input, which also melted the connector material. This led to blockage of the internal tubing, rendering the connectors unusable. To counter this, a small metal rod had to be inserted into each connector during welding to prevent collapse.

Given these complications, further investigation into the connector installation process was undertaken. Initial tests explored whether increasing the trigger and weld forces could offset the tilting effect without inducing excessive energy input that would damage the connectors. However, this approach did not achieve a consistently reliable seal. A second approach attempted to improve connector positioning by modifying the channels in which they were placed. Additional recesses were milled to reduce the tilting of the upper chip half during setup. Nevertheless, this also failed to produce consistent and even weld seams. These efforts are documented in detail in [112].

The successful solution involved separating the bonding and connector installation processes. In the revised method, the chip halves were first welded shut without the connectors. Then, the inlet and outlet ports were opened using a conical drill bit with a 1.72° taper angle (see figure 3.14). A male Mini-Luer connector (figure 3.14D) was inserted into the drilled opening and gently pressed into the conical channel. The resulting friction fit generated a self-sealing effect that ensured leak-proofness.

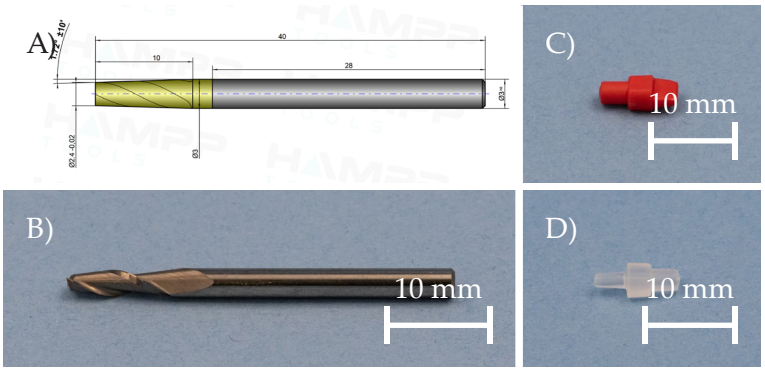

Figure 3.14: A) Technical drawing of the conical drill bit used to create the openings for the male Mini-Luer connectors. The taper angle of the conus is 1.72° on each side. Drawing provided by Hampp-Tools GmbH & Co. KG, Freiberg a.N., Germany. **B)** Photograph of the conical drill bit. **C)** Photograph of a male Mini-Luer plug. **D)** Photograph of a male Mini-Luer connector.

This approach was initially proposed by Fedder [112], but the drill bit used at the time featured only a single cutting edge. This introduced asymmetries in the openings, requiring a subsequent polishing step. In the present work, a two-flute drill bit was introduced, significantly improving the precision of the drilled ports. Leakage tests confirmed that the additional polishing step was no longer necessary. A completed MBR is shown in figure 3.15.

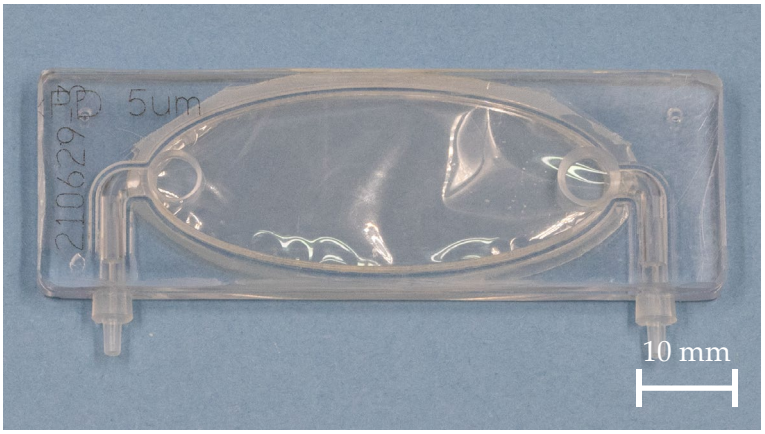

Figure 3.15: A completed MBR of the base design. The mini Luer are installed in the in- and outlet channels and the membrane separates the upper cultivation chamber from the lower supply chamber.

3.1.4 Testing for leakages

To conduct biological experiments using MBR requires a leak-proof seal to avoid serious consequences through spillings. It was therefore essential to ensure that each MBR used in these experiments was reliably leak-proof. Every unit underwent quality control using the following procedure:

The access openings for inserting and extracting plant cells from the cultivation chamber were sealed with 3M™ Circuit Plating Tape 851. One of the supply channels – typically the left – was connected to a pressure-controlled compressed N_2 line, while the opposite channel was closed using a short tube sealed with a male Mini-Luer connector. The prepared MBR was then submerged in a glass beaker filled with water and held in place with a small weight. Compressed N_2 was applied to test for leaks. To pass, the MBR had to withstand a peak pressure of 0.4 MPa, demonstrating its structural integrity under conditions similar to those in long-term experiments. Any leakage was easily identifiable by the appearance of N_2 bubbles, enabling immediate detection and further analysis. The setup is illustrated in figure 3.16, where the tested MBR shows no leakage, but N_2 bubbles are visible because the sealing tape was loosened for visualisation purposes.

Every MBR was tested using this setup to ensure leak-proof performance under experimental conditions. This method offered a significant advantage over the dyed water testing approach employed by Finkbeiner [14]: it enabled equally reliable leakage detection while avoiding the extensive cleaning required after dye-based tests. This concludes the manufacturing process of the initial design of the MBR starting from the thermoforming process to testing the final microfluidic chips before providing them to the partners in the DialogProTec collaboration.

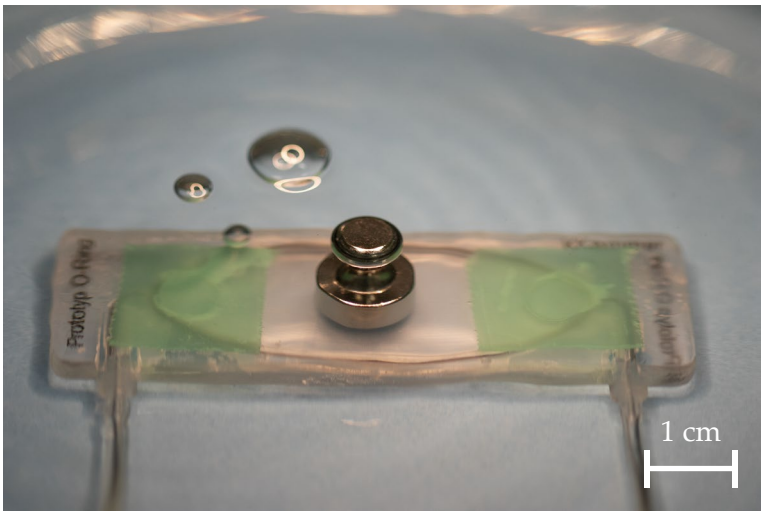

Figure 3.16: Leak testing of the MBR. The access openings for introducing plant cells into the upper chamber were sealed using 3M™ Circuit Plating Tape 851. One supply channel was connected to a pressure-controlled compressed N_2 source, while the second was closed off. The MBR was fully submerged in a water-filled glass beaker and secured with a small weight. Upon applying compressed N_2, the emergence of air bubbles indicated the presence and location of any leaks. In the example shown, the MBR is leak-proof; however, air escapes through the sealing tape at the top left opening as it was loosened for visualisation purposes.

3.2 Design optimisation of the Microfluidic Bioreactor for plant cell analysis

Refinements and alterations on the initial MBR design were conducted to facilitate the successful cultivation of fungus hyphae. Furthermore, it was noticed that initially stable and reproducible cultivation conditions were not achieved in the MBR. Therefore, the internal flow dynamics were evaluated in detail (3.2.2). Based on these results and the observation of excessive wrinkle formation in the initial design, the method for installing the membrane separating the cultivation and supply chambers was fundamentally revised to improve membrane integrity and ensure consistent performance (3.2.3).

3.2.1 Ultrasonic welding of ultra-thin membranes

To adapt the MBR for fungal cultivation, as outlined in section 1.1, modifications were required due to the ability of *Neofusicoccum parvum (N. parvum)* hyphae to reduce their diameter to approximately 4 µm, allowing them to penetrate physical barriers. As a result, the standard membrane with a pore diameter of 5 µm was no longer suitable and had to be replaced. However, the available PET membranes with smaller pore sizes were substantially thinner than the previously used standard membrane. Specifically, the membrane with ∅1 µm pores had a thickness of only 11 µm, while the ∅3 µm variant was even thinner at 9 µm. In contrast, the standard PET membrane had a specified thickness of 19 µm.

Applying the standard imprinting USW process to these ultra-thin membranes unsurprisingly led to membrane rupture, rendering the resulting MBRs unusable. Moreover, these thin membranes were particularly vulnerable to the oil-canning effect discussed in section 2.4.

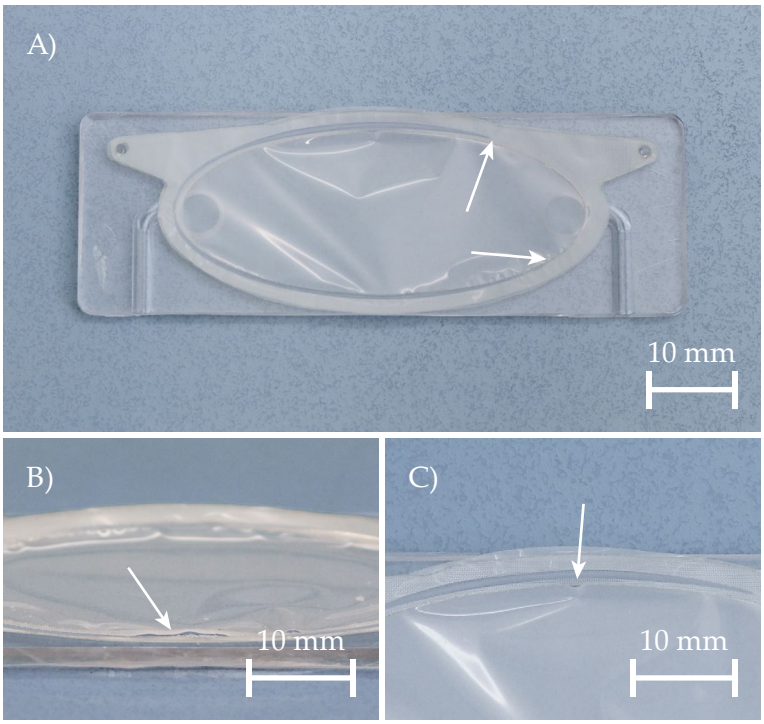

Figure 3.17: A) Imprinted ultra-thin membrane (pore diameter 3 µm) showing partial detachment from the upper chip half after the imprinting step, particularly around the right side of the cultivation chamber. **B)** Side view of an imprinted ultra-thin membrane that was torn during the imprinting process. **C)** Top view of an imprinted ultra-thin membrane exhibiting a small but distinct tear at the junction between the rim of the cultivation chamber and its semi-minor axis.

To accommodate the reduced membrane thickness, a series of experiments was conducted to identify suitable welding parameters. The maximum energy input was lowered, and cut-off energies in the range of 10 J to 60 J were tested. In parallel, the vibration amplitude was reduced to slow the rate of energy transmission. Several amplitude levels were investigated, including values of 22.1 µm, 17.68 µm, and 15.47 µm (cf. equation (A.1) for calculating the resulting amplitude of a stack) mainly through manipulating the amplitudes capacity ($\%_{Amplitude}$). The imprint quality was assessed based on two key criteria: the membrane remained intact without tearing, and it could not be detached from the chip surface following the imprinting process.

Examples of each failure mode observed during the imprinting process are shown in figure 3.17B and C. Through systematic testing, the optimal cut-off energy values were identified as 24 J for the ∅1 µm membrane and 22 J for the ∅3 µm membrane, both using a vibration amplitude of 15.47 µm.

In addition to optimising the imprinting parameters, it was necessary to address the inherent warping of the chip halves caused by the hot embossing process. This deformation often led to incomplete sealing along the perimeter of the imprint, as illustrated in figure 3.17A. To counteract this issue, the welding force was increased incrementally from 180 N to a maximum of 500 N. The optimal welding force for both ultra-thin membranes was determined to be 490 N, which enabled full perimeter contact and reliable sealing. Representative successful imprints achieved under these conditions are shown in figure 3.18. A complete overview of all tested and optimised parameters is provided in table 3.4.

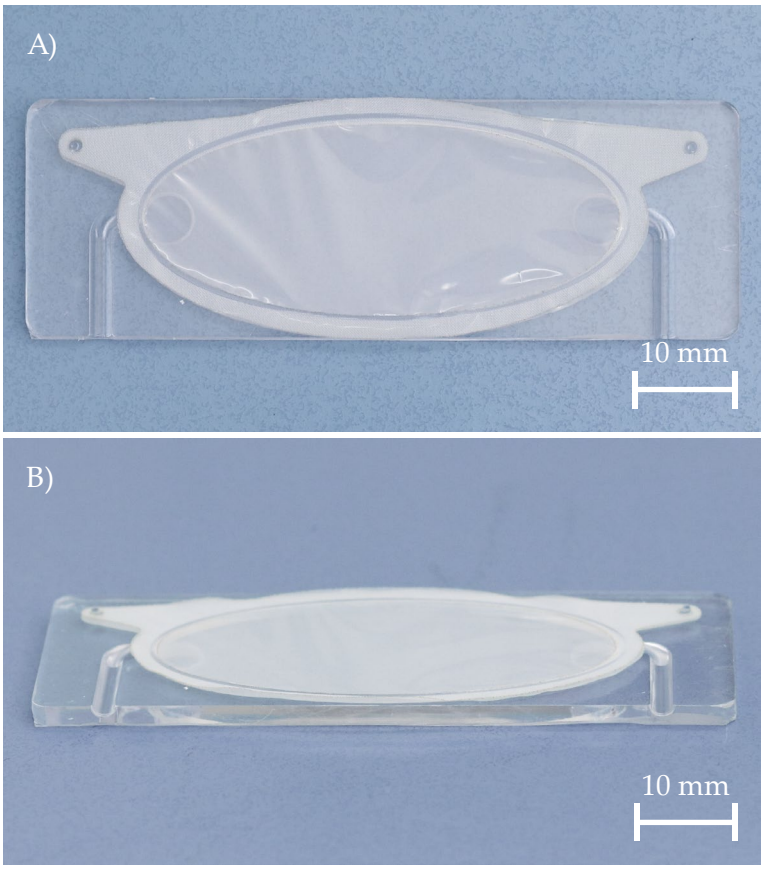

Figure 3.18: A) Top view of a successful imprint of an ultra-thin membrane with a pore diameter of 3 µm. The imprint is evenly centred around the oval chamber and forms a continuous seam. The membrane remains intact, with no visible tearing or detachment in the imprinted area. **B)** Side view of the same imprint. This perspective allows for the inspection of potential membrane rupture, which is absent in this example, confirming the structural integrity of the imprint.

Parameters	Ultra-thin membranes	
Membrane pore diameter ⌀ [µm]	1	3
Membrane thickness h [µm]	11	9
Welding mode	Energy-controlled	Energy-controlled
Induced welding energy [J]	24	22
Welding force [N]	490	490
Holding period [s]	1	1
Amplitude [µm]	15.47	15.47

Table 3.4: Parameters for ultrasonic imprinting of ultra-thin membranes onto the upper chip half of the MBR.

3.2.2 Simulational Analysis of nutrient distribution in the MBR

A thorough analysis of the cultivation conditions in the MBR was essential to ensure reliable and reproducible environments for plant cell culture and experimental applications. Finkbeiner [14] previously investigated the diffusion of nutrients and other chemical compounds through the membrane that separates the supply chamber from the cultivation chamber. However, the aim of that study was solely to demonstrate that the membrane permitted adequate nutrient transport into the upper chamber. Consequently, the simulation period was limited to 250 s, which is insufficient for assessing how and when the entire cultivation chamber becomes fully perfused.

This information, however, is critical for experimental planning and interpretation of results. Therefore, the perfusion behaviour of the complete MBR was re-evaluated using extended simulations. Together with my student Laura Supp, a more comprehensive study was conducted, initially employing a 2D model and subsequently a 3D model. The key aspects of the simulation setup, methodology, and derived insights are summarised below. A detailed account of this theoretical analysis can be found in Ms Supp's Master's thesis [113].

The following subsections are structured according to the standard progression of a simulation study: pre-analysis, preparation, computation, and post-processing. Finally, the simulated results are compared with experimental flow data obtained from the MBR.

3.2.2.1 Pre-analysis: Fluid parameters

For plant cell cultivation experiments, the lowest flow rate applied to the MBR is 20 µL/min, and the highest is 100 µL/min, as reported by Metzger [48]. Accordingly, both cases were analysed in the simulation study to define the range of fluid flow conditions within the system.

To investigate the flow behaviour and the distribution of nutrients in the MBR, the simplified Navier-Stokes equations (3.1) and the convection-diffusion equation (3.2) were solved numerically.

$$\rho\frac{\partial \mathbf{u}}{\partial t} + \rho(\mathbf{u}\cdot\nabla)\mathbf{u} = -\nabla \tag{3.1}$$

$$\frac{\partial c}{\partial t} + \mathbf{u}\cdot\nabla c = D\nabla^2 c \tag{3.2}$$

For this purpose, the properties of the adapted Murashige- and Skoog (MS) medium used for plant cell cultivation in the MBR (compound list see section 5.1 and [48]) were evaluated and compiled. The relevant parameters are summarised in table 3.5. For the simulation, the nutrient medium was approximated as a sucrose-water solution with a sucrose concentration c_{sucrose} of 30 g/L. Using the molar mass of sucrose (342.3 g/mol), the corresponding initial molar concentration was calculated as 87.64 mol/m^3. The solution is treated as an incompressible Newtonian fluid. As the material properties of the solution do not depend on the sucrose concentration, the convection-diffusion equation and the simplified Navier-Stokes equations are both independent.

Similar to the approach used by Finkbeiner [14], the diffusion coefficient was calculated using the Stokes-Einstein equation:

$$D = \frac{k_B T}{6\pi\mu R_0} \tag{3.3}$$

Parameter	Sign	Value
Temperature	T	21 °C
Dynamic viscosity	μ	0.998 mPa s
Density	ρ	998 g/m^3
diffusion coefficient of sucrose in water	D	3.81×10^{-10} m^2/s
Initial sucrose concentration	c_{in}	87.64 mol/m^3

Table 3.5: Parameters used for the diffusion simulation. The values for dynamic viscosity and density were obtained from Kretzschmar and Wagner [114]. The diffusion coefficient was calculated using equation (3.3).

where D is the diffusion coefficient, k_B is the Boltzmann constant, T is the absolute temperature, μ is the dynamic viscosity of the solvent, and R_0 is the hydrodynamic radius of the diffusing particle. This empirical equation is valid under the assumption that the solute particles are spherical and significantly larger than the solvent molecules. The diffusion coefficient D was determined to be 3.81×10^{-10} m^2/s, based on an estimated molecular radius of sucrose of 5.4 Å, compared to the smaller water molecule radius of 3 Å [115].

Next, it is essential to pre-analyse the flow behaviour of the fluid. For this purpose, the Reynolds number Re was calculated using the fluid's density ρ, the flow velocity u, its dynamic viscosity μ, and the characteristic length L, according to

$$Re = \frac{uL\rho}{\mu} \tag{3.4}$$

This dimensionless number helps categorise fluid flow. For a pipe flow, values of $Re < 2300$ typically indicate laminar behaviour [116]. In microfluidic chips, the Reynolds number is generally very small, illustrating the dominance of viscous over inertial forces. As a result, inertial effects can be neglected in most cases [117].

In addition, the Péclet number $Pé$ was calculated using the characteristic velocity u, the characteristic length L, and the diffusion coefficient D:

$$Pé = \frac{uL}{D} \tag{3.5}$$

The Péclet number quantifies the relative influence of convective versus diffusive transport mechanisms in a fluid. A low $Pé$ ($\ll 1$) indicates that diffusion dominates, while a high value ($Pé > 10$) implies that convection – i.e. transport coupled directly to fluid flow – is the prevailing mechanism [118]. This number is particularly relevant for fluid flow analysis using finite element model (FEM), such as the COMSOL Multiphysics® [119] transport of diluted species (tds) module employed in this work. For FEM models with uniform mesh and first-order shape functions, it has been mathematically demonstrated that numerical instabilities arise when the Péclet number of an individual element exceeds 1 [120]. Given the highly laminar flow in the MBR and the small diffusion coefficient (see table 3.5), $Pé$ values exceeding 1 are expected. This necessitates appropriate stabilisation measures in the numerical model.

The characteristic length L has to be chosen with the dominant transport process in mind. In case of the MBR the fluid flow behaviour is strongly influenced by the dimensions of the

inlet. Since this rectangular channel is fully filled with fluid, thus all boundaries are wetted surfaces, the characteristic length for this study was calculated according to equation (3.6). The inlet is 0.5 mm high and 2.36 mm wide.

$$L = \frac{4bh}{2b + 2h} \tag{3.6}$$

As discussed in the beginning of the analysis and according to Metzger [48], flow rates applied in plant cell experiments range from 20 µL/min to 100 µL/min. Therefore, the Reynolds and Péclet numbers were calculated for these extreme flow rate cases. The results are summarised in table 3.6.

Flow rate	Char. length L	Char. flow velocity	Re	$Pé$
20 µL/min	0.825 mm	0.2825 mm/s	0.233	583
100 µL/min	0.825 mm	1.412 mm/s	1.166	2915

Table 3.6: Calculated Reynolds and Péclet number for volumetric flow rates of 20 µL/min and 100 µL/min.

Since both Reynolds numbers are well below the critical value of 2300 for pipe flow, the fluid behaviour in the MBR is classified as laminar in both cases. At a flow rate of 20 µL/min, the Péclet number is below 1000, indicating that while convection is the dominant transport mechanism, diffusion cannot be entirely neglected. At the higher flow rate of 100 µL/min, the Péclet number increases to 2915, meaning that diffusive transport becomes comparatively negligible.

3.2.2.2 Preparation: Geometry and simulation setup

The aim of this simulation study was to analyse the flow conditions and resulting nutrient distribution within the cultivation chamber of the MBR in both 2D and 3D, thereby ensuring reproducible experimental conditions. Three simulation setups were considered and are depicted in figure 3.19. Setup 1: The oval geometry of the cultivation chamber in 2D, setup 2: A 2D cross-section through the supply and cultivation chambers, separated by the membrane, and setup 3: The full 3D geometry of the chambers.

The geometries used for the 3D and 2D oval simulations were derived directly from the CAD model of the MBR and imported into COMSOL Multiphysics® [119]. In contrast, the geometry for setup 2 was constructed directly in COMSOL using simple rectangular domains.

The simulation studies were conducted using the laminar single phase flow and transport of diluted species (tds) physics modules. As established previously, the nutrient concentration at the inlet was set to 87.64 mol/m^3. All impermeable walls were defined with a no-flux boundary condition. For the 2D simulations, the "shallow channel approximation" was enabled to account for the disproportionate aspect ratio between the chamber height (supply chamber: 0.5 mm; cultivation chamber: 1.0 mm) and its lateral dimensions. In such flat geometries, walls – particularly the membrane interface and chamber bottoms – strongly influence the development of the flow profile. To incorporate this effect, an additional volume force F_μ was applied, dependent on the fluid's dynamic viscosity μ, the velocity field $\mathbf{u}$, and the channel height h_k:

$$F_\mu = \frac{\mathbf{u}\mu}{h_k^2} \tag{3.7}$$

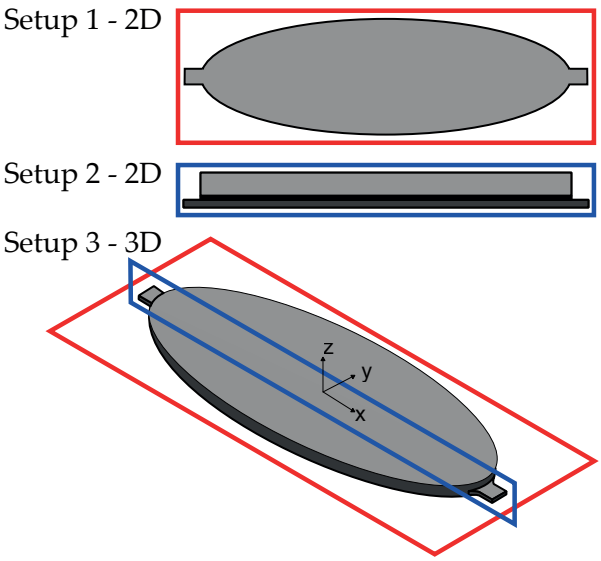

Figure 3.19: Visualising the three geometric setups analysed for the nutrient distribution. **Setup 1)** assesses the distribution in 2D representing the nutrient supply within the ovally shaped supply chamber. **Setup 2)** analyses the supply of nutrients through the membrane in 2D from the supply chamber to the cultivation chamber. **Setup 3)** examines the flow behaviour and nutrient distribution in 3D in the MBR.

The 3D setup could not be calculated with these models as the computational resources required exceeded the available options. Instead, isotropic diffusion was assumed. Although this approximation led to an artificially broadened interface between $c_{\max}$ and $c_{\min}$ and increased diffusive mass transport – thereby accelerating nutrient distribution throughout the cultivation chamber – the results still offer a reliable estimation when considered in conjunction with the 2D simulations.

A central element of the model was the membrane separating the cultivation and supply chambers. To reduce computational effort, it was implemented as a porous medium with effective transport properties. This approach significantly lowers mesh complexity, as it avoids the need for highly anisotropic elements required to resolve the membrane's small thickness relative to the surrounding chamber volumes. It also shortens simulation time, as it eliminates the need to solve full three-dimensional Navier-Stokes or convection-diffusion equations within a thin domain. Instead, simplified transport laws can be applied while still capturing the membrane's essential transport characteristics. The porosity was adopted from Finkbeiner [14] as $\epsilon = 6.9\,\%$. The permeability was then calculated using Darcy's law in combination with the water passage rate under a pressure of 68.9 kPa [121], yielding $3.46 \times 10^{-14}\,\mathrm{m}^2$.

$$q = -\frac{\mu}{K} \cdot \nabla p \tag{3.8}$$

The mesh for all simulations was generated to balance numerical accuracy with computational efficiency. For the 2D simulations, the mesh was created using COMSOL's physics-controlled mesh generator. Mesh-independent results were achieved upwards of a resolution of 214,216 elements, corresponding to the "finer" setting in COMSOL.

In the 3D study, special attention was required for discretizing the membrane and its surroundings. The membrane itself was again implemented as a porous medium. However, with a thickness of only 19 µm, the membrane was two orders of magnitude thinner than the chamber height (1.5 mm). Uniform meshing would have been computationally prohibitive.

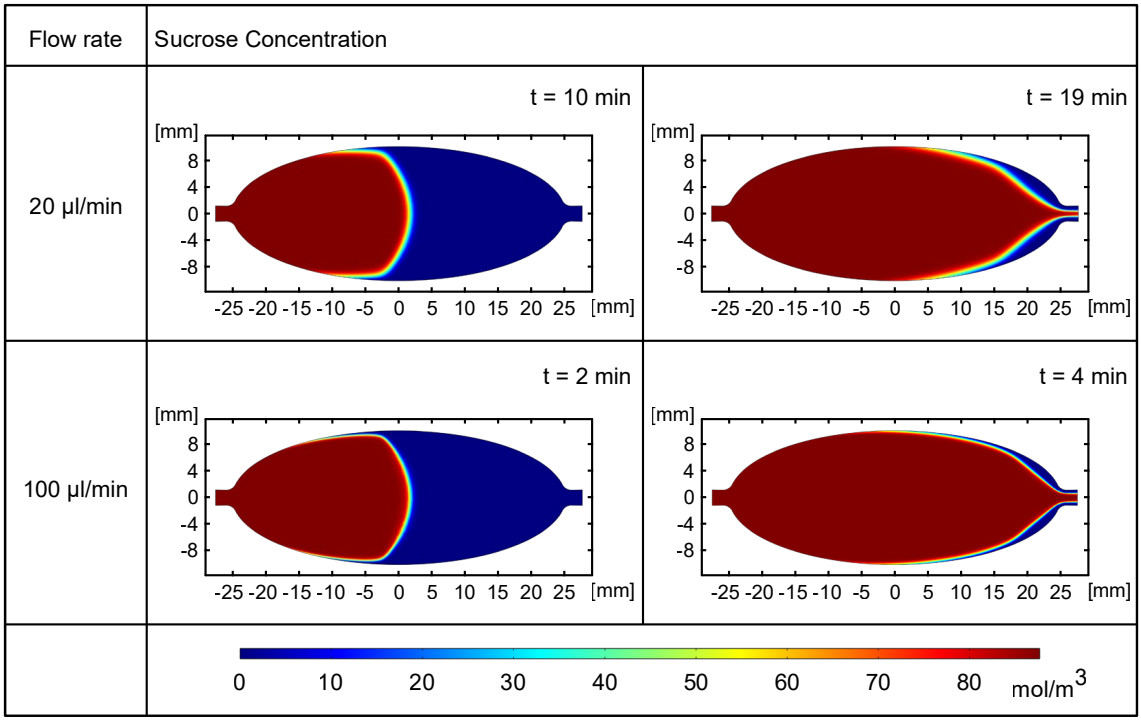

Figure 3.20: Results of the simulation studies for setup 1, analysing nutrient distribution within the oval chamber geometry at flow rates of 20 µL/min and 100 µL/min. While the overall nutrient distribution profiles appear largely similar, the transition zone between c_{max} and c_{min} is noticeably narrower at the higher flow rate, indicating a sharper concentration gradient. Additionally, the significantly faster nutrient distribution at 100 µL/min is clearly visible.

Instead, adaptive discretization was applied – finer meshing near the membrane and other critical geometries – like walls or in- and outlet – and coarser elsewhere. Moreover, the symmetry along the flow axis (x-axis) and the assumption of strictly laminar flow enabled simulation of only half the geometry. Mesh independence was reached from a total element count of approximately 150,000.

3.2.2.3 Computation and post-processing

The distribution of Murashige- and Skoog media – simplified for the studies here as a diluted sucrose solution – within a water-filled MBR was analysed using 2D and 3D geometries at the minimum and maximum flow rates: 20 µL/min and 100 µL/min.

From figure 3.20 it is visible that for the 2D-setup analysing the fluid flow with a flow rate of 20 µL/min in an ovally shaped chamber it takes 10 min for the nutrients to reach half of the area. After 35 min the chamber is filled completely, but figure 3.20 displays the state after 19 min to visualise the broadening of the area between c_{min} and c_{max} towards the centre of the chamber, resulting from the diffusion, and that after 19 min already most of the chamber is filled to c_{max} with nutrients and comparatively small areas around the perimeters take the rest of the time to be reached by the nutrients. This is due to the no-flux condition at the walls which slows down nutrient transport to the areas close to walls.

At the higher flow rate of 100 µL/min, the nutrient concentration profile is displayed at time points of 2 min (first appearance of $c_{\max}$ at $x = 0$) and 4 min (first occurrence of $c_{\max}$ at the outlet). Complete saturation of the chamber with nutrients at $c_{\max}$ occurs within 10 min. While the overall distribution trends are comparable between the two flow

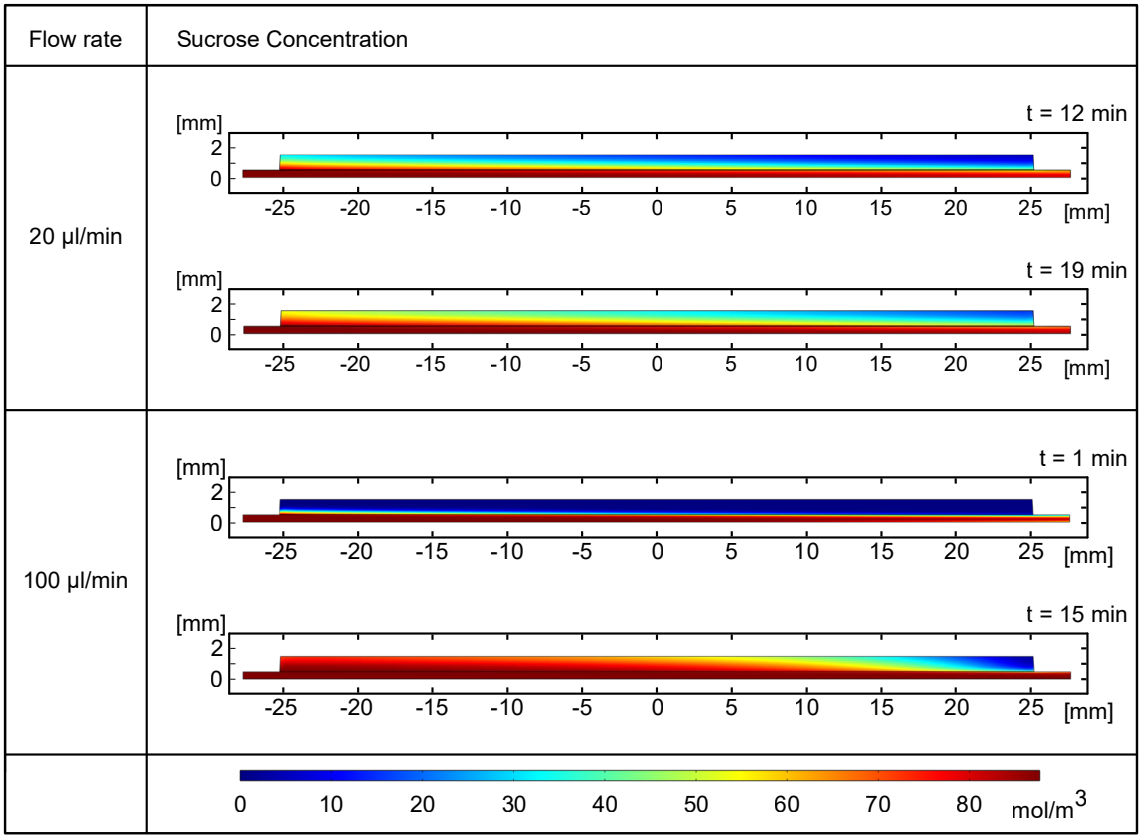

Figure 3.21: Results of the simulation studies for setup 2, analysing nutrient distribution from the supply chamber across the membrane into the cultivation chamber, at flow rates of 20 µL/min and 100 µL/min. Similar to figure 3.20, the profiles of nutrient distribution at the two different flow rates appear nearly identical in shape. However, in these cross-sectional flow studies, the widening of the transition zone between c_{max} and c_{min} at the slower flow rate of 20 µL/min is even more pronounced when compared to its higher flow rate counterpart.

rates, a key difference is the significantly narrower transition zone between $c_{\max}$ and $c_{\min}$ at the higher flow rate. This suggests a steeper concentration gradient and more efficient convective transport, with diffusion playing a reduced role compared to the lower flow rate of 20 µL/min.

The second 2D setup incorporates nutrient diffusion through the membrane (figure 3.21), resulting in a slower nutrient distribution compared to setup 1. A notable feature of this configuration is the bidirectional flow across the membrane: fluid initially flows from the supply chamber into the cultivation chamber up to the centre of the geometry. Due to the incompressible nature of the nutrient medium, the flow direction then reverses, generating an outward flow from the centre of the cultivation chamber towards its ends.

Figure 3.21 shows that at a flow rate of 20 µL/min, c_{max} is first reached at the outlet of the supply chamber after 12 min. The nutrient front subsequently propagates through the membrane into the cultivation chamber, reaching its far end at 60 min. However, it takes a total of 90 min for the entire cross-section to reach c_{max}. At the higher flow rate of 100 µL/min, c_{max} appears at the outlet of the supply chamber after roughly 1 min, but a complete distribution across the entire cross-section still requires approximately 60 min.

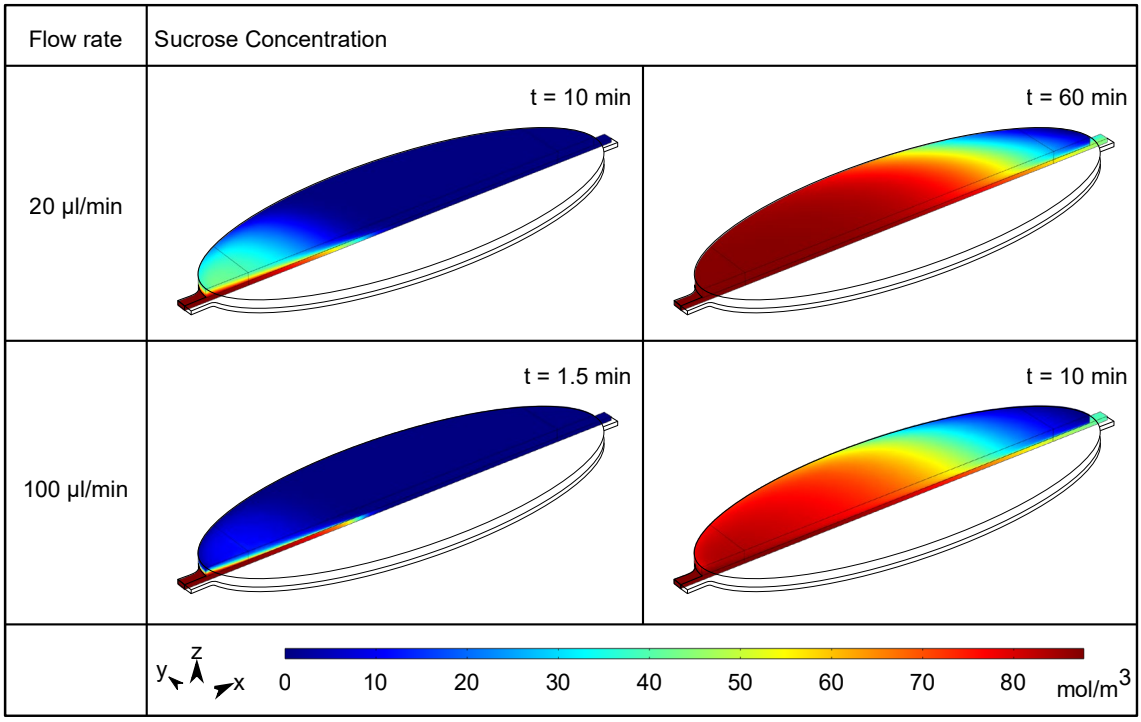

Figure 3.22: Results of the simulation study for setup 3. This study examines the nutrient distribution throughout the chambers of the MBR in 3D at two different flow rates (20 µL/min and 100 µL/min). It visualises clearly that at the higher flow rate the nutrients get distributed faster than at the slower flow rate. In addition, setup 3 visualises the interaction between the previous 2D setups. E.g., it is clearly visible that the supply chamber is perfused quicker than the cultivation chamber, which results in a spike in the supply chamber volume protruding the half dome front developing in the cultivation chamber.

To analyse the distribution of nutrients in 3D, isotropic diffusion was applied as the model combination of laminar single phase flow and tds would have exceeded the computational resources available. Figure 3.22 illustrates the nutrient distribution throughout the 3D geometry after 10 min at a flow rate of 20 µL/min. The simulation indicates that $c_{\max}$ is reached at the outlet of the supply chamber after 115 min, and a complete distribution of nutrients throughout the system is achieved after 160 min. At a flow rate of 100 µL/min, the process is considerably accelerated, with $c_{\max}$ reached at the outlet already after 17 min, and a uniform distribution observed after 30 min.

Overall, it can be concluded that setup 1 (2D, ovally shaped chamber) excludes the membrane entirely and therefore cannot capture either the reduction in flow velocity due to membrane resistance or the transport of sucrose across it. Despite these limitations, the simulation reliably reproduces the flow conditions within the supply chamber and confirms the expected symmetry of the flow field. As a simplified model, it serves as a useful tool for initial investigations of fluid dynamics restricted to the supply region.

Setup 2 (2D, cross-sectional model of the cultivation and supply chambers) includes the membrane but simplifies the geometry by omitting the elliptical base shape. This simplification results in an underestimated cross-sectional area and consequently overestimated flow velocities. The elevated flow speeds enhance convective transport, causing sucrose to distribute more rapidly in the model than would occur under realistic conditions. While this setup marks a good addition to setup 1 by accounting for membrane effects, its geometric simplifications limit its predictive accuracy.

Setup 3 (3D model) incorporates both the membrane and the chamber's elliptical geometry.

This significantly increases computational demands, particularly in terms of mesh resolution and simulation duration. Nevertheless, the additional effort is justified, as this model enables representative simulation of both the supply and cultivation chambers. The resulting flow profiles remain qualitatively consistent with those from setups 1 and 2, indicating a robust general flow pattern across all configurations. But, the 3D model visualises the interaction of the individual 2D flow behaviours which otherwise might go unnoticed. Regarding the flow analysis however, the use of isotropic diffusion – implemented to reduce computational time – artificially broadens the concentration gradient between regions of low and high sucrose concentration. This leads to an increased rate of diffusive transport into the cultivation chamber and a faster rise in outlet concentration than would be expected under more accurate modelling conditions.

Despite this limitation, the results obtained from setup 3 offer valuable insights for a first assessment of solute distribution, particularly since the selected diffusion coefficient remains within a physically reasonable range. The comparison across all three setups underscores the importance of incorporating both membrane transport and realistic chamber geometry to achieve accurate predictions of solute dynamics. At the same time, it highlights the compromises and potential inaccuracies that arise from simplifying assumptions in lower-dimensional models.

Following consultation with biologists from the DialogProTec project, these theoretical results were deemed sufficient to confirm that both the nutrient distribution profiles and the timescales for filling the MBR are suitable for multi-day plant cell experiments.

3.2.2.4 Comparing study results to real flow profile

To assess how closely the simulation studies approximated real conditions, filling experiments were conducted using fully assembled MBRs. As the flow across the membrane had already been analysed both theoretically and experimentally by Finkbeiner [14], the present investigation focused solely on the distribution of nutrients throughout the complete MBR. For the sake of simplicity and improved visualisation, blue-dyed distilled water was used instead of the adapted MS medium.

Three MBRs were tested for each experimental condition. The access ports were sealed with transparent tape. Each device was initially filled with distilled water using a syringe pump (PHD ULTRA™ Syringe Pump Infuse/Withdraw, Harvard Apparatus, Holliston, MA, USA). Once the chambers were completely filled and all air bubbles had been removed, the water supply was replaced with a syringe containing blue-dyed distilled water, serving as a visual analogue for the nutrient solution later used during biological experiments. This dyed solution was introduced into the MBR via the inlet connector at a constant flow rate of 20 µL/min and 100 µL/min, respectively. The distribution of the dye throughout the cultivation chamber was recorded using a monochrome camera (uEye SE, UI-2220SE-M-BG, IDS Imaging Development Systems GmbH, Obersulm, Germany).

The initial flow analysis was performed on completed MBRs, prepared as described in section 3.1, and representative of those distributed to research partners for plant cell cultivation studies. However, the observed flow profiles were inconsistent and not reproducible across trials (see figure 3.23A), although full chamber filling was consistently achieved after 90 min. To determine whether these irregularities originated from design constraints or were caused by variability in the manufacturing process, additional MBRs were tested under identical conditions but without a membrane installed between the supply and cultivation chambers. In these modified setups, the resulting flow profiles aligned well with the predictions made by the simulation studies (see figure 3.23B). However, as these configurations lacked the membrane, the results could only be used for qualitative comparison.

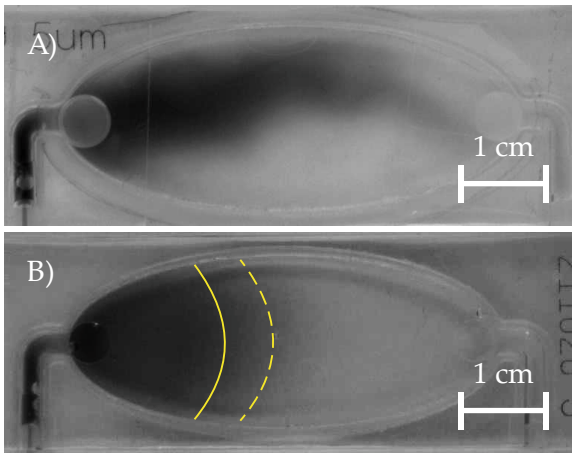

Figure 3.23: A) Flow profile developing in a completed MBR. Wrinkles in the membrane lead to an uneven profile that varies between chips, reducing reproducibility. **B)** Flow profile in an MBR manufactured without the membrane separating the supply from the cultivation chamber. The resulting profile develops consistently and reproducibly across five different MBRs, indicating that the overall design is suitable for plant cell experiments requiring stable flow conditions. Moreover, the observed flow behaviour qualitatively matches the simulation results presented in this section. Adapted from [113].

Following further analysis of the completed MBRs, wrinkles in the membrane were identified as the primary cause of the inconsistent and non-reproducible flow profiles. To enable repeatable and therefore more reliable flow conditions throughout the MBR, the membrane installation process required optimisation. The subsequent section (3.2.3) outlines the improvements made to both the manufacturing process and the MBR design. The resulting flow behaviour of the revised design is presented in 3.2.3.5.

3.2.3 Wrinkle-free membrane installation approaches

As described and illustrated in 3.2.2, in theory the MBR provides suitable flow conditions and nutrient distribution for plant cell cultivation. However, the installation of the membrane with wrinkles led to impaired and uneven flow profiles in the completed MBR. Consequently, it was necessary to develop methods to minimise membrane wrinkling and improve the reliability of the flow conditions.

3.2.3.1 Simulation of membrane stretching

Two primary sources of membrane wrinkling were identified through a possible root cause analysis: the oval layout of the membrane, which causes an uneven distribution of stress across its surface, and the bonding method, ultrasonic welding, which introduces additional stress and stretching during the closing of the MBR.

To investigate the stretching behaviour of an ovally shaped membrane, a simulation study was carried out in collaboration with Khai Chau-Nguyen using COMSOL Multiphysics® [119]. The study first considered a circular membrane subjected to an equivalent even perimeter load, serving as a simplified analogue of the oval membrane geometry. Subsequently, the displacement resulting from an evenly distributed load applied along the perimeter of an oval membrane was examined. Finally, an oval membrane shape was designed to yield an even displacement profile, and the corresponding non-uniform load distribution required along its perimeter was determined.

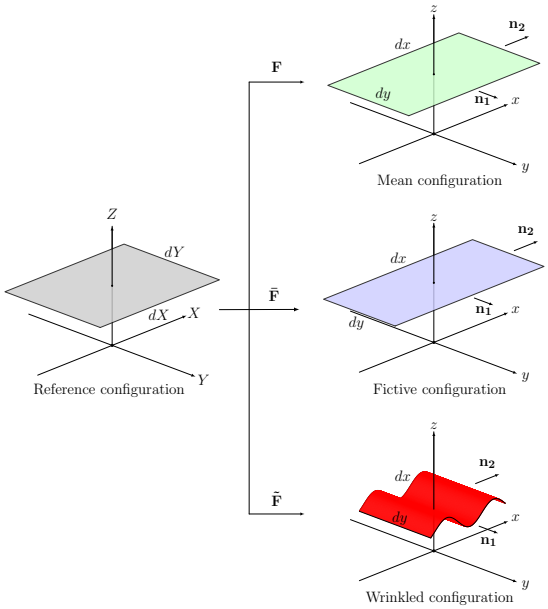

Figure 3.24: Kinematics of wrinkling.

It was assumed that the membrane's behaviour is symmetric with respect to two planes intersecting the semi-major and semi-minor axes. Therefore, the computational model could be simplified by analysing only a quarter of the membrane, imposing by Dirichlet boundary conditions on the corresponding symmetry planes, where $\mathbf{u} \cdot \mathbf{n} = 0$, and $\mathbf{n}$ denotes the normal vector of the symmetry plane. The coordinate system was placed at the centroid of the membrane. The oval membrane shape was described mathematically as an ellipse following $x^2/a^2 + y^2/b^2 = 1$, while the circular geometry was defined by $a = b = 1$. For all three simulation setups, the line load was applied along the boundary of the respective shape.

$$\mathbf{F_1} = \mathbf{F_0} \begin{bmatrix} 1/a \\ 1/b \\ 0 \end{bmatrix} \cdot \mathbf{n_\Gamma} \text{ and } \mathbf{F_2} = \mathbf{F_0} \begin{bmatrix} 1 \\ 1 \\ 0 \end{bmatrix} \cdot \mathbf{n_\Gamma} \tag{3.9}$$

In the modified membrane theory, the properties of wrinkles are introduced on the membrane's mean surface. Two techniques can be employed to extend conventional membrane theory by incorporating tension field theory. One approach involves presenting the relaxed strain energy density, while the other entails adjusting the deformation gradient. The former method is limited to isotropic membranes, whereas the latter offers broader applicability across different membrane types [122].

The initial configuration of the membrane is described using material coordinates X, Y, and Z. Here, X denotes the direction of uniaxial stress, Y represents the direction of wrinkling, and Z corresponds to the normal vector to the membrane plane, as illustrated in figure 3.24. The deformed configuration is indicated by lower-case coordinates x, y, and z. After deformation, the membrane can be in one of the following three states:

A taut state occurs when both in-plane principal stresses are positive, and no modification to the deformation gradient tensor is required. A wrinkled state arises when one of the principal stresses is negative, necessitating an adjustment of the deformation gradient tensor. A slack state is present when both principal stresses are negative, leading to the stress tensor being neglected.

As depicted in figure 3.24, the mapping procedure transitions the membrane from its reference configuration to a fictitious, extended configuration, ensuring that the surface area of the mapped domain matches the actual wrinkled region. In this framework, it is assumed that uniaxial extension occurs along the $\mathbf{n_1}$ direction, while $\mathbf{n_2}$ represents the direction of wrinkling. Based on these assumptions, the modified deformation tensor $\bar{\mathbf{F}}$ is defined as

$$\bar{\mathbf{F}} = (\mathbf{I} + \beta \mathbf{n_2} \otimes \mathbf{n_2}) \cdot \mathbf{F}, \tag{3.10}$$

$$\mathbf{F} = (\mathbf{I} + \beta \mathbf{n_2} \otimes \mathbf{n_2}) \cdot \mathbf{F} \tag{3.11}$$

where $\mathbf{I}$ is the unity tensor, and β is the wrinkling parameter ($\beta = 0$ in the taut state). According to the orthogonality condition in the tension field theory:

$$\begin{aligned} \mathbf{n_1} \cdot \sigma \cdot \mathbf{n_2} &= \mathbf{0}, \\ \mathbf{n_2} \cdot \sigma \cdot \mathbf{n_2} &= \mathbf{0}, \end{aligned} \tag{3.12}$$

where σ is the Cauchy stress tensor derived from the second Piola-Kirchhoff stress tensor $\mathbf{S}$,

$$\sigma = J^{-1} \bar{\mathbf{F}} \cdot \mathbf{S}(\bar{\mathbf{F}}) \cdot \bar{\mathbf{F}}^T, \tag{3.13}$$

with

$$J = \det(\bar{\mathbf{F}}^T). \tag{3.14}$$

The wrinkling condition is determined as follows

$$\mathbf{n_2} \cdot J^{-1} \bar{\mathbf{F}} \cdot \mathbf{S}(\bar{\mathbf{F}}) \cdot \bar{\mathbf{F}}^T = 0. \tag{3.15}$$

Since the mean configuration $\mathbf{F}$ is represented by basis functions in the finite element formulation, both β and $\mathbf{n_2}$ remain as unknown quantities. Given that the material properties and the membrane theory are defined within the reference configuration, equations (3.10) and (3.12) must first be transformed accordingly. Following this transformation, the fictitious Green-Lagrange strain tensor can be expressed as

$$\begin{aligned} \bar{\mathbf{E}} &= \frac{1}{2}(\bar{\mathbf{F}}^T \cdot \bar{\mathbf{F}} - \mathbf{I}) \\ &= \mathbf{E} + \left(\beta + \frac{\beta^2}{2}\right) \mathbf{F}^T \cdot \mathbf{n_2} \otimes \mathbf{n_2} \cdot \mathbf{F} \\ &= \mathbf{E} + \beta^* \mathbf{N_2} \otimes \mathbf{N_2} \end{aligned} \tag{3.16}$$

and β^* and $\mathbf{N_2}$ represent the wrinkling measure and the wrinkling direction in the reference configuration, respectively. These two replace β and $\mathbf{n_2}$ from the deformed configuration as the new unknowns in the formulation. Since the membrane surface is defined in a coordinate system spanned by two unit vectors, $\mathbf{e_1}$ and $\mathbf{e_2}$, the vectors $\mathbf{N_1}$ and $\mathbf{N_2}$ can be described in terms of the wrinkling angle α.

$$\begin{aligned} \mathbf{N_1} &= \cos(\alpha)\mathbf{e_1} + \sin(\alpha)\mathbf{e_2} \\ \mathbf{N_2} &= -\sin(\alpha)\mathbf{e_1} + \cos(\alpha)\mathbf{e_2} \end{aligned} \tag{3.17}$$

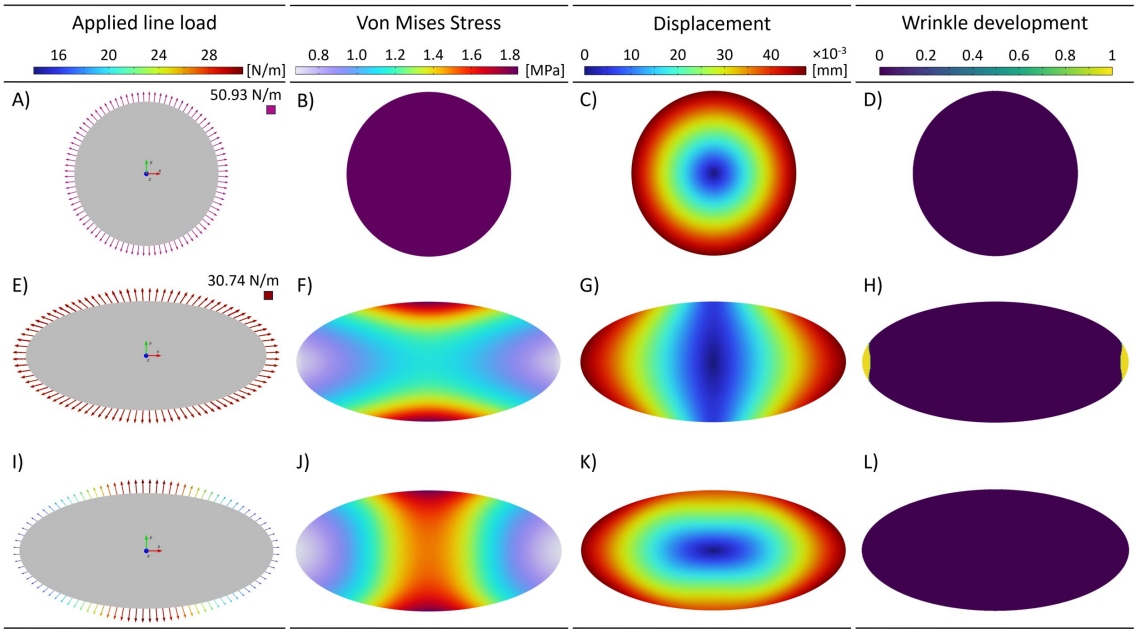

Figure 3.25: Setup and results of the stress and stretch simulation. Panels (A, E, I) illustrate the applied line loads, (B, F, J) show the resulting von Mises stress distributions, (C, G, K) depict the membrane displacement profiles induced by the respective stress states, and (D, H, L) visualise the predicted regions where wrinkle formation is most likely. As can be seen in (B), applying a circular line load to a circular membrane produces an even von Mises stress distribution, leading to a uniform membrane displacement (C). Row 2 presents the results for the current oval chamber geometry with an evenly distributed line load. Here, (F) clearly demonstrates an uneven stress distribution, which leads to an irregular displacement profile (G). Row 3 illustrates an optimisation strategy: the original oval chamber geometry is retained, as it provides optimal cultivation conditions, but a circular line load is applied instead. This could be achieved, for example, by arranging the pins that span the membrane along a circular perimeter. As shown in (K), the resulting displacement profile is considerably more even, closely resembling the ideal displacement achieved in the circular membrane setup (C).

The nonlinear system of equations given in equation (3.12) is solved to determine α and β^*. Based on these solutions, the deformation gradient and the second Piola-Kirchhoff stress tensor are corrected to obtain the final stress distribution and to identify the regions where wrinkling occurs.

The simulation results are presented in figure 3.25. It was observed that a circular membrane subjected to a uniform line load along its perimeter exhibits an even von Mises stress distribution across its surface. This stress distribution results in a rotationally symmetric displacement profile, with the highest displacement – and therefore stretching – occurring at the boundary and zero displacement at the centre. Under these conditions, no wrinkle formation is expected. In contrast, when the same uniform line load is applied to an ovally shaped membrane, the von Mises stress distribution becomes symmetric but uneven. In this case, there is little to no material stretching along the semi-minor axis, while significant displacement develops along the semi-major axis, peaking at the boundary. Based on these profiles, the development of wrinkles is inherently expected.

To investigate a potential improvement, a third case was simulated. Here, a non-uniform line load was applied: lower along the semi-major axis and higher along the semi-minor axis. This approach produced a von Mises stress distribution that concentrated tensile stresses along the semi-minor axis while reducing stress at the ends of the semi-major axis. The resulting displacement profile was more uniform, resembling an oval-shaped analogue of the

circular membrane case, with zero displacement at the centre and maximum displacement at the perimeter. As in the circular case, this evened displacement profile is expected to minimise or prevent wrinkle formation.

It is important to note that these simulations represent idealised conditions for membrane stretching. Consequently, deviations are to be expected under real-world manufacturing and operational scenarios. Nevertheless, the insights gained from these studies provided valuable guidance for the re-design of the MBR to improve membrane installation and reduce wrinkling in 3.2.3.3.

3.2.3.2 Laser transmission welding of MBR

Laser transmission welding (LTW) is a bonding method that applies no mechanical stress to the joining partners and would therefore be a suitable alternative to replace the mechanical ultrasonic welding (USW) process for assembling the upper and lower chip halves of the MBR.

The applied laser system was an EVO 1800 (Evosys Laser GmbH, Erlangen, Germany), equipped with a thulium fibre laser ($\lambda = 1940\,\mathrm{nm}$), providing a maximum output power of 120 W. The welding setup was based on recommendations and protocols from the existing literature (cf. section 2.5 for a detailed overview). The chip halves, with the membrane positioned between them, were placed in an aluminium fixture. Aluminium was chosen due to its high thermal conductivity, which enables rapid dissipation of heat away from the weld seam. The focal plane of the laser was positioned 59 mm below the contact surface between the chip halves and membrane, following the strategy proposed by Mamuschkin, Engelmann and Olowinsky [109] to prevent local burning. To achieve a line energy E of $3\,\mathrm{J/mm}$ (cf. appendix A.3.3), the laser was operated at a power of $P = 24\,\mathrm{W}$ with a scanning speed of $v = 40\,\mathrm{mm/s}$, and the contour was traversed $n = 5$ times.

However, the resulting weld seams proved unsuitable (see figure 3.26). Frequent material burning occurred, especially at the inlets and outlets where the channel geometry narrows. Additionally, random burns were observed along the contour path. Several factors likely contributed to these defects: first, the proximity of adjacent weld seams at narrow points increased the local energy density; second, PC is known to be a challenging material for laser welding, as it readily yellows and subsequently chars under thermal load. Even minor local overheating can trigger progressive charring along the weld seam, severely compromising the bonding quality. Moreover, burns often originated from areas where the membrane was sandwiched between the chip halves. Air pockets trapped between layers can be a cause of burning in LTW, suggesting that the membrane's presence impeded the formation of an intimate contact between the chip halves, promoting local overheating and material degradation. Given these challenges, laser transmission welding was not pursued further for the fabrication of the MBR.

3.2.3.3 New design for ultrasonic welding of MBR

Since laser transmission welding did not yield satisfactory results for bonding the PC chip halves of the MBR as previously demonstrated (3.2.3.2), alternative bonding methods that enable leak-proof sealing and reduce membrane wrinkling – as discussed in 3.1.2.2 – had to be explored. Glueing was ruled out, as it could introduce unwanted substances into future cultivations. Similarly, screwing or clamping the chip halves would enlarge the MBR design, potentially interfering with microscopy setups, and was therefore also excluded. Ultrasonic welding remained the most suitable bonding method for connecting the chip halves, given the intended application of the MBR for plant cell cultivation and experimentation, but a redesign of the weld joints was required.

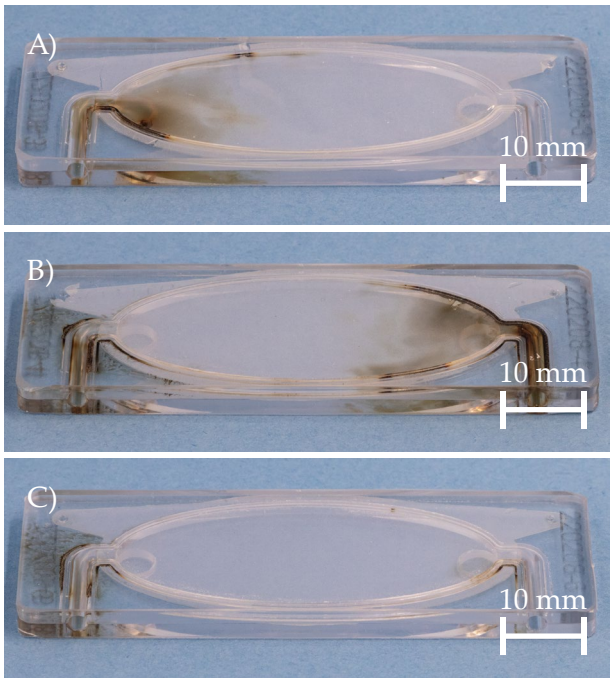

Figure 3.26: Samples of MBR assemblies bonded using LTW. Local burns frequently appeared at the inlet and outlet regions, as well as sporadically at random locations along the rest of the weld seam.

The new design had to meet two key requirements: 1) reduction of membrane wrinkling during installation and bonding of the chip halves and 2) establishment of a leak-proof seal for the chambers and the entire MBR.

As outlined in 2.4.2, only a single source (Dukane Intelligent Assembly Solutions [95]) offered possibilities for bonding ultra-thin membranes, namely, welding at a higher frequency – which was not feasible without a different ultrasonic welding machine – or dampening the welding area. Furthermore, the simulations in 3.2.3.1 showed that an uneven load distribution around the perimeter of the ovally shaped membrane would help to even out material displacement, thereby reducing the formation of wrinkles.

Taking these findings into account, the layout of the energy director (ED) for the MBR was fundamentally revised. Instead of a continuous ED along the chamber perimeter, a sealing ring was integrated around the perimeter of the chambers to achieve a leak-proof seal and dampen the membrane during welding. A groove was incorporated into the design to position and hold the sealing ring before and during the welding process. To combine the two chip halves, the continuous ED along the chamber perimeter was replaced by ten evenly spaced pillar EDs on the top chip half, which fit into ten matching grooves on the lower chip half. During welding the chip halves were pressed together and the sealing ring was grouted, creating the seal. The post-welding hardened pillar-and-groove EDs retain the chip halves in place. The continuous EDs next to the inlet and outlet channels were kept because their squeeze-out is necessary for the installation of the luer-connectors. The new setup is illustrated in figure 3.27 A–C.

The sealing rings are made from Fluor-Kautschuk-Material – a Food and Drug Administration-approved material – and were sourced from Industrie Dichtungs Service (IDS, Willich, Germany). Each ring spans a diameter of 38 mm with a cross-sectional thickness of 0.5 mm. To determine the optimal compression necessary for achieving a leak-proof seal while simultaneously ensuring even membrane tensioning, two different groove depths – and consequently different levels of sealing ring grouting – were tested. The tested parameters are summarised in table 3.7.

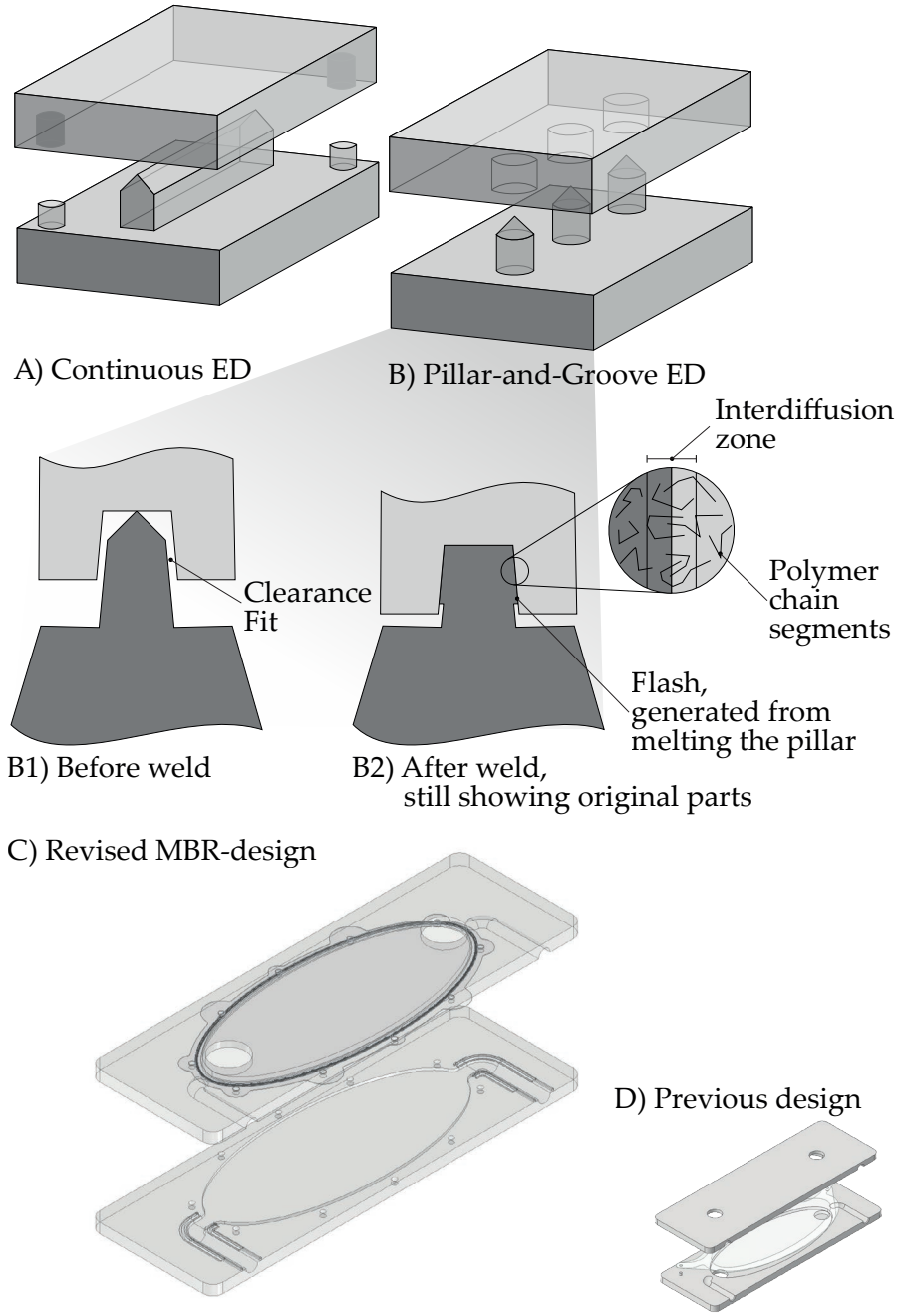

Figure 3.27: A) Conceptual sketch of the energy director used in the initial design of the MBR. **B)** In the revised version of the MBR, the continuous EDs were replaced with pillar-and-groove EDs, enabling a cleaner installation of the chamber-separating membrane with fewer wrinkles. **B1)** Prior to welding, the pillar fits easily into the corresponding bore or groove. **B2)** Following welding, the two previously separate components form a single unit, with an interdiffusion zone indicating the transition between the original parts. **C)** The revised MBR design facilitates a more controlled membrane installation between the chip halves, as the membrane is no longer welded (as shown in **D**), the initial MBR design), but is instead stretched and tensioned across a thin sealing ring.

Sealing ring groove depth	250 µm	350 µm
Final sealing grouting	avg. 249 µm	avg. 163 µm
Welding mode	RPN-controlled	RPN-controlled
Reference Point Numeric (RPN) [mm]	0.2	0.3
Final gap btw. chip halves [µm]	150	50

Table 3.7: Different sealing ring compression analysed while finding the optimal pillar-and-groove design. Due to the sealing ring a final small gap remains between the upper and lower chip halves depending on the groove depth.

The membrane-cut was adjusted to introduce a certain amount of preload in accordance with the results from the theoretical study (figure 3.25I-L). To achieve this, the cutouts for the pins along the semi-minor axis of the membrane were shifted inward by 100 µm, while the cutouts closer to the semi-major axis were positioned progressively nearer to a neutral location between the pin and the membrane, where no preload was applied. The precise arrangement of the membrane cutouts is shown in figure H.1 in appendix H.

3.2.3.4 Welding new pillar-and-groove design ultrasonically

The ultrasonic weld setup for the revised MBR followed a procedure similar to that used for closing the standard MBR described in 3.1.2.2. First, the sealing ring was placed into the designated groove. Then, the membrane was fixed over the ring by positioning it between the ten pins. The weld itself was performed in RPN mode, with a set limit of 0.30 mm and a secondary cap-out condition at 143 J. Initially, both the trigger force and welding force were set to 300 N, but these were subsequently increased to a trigger force F_T of 400 N and a welding force F_S of 500 N. This adjustment was made to reduce the welding time and thus minimise the risk of bubble formation in the weld seam. The full parameter set used for successfully closing the revised MBR is summarised in table 3.8.

Parameters	Pillar-and-groove-design
Sealing ring grouting	163 µm
Welding mode	RPN-controlled
RPN [mm]	0.30
Secondary condition energy [J]	143
Tigger force [N]	400
Welding force [N]	500
Holding period [s]	1
Amplitude [µm]	24.38

Table 3.8: Parameters for welding the revised design for the MBR with a sealing ring compression of 163 µm for a depth of 350 µm for the groove the sealing ring sat in.

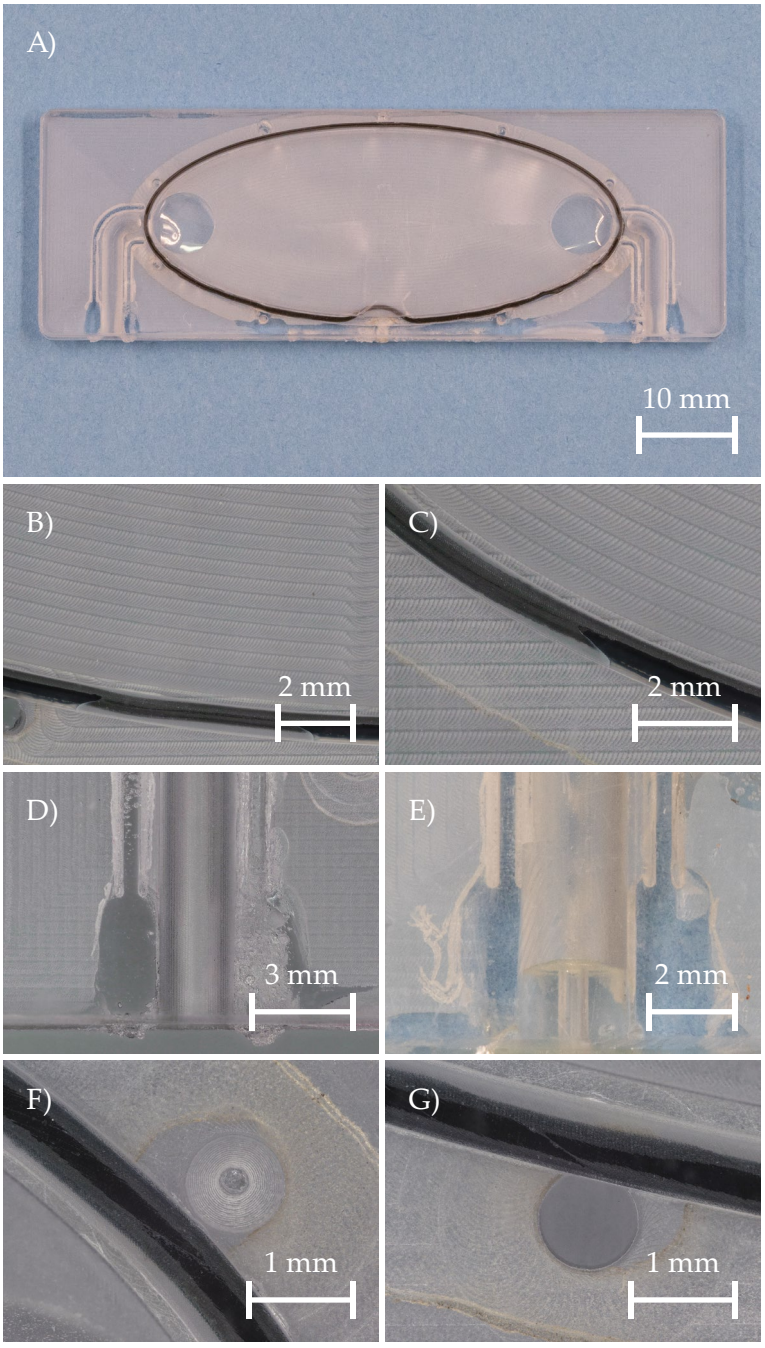

Figure 3.28: Visualisation of good and improperly met assembly criteria: **A)** An MBR where the sealing ring escaped the groove – as a result, the system is not leak-proof. **B)** and **C)** show a sealing ring that is not evenly compressed. Where the ring appears darker and more clearly visible, proper compression is achieved. In areas where it appears greyish, insufficient or no compression is present – leading to leakage. **D)** and **E)** present examples of poor and proper weld seams at the in- and outlet channels. In **D)**, the seams are bubbly and therefore unlikely to be leak-proof. **E)** shows solid and well-defined weld seams where material integrity can be expected. **F)** shows a poor pin weld – the pin is barely fused, and milling grooves are still clearly visible. Only the tip appears to have fused, indicated by a transparent dot in the centre. **G)** presents a high-quality pin weld. It is completely clear, with no visible remnants of the original pin surface, and free of bubbles that might compromise its mechanical stability.

The weld quality was judged on these criteria, which are visualised in figure 3.28:

- The sealing ring was pressed into the groove around the entire perimeter: no breech of the groove, no unpressed areas.
- No bubble formation in the weld seams.
- Sufficient material-squeeze out in the channel areas to install the Mini-Luer connectors after welding (for more information see 3.1.3)

Successfully welded MBRs of the revised design were subsequently fitted with fluidic connectors (3.1.3) and tested for leakage (3.1.4). A completed MBR is shown in figure 3.29. Although a single wrinkle remains in most of the new MBRs, it is significantly less prominent than in the previous design (cf. figure 3.23).

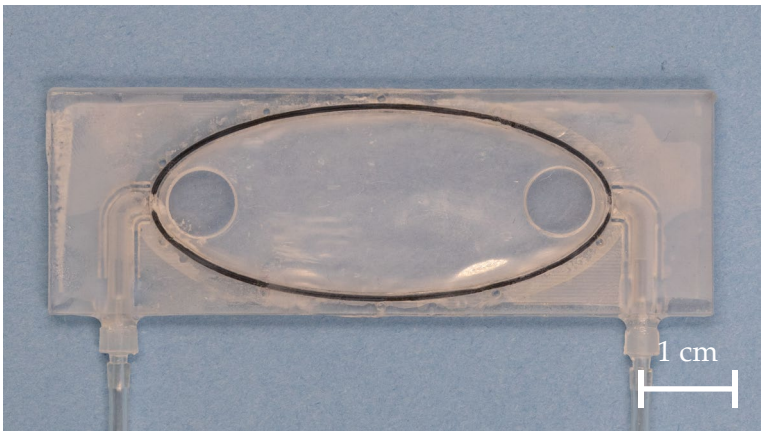

Figure 3.29: A completed MBR of the revised design. It fulfils all the criteria that were introduced previously well. The membrane is installed almost completely wrinkle free. Only minor wrinkles are visible in isolated areas visible through uneven light reflections, e.g. in the lower right area of the oval chamber.

3.2.3.5 Improved flow conditions in new MBR-design

As demonstrated in 3.2.2, theoretical analyses predicted an even nutrient distribution throughout the MBR. However, when the membrane was installed in the original design, the resulting flow profile was uneven and unsuitable for the cultivation of plant cells. With the revised MBR design (3.2.3.3), the membrane separating the cultivation and supply chambers can now be installed with significantly fewer wrinkles.

To evaluate the resulting flow profile, the revised MBR was perfused with tinted water and the flow was visually analysed as described in 3.1.4. The spreading of this solution throughout the cultivation chamber was monitored and recorded using a Canon EOS 7D Mark II with a macro lens (Canon EF100mm f/2.8 Macro USM). This analysis was repeated with three MBRs.

Figure 3.30A shows the filling state of an MBR at a flow rate of 20 µL/min after 50 min. The developed flow profile, indicated by a yellow line, exhibits even distribution along the chamber sides, with a persistent central spike. Two considerations are essential when interpreting this result:

1) The transition from clear to dyed water occurred gradually, as the fluids had already mixed within the tubing connecting the syringe pump to the MBR. Consequently, the blue dye was initially more diluted and first appeared distinctly along the primary flow

axis within the supply chamber. This contrasts with the flow simulation, which assumed an abrupt and complete fluid change. That assumption resulted in a sharper and more concentrated transition zone, while the rainbow-scale display in the simulation – adjusted to maximum intensity values – created a misleadingly clear depiction of the transition region.

2) The image compresses a three-dimensional situation into a two-dimensional representation. Due to the high transparency of the MBR, it is challenging to determine the precise spatial development of the flow profile. In certain areas, the vertical extent of the inserted dye can be inferred; however, in most regions, one must assume that stronger colour intensity indicates dyed water entering both the supply and cultivation chambers. Overall, despite the persistent central spike, the side regions of the chamber displayed a symmetric flow progression.

Figure 3.30B presents the distribution of dyed water within the MBR at a flow rate of 100 µL/min after 3 min minutes. A key difference compared to figure 3.30A is the presence of a small air bubble trapped in the tubing between the clear and dyed fluids. This resulted in an abrupt transition between the two liquids – similar to the simulation conditions – leading to a flow profile that more closely resembled the predicted outcome of setup 1 (2D, oval chamber). The overall flow behaviour was nearly ideal, with only minor imperfections near the edges of the oval chambers. These imperfections resulted from minor membrane wrinkling caused by non-uniform load distribution at the membrane pinning points. Such trapped air was not present in all perfusion tests. It is included here, alongside a standard experimental result without trapped air, to illustrate and emphasise the contrast between a gradual introduction of the nutrient solution (represented by the dyed water), as will occur in future experiments, and the abrupt transition from water to nutrient solution assumed in the simulation. Apart from this abrupt transition, the air bubble visible in figure 3.30B is expected to have had only minimal influence on the development of the flow or mixing profile within the cultivation chamber, as it was located in the threaded opening, thus, largely out of the main flow path and unlikely to interfere significantly with chamber perfusion.

These observations confirm that the ideal flow conditions predicted in 3.2.2 were successfully realised. The revised design has significantly improved flow uniformity compared to the initial configuration (cf. figure 3.23). Furthermore, flow symmetry along the longitudinal axis of the oval chambers has been restored. Minor residual wrinkling persists, which is consistent with the current placement of membrane pinholes that does not yet fully

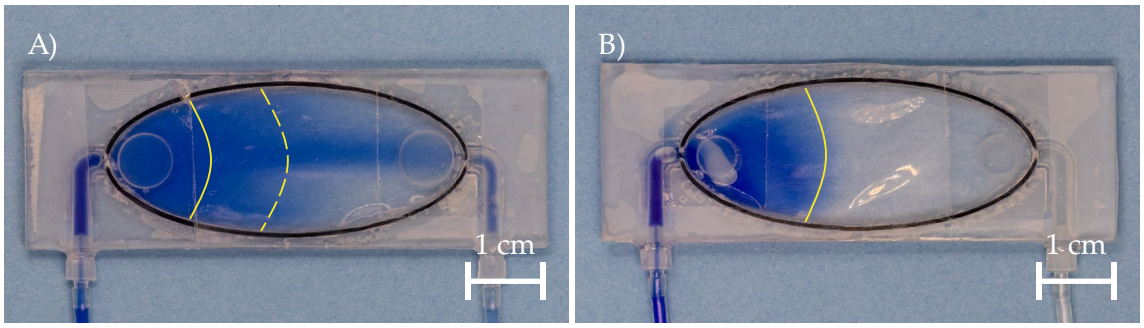

Figure 3.30: A) Flow profile observed in the revised MBR design after 50 min at a flow rate of 20 µL/min. It corresponds well to the flow profile simulated in setup 3 (3D). **B)** Developing flow profile at a flow rate of 100 µL/min after 3 min. An air bubble – still visible in the left threaded opening of the cultivation chamber – caused an abrupt transition between pure and dyed water, resulting in a flow pattern more closely aligned with the simulated nutrient distribution of setup 1 (2D, oval chamber).

achieve the ideal pre-tensioning illustrated in figure 3.25I-L. In summary, the revised design significantly improves flow conditions within the MBR, achieving sufficiently even and reproducible flow profiles to support consistent plant cell cultivation and experimentation.

3.3 Sensors for the Microfluidic Bioreactor

Following the establishment of robust and reproducible cultivation conditions within the MBR, the integration of sensing capabilities for monitoring plant cell experiments represented the next logical development step. In line with the system's adaptive design philosophy, a modular sensor screw was developed and evaluated to enable straightforward integration and replacement of measurement components (3.3.1). A proof of concept was carried out by incorporating an optical pH sensor into the screw design (3.3.2). In addition, a qualitative measurement of H_2O_2 was successfully conducted by C. Metzger at the JKIP to assess the MBR's suitability for detecting biochemical markers relevant to plant stress responses using the Amplex™ Red Hydrogen Peroxide/Peroxidase Assay (Thermo Fisher Scientific Inc., Waltham, MA, USA). Since this did not warrant a redesign or special manufacturing, it is briefly summarized in (5.1.4).

3.3.1 Sensor screw design

When developing removable sensor connectors for the MBR, the requirements for the connection system were analysed first. Key criteria included ensuring a leak-proof yet removable seal of the growth chamber and providing intuitive and straightforward handling (see table 3.9). Additionally, minimising the overall height of the connectors was a priority to maintain compatibility with microscopic observation. Based on these specifications, four designs of an M6 sensor screw with a fine thread (pitch of 0.5 mm to account for the thin upper wall of the cultivation chamber) were developed and manufactured. The connectors were subsequently tested within an MBR, and their performance was evaluated with respect to the initially defined requirements. The observed performances and their potential causes are discussed conclusively at the end of this section. To evaluate the effect of larger openings to the MBR's cultivation chamber, M8 sensor screws were tested as well.

Requirement	Objective
Sealing leak-proof	Preventing contamination from inside the MBR to outside and vice-versa.
Removable	Openings for the insertion of the connectors are as well needed for introducing the cells to be cultivated into the cultivation-chamber of the MBR.
Sufficient transparency	Due to optical working-principle of some sensors.
Easy and intuitive handling	To simplify handling in a lab.
(Simple) producibility	To enable quick production in suitable amounts for experiments.
Small building height	To prevent collision of the sensor and the connection with the microscope.

Table 3.9: Requirements for a sensor screw that connects the MBR as well as sensor for measuring parameters in plant cell cultivations. In this thesis measuring of the pH value was conducted using this screw.

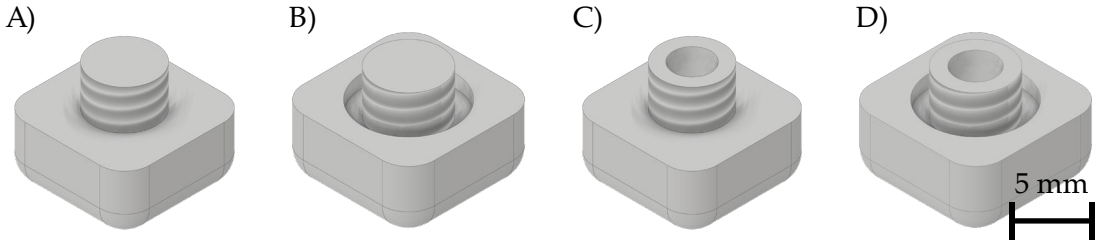

Figure 3.31: Tested connector designs for the M6 sensor screw: **A)** Blind drilled connector, **B)** Blind drilled connector with groove for a sealing-ring, **C)** Drilled through connector, **D)** Drilled through connector with milled out groove for a sealing-ring.

The sensor screws were initially designed for an optical sensor, specifically a pH measurement was conducted optically to minimise disturbance to the plant cell cultivations (for further information on pH measurement using the sensor screw, see 3.3.2). Four M6 connectors for the optical fibre connecting the MBR and the sensor (see figure 3.31) were manufactured from PC, keeping the material consistent with the MBR's housing material. Two connectors were fabricated with blind drillings, while the other two were drilled through and subsequently sealed. This was to analyse the influence of scratches at the bottom of the blind holes on the sensor readouts. Drilled through connectors offered the possibility to seal the opening with a clear foil avoiding the influence of drilling marks. For sealing, three approaches were tested: covering with a PC foil, application of simple adhesive tape, and use of PDMS. This experimental setup was intended to assess whether the optical transparency – reduced in the blindly drilled connectors due to scratch marks from the drilling tool – had a measurable impact on the precision of the optical measurements. Additionally, one connector of each type (blindly drilled and drilled through) was modified with a supplementary groove designed to accommodate an additional sealing ring, providing an alternative sealing strategy should leakage occur without supplementary measures.

To test the transparency of the manufactured connector screws the transmission through the bottom of the blind-drilled hole as well as the sealing-foils were measured using a Leitz Ergoplan microscope in combination with the Red Tide USB650 Fiber Optic Spectrometer from OceanInsight and compared. The PDMS-sealed connector showed the lowest transmission-rate while the PC-foil-sealed connector transmitted about 95 % of the light (see figure 3.32).

Furthermore, the manufactured connector-screws were tested regarding their sealing-capability by sealing an MBR with the tested connector. The sealed MBR was then hooked up to a syringe pump (Harvard Apparatus PHD Ultra), and deionised water was pumped through the MBR at a steady flow rate of 2 mL/min. The test was continued for 15 min to ensure that the sealing was fully tight and stayed dry as such.

The two connector designs with the drilled-through opening for the optical fibre were covered with a PC-foil, PDMS and, 3M polyester tape 851 ("green tape") to create a leak-proof boundary between the cultivation-chamber and the optical fibre outside the MBR. The PC-foil could not be bonded sufficiently in our experiments, but the 3M polyester tape 851 sealed the connector plug adequately. However – of course – this tape-sealed-connector could not be used for pH-measurements due to the green colour and low light transmission of the tape. The PDMS-sealed drilling-hole was sealed leak-proof, too. Furthermore, the blindly drilled connectors both sealed the MBR sufficiently. There was no observable advantage for sealing the system in including an extra groove and additional sealing ring

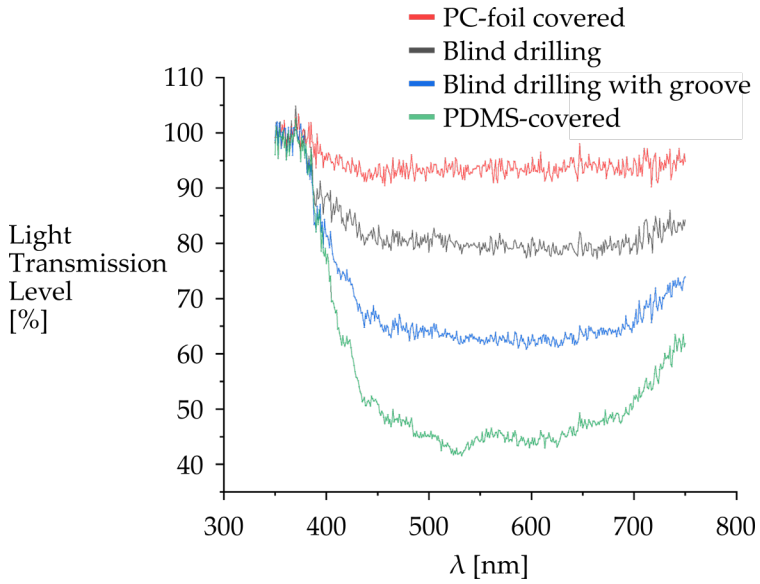

Figure 3.32: Light transmission trough different materials as connector tops measured using a Leitz Ergoplan microscope in combination with the Red Tide USB650 Fiber Optic Spectrometer by OceanInsight.

compared to the connector without those. The simple blindly drilled connector sealed the MBR sufficiently.

From the results of these experiments on the different designs it was concluded that the light transmission through the different connector designs did not seem to affect the measuring significantly. Thus, for further experiments, blindly drilled connectors without an additional groove and sealing ring were applied.

In addition to evaluating the suitability of the sensor screw for use with optical sensors, approaches to facilitate the insertion of plant cells into the cultivation chamber were investigated. For this purpose, MBRs with larger threaded openings (M8 instead of M6) were fabricated. The combination of the sensor screw with the larger MBR was found to be equally leak-proof and suitable for optical sensing as its smaller counterpart.

However, the pipettes required to fill these MBRs – which had to be substantially larger – were not part of the standard laboratory equipment available at our biology partner institutes. As a result, such pipettes were less readily available, which conflicted with the fourth requirement for the sensor screw defined in table 3.9 – easy and intuitive handling – since specialised equipment would have to be procured. Moreover, the enlarged openings did not significantly improve the ease of inserting plant cells into the cultivation chamber. Consequently, it was decided to retain the existing design based on an M6 sensor screw. Proof-of-concept experiments applying these connectors are discussed in the following section and in 5.1.3.

3.3.2 Sensor screw application for measuring pH

As sessile organisms, plants cannot escape environmental stressors by relocation. Instead, they have evolved complex signalling pathways to evaluate and respond to abiotic and biotic challenges. Frequently, molecular patterns associated with potential pathogens are detected at the level of the plasma membrane. Upon recognition, the signal is transmitted from the cell exterior into the cytoplasm, ultimately triggering a defence response, if possible [123]. In pathogen triggered immunity, a basal immune response signal transduction often involves the secondary messenger Ca_2^+. The extracellular space typically contains a much higher

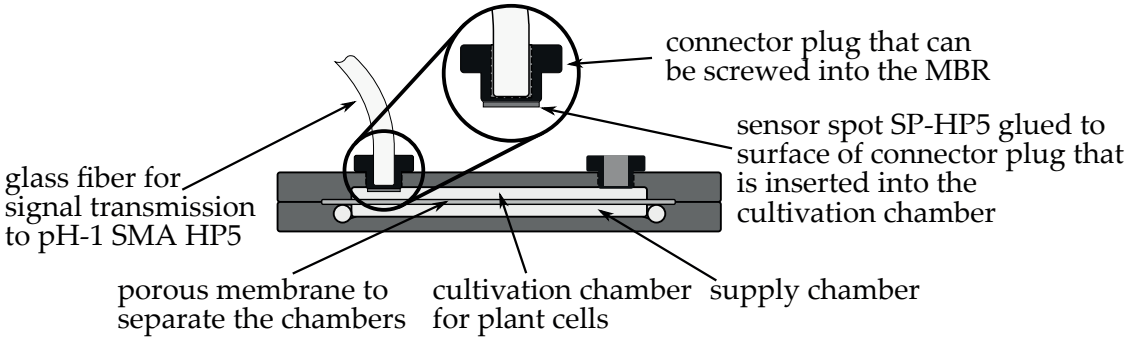

Figure 3.33: Setup for measuring the pH value in the MBR: A sensor spot (SP-HP5) is affixed to the surface of the connector plug that faces the plant cells within the cultivation chamber. A blind-drilled opening allows a glass fibre to transmit the optical signal from the SP-HP5 to the external pH sensor (pH-1 SMA HP5, PreSens Precision Sensing GmbH, Regensburg, Germany). This arrangement enables straightforward retrieval and replacement of the sensor spot once it has reached the end of its service life.

concentration of $Ca_2{}^+$ compared to the cytoplasm. Upon pathogen detection, $Ca_2{}^+$ ions are transported into the cell, where they modulate cellular activities through transcription factors [124]. This import of $Ca_2{}^+$ is accompanied by the movement of protons (H^+) across the plasma membrane [125], resulting in a shift in the extracellular pH that can be easily quantified. Consequently, pH changes are widely used as a reliable readout to monitor the initiation of a PTI response.

To enable the rapid screening of multiple fungal metabolites for their immunoactivity, the measurement of pH changes in the MBR needed to be both simple and reliable. For this purpose, a retractable and sealable sensor screw (described in 3.3.1) was employed to connect the PreSens pH-1 SMA HP5 sensor (PreSens Precision Sensing GmbH, Regensburg, Germany) to the corresponding sensor spot SP-HP5 (PreSens Precision Sensing GmbH, Regensburg, Germany) integrated into the MBR (concept visualisation see figure 3.33).

The connector-sensor setup was evaluated for its precision in measuring pH values. Measurements were compared against those obtained with the Mettler Toledo SevenCompact S220 (external pH sensor) as well as the nominal pH buffer values provided by the manufacturers. In the MBR, the pH of the respective buffer was measured three times under each flow condition: for 10 min at flow rates of 0 mL/min and 2 mL/min, and for 45 min at a flow rate of 0.2 mL/min. The absolute deviation from the reference buffer values was determined. Across all three conditions and for all three pH buffers, the interquartile range remained small, ranging between 0.014 pH and 0.005 pH. Median and average values were – apart from the pH evaluation in the pH 6 buffer under static conditions – nearly identical, suggesting a symmetrical distribution of the measured data (see figure 3.34).

However, when comparing measurements taken with the connector setup to those obtained in a glass beaker, the MBR measurements consistently indicated a higher pH value for the same buffer (figure 3.34). This discrepancy likely arises from the sensor being designed for use with glass reactors rather than for measurements through polymer materials. Since no correlation could be established between the measured offsets and the different transparencies of the connectors (cf. figure 3.32), it is assumed that the variations in optical transmission were not the primary cause of the observed measurement offset, but instead the offset is material related.

So, it appeared that the polymer connectors introduced a shift in the measured pH values compared to reference measurements conducted using a glass beaker. Since glass is the recommended reactor material according to the sensor specifications, it is likely that the sensor calibration is specifically adjusted to compensate for the optical properties of glass.

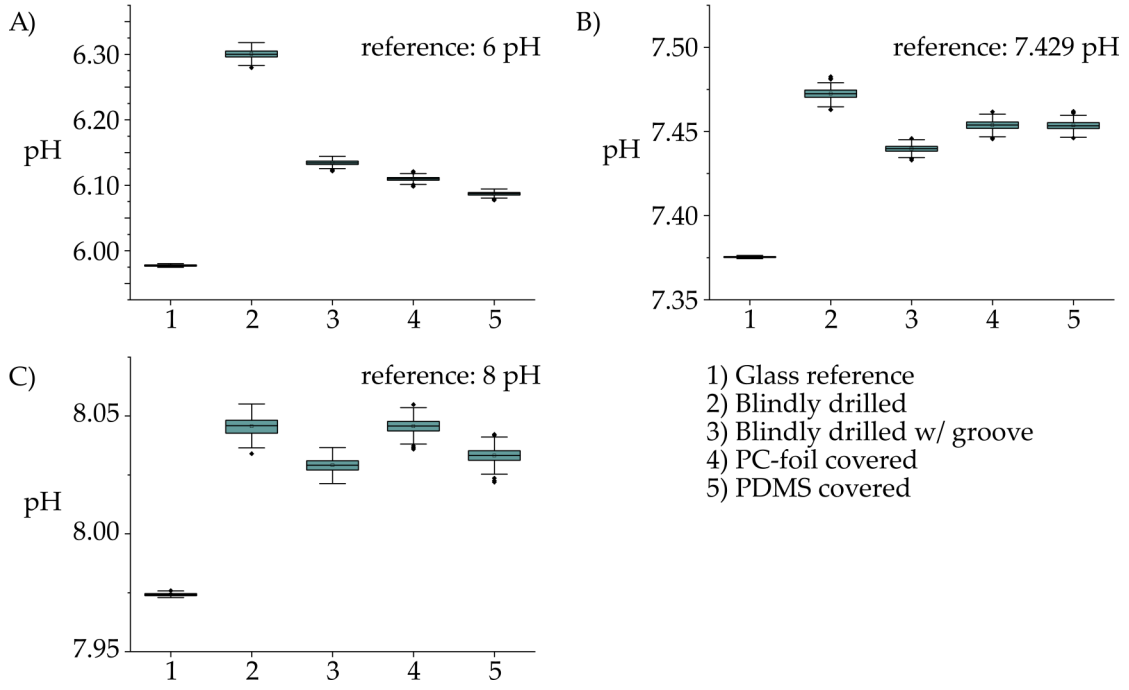

Figure 3.34: Measured pH through different connector types in the MBR. The display summarizes the measurements at a flow rate of 0.2 mL/min. As a reference the pH-value of the according pH-buffer was measured through the wall of a glass beaker. **A)** Buffer: 6 pH, **B)** buffer: 7.429 pH, **C)** buffer: 8 pH.

As a result, measurements conducted through a polymer material exhibit a systematic deviation. However, if this shift is accounted for through appropriate calibration, the pH-1 SMA HP5 sensor combined with the corresponding sensor spots is suitable for measuring pH values within the MBR. A proof-of-concept experiment demonstrating the application of the installed PreSens pH-1 SMA HP5 sensor is detailed in 5.1.3.

This concludes the developments of the MBR presented in this thesis. Several aspects of the MBR were addressed, ranging from its manufacturing and design refinements to the introduction and application of the sensor screw for the microfluidic chip (MFC).

The initial sections established the foundation for understanding how the MBR is fabricated and what challenges and opportunities arise from the process. Notably, while the hot embossing process enables straightforward fabrication of PC chip halves, demoulding them from the hot embossing (HE) mould can cause deformation and warping, leading to alignment difficulties during ultrasonic welding, where precise positioning of the halves is essential. To improve demoulding, the polished chrome-coated plate used as the baseplate during hot embossing was redesigned and newly manufactured with circumferential grooves that facilitate even release of the cast chip halves.

The ultrasonic welding process is not an easy bonding method to adapt to any chip layout. However, it offers the major advantage of avoiding additives such as glues, aggressive solvents, or absorbers. This is particularly attractive to biologists who aim to eliminate – known or undetected – external influences on their experiments. Consequently, the design of the MBR followed the guiding principle of using as many materials as necessary for constructing the MFC, but as few as possible.

Another key objective for the MBR was to unify cultivation conditions in the MFC and adapt the system for successful fungal hyphae cultivation. This was achieved by replacing the installed membrane with variants of smaller pore diameter already available at the IMT. Two challenges emerged: first, the thinner membranes tended to wrinkle and tear

during USW. This was mitigated by adjusting the welding parameters to achieve a stable installation. Second, during initial cultivation experiments (presented in 5.1.2), fungal hyphae grew out of the cultivation chamber towards the inlet of the supply chamber after two days, likely attracted by the higher nutrient concentration in that area. Within the scope of this thesis, it was not possible to procure and install new membranes for further testing. However, preliminary testing for interkindgom communication dissection using two connected MBRs was still successful.

Addressing the second challenge, membrane wrinkling was substantially reduced and nutrient distribution further homogenised through a revised design of the MBR still applying USW. In this new design, the previously continuous energy director along the oval chambers was replaced by ten evenly spaced pillar EDs, with corresponding holes in the opposite chip half. The membrane separating the chambers was spanned by these pillars and across a sealing ring encircling the chambers. After welding, the pillars bonded the halves together, stretching the membrane across the sealing ring like a drumhead. This resulted in wrinkle-free membranes and more uniform flow conditions across both chambers. Furthermore, the new design simplifies the installation of different membranes, as the USW parameters no longer need adjustment for varying membrane materials or thicknesses.

Finally, to simplify the use of the MBR in biological applications, a sensor screw was developed that seals the in- and outlets for plant cells in the cultivation chamber. This design allows any integrated sensor to be placed in close proximity to the cells it monitors – for instance, measuring stress indicators – without obstructing them. The screw design was tested for transparency and leak-tightness, and subsequently applied with an optical pH sensor to monitor a chitosan-induced pH shift. The results of this experiment are presented in 5.1.3.

Through this work, the design and usability of the MBR have been significantly improved and simplified. The presented methods and concepts provide a robust foundation for future research and applications in biological laboratories, facilitating controlled and modular setups for the cultivation of plant cells and the investigation of intra- and interkingdom communication.

4. The Root Chip

Analysing seedlings and their root systems within MFCs is of central interest to many biologists. The RC provides an efficient platform for such studies. The following sections summarise its fabrication from PDMS (section 4.1). Next, adaptations to the RC design and the process of manufacturing PDMS-moulds are presented (section 4.2). Special attention is given to integrating micro-mixing structures upstream of the analysis channel to enable more flexible administration of different compounds to the root under observation; the corresponding MFCs are discussed in section 4.3. Finally, a key objective was to create an RC that could be sterilised by autoclaving. In section 4.4, an RC fabricated from polycarbonate is presented and discussed that satisfies this goal.

4.1 Manufacturing of the initial Root Chip from PDMS

To lay the groundwork for understanding the challenges inherent in the design of the RC and its manufacturing procedures, the manufacturing procedures for the initial PDMS Root Chip are briefly described in the following sections. These sections are arranged in process-chronology: Casting, covering, and, finally, testing of the RC. A general introduction of manufacturing microfluidic chips from PDMS is provided in appendices A.1.2, A.2.2 and A.3.1.

4.1.1 PDMS casting

The upper chip halves of the RC are moulded from PDMS. For this moulds were micro-milled from PMMA (figure 4.1) with the negative structures of the channels as well as markers were the openings for the in- and outlet and the entrance for the seedlings are planned. Prior to casting, the moulds were cleaned with compressed N_2 to remove any dust from the moulding posts.

The PDMS used was Sylgard™ 184 Silicone Elastomer Kit (Dow, Midland, MI, USA). The elastomer base was mixed thoroughly with the curing agent in a 10:1 ratio. The mixture was then degassed in an evacuated desiccator to eliminate air bubbles, as described in appendix A.2.2. This avoided that entrapped air could adhere to fine structures or obstruct the optical path, rendering the chip unusable.

Once degassed, the PDMS was poured into the mould. To ensure consistent thickness, the volume was limited to between 11.5 g and 12 g, yielding a chip half thickness of approximately 3.5 mm. The cast was checked again for air bubbles, re-degassed if necessary, and then cured in an oven at 65 °C for 60 min. After curing, the mould was cooled to room temperature, and the cast was carefully demoulded. Care was taken not to damage or tear the cast during removal. Edges were trimmed with a scalpel. Figure 4.2 shows a completed chip half. Casts were stored in clean, transparent polystyrene containers in individual compartments to maintain cleanliness between processing steps.

After cooling and demoulding, holes for the inlet and outlet were drilled at the marked locations using a 1 mm drill bit. Additional openings for seedling insertion were drilled at an angle of 45° to encourage root growth along the channel axis in subsequent experiments. The effect of different insertion angles on successful seedling entry into the analysis channel is examined in 4.2.1.

Figure 4.1: Micro-milled mould for casting the initial PDMS RC, fabricated from PMMA. All features are created in reverse, such that raised blocks in the mould result in channel cavities in the PDMS-cast and, ultimately, the final MFC. To reduce manufacturing time, the mould accommodates three casts simultaneously. Each cast matches the dimensions of a thin cover slip (60 mm × 24 mm).

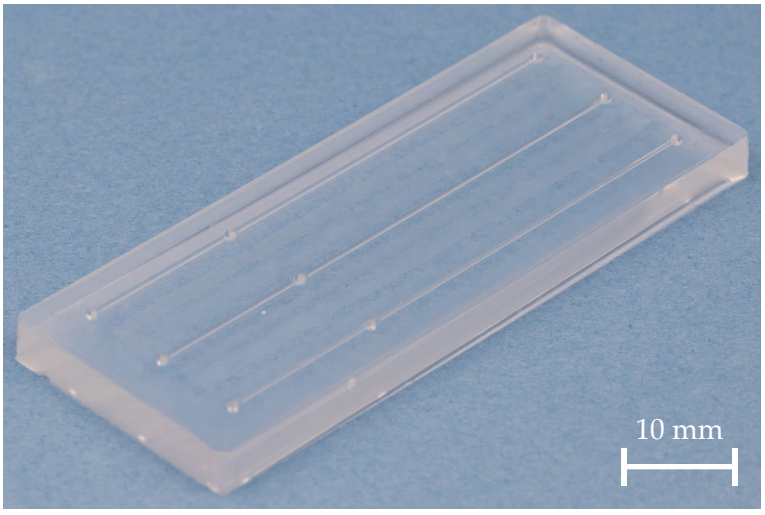

Figure 4.2: Demoulded PDMS-cast of the initial RC, with channel structures and the intended bonding surface to the cover glass facing upwards.

4.1.2 Covering

Before covering the PDMS-halves of the RC with glass slides, all components were thoroughly cleaned. This procedure was conducted in a cleanroom environment to minimise contamination by dust or debris. Each glass slide underwent a three-step ultrasonic cleaning process: in (1) acetone, (2) isopropanol, and (3) DI water, each for 3 min. The slides were subsequently dried using compressed N_2. As acetone degrades PDMS, the chip halves were cleaned only in isopropanol and DI water, following the same timing and drying protocol.

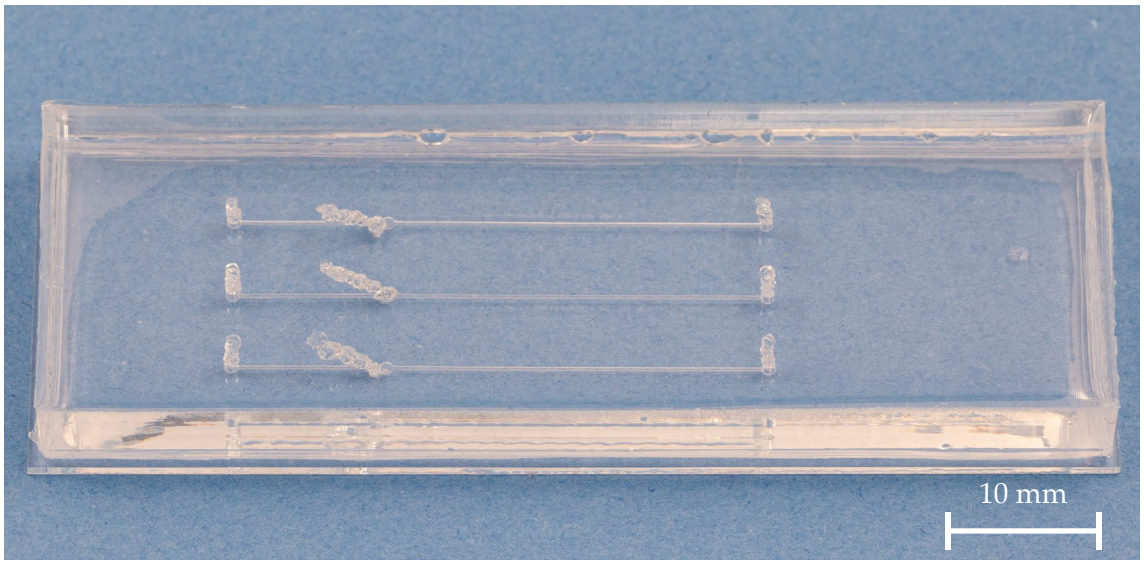

Figure 4.3: Completed PDMS RC of the initial design with three straight analysis channels for monitoring individual seedlings.

Following cleaning, the PDMS-casts and corresponding glass slides were placed in a 4tec plasma etcher (4-TEC Vakuum-Anlagenbau, Vierkirchen, Germany) with their bonding surfaces facing upwards. Either side of the glass slides was suitable; for the PDMS parts, the structured side was used. The bonding surfaces were activated by exposure to 100 W oxygen plasma for 7 s. After removal from the chamber, each activated PDMS surface was carefully but quickly aligned with a glass slide and pressed together to form a permanent bond, as the bonding partners had to be assembled within 2 min to achieve a strong bond. Figure 4.3 shows a completed RC.

Two types of glass slides were used for sealing the RC. Standard versions used 1 mm-thick glass slides (Ref 302980, Knittel Glass, Braunschweig, Germany; 75 mm × 25 mm). For applications requiring closer proximity to a microscope objective, thinner 190 µm cover slips (Menzel-Gläser, Gerhard Menzel GmbH, Braunschweig (BW), Germany; 60 mm × 24 mm) were used. However, these thinner slides were more fragile, requiring especially careful handling during fabrication and experimentation.

4.1.3 Testing

For quality assurance, each fabricated chip was subjected to leak testing. Isopropanol was pumped through each individual channel at a flow rate of 500 µL/min using a syringe pump (PHD ULTRA™, Harvard Apparatus, Holliston, MA, USA, figure 4.4). Only chips that remained leak-tight under these high-flow conditions were subsequently dried, packaged, and distributed to collaborating biologists.

4.2 Optimisation of moulds and protocols for the PDMS-based Root Chip

During the prototyping phase of the Root Chip, PDMS was the material of choice. Different designs were tested. The most important are summarised here. The following sections cover the approaches to optimising the inlet-angle for the seedlings (4.2.1), improving mould manufacturing (4.2.2 and 4.2.4), as well as changing the design so that the MFC can hold more seedlings at once (4.2.3).

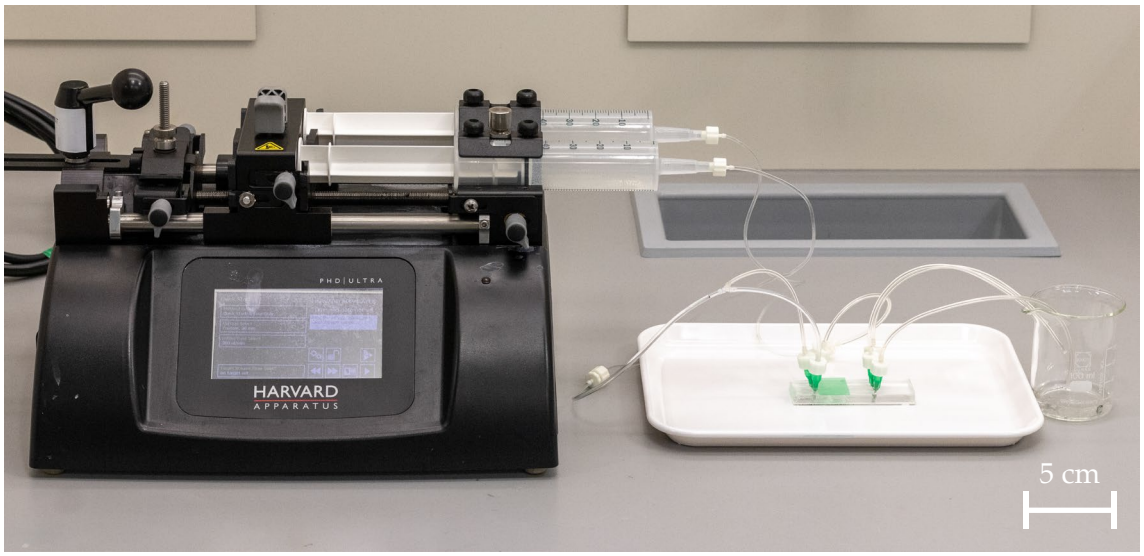

Figure 4.4: Setup for leak testing PDMS Root Chips. A syringe pump (PHD ULTRA™, Harvard Apparatus, Holliston, MA, USA) is used to pump isopropanol through each channel of an RC at 500 µL/min.

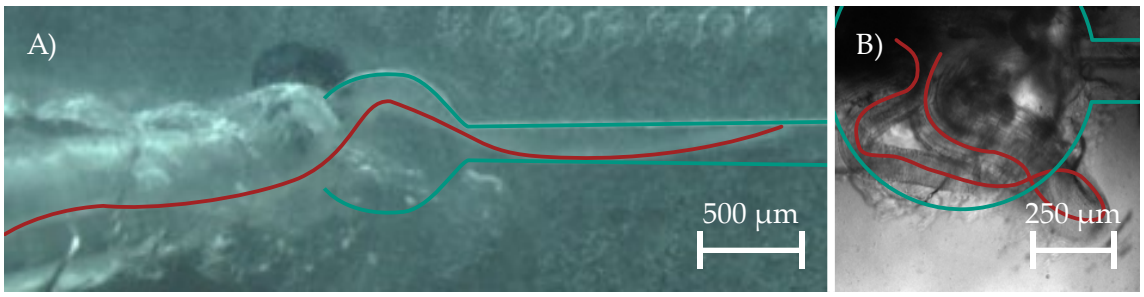

Figure 4.5: A) Root that had just entered the analysis channel, with its progression highlighted in red and the channel outline in green. Taken on day two of the in-chip cultivation. **B)** A root that failed to enter the analysis channel and instead turned around. Pictures courtesy of A.-C. Schmit, IBMP (CNRS, Strasbourg, France).

4.2.1 Different intro angles for seedlings

An early challenge with the RC was the unexpected behaviour of the primary root of transferred seedlings, which often turned around and grew upstream toward the inlet or which turned 180° and grew back upwards into the transferring tip, rather than progressing through the analysis channel towards the outlet [126], [127]. An example of this phenomenon is shown in figure 4.5B.

Following discussions with colleagues at IBMP (CNRS, Strasbourg, France), it was hypothesised that these reversals might be caused by an unfavourable seedling entry angle. Previously, openings were drilled at 45° from the analysis channel upwards, causing a relatively sharp turn for the developing root. Although the mechanism behind the reversals remained unclear, smaller entry angles were tested to identify potential improvements.

A series of Root Chips was produced in which the seedling inlets were drilled at varying angles: 45°, 40°, 35°, 30°, 25°, and 20° relative to the analysis channel. Inlets and outlets were drilled straight down as usual. The casts were then cleaned and covered, and the devices tested as described in 4.1.2. Prior to shipment to the IBMP (CNRS, Strasbourg, France), side-view photographs were taken of several completed RCs for each tested angle, and actual entry angles were measured (see figure 4.6). It became evident that the resulting angles were steeper than intended. This discrepancy was attributed to deformation during

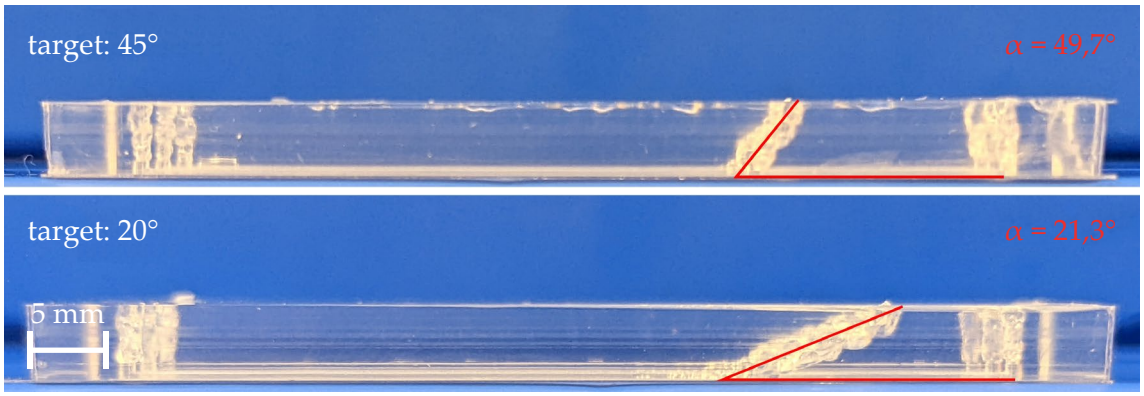

Figure 4.6: Root Chip with seedling entries drilled at different angles. White (left) displays the target angle, while the measured angle is displayed in red (right) and averaged over all successfully manufactured RCs of this angle. Angles are measured between the seedling inlet and the horizontal plane.

		Measured root length [mm]		
Entry angle	Imaging after	Top inlet	Middle inlet	Bottom inlet
40°	7 d	5.5	14.5	15.5
CTRL (45°)	7 d	no entry	17	no entry
35°	6 d	4.5	no entry	no entry
CTRL (45°)	6 d	no entry	19.5	5
25°	6 d	17	no entry	no entry
CTRL (45°)	6 d	27	11 (2 root parallel)	13
20°	7 d	8.5	7	21.5
CTRL (45°)	7 d	36 (until outlet)	36 (until outlet)	36 (until outlet)

Table 4.1: Cultivation results for varying entry angles for the seedling inlet into the analysis channel. Cultivation experiments conducted by E. Herzog at IBMP (CNRS, Strasbourg, France).

drilling into the soft PDMS material. This issue and potential solutions are discussed further in 4.2.2 and section 4.4.

At IBMP, pregerminated seedlings were transferred into the Root Chips, as shown in figure 4.7A. During cultivation, the chips were positioned at a 45° incline to support root guidance via gravity. Accordingly, the configuration with a 45° seedling inlet aligned root growth best with gravitational pull. While smaller angles provided smoother transitions into the analysis channel, they also diverted root growth away from the gravitational direction (conceptually visualised in sketch in figure 4.7B). Experiments and data collection was conducted by Etienne Herzog, IBMP (CNRS, Strasbourg, France).

Each chip variant was evaluated against the current standard RC with a 45° seedling entry angle. Observations included whether the root entered the analysis channel and, if so, how far it grew within six or seven days. The outcomes are summarised in table 4.1.

The findings suggest that entry angles of 20°, 40°, and 45° supported successful root entry. However, the 20° angle resulted in proximity issues with tubing connected to the inlet and was thus excluded from further consideration.

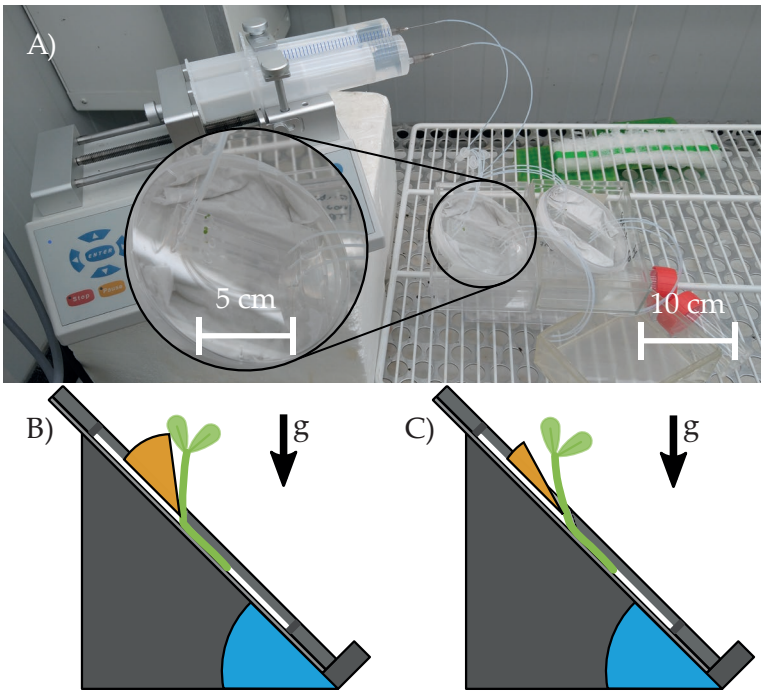

Figure 4.7: **A)** Cultivation of seedlings in the RC on a Petri dish propped at 45°, facilitating gravity-assisted guidance. Pictures taken at IBMP (CNRS, Strasbourg, France). Sketches of the cultivation setup with different inlet angles that guide the seedlings primary roots into the analysis channels. **B)** Standard inlet angle. **C)** Smaller inlet angle. It smoothed the channel transition but deviated more from gravitational alignment.

While the RC with a 40° entry angle achieved a 100 % root entry success rate into the channel, roots grew on average only 8.5 mm over seven days. In comparison, roots in the standard 45° setup reached an average of 23.7 mm. This significant difference would necessitate new baseline experiments and invalidate prior data for comparative studies. Moreover, the 45° configuration achieved a 73 % root entry success rate. Based on these considerations, the 45° entry angle was retained for future RC designs. However, the manufacturing process will be optimised to achieve more accurate and reproducible drilling at this angle (cf. 4.2.2).

4.2.2 Casting openings directly

The chip halves containing the analysis channels were cast in PDMS to leverage its suitability for rapid prototyping, enabling quick and cost-effective design iterations. However, for each MFC variant to be meaningfully tested in a biological context, it had to be produced at least three times, but typically more than ten chips were produced each month for years. As such, reducing fabrication time became a critical objective.

One labour-intensive and contamination-prone step was drilling the marked positions for the inlet, outlet, and seedling entry. Drilling also created particulate matter – undesirable in biological setups–and often resulted in poor-quality openings due to the elastic nature of PDMS. Initial improvements involved freezing the chip halves to −65 °C before drilling, but this did not sufficiently increase rigidity. Using liquid nitrogen to reach −190 °C was dismissed due to practical handling constraints with available equipment.

Instead, a faster drilling machine and a sharper drill bit were employed, leading to slight improvements in hole quality. Alternative approaches such as using a biopsy punch were also considered. However, no punch of the required 800 µm diameter could be sourced.

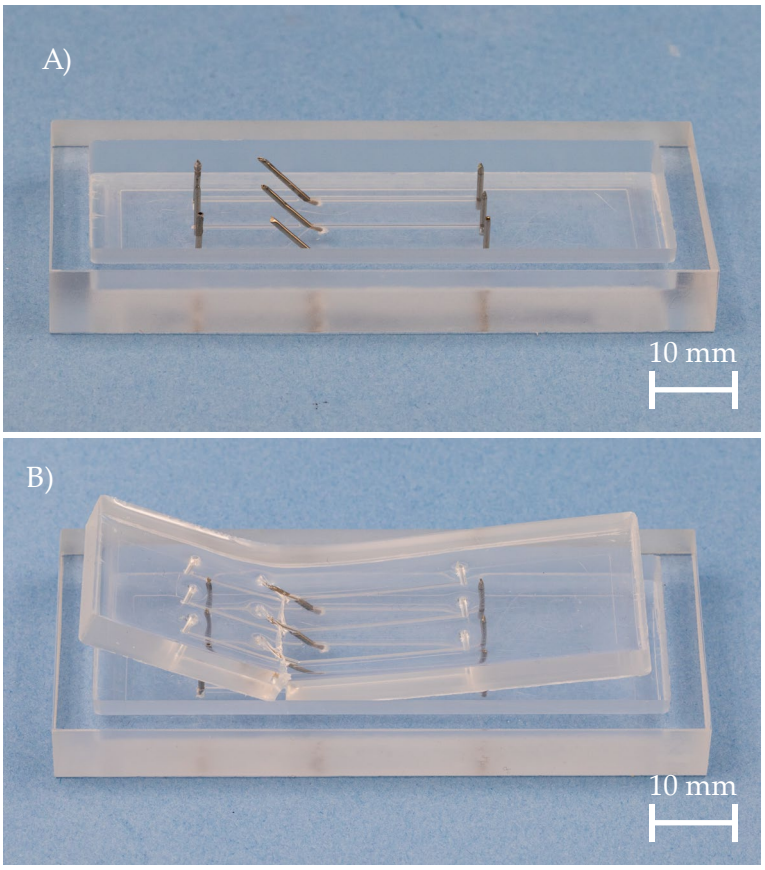

Figure 4.8: A) Modified PDMS-mould with 800 µm pins for pre-forming inlet, outlet, and seedling entry holes. **B)** Partially demoulded PDMS-cast, showing failure in the seedling inlet area. The pins angled at 45° in close proximity to the pins opening the inlets are hardest too demould, which could only rarely be completed successfully.

This size was specifically requested by biologists at IBMP (CNRS, Strasbourg, France), as larger openings had previously caused leakage with their tubing systems [128]. Commonly available biopsy punches ranged from 1 mm to 10 mm in 1 mm increments.

As an alternative, integrating the inlet and outlet formation directly into the casting process was explored. For this, the mould was micro-milled from PMMA as usual. However, instead of using surface markers for future drilling, 800 µm diameter holes were drilled directly into the mould, and corresponding pins were inserted (figure 4.8A). Directly milling such high-aspect-ratio features into PMMA was not feasible due to mechanical fragility.

The PDMS was cast using the modified mould as described previously (cf. 4.1.1). Unfortunately, demoulding proved problematic: many chip halves tore near the pin sites, particularly around the seedling inlets, which had a steep 45° angle. These areas were consistently prone to damage (figure 4.8B).

Thus, further adaptation of the mould design would have been necessary and, additionally, changing designs was still difficult. As a result, the use of additive manufacturing (AM) for creating moulds suitable for PDMS-casting was explored instead. These results are discussed in the following section.

4.2.3 9-channel Root Chip

In discussions with the partnering biologists, the idea of a larger Root Chip – containing nine instead of three analysis channels – was proposed. The aim was to reduce the influence of external cultivation conditions, such as tilt (cf. table 4.1), and to simplify handling

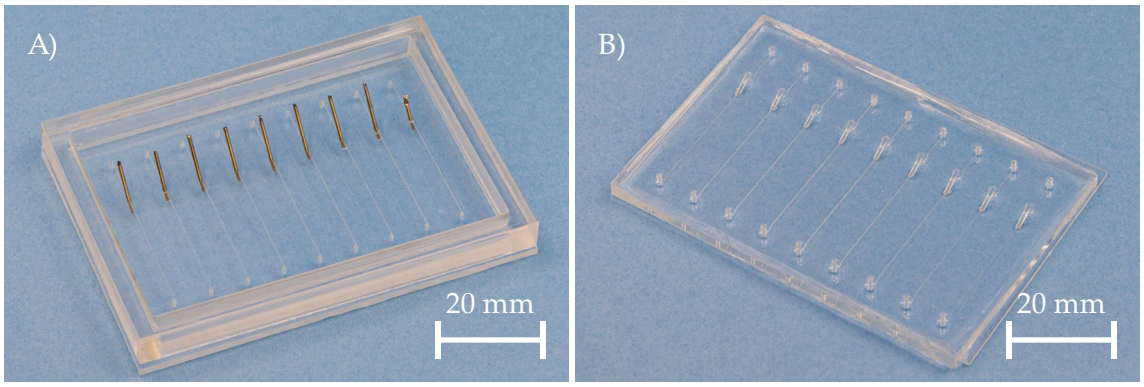

Figure 4.9: A) PDMS-mould for the 9-channel RC. At this stage, pins were still used to cast openings for tubing and seedling inlets (cf. 4.2.2). **B)** A successful PDMS-cast of the 9-channel RC, with all openings cast directly and the cast demoulded without damage.

in biological laboratories. In collaboration with Eugenia Pawlenko, the RC design was accordingly adapted and the fabrication of the modified microfluidic chip was investigated. The following summarises the process and key findings, while further details can be found in E. Pawlenko's Master's thesis [80].

A new mould was designed to cast the updated PDMS chip halves. To accommodate the larger cover slides (76 mm × 52 mm) and the thin cover slips (cf. section 4.1), the length of the analysis channels was shortened to 27.81 mm, as agreed with biologists at IBMP (CNRS, Strasbourg, France). The corresponding technical drawing is provided in figure I.1. The mould was micro-milled by the IMT workshop, and 0.91 mm diameter pins were used to directly cast the required inlets, outlets, and seedling ports (cf. 4.2.2). The mould and a successfully cast PDMS-chip are shown in figure 4.9.

The chips were then cleaned and bonded as usual (cf. 4.1.2). During functional testing, it was observed that the same three channels (1, 6, and 9; see figure 4.10) were consistently clogged at their inlets. Investigation revealed that the pins used to cast the inlets in these regions were not properly aligned with the milled channel features, leading to thin PDMS-membranes forming between inlet and channel, thus obstructing flow (figure 4.10). This was temporarily corrected by drilling open the affected ports and replacing the pins with ones of 1.05 mm diameter.

Another issue was the presence of PDMS-debris clogging certain channels (figure 4.10). Microscopic inspection of the mould revealed scratches in these areas. These defects transferred to the PDMS-cast, forming obstructions. For initial tests, the debris was carefully removed using a scalpel.

Following mould replacement, adjustment, cleaning, and bonding, three 9-channel RC devices were successfully produced, though some still had one or two non-functional ports (figure 4.11). However, biologists at IBMP (CNRS, Strasbourg, France) noted that their syringe pump setup supported only six channels. Additionally, the three-channel RC format proved more convenient for lab handling compared to this new version. Consequently, no further development of the 9-channel variant was pursued at this point. Nonetheless, this design remains promising for future experiments involving larger-scale screening or parameter sweeps.

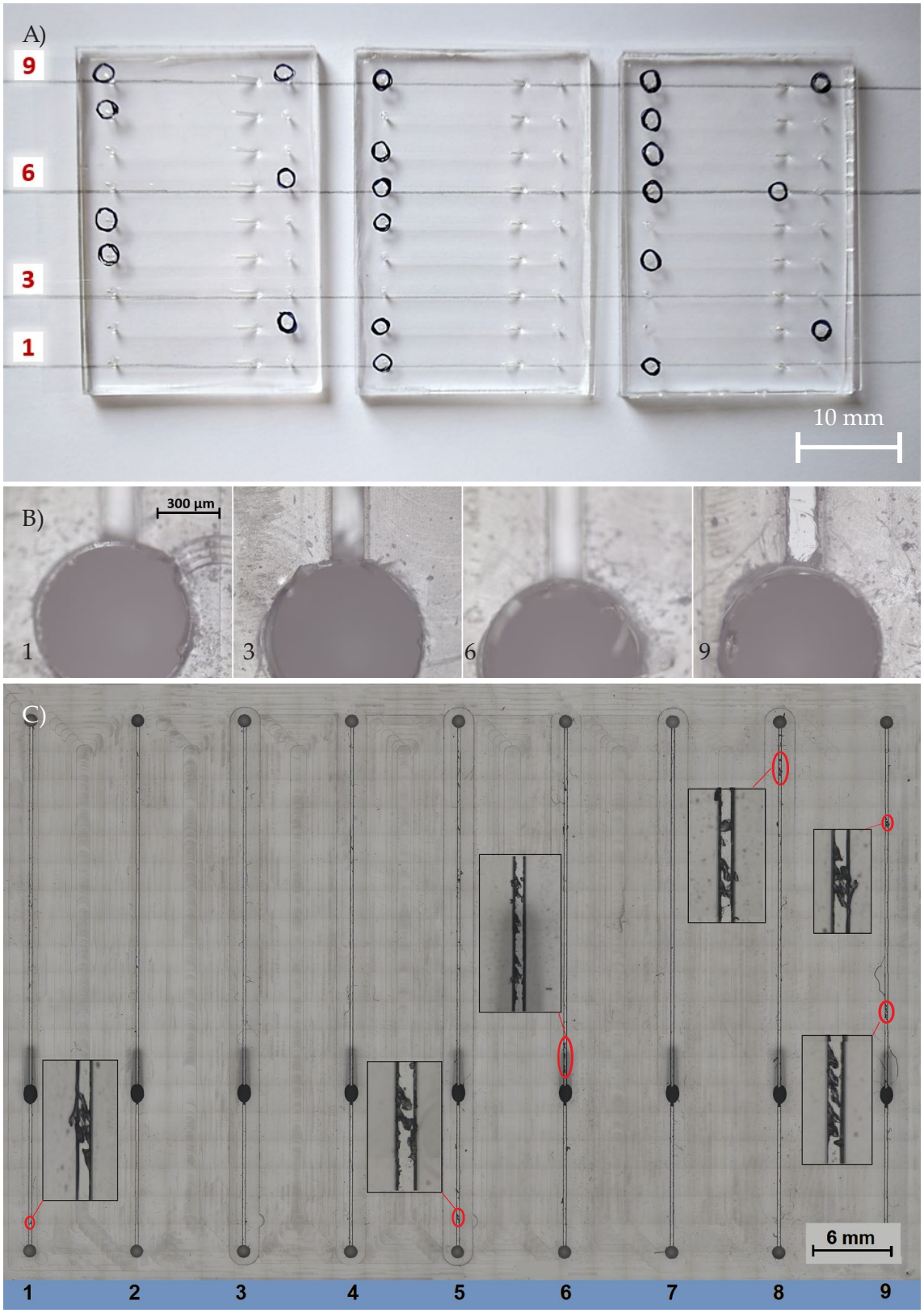

Figure 4.10: **A)** Flow test results of the 9-channel RC. Circled inlets and outlets were blocked. **B)** Microscopic images of outlets 1, 3, 6, and 9. At outlets 1 and 9, the PDMS-membrane between outlet and channel is clearly visible. **C)** Debris-obstructed areas inside the channels. These correlate with scratches in the mould, highlighting the need for mould replacement.

Figure 4.11: Completed 9-channel RCs with mostly functional channels. Circled ports indicate those without flow. Checkmarks denote openings that were initially blocked but could be cleared successfully.

4.2.4 Additive Manufacturing of moulds for PDMS-casting

Since the widespread adoption of additive manufacturing (also known as 3D printing) in the late 2000s and mid-2010s, printer precision, print times, and available resin types have significantly improved. Therefore, in 2020, in collaboration with Tobias Mellert, we evaluated whether available printers at the IMT could be used to manufacture moulds suitable for PDMS-casting. Several fused filament fabrication (FFF) and stereolithography (SLA) printers were tested (see table 4.2), and in 2023, three additional SLA printers were evaluated to assess any improvements. For printers applying SLA, versions using both common illumination techniques were tested: A digital micromirror device (DMD), which employs micromirrors to project light patterns with high precision, and an LCD display, which relies on a liquid crystal screen to selectively block or transmit light across the build area. The most relevant findings are summarised below; additional details can be found in T. Mellert's Master's thesis [129] and in [130].

The benchmark structures are shown in figure 4.12A, B, and C. Tested was the printing of straight channels, pins with a diameter of 1 mm, triangular cavities to create directional pillars in the casting process as well as a wavy structure. The latter was printed as

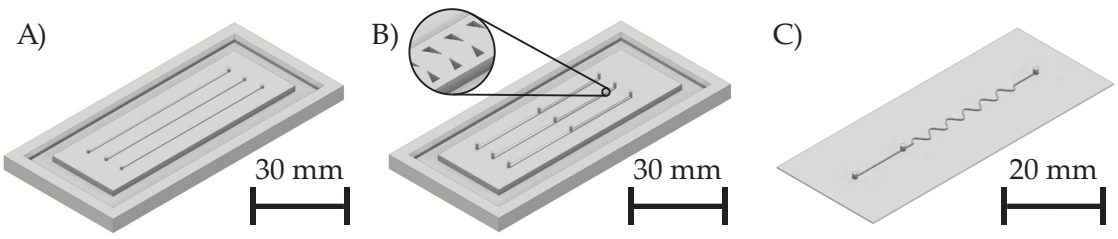

Figure 4.12: Benchmark structures tested for additively manufacturing PDMS-moulds. **A)** Standard structure of straight square analysis channels for the Root Chip. **B)** Channels with triangular cavities for casting directional pillars, guiding the root down the channel. For clarification the directional cavities are magnified. **C)** Wavy structure for exploring precision of SLA printers.

Printer/ Milling machine	Limiting factor (min. value)	Material	Layer thickness/ Stepdown	Post processing of mould
Deckel FP3 NC Milling	Tool-diameter (smallest used tool: ⌀ 100 µm)	PMMA	Standard 40 µm, directional: 5 µm	PFOTCS coating of PDMS-cast of the positive PMMA structure
Ultimaker 3 FFF	Nozzle (⌀ 250 µm)	ABS	60 µm	None
Prusa i3 Mk3S FFF	Nozzle (⌀ 250 µm)	PLA	250 µm	None
MiiCraft+ SLA	DMD (450 ppi $\hat{=}$ 56 µm)	RRB	25 µm	> 14 h, oven at 85 °C
Prusa SL1 (2020) SLA	LCD-display (540 ppi $\hat{=}$ 47 µm)	RRB & RRC	25 µm	> 14 h, oven at 85 °C
Creality LD-002H SLA	LCD-display (504 ppi $\hat{=}$ 51 µm)	ESR	50 µm	> 12 h, sunlight
Phrozon Sonic Mighty 8k (2023) SLA	LCD-display (1152 ppi $\hat{=}$ 28 µm)	PAR	10 µm	intensive UV curing for 1 h
Phrozon Sonic Mini 4k (2023) SLA	LCD-display (722 ppi $\hat{=}$ 35 µm)	PAR	10 µm	intensive UV curing for 1 h
Prusa SL1 (2023) SLA	LCD-display (540 ppi $\hat{=}$ 47 µm)	LOM	25 µm	intensive UV curing for 1 h

Table 4.2: 3D-printers tested for suitability of manufacturing RC moulds.

a full mould like the setups in A and B, on a thin baseplate (figure 4.12C), and with solely the wavy structure mounted on a glass slide or wafer. The evaluation focused on: manufacturing precision for circular pins (1 mm diameter), straight channel edges (100 µm, 250 µm, 500 µm), 90° corners, triangular cavities, and overall surface quality. Furthermore, resin compatibility with PDMS was assessed, which is a known issue for SLA processes.

The structural accuracy was compared with CAD references. The triangular cavities (figure 4.12B), however, could not be milled directly. Instead, a positive structure was first milled in PMMA, replicated in PDMS, and then silanised to serve as the final reusable mould. This was done by plasma-activating the PDMS-cast for 30 s, placing it in a desiccator at 65 kPa below atmospheric pressure for 2 h, in the presence of 20 µL of a 0.3 vol% trichloro(1H,1H,2H,2H-perfluorooctyl)silane (PFOTCS) solution in cyclohexane. This treatment prevented adhesion during further casting steps.

The FFF-printed moulds used Acrylonitrile-Butadiene-Styrene (ABS) for the Ultimaker 3, and polylactic acid (PLA) for the Prusa i3 Mk3S. PLA is suboptimal due to its low glass transition temperature of 56 °C [131], which is below the PDMS curing temperature of 65 °C, but at the time no other material was available for the Prusa i3 Mk3S. For the SLA printers different resins were used for printing the moulds: NOVA3D LCD UV Resin 405nm

Rapid Resin Black (MiiCraft+ and Prusa SL1 in 2020), NOVA3D LCD UV Resin 405nm Rapid Resin Cyan (Prusa SL1 in 2020), Elegoo Standard LCD UV-Curing Photopolymer Rapid Resin (Creality LD-002H), Prusa UV Sensitive Resin Super Low Odor Magenta (Prusa SL1 in 2023), and Phrozon Aqua Resin (Phrozon Sonic Mighty 8k and Phrozon Sonic Mini 4k in 2023).

The printed structures were compared with the initial CAD-model as reference. While the structural performance was analysed via microscopic imagery (Axioscope 7 equipped with Axioscope 205 Color camera, Zeiss, Germany), the generated surface quality was evaluated in five different areas on the finished mould using vertical scanning interferometry (Contour GT-K, Bruker Corporation, USA). Both strongly depended on the combination of material and manufacturing device. Additionally, PDMS was cast in the created moulds and the resulting cast's transparency was a first indicator of the surface quality of the mould and if any material has bled into the cast. The latter was only an issue for resin-based printers.

Shape accuracy results are summarised in table 4.3. Two printers failed to produce the smallest channel blocks (100 µm). Milling remained the most accurate method overall. For all approaches, smaller feature sizes led to increased relative deviations.

Printer/ Milling machine	Model channel width [µm]	Relative deviation from model dimensions [%]		
		Height	Top width	Bottom width
Deckel FP3 NC Milling	500	4	1	41
	250	7	6	75
	100	5	39	150
Ultimaker 3 FFF	500	-8	-6	21
	250	6	33	67
	100	6	116	188
Prusa i3 Mk3S FFF	500	47	0	18
	250	52	48	116
	100	not manufactured		
MiiCraft+ SLA	500	-40	-11	31
	250	-43	-14	62
	100	-45	-33	83
Prusa SL1 (2020) SLA	500	-8	4	38
	250	-10	-17	51
	100	not manufactured		
Creality LD-002H SLA	500	-52	5	55
	250	-50	37	110
	100	-51	12	143

Table 4.3: The achieved shape accuracy of the individual printers. Judged are the standard rectangular channel structures compared to the CAD-model. Positive deviation indicate larger structures, negative smaller structures than planned. Only the prints from 2020 were judged according to their shape accuracy, since the moulds manufactured in 2023 could not withstand a single PDMS-casting process due to resin inbleed into the PDMS or destruction during the demoulding step, which was a requirement for taking them into further consideration as replacement manufacturing processes for micro-milling.

The results of the surface roughness measurements are displayed in table 4.4. Here it is notable, that the here applied micro-milling process created a rougher surface than the other fabrication methods. And, it is to note that the measured parameters were analysed on top of the generated square structures as these would be of functional value to the root cultivation on the final. The base surface of the chip – relevant for plasma-bonding the PDMS-cast to a glass slide – was not analysed. But especially for the ABS-based moulds, as well as the other FFF generated moulds, ripples from material deposition hampered the transparency and bond ability of the final casts. Different approaches to improve this surface quality were tested, but did not lead to satisfactory results (more information in [129]).

Printer / Milling machine	Ra [nm]	Rq [nm]	Wa [nm]
Deckel FP3 NC (Milling)	1895 ± 394	2273 ± 686	2210 ± 708
Ultimaker 3 (FFF)	425 ± 32	550 ± 45	1184 ± 554
Prusa i3 Mk3S (FFF)	152 ± 33	197 ± 41	743 ± 54
MiiCraft+ (SLA)	130 ± 61	172 ± 78	443 ± 108
Prusa SL1 (2020) (SLA)	107 ± 32	120 ± 27	241 ± 76
Creality LD-002H (SLA)	246 ± 171	281 ± 230	161 ± 408

Table 4.4: Surface quality measured on top of the printed structures (key area for chip functionality). Five measurements in different orientations were averaged for each displayed surface quality parameter and their standard deviation calculated. Only the prints from 2020 were analysed this way, because the SLA-generated structures in 2023 could not withstand a single PDMS-cast or be cured sufficiently for no resin-inbleed, thus an analysis of the surface quality was beside the point.

The SLA-based prints showed mixed performances. On one hand the printing time was short – thanks to the use of DMD and LCD-displays which allowed for quick exposure times for each layer – and the surface quality was overall good for moulds generated with these printers, but it was difficult to post-process them in a way that no residues from the resins like solvents bled into the cast PDMS. This could lead to strong reactions in the beginning like the PDMS not hardening through in all spots. After more intense post processing this extreme reaction was not seen any more, however casts tended to have a sheen to them in areas that were directly in contact with the mould, indicating that there was still cross-contamination from the mould-resin. Unfortunately, that made these moulds unusable for an application in plant biology experiments as the risk of relevant influences on the plantlets from these resin-residues was too strong. Additionally, for resin-based moulds larger flat surfaces (like the area intended for casting the future contact surface between the PDMS-cast and a cover glass slide) repeatedly showed collapsed surfaces (see figure 4.13A) with dips in the depth-range of 80 µm. These areas were then cast as protrusions in PDMS, pushing the final cast away from the cover glass slides and preventing it from bonding in all necessary areas. It was tried to print the structures directly on a glass plate or wafer (figure 4.13B), however – even with plasma-surface activation – the generated structures did not withhold a single PDMS-casting process (figure 4.13C).

The PFOTCS-covered PDMS-moulds performed well. The initial casts – which later formed the mould – copied the PMMA mould well and the silanization of the PDMS-cast deposited a microns thick layer which was expected to reduce the effects of the slightly too big micro-milled mould, even though it was not measured again. The generated silanized mould hold up well during casting experiments (> 15 casts completed with these moulds).

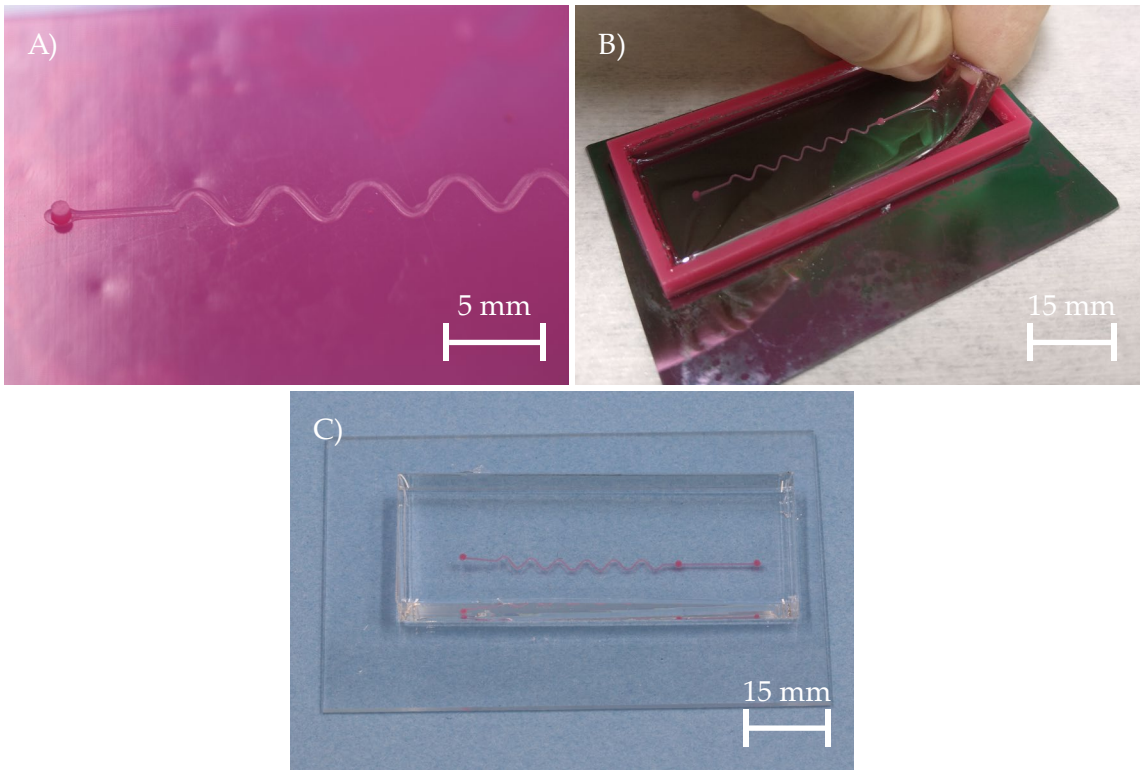

Figure 4.13: A) SLA-print with a baseplate that shows the significantly collapsed holes that were present in several prints. **B)** Structure printed directly on a wafer. However, during the demoulding process the print detached from the substrate. In addition, unhardened material can be seen at the edges of the mould, which is caused from bleeding resin compounds into the PDMS despite extensive washing and hardening of the print. **C)** Structure printed on a plasma activated glass slide. The plasma activation generally enhances the connection between glass and other materials. However, as can be seen at the left side of the structure, it was not sufficient and the structure started to lift of the substrate during demoulding.

The original motivation behind testing AM was faster mould production. In this area, the AM approaches showed similar necessary time-investments as the micro-milling process. The results are displayed in table 4.5. The FFF-based printers took the longest for the actual printing job. SLA-based printers were faster regarding the print job, however, overnight post-processing needed to be performed in most cases. The milling process itself took about 4 h, however first casting the future mould (1.5 h) and then covering it with PFOTCS (3.5 h), increased the final mould-manufacturing period to 9 h, a similar result as the AM approaches achieved. Thus in about one business day a new mould could be created, if no wait times for machine- or personnel-availability were taken into account.

In conclusion, a viable mould for PDMS casting must permit residue-free demoulding and produce functionally accurate and optically clear structures. For features smaller than 250 µm, the AM methods available at IMT currently fall short of the required combination of dimensional precision and suitable sizing for an RC-mould. While SLA-based techniques showed promising structural accuracy, they did not yet match the reliability of micro-milling. Therefore, at the moment AM approaches remain unsuitable for producing moulds used in biologically relevant microfluidic chips such as the Root Chip. Nonetheless, the field is progressing, and future advancements may well make AM viable even in manufacturing-distant labs such as those in biological research environments.

Printer / Milling machine	Manufacturing time
Deckel FP3 NC (Milling)	9 h
Ultimaker 3 (FFF)	7 h
Prusa i3 Mk3S (FFF)	3 h 40 min
MiiCraft+ (SLA)	15 h 30 min
Prusa SL1 (2020) (SLA)	15 h
Creality LD-002H (SLA)	12 h 30 min

Table 4.5: Manufacturing times for creating a PDMS-mould. The manufacturing times are displayed for the total time passed until a mould was created, thus the printing or milling period plus time needed for post-processing. Only the prints from 2020 were analysed this way, because the SLA-generated structures in 2023 could not withstand a single PDMS-casting process or be cured sufficiently for no resin-inbleed.

4.3 Simplified compound control through integrated mixing structures

The initial design of the RC consisted of three straight analysis channels, enabling compound testing and the monitoring of growth rates and root behaviour. However, during discussions with collaborating partners at the IBMP (CNRS, Strasbourg, France), there was repeated interest in adapting the standard Root Chip design to enable a more flexible compound administration to the seedlings [132], [133].

To address this need, three modified RC variants were developed, each incorporating different microfluidic mixing structures. This work was conducted in collaboration with Yannick Peiffer and is summarised below. Further details are available in Y. Peiffer's Master's thesis [134].

The three mixer designs included a T-mixer (figure 4.14A), a Zigzag-mixer (figure 4.14B), and a Tesla-mixer (figure 4.14C). Each RC could be supplied with liquid compounds via one, two, or all three inlet channels, allowing the seedling to be exposed either to a single fluid or a combination of media. Due to the highly laminar nature of microfluidic flow, media were only introduced into the analysis channel by active flow; stopped channels acted effectively as fluidic plugs, aside from negligible backflow.

The T-mixer design, based on Stanley *et al.* [64], enabled the application of two- or three-phase flows. Given the ultra-laminar flow conditions conditions, the phases did not mix upon meeting at the junction. In case of the two compound insertions, the analysis channel was split between these two compounds. However, to improve separation in case of diffusion at the fluids interface, a third – central – channel could deliver a neutral medium – establishing a three-phase flow – to act as a barrier between the test compounds.

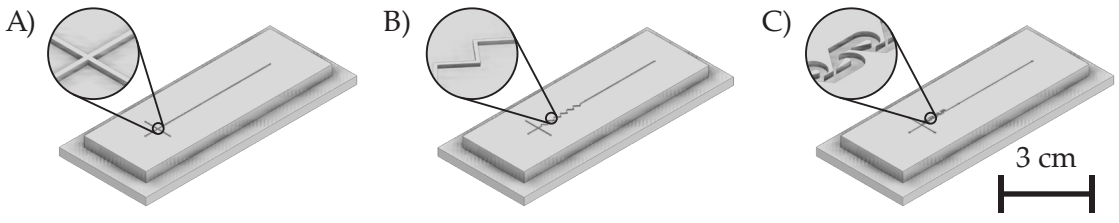

Figure 4.14: CAD sketches of the moulds for fabricating the **A)** T-mixer RC, **B)** Zigzag-mixer RC, and **C)** Tesla-mixer RC. Designs created in collaboration with [134].

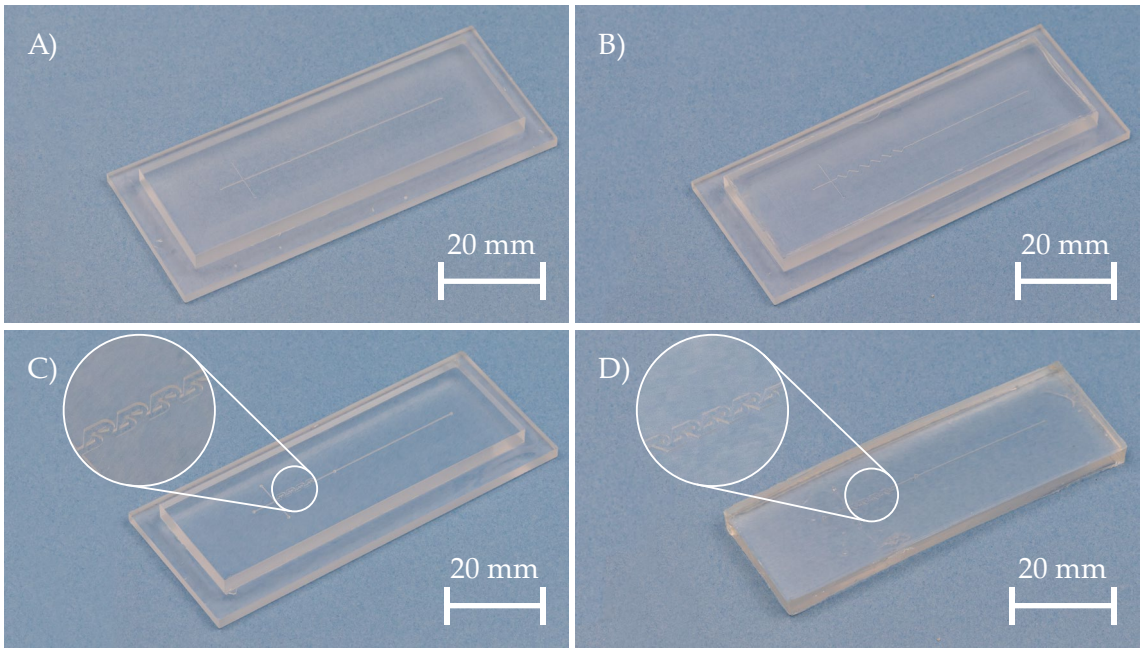

Figure 4.15: Micro-milled moulds for **A)** T-mixer, **B)** Zigzag-mixer, and **C)** Tesla-mixer designs. The Tesla-mixer mould could not be produced directly with the negative structures due to sharp corners and complex geometry. Instead, a positive mould was micro-milled, and then cast in PDMS. To create the final mould, this PDMS-cast with the negative – thus inverted – structures, was silanised (PFOTCS), to create a non-stick barrier between the PDMS-mould and future PDMS-casts (**D)**).

The Zigzag-mixer introduced partial mixing, creating concentration gradients across the channel. Side regions retained the original media, while the centre contains intermediate concentrations. This configuration allowed basic assessment of concentration-dependent effects on seedling behaviour.

The Tesla-mixer design followed Hong, Choi and Ahn [135] and was tailored for effective mixing under slow, laminar conditions typical in the RC (e.g. 10 µL/min). The plan was to enable full mixing of two fluids or dilution of both with a central stream of neutral medium like standard nutritional medium.

All three designs were realised as PDMS-based microfluidic chips. The moulds for the T-mixers and Zigzag-mixers were directly micro-milled. The Tesla-mixer required a different approach due to the complexity of its eight drop-shaped pillars and sharp outer corners. A positive master was first milled, cast in PDMS, then silanised with PFOTCS to create the final negative mould (figure 4.15D), following procedures outlined in 4.2.4. The resulting mixer chips were then cast, bonded to glass and tested as described in 4.1.2 to 4.1.3.

Completed mixer MFCs are shown in figure 4.16. After leak testing, each design was evaluated with coloured fluids at flow rates of 10 µL/min, 20 µL/min, 50 µL/min, 100 µL/min, and 200 µL/min. These rates refer to total analysis channel flow, so when using two or three fluids, the per-inlet flow rates were set to 5 µL/min or 3.33 µL/min, respectively. Each mixer was hooked up to two or three syringes filled with isopropanol coloured in red, blue or yellow. A syringe pump (PHD ULTRA™, Harvard Apparatus, Holliston, MA, USA) is used to administer the fluids continuously to the Root Chips to be tested.

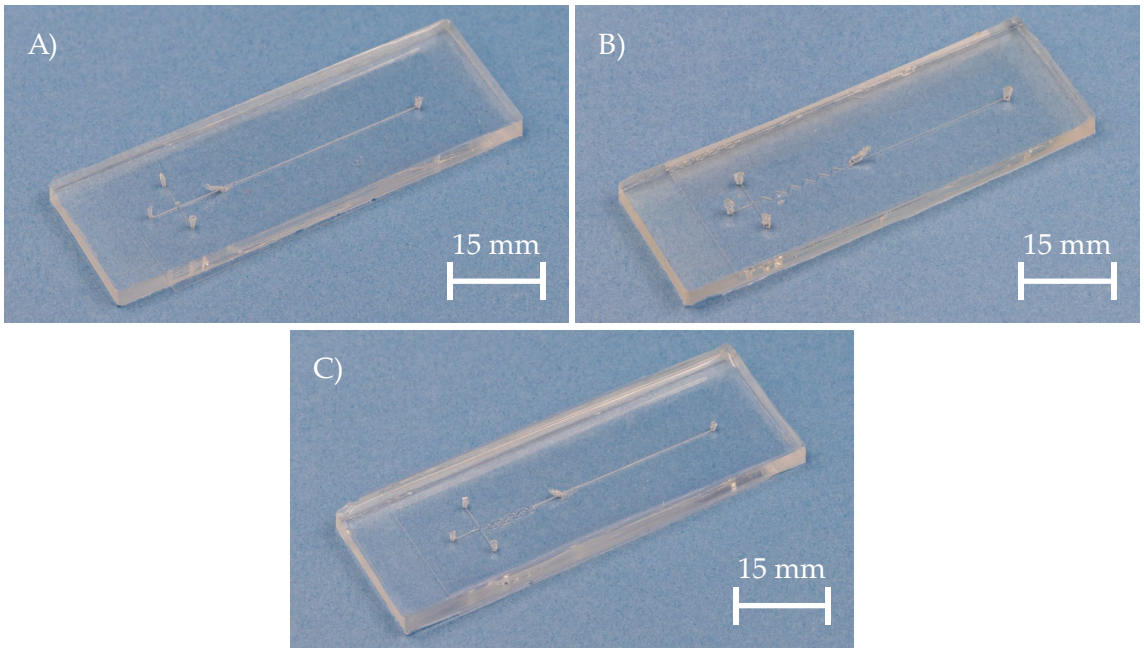

Figure 4.16: Completed RC devices with integrated mixers: **A)** T-mixer, **B)** Zigzag-mixer, **C)** Tesla-mixer.

For the T-mixer (figure 4.17), fluids behaved as expected, showing a clear boundary between each of the laminar streams. When using three fluids, the central one formed a distinct barrier. In both cases, different flow rates did barely change the forming flow profile. In case of the two highest flow rates the edges of the individual fluid layers became even more crisp, while at the two lowest flow rates extremely thin transition zones developed.

The Zigzag-mixer results (figure 4.18) confirmed the presence of gradients at flow rates up to 50 µL/min. At faster flow rates, the transition zone became very small rendering it improper for experiments where a root should be exposed to a compound gradient. With three fluids, the centre stream diluted both flanking streams, producing dual gradients, again up to a flow rate of 50 µL/min. Overall, this setup still enables basic investigations of concentration-dependent responses.

The Tesla-mixer (figure 4.19) provided adequate mixing for two fluids at flow rates of 10 µL/min and 20 µL/min. At higher flow rates, mixing was insufficient, with side streams remaining distinct. For three fluids, the existing eight-stage mixer was not able to fully mix the streams. COMSOL Multiphysics® simulations [119] indicated that 24 mixing stages would be required for effective mixing in this configuration. Consequently, future versions of the Tesla-mixer MFC should be revised accordingly.

In summary, the mixer structures functioned largely as intended. Devices from all three designs were provided to the IBMP (CNRS, Strasbourg, France) for further testing. One key criticism was the relatively large volume of fluid required to fill each Root Chip, which may serve as a starting point for future redesigns. The chips remain with the IBMP and await application in biological experiments.

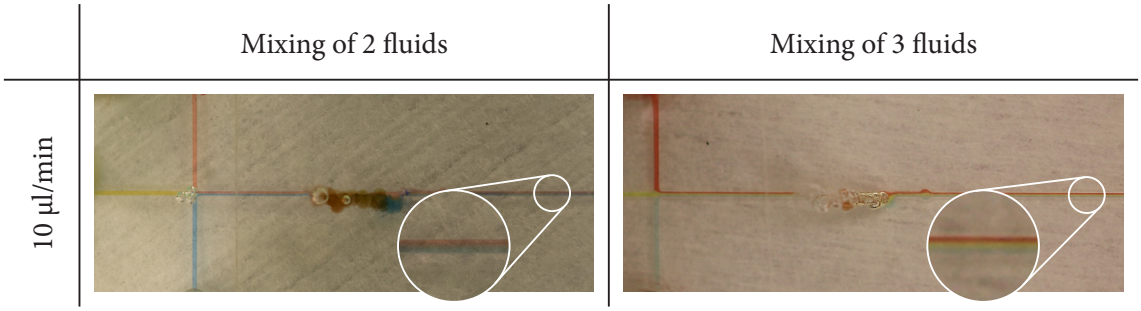

Figure 4.17: Flow behaviour of two and three fluids in the T-mixer. As expected, two fluids form an extremely thin transition zone. The introduction of a third (yellow) fluid clearly separates the side streams. Three fluids pictures adapted from [134]

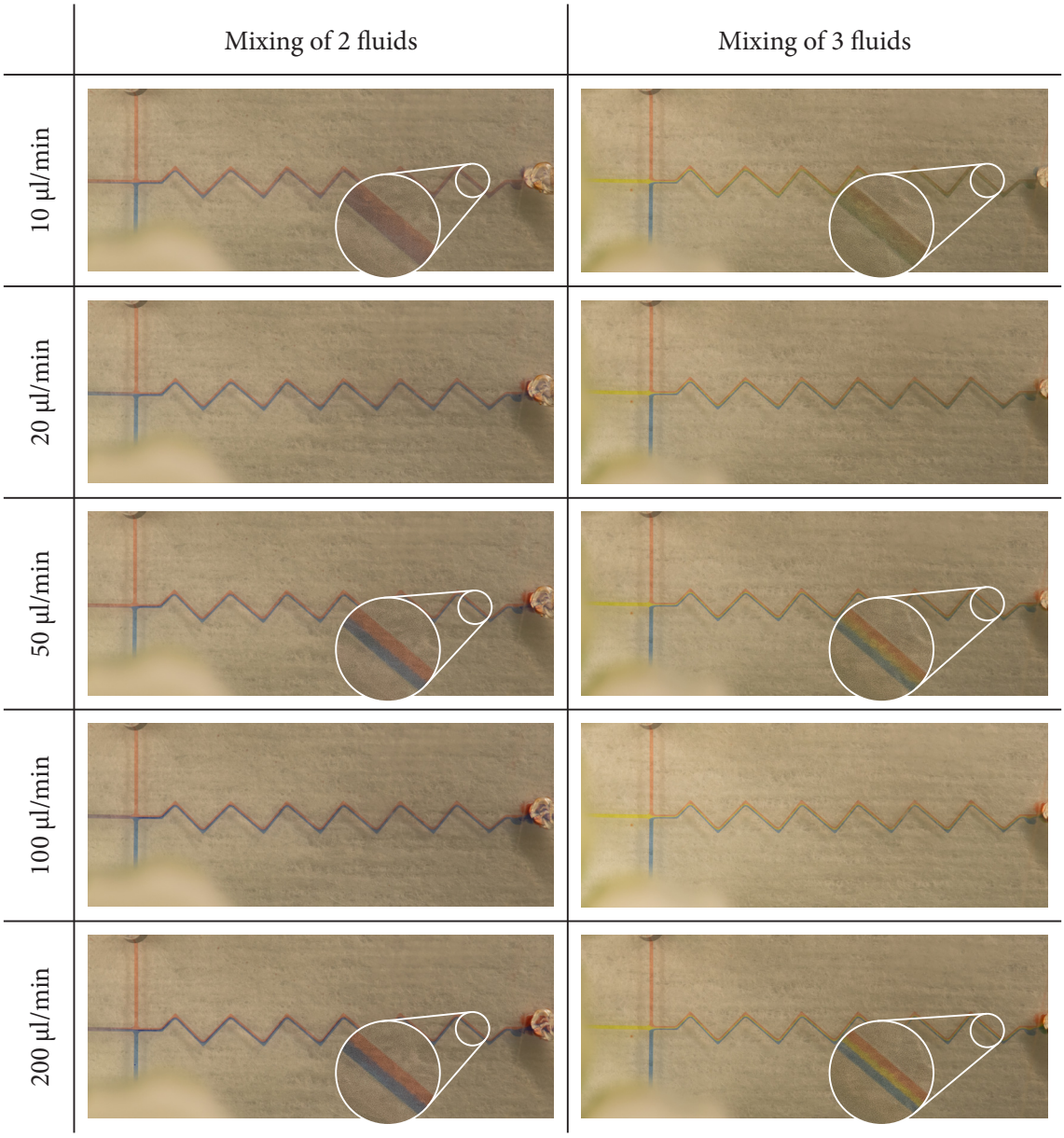

Figure 4.18: Flow behaviour in the Zigzag-mixer. At lower flow rates ($\leq 50\,\mu L/min$), a clear concentration gradient formed. At higher flow rates, mixing was reduced.

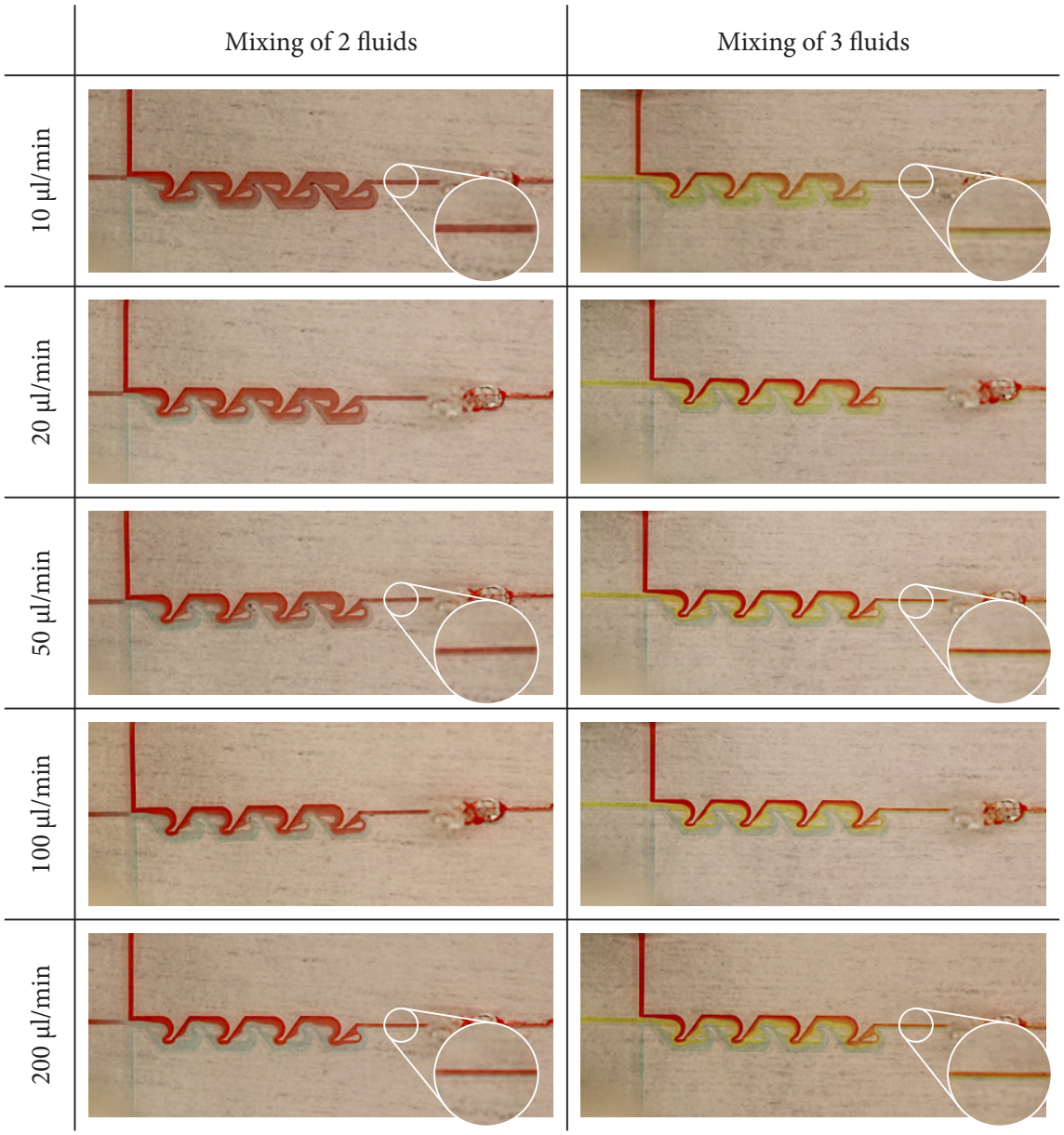

Figure 4.19: Flow behaviour of two and three fluids in the Tesla-mixer. Effective mixing occurred at 10 µL/min and 20 µL/min. Three-fluid mixing was incomplete. Images adapted from [134].

4.4 Manufacturing of Root Chips from PC

The PDMS-based version of the RC is well suited for both prototyping and initial testing of individual designs. However, PDMS presents certain limitations, such as the absorption of surrounding chemicals into the material, as discussed in appendix A.1.2. Additionally, the PDMS-based RC incorporates mechanically fragile components, notably the thin cover slips used to seal the channel structure (4.1.2). Consequently, an early consideration in the development process was whether the RC could be realised in an alternative material offering greater mechanical and chemical stability, similar to the MBR.

The revised design retained the general layout of the initial version, featuring three parallel, straight analysis channels (see figure 4.20A). The channels maintained a square cross-section of 200 µm×200 µm. To minimise the thickness of the covering foil and enhance imaging capabilities, the analysis channels were located in the lower chip half. The upper chip half was designed to be 3.4 mm thick and to accommodate the seedling transfer tip. This tip had to be securely fixed in place. One of the first strategies explored involved embedding the tip using Agar Agar [134]; however, this method was found to provide insufficient mechanical stability and was subsequently abandoned. Instead, a plug was developed, designed to fit precisely into a dedicated opening in the upper chip half (figure 4.20B and C). These plugs are currently fabricated from PDMS due to its compatibility with autoclaving, a standard sterilisation process in biological laboratories. In the future, the plug material may be reconsidered to further reduce compound absorption or enhance sterilisation compatibility.

Following discussions with partners at the IBMP (CNRS, Strasbourg, France), and process experts at the IMT, it was agreed to adopt PC as the material for the revised design. This thermoplastic can be processed via hot embossing (HE) and offers sufficient autoclaving capability over several cycles for biological use. It is also suitable for bonding via ultrasonic welding or laser transmission welding (LTW). Further details regarding the bonding process

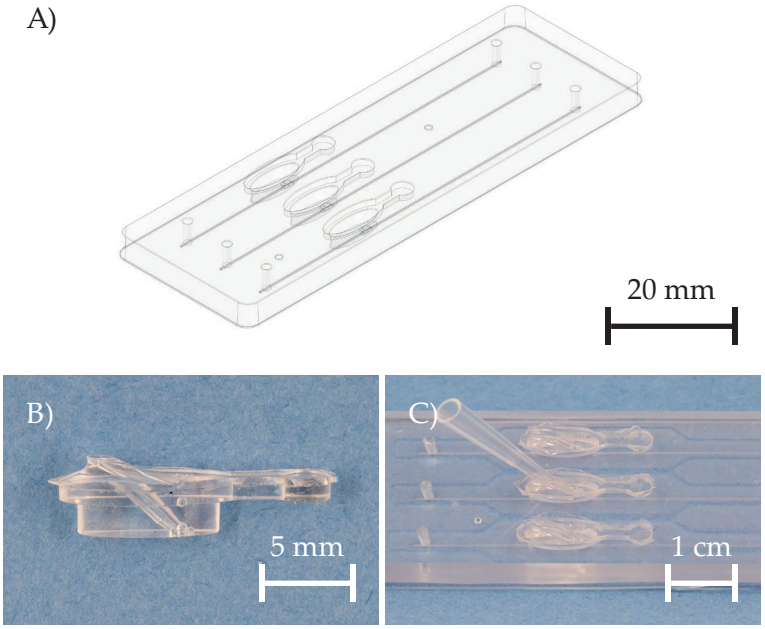

Figure 4.20: A) CAD screenshot of the PC-Root Chip design. The lower chip half is a thin foil of 200 µm thickness and contains the straight channels for root growth and analysis, while the upper chip half (3.4 mm thick) houses the openings for the plugs that hold the seedlings. **B)** PDMS-plug used for securing the seedling transfer tip. **C)** Seedling transfer tip installed in the PC-RC using the PDMS-plug.

are provided in 4.4.2 and 4.4.3, respectively. The following section presents the fabrication of the PC chip halves via hot embossing.

4.4.1 Hot embossing of chip halves

The hot embossing process followed a procedure analogous to that described in 3.1.1. Both chip halves were fabricated using the WUM 02 embossing machine (Jenoptik Mikrotechnik, Germany) at the IMT. The upper chip half, which includes the seedling inlet, was produced from two stacked raw blanks of Makrolon® GP clear 099 (Covestro Deutschland AG, Leverkusen, Germany [111]), each 2 mm thick and 78 mm × 28 mm long and wide. The lower chip half – containing the analysis channels – was formed in pairs from two stacked foils of Lexan™ 8B35E, each 250 µm thick (SABIC, Riyadh, Saudi Arabia). These Lexan™sheets were cut from a 1220 mm × 915 mm raw stock sheet to a working size of 75 mm × 80 mm. The embossing process for the upper chip half is detailed in the following subsections, while the process for the lower chip half is described subsequently.

4.4.1.1 Upper RC chip half

The mould (cf. appendix J) used for hot embossing the upper chip half was first cleaned in an ultrasonic bath, using isopropanol followed by DI water. It was then mounted in the WUM 02 with the structured side facing down. Initial tests assessed the suitability of a polished chrome-coated baseplate, as used in 3.1.1. However, this configuration proved impractical for the current application, as demoulding of the chip halves was extremely difficult due to the chip half's large thickness and frequently resulted in damage. Consequently, a sandblasted baseplate was selected instead, providing improved grip and facilitating easier demoulding.

The Makrolon® sheets were positioned below the moulding posts. Due to the initial height of the stacked raw blank, the embossing chamber could not be fully closed immediately. Instead, the machine was partially closed and the substrates were preheated to 170 °C to plasticise the polymer. Subsequently, the chamber was closed by an additional 2 mm at a controlled rate of 0.5 mm/min. After a stabilisation period of 20 s, the mould was pressed into contact with the substrate using a preload force of 250 N. A vacuum was then applied, and following an additional waiting time of 20 s, the force sensor was zeroed.

Next, the mould was advanced at a rate of 0.5 mm/min until a maximum embossing force of 50 kN was reached, pressing the softened polymer into the mould structure. To allow stress relaxation and shape fixation, a hold time of 120 s was maintained at maximum force. The mould and substrate were then cooled to below 130 °C, after which the mould was partially opened by 3.5 mm at a demoulding rate of 1 mm/min. Cooling continued until the substrate temperature dropped below 85 °C, at which point the mould was fully opened and the embossed chip halves were removed from the machine.

The two chip halves produced in each cycle were then separated and stored in clear PS containers until further processing. The process parameters are summarised in table 4.6.

4.4.1.2 Lower RC chip half

As with the upper chip halves, the mould (cf. appendix K) for fabricating the lower RC chip halves was cleaned in an ultrasonic bath, first in isopropanol, then in DI water. The mould was subsequently mounted in the WUM 02 embossing machine with the structured side facing down. Given that the mould posts for the lower chip half are comparatively shallow (depth 200 µm), the polished chrome-coated plate with integrated grooves (cf. figure 3.6) was used as the baseplate.

Parameter	Value
Embossing temperature [°C]	170
Contact pressure [kN]	50
Embossing path [mm]	3.5
Embossing velocity [mm/s]	0.5
Demoulding temperature [°C]	85
Demoulding velocitiy [mm/s]	1
Cycle period [min]	35

Table 4.6: Parameters for hot embossing of the upper chip halves for the PC-RC.

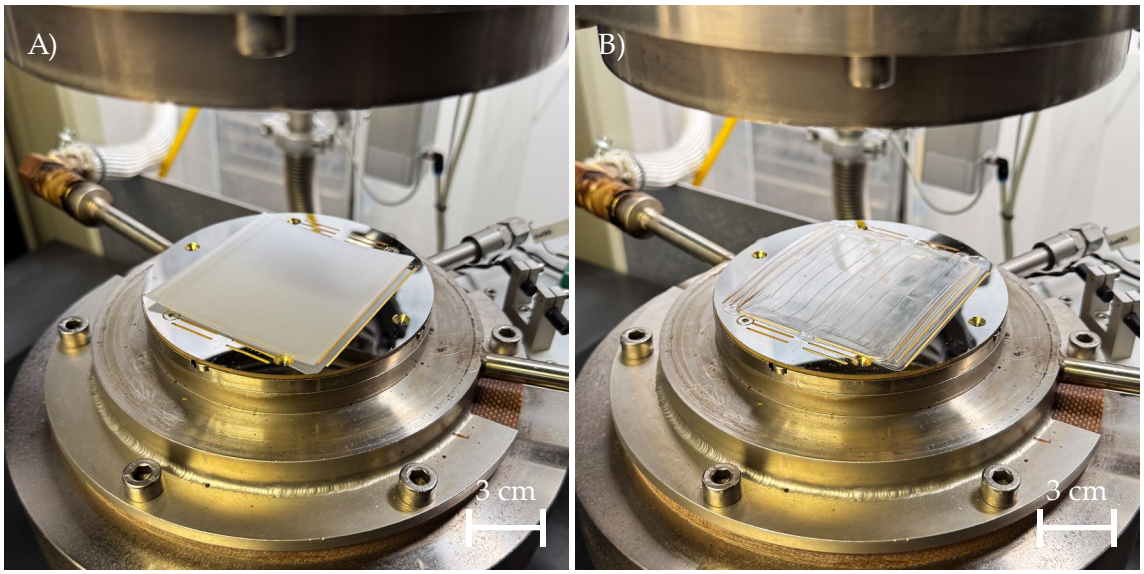

Figure 4.21: A) Two stacked raw blanks positioned before HE underneath the mould posts. **B)** Hot embossed chip halves after demoulding. They were pulled out evenly from their mould posts through flash adhering to the rougher surfaces in the grooves of the polished chrome-coated plate (cf. figure 3.6).

The Lexan™ raw blank sheets were cleaned using compressed air and aligned within the grooves of the chrome-coated plate (see figure 4.21A), ensuring proper positioning relative to the mould posts. To initiate the embossing process, the chamber of the WUM 02 was closed and evacuated. After a stabilisation period of 20 s, the force sensor was zeroed and the chamber was closed further until a contact force of 250 N was achieved.

The substrates were then heated beyond the glass transition temperature of PC (148 °C) to a process temperature exceeding 167 °C, rendering the polymer sufficiently plasticised. The mould was then advanced at a rate of 0.5 mm/min until the maximum embossing force of 50 kN was reached. A holding time of 120 s was applied to ensure complete mould cavity filling and to facilitate stress relaxation within the formed structures.

Subsequently, the system was cooled to 100 °C, at which point the mould was partially opened by 1 mm at a demoulding rate of 1 mm/min to release the chip halves from the mould posts. Cooling continued until the substrate temperature dropped below 85 °C. Finally, the vacuum chamber was vented and the embossing machine fully opened (see figure 4.21B, summary of parameters in table 4.7).

The embossed chip halves were then separated and their edges trimmed as necessary. These components were subsequently stored in clear PS containers pending further processing.

Parameter	Value
Embossing temperature [°C]	167
Contact pressure [kN]	50
Embossing path [mm]	0.5
Embossing velocity [mm/s]	0.5
Demoulding temperature [°C]	100
Demoulding velocitiy [mm/s]	1
Cycle period [min]	25

Table 4.7: Parameters for hot embossing of the RC lower chip halves.

4.4.2 Ultrasonic welding of chip halves

For the bonding process, ultrasonic welding was initially considered for joining the two chip halves, as it is an additive-free technique known to yield strong bonds between PC MFC components. Prototypes were milled and the bonding procedure tested accordingly.

However, initial trials revealed that ultrasonic welding of the RC introduced significant challenges in relation to the energy director (ED). Two primary issues emerged: if the ED was positioned too close to the channel structure and fully fused, molten material would be displaced as flash into the analysis channels. Alternatively, if the ED was positioned further away from the channels or if the ED was not entirely molten, a T-shaped cavity would consistently form at the bond interface (see figure 4.22 for visualisation). Even under optimal conditions, the vertical portion of this T-feature would remain several micrometres deep – a substantial discontinuity relative to the channel's dimensions and problematic for developing roots and their root hairs. As discussed in section 2.2, Singh *et al.* [71] demonstrated that several root hairs at the same time can enter side channels as small as 20 µm. Additional details on the bonding tests can be found in [134].

Given these limitations, ultrasonic welding and the use of an ED were abandoned for the revised RC design. Instead, LTW was selected as the bonding technique to achieve a clean, absorber-free weld between the PC chip halves.

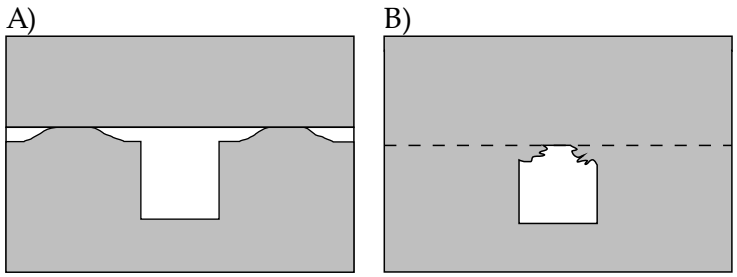

Figure 4.22: Visualisation of bonding results when chip halves were joined using ultrasonic welding. **A)** T-shaped cavity formed when the energy director was not fully melted. **B)** Flash from the welding process intruding into the channel when the ED was fully melted but located too close to the microchannel.

4.4.3 Laser transmission welding of PC

Polycarbonate is a challenging polymer to weld using laser transmission techniques without absorbers, as it tends to yellow and subsequently char rapidly upon laser exposure. As reviewed in 2.5.1, successful absorber-free laser welding of PC has only been demonstrated a couple times.

The experiments described herein were conducted at the IMT using a thulium-fibre laser, consistent with the setup employed by Nam-Phong Nguyen [106] and Viktor Mamuschkin [136] – the two principal contributors to prior research on absorber-free laser welding of PC. It is important to note, however, that in their work, the welding partners were typically bulk parts of equal thickness, measuring several millimetres. In his dissertation, Nguyen [106] demonstrated that applying a quasi-simultaneous welding (QSW) strategy resulted in uniform heating throughout the entire bulk of the welding partners. Consequently, the heat-affected zone (HAZ)/weld seam were centred within the overall stack thickness, and their vertical positioning was largely unaffected by the laser's focal plane. By contrast, when using a contour welding (CW) strategy, Nguyen observed that the vertical position of the weld seam was strongly dependent on the focal plane.

The ability to control the vertical positioning of the weld seam is particularly relevant when bonding components of unequal thickness. This configuration has only been reported once in the literature by Kumar Goyal and Kant [110], who bonded a 4 mm thick PS sheet to a 2 mm thick PC sheet. However, in that study, an electrolytic iron powder was applied to the PC in the contact area, meaning the process was not absorber-free.

The present work aims to realise a fully absorber-free weld between a PC foil and a hot-embossed PC chip half. Welding a foil to a bulk part introduces additional complexity, as the weld seam and HAZ must be positioned with high precision to ensure sufficient bond strength without thermally degrading the foil. The following paragraphs discuss key factors influencing weld quality. To successfully apply these insights to bond the hot-embossed chip halves of the RC, a systematic methodology was followed for identifying appropriate process parameters, which is outlined in 4.4.3.6.

4.4.3.1 Material preparation

A key factor in achieving successful absorber-free laser transmission welding of PC is the preparation of the bonding surfaces. Several parameters were identified that influence weld quality and consistency like surface roughness, electrostatic charge, moisture in the material, handling of prepared chip halves, and ambient humidity.

Post hot embossing, the chip halves – particularly the upper ones – underwent a milling step to remove flash and other excess material. This process introduced grooves and scratches (see figure 4.23A), which significantly impaired laser transmission and absorption. To address this, the first step in the preparation process was to sand and polish the chip surfaces. The chip halves were fixed to a levelled baseplate on a central force mounting disc using double-sided adhesive tape.

Initial sanding was conducted with 2500 grit paper for a total of eight minutes. Following an intermediate cleaning step, a three-stage polishing process using monocrystalline diamond suspensions was applied. The full parameter set is given in table 4.8. This surface treatment reduced the average surface roughness Sa from 1.85 µm to 0.096 µm. While this value does not reach the reference level of Sa = 0.066 µm measured for the raw blank, it nonetheless represents a substantial improvement. Roughness measurements were performed using a confocal microscope (MarSurf CM Select, Mahr GmbH, Göttingen, Germany). Samples were measured in three areas on each chip, then averaged.

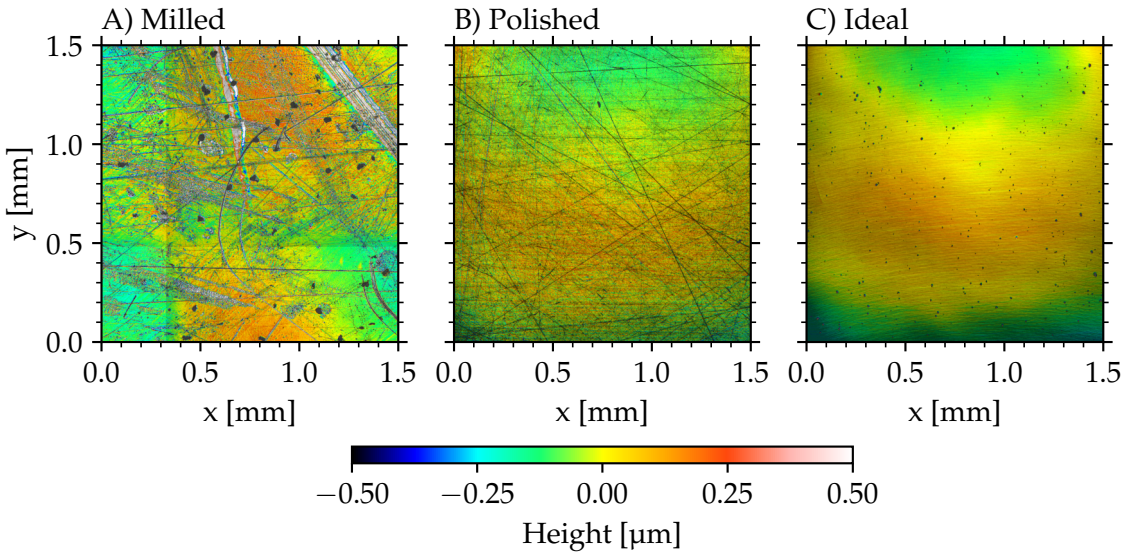

Figure 4.23: Surface measurements of the PC-RC chip halves. Surface roughnesses were examined in three areas on each sample, then averaged. **A)** Chip half after milling off the excess material after the HE-process. Sa = 1.85 µm. **B)** Polished chip half which can be used for LTW. Sa = 0.096 µm. **C)** Ideal surface roughness of a clear raw stock material where the surface was prepared directly by the manufacturer (Makrolon® GP clear 099 sheets, manufactured by Covestro Deutschland AG, Leverkusen, Germany [111]). Sa = 0.066 µm.

Sanding/Polishing with	Time	Head speed	Grain size
Wet sanding sandpaper	20 × 30 s	150 rpm	2500 grit and water
MD-SAT polishing cloth	5 min	130 rpm	6 µm diamond suspension
MD-DUR polishing cloth	5 min	130 rpm	3 µm diamond suspension
MD-DAC polishing cloth	5 min	130 rpm	1 µm diamond suspension

Table 4.8: Sanding and polishing parameters. All steps were performed on a Buehler Automet 300 (Buehler Ltd., Leinfelden-Echterdingen, Germany) under central force at 60 N and 60 rpm platen speed. Monocrystalline diamond suspensions (50 cts/L, Schmitz Metallographie GmbH, Herzogenrath, Germany) and oil-based lubricant coolTec III (Schmitz Metallographie GmbH, Herzogenrath, Germany) were applied throughout. Polishing cloths were supplied by Struers GmbH, Willich, Germany. Sandpaper: WS Flex 18C, 2500 grit, Hermes Schleifmittel GmbH, Hamburg, Germany.

After polishing, the chip halves were carefully detached from the mounting plate and residual adhesive was removed with isopropanol. If not immediately used, the chip halves were stored in clear PS containers. Prior to welding, they were cleaned in two consecutive ultrasonic baths of isopropanol (2 min each), followed by two consecutive baths in DI water (2 min each). This treatment reduced electrostatic charge, which otherwise could impede the precise alignment of the chip halves in the welding fixture. The cleaning process concluded with drying the chip halves with compressed N_2.

Given the hygroscopic nature of PC, moisture must be eliminated prior to welding. Therefore, the chip halves were placed in a vacuum oven at 115 °C for a minimum of 12 h (typically overnight) to ensure adequate drying. Immediately before welding, the parts were transferred to airtight containers flushed with a predominantly N_2 atmosphere, in order to limit reabsorption of ambient humidity.

Ambient humidity was also found to be a critical parameter. At relative humidities exceeding 55 %, welding quality deteriorated – manifesting in increased localised burning, charring, and poor reproducibility. After identifying this effect, all welding experiments were conducted under controlled conditions at relative humidities below 55 %.

Throughout surface preparation and immediately prior to welding, all chip halves were inspected for scratches, which significantly affect weld integrity. Scratches on the top or bottom surfaces of the welding partners occasionally disrupted the laser path, but in approximately 75 % of cases did not result in major weld defects. In contrast, areas with more diffuse or frosted surface damage were more critical: such zones led to burns or char formation in around 75 % of tests. Avoiding these areas and adhering to the outlined preparation protocol was essential for achieving reliable and repeatable absorber-free welds in PC.

4.4.3.2 Positioning of the focal plane

Accurate positioning of the laser's focal plane is a critical factor in scaling the energy delivered to and absorbed within the welding partners during absorber-free laser transmission welding of PC. Two main parameters determine the focal plane's vertical location: 1) the lens position along the z-axis, which is manually set in the machine's software, and 2) the optical path length and refractive indices of the materials between the laser source and the weld interface.

In this work, four typical material stack configurations were used: i) plain foil on plain bulk substrate, ii) plain foil on seedling inlet (embossed), iii) channel-embossed foil on plain bulk, and iv) channel-embossed foil on seedling inlet. In all cases, the sample stack was placed on the machine's mounting glass and separated from it by an additional protective glass plate. This protective plate was introduced to safeguard the mounting glass from localised burns, which are frequently encountered when processing PC. Figure 4.24 illustrates the effect of beam waist shift caused by the layered material stack. The focal point of a Gaussian beam shifts deeper into the stack with each layer of increasing refractive index, according to the relation $n_{\mathrm{LaserSetup}} < n_{\mathrm{ProtectiveGlass}} < n_{\mathrm{Foil}}$ [137].

According to the manufacturer (Evosys GmbH, Erlangen, Germany), the focal plane of the EVO 1800 lies directly beneath the mounting glass at a lens position of $z = 89$ mm without the influence of stacked material underneath. For the following calculations, the refractive indices of the mounting and protective glass are assumed to be identical or negligibly different, and the influence of the mounting glass is considered already accounted for in the given z-position.

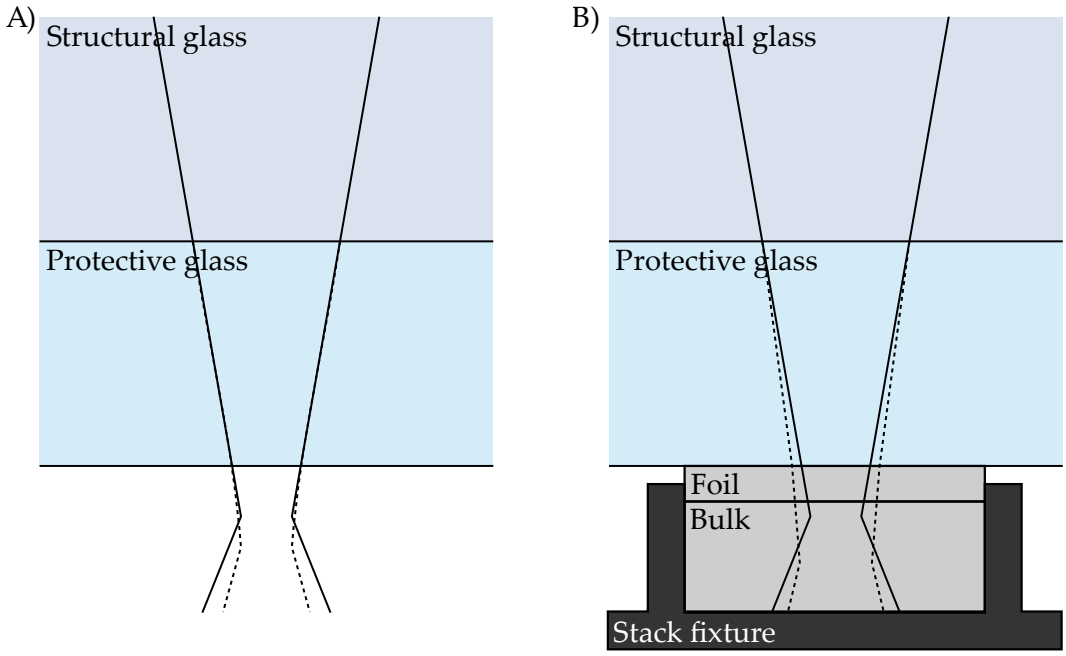

Figure 4.24: Stack setups and generic beam waist shift of **A)** the mounting and protective glass, and **B)** a complete stack comprising mounting glass, protective glass, foil, and bulk welding partner.

Following Nemoto [137], the shift in beam waist Δz as the beam propagates through a material of thickness d and refractive index n is calculated as:

$$\Delta z = d \cdot (1 - \frac{1}{n}) \tag{4.1}$$

The calculated waist shifts for the materials in the stack are summarised in table 4.9.

Material	Thickness d	Refractive index n	Waist shift Δz
Protective glass (Floatglass)	6 mm	1.499	2 mm
Plain foil (Makrofol®, Covestro Deutschland AG, Germany)	250 µm	1.585	92 µm
Channel embossed foil (Lexan™, SABIC, Saudi Arabia)	340 µm	1.60	128 µm

Table 4.9: Calculated beam waist shifts for various materials in the laser path.

From these values, it is evident that the protective glass contributes the largest shift to the beam waist, while the foils have a comparatively minor effect. Therefore, when aiming to focus the beam within the lower (bulk) welding partner, the overall waist shift of approximately 2.1 mm must be considered. Consequently, to position the focal point just below the contact plane of the welding partners, the lens should be set to $z = 84.9$ mm for plain foil configurations, and $z = 84.8$ mm for channel-embossed foil configurations. However, in accordance with previous works, the lens is typically set to create a focal point

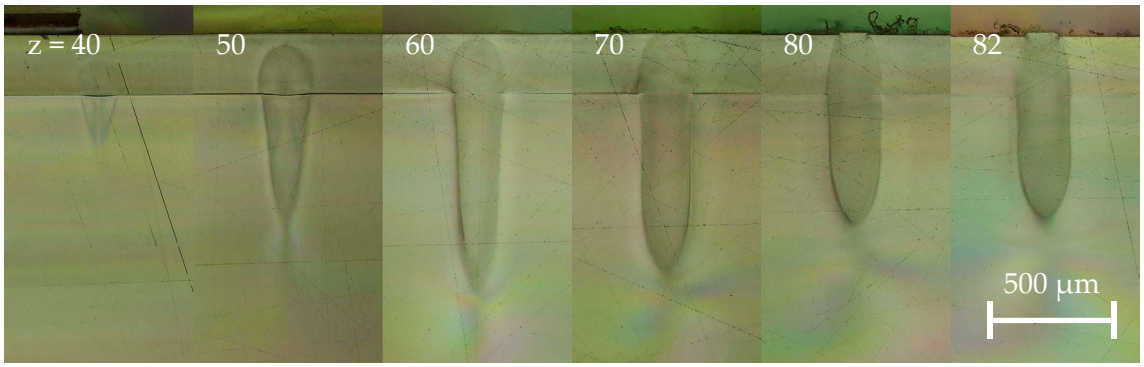

Figure 4.25: Cross-sections of weld seams and corresponding HAZ generated at different vertical positions of the focal plane. Welding was performed at constant laser power of 20 W with a scanning speed of 10 mm/s. From left to right, the focal plane position increases. A less deep but wider HAZ and seams are preferred because it creates a stronger bond between the welding partners.

at least 3 mm below the contact plane to avoid charring in the contact plane due to too high energy intensity here.

Knowing the focal plane location is crucial for determining the irradiance (power per area) delivered at different depths within the material stack. Figure 4.25 presents cross-sectional images of HAZs produced at various focal plane depths (preparation of such cross-sections see appendix L). It is observable that, up to a point, deeper focal planes result in wider HAZ regions. However, there exists a lower limit beyond which insufficient power density prevents proper melting in the upper welding partner. This results in weld seams with a characteristic narrowing or necking at the contact interface, particularly visible $z = 60$ mm.

Mamuschkin, Engelmann and Olowinsky [109] demonstrated that the mechanical strength of laser-welded joints in thermoplastics correlates stronger with the seam's width than its depth. Therefore, wider seams are generally preferred. In the present study, focal plane settings of $z = 80$ mm and $z = 82$ mm produced the most favourable results. Welds created with lower focal positions exhibited elongated but constricted seams, especially around the welding partners' interface, due to insufficient energy delivery in the upper region.

4.4.3.3 Power

The laser power used during welding is another major factor influencing the geometry and quality of the resulting weld seam. According to the Lambert-Beer law (cf. equation (A.2)), the energy deposited within the material depends on the incident intensity at the surface. The laser intensity I is defined as:

$$I = \frac{P_{\text{Laser}}}{A_{\text{Beam}}} \tag{4.2}$$

where P_{Laser} is the applied laser power, and A_{Beam} is the cross-sectional area of the laser beam [138], [139]. Thus, increasing the laser power results in a greater amount of energy being delivered into the material, enhancing localised melting and, consequently, weld formation, or cause charring.

Figure 4.26 displays cross-sections of weld seams generated with identical focal plane positioning and scanning speed, but with varying laser powers (cross-section preparation see appendix L). All welds were produced at a speed of 10 mm/s and a lens position of $z = 82$ mm.

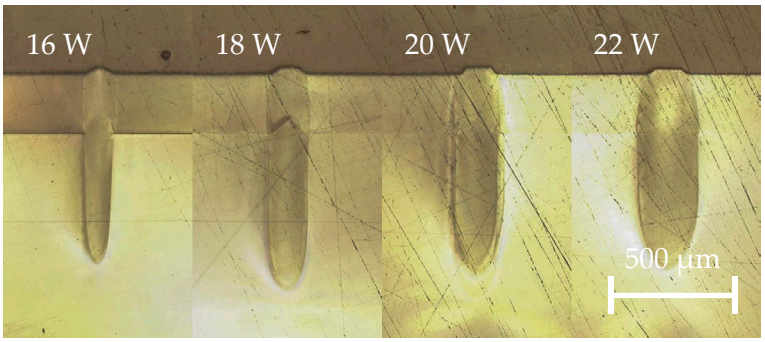

Figure 4.26: Cross-sections of weld seams created with a single pass at a speed of 10 mm/s and the f-theta lens positioned to $z = 82$ mm but at different laser powers. The weld seam width increases with rising laser power.

The cross-sectional images clearly show that, under otherwise constant parameters, increasing the laser power leads to a wider weld seam. At lower power, the weld seam remains narrow, and the interface between the two PC parts is still distinguishable, indicating incomplete fusion. In contrast, higher power results in a more homogeneous seam, with improved fusion between the welding partners.

Importantly, increasing laser power does not significantly elongate the HAZ, but rather increases its width. From an engineering perspective, this is advantageous, as it was previously established that the weld seam strength correlates stronger with seam width than with HAZ depth. Hence, under comparable material and processing conditions, a wider weld seam is generally more desirable in terms of mechanical performance.

4.4.3.4 Unevenly thick welding partners

Welding unevenly thick components has a considerable impact on laser beam propagation and the resulting weld seam geometry. As was previously discussed Nguyen [106] demonstrated that, when using a contour welding strategy, the position of the beam waist strongly determines the vertical placement of the centre of the HAZ. As shown in table 4.9, both the optical properties and the thickness of each part in the stack affect the beam's focal position. In the present stack configurations, the focal plane is shifted downward (i.e., away from the lens) due to material refraction. For foil thicknesses ranging between 200 µm and 400 µm, this downward shift is approximately 100 µm, which is relatively minor in the context of the employed EVO 1800 laser system. However, for thicker components such as 1 mm, the focal shift increases significantly to approximately 357 µm.

This behaviour is illustrated in figure 4.27, where three different upper welding partners were used: A) a 1 mm thick Makrolon® sheet, B) a 340 µm Lexan™foil, and C) a 250 µm

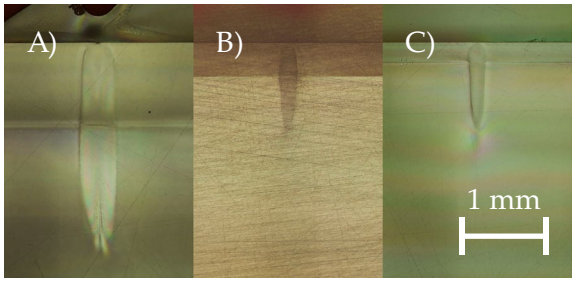

Figure 4.27: Cross-sections of weld seams created with a laser power of 20 W, single pass, and speed of 10 mm/s. The f-theta lens was positioned at $z = 60$ mm. The upper welding partner differs in each configuration: **A)** 1 mm Makrolon®, **B)** 340 µm Lexan™, **C)** 250 µm Makrofol®.

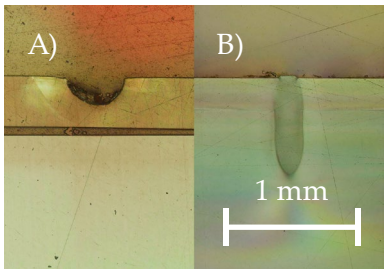

Figure 4.28: Weld seam outcomes when bonding a thin upper welding partner to a bulk lower partner without absorbers. **A)** Excessive energy absorption in the foil leads to charring. Once discolouration begins, the foil's absorption behaviour changes, concentrating energy and intensifying thermal degradation, forming a semicircular HAZ. **B)** Proper weld parameters yield a seam with the widest region at or just below the contact plane. The HAZ appears truncated due to the thin upper partner.

Makrofol® foil. All samples were welded using identical power, welding speed, and lens height settings (z-parameter). The resulting differences in weld seam position highlight the influence of both material and thickness on the focal plane location.

In general, the objective is to position the focal plane – and thus the widest part of the weld seam – just below the contact plane to achieve optimal bonding strength. However, when welding a foil to a bulk component, as in the case of the PC-RC, this approach may lead to excessive energy absorption in the thin foil layer. Depending on the energy input, this can result in two main outcomes:

1. If the introduced energy exceeds the foil's thermal tolerance, the material begins to discolour (yellowing), followed by charring and eventual burning. This results in a crater-like defect, as illustrated in figure 4.28A.

2. If energy input is more appropriately tuned, a weld seam forms such that the widest part of the HAZ lies at or just below the contact interface. Due to the foil's small thickness, the upper portion of the HAZ may appear truncated, but the weld remains strong, as shown in figure 4.28B. A slight material elevation in the weld seam region (1 µm to 3 µm) is commonly observed.

An alternative approach for managing uneven partner thicknesses involves inverting the configuration – placing the foil underneath and the bulk part above. However, this introduces two disadvantages: 1) The bulk component inherently absorbs and scatters more of the laser beam, which can significantly attenuate the energy reaching the contact plane, even when the focal plane is positioned correctly. 2) Precise alignment of features between the bulk and foil becomes more challenging in this reversed configuration, particularly for structures embossed in either part.

4.4.3.5 Double passes on weld seam

A CW strategy has proven to be the most suitable approach for producing strong and consistent weld seams when bonding unevenly thick welding partners. However, for these weld seams to be applicable in the fabrication of microfluidic chips, they must also be leak-tight. Achieving a continuous and uniformly wide weld seam is therefore critical.

The laser system (EVO 1800, EvoSys GmbH, Erlangen, Germany) available at the IMT does not provide optimal conditions for producing consistent weld seams in PC. Instead, seams typically exhibit discontinuities – often in the form of small holes or gaps, sometimes in the

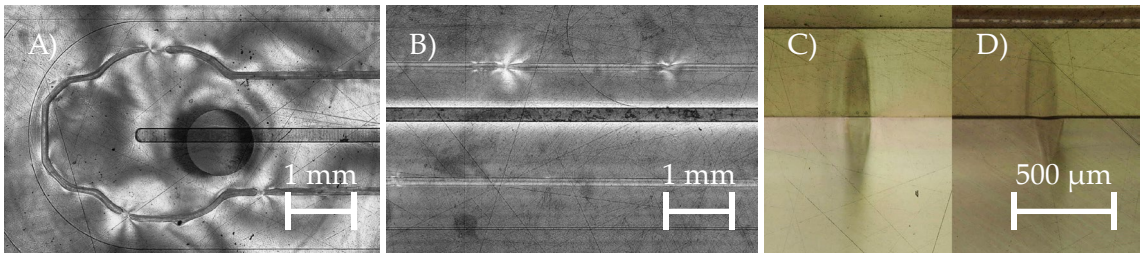

Figure 4.29: Examples of weld seams generated with a single pass. Likely causes for the observed holes include fluctuations in laser power and artefacts introduced by scanner direction changes. **A)** Interrupted weld seam in a circular pattern. **B)** Holes appearing along a straight weld pass. The gaps in both pictures are naturally highlighted by the refractions of the polarized light at their edges. **C)** and **D)** Cross-sections of the same weld seam captured at different points along the contour, showing noticeable differences in the HAZ formation due to suboptimal welding conditions.

form of significant seam thinning – as shown in figure 4.29A and B. These imperfections occur both in curved geometries and straight passes.

The limitations of the system likely stem from its original design intent, which appears to favour high-speed QSW welding at elevated powers. One indication of this is the restricted control of scanner speed, which can only be adjusted in increments of 10 mm/s. While this resolution is acceptable at high velocities, it is inadequate for slower welding speeds required by CW strategies in PC, where a change from 10 mm/s to 20 mm/s results in a substantial alteration in energy deposition. Moreover, the laser source exhibits power fluctuations of approximately ± 2 W around the set value. While such deviations are minor when operating at higher power levels, they become critical at lower powers typically used in CW welding. For instance, a drop from 20 W to 18 W can prevent sufficient melting of the material, resulting in gaps or incomplete bonding, as illustrated in figure 4.29A and B. Gaps appear as refracted edges under polarised light. Figure 4.29C and D show cross sections of the same weld seam in different positions along it, visualising the differences in its width and depth.

To ensure a leak-tight bond, it was necessary to apply a second welding pass along the seam to close any gaps remaining from the first pass. In this second pass, two factors contribute to an increased energy input compared to a single pass: First, the optical properties of the previously welded region are altered, which may lead to increased absorption of the laser energy. Second, the material has already been thermally affected during the initial pass, and residual heat is likely still present. As a result, the total energy absorbed in the second pass can exceed that of a single pass at the same or even slightly higher power. To compensate for this, the laser power was reduced from 20 W to 16 W to weld two passes without charring or burning. This adjustment successfully closed visible holes and improved seam continuity. Nevertheless, due to the lower energy input, the overall mechanical strength of the resulting weld seam was reduced.

4.4.3.6 Laser transmission welding of PC-RC

To develop a suitable welding process for bonding the hot embossed PC-RC chip halves, a stepwise approach was employed. Initially, plain foil and bulk parts were welded to establish a baseline parameter set. Subsequently, each plain part was paired with its corresponding hot embossed chip half to refine the parameters further. In the final stage, both hot embossed halves were welded together. Figure 4.30 provides an overview of this process.

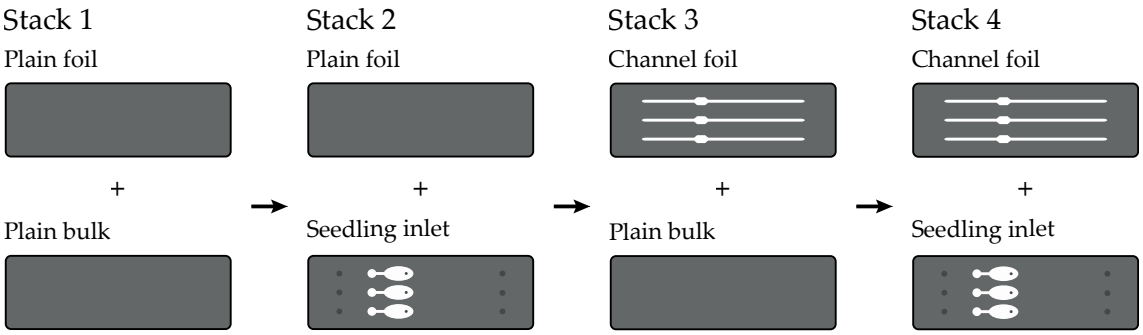

Figure 4.30: Stack setups used to determine suitable parameters to laser weld PC without absorbers. The process started with welding ideal parts, then gradually hot embossed parts were paired with plain parts. In the end, both welding partners were hot embossed and formed the PC-RC.

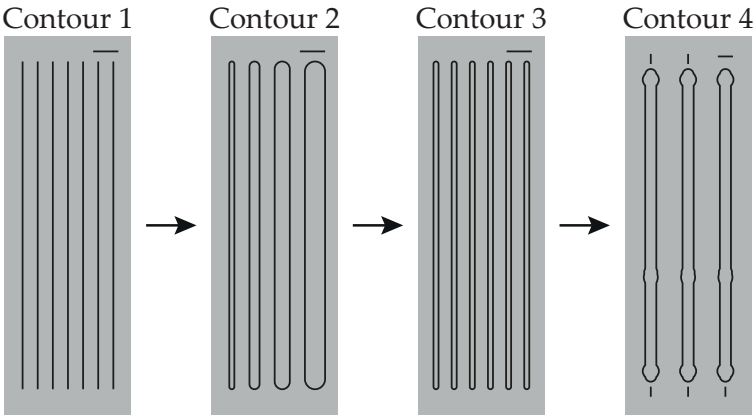

Figure 4.31: Applied contour layouts for establishing parameters for absorber-free laser transmission welding of polycarbonate.

Plain foil and bulk part were welded first to establish initial parameters for absorber-free LTW of PC. Straight-line contours (contour 1, figure 4.31) were used to evaluate weld quality. Parameter set 1 in table 4.10 (22 W, 10 mm/s, 82 mm, 1 pass) yielded reliable seams. Subsequently, rectangular contours with rounded ends (initially contour 2, later 3) were tested. Their width was reduced from 4 mm to 1 mm to match final chip geometries. Parameter set 2 (16 W, 10 mm/s, 82 mm, 1 pass) produced robust and repeatable welds for this contour.

Seedling inlet and plain foil were welded based on parameter set 2. The channel outlines and seedling inlet were converted into a contour with an offset of 1 mm (contour 4). This setup was based on a stack comprising a plain foil and plain bulk part. For the new stack it was observed that the absorption of the hot embossed bulk part was higher than that of the plain bulk. Consequently, the laser power had to be reduced to 15 W (parameter set 3) to avoid thermal degradation while achieving strong weld seams. Nevertheless, the resulting seams typically contained two to three interruptions. To form a continuous – and therefore leak-tight – weld seam, all subsequent welds were performed using two continuous passes. This change required a further reduction in laser power to 14 W (parameter set 4).

Plain bulk and channel embossed foil were welded starting from the conditions of parameter set 4. The channel embossed foil exhibited significantly higher absorption, frequently leading to local charring. To reduce the beam intensity within the foil and the

contact plane, the f-theta lens was repositioned to $z = 70\,\text{mm}$, shifting the focal plane to a theoretical depth of 12.57 mm below the bottom of the stack – corresponding to 15.97 mm beneath the contact interface. This adjustment sufficiently widened the laser beam to avoid thermal damage to the channel embossed foil and enabled the creation of intact weld seams. Parameter set 5 yielded the best results for this stack configuration, although the weld strength did not reach the level achieved in previous configurations.

Seedling inlet and channel embossed foil formed the final stack to be welded in order to manufacture the complete PC-RC. The combination of two hot embossed and subsequently post-processed components resulted in an even higher absorption rate than previous stack variants. Accordingly, the f-theta lens position was shifted further downward to generate a weld seam without damaging the stack. However simultaneously, the power was raised to 19 W to still provide sufficient energy for melting the material (parameter set 6). Table 4.10 summarises all parameter sets identified as optimal for each stack and contour configuration and used as the starting point for subsequent development stages.

Set	Stack	Power [W]	Lens position [mm]	Welding velocity [mm/s]	Passes
1	B + F	22	82	10	1
2	B + F	16	82	10	1
3	I + F	15	82	10	1
4	I + F	14	82	10	2
5	B + C	14	70	10	2
6	I + C	19	55	10	2

Table 4.10: Successful welding parameters for absorber-free LTW of PC for different stack combinations. F = foil, B = bulk, I = hot embossed seedling inlet, C = channel embossed foil. The current final parameter set for welding a complete PC-RC is set 6.

Leak-testing of the final LTW parameters followed the same approach as for the PDMS RC (cf. 4.1.3). Tubes with an outer diameter of 1 mm were glued into the chip inlets and outlets using 302-3M adhesive. The chips were placed in an oven at 65 °C for 3 h to accelerate curing. Each chip was then connected to a syringe pump (PHD ULTRA™, Harvard Apparatus, Holliston, MA, USA), and isopropanol dyed blue, yellow, and red was pumped through the channels at 150 µL/min.

Results of manufacturing Root Chip from PC using LTW were not satisfactory. However, the underlying laser transmission welding process was systematically investigated and significantly improved when welding unevenly thick welding partners. But, despite the careful preparation of each stack configuration, none of the manufactured PC-RC devices passed the final leak test. Several interrelated factors contributed to the failure of the microfluidic chips to remain leak-tight under pressure.

A significant challenge arose from the technical limitations of the Evo 1800 laser welding machine. Although this system was used throughout the process development, it is not well suited for a slow contour welding strategy that is required when welding unevenly thick PC components absorber-free. As discussed in 4.4.3.5, the machine appears to be optimised for high-speed quasi-simultaneous welding, where higher laser power and rapid scanning are typically applied. In contrast, the CW strategy for PC demands lower scanning speeds

and precise energy delivery. The limited resolution of the scanner speed settings and the observable power fluctuations during operation made it difficult to achieve consistent results at the slow welding speed and low power levels needed. These limitations affected both the reproducibility and integrity of the weld seams.

In addition to equipment constraints, practical difficulties during chip assembly further compromised performance. During the insertion and glueing of tubes into the inlets and outlets of the chips, several connections were inadvertently blocked. In some cases, the adhesive sealed the inlet entirely, preventing the dyed isopropanol from entering the channel during leak testing. In other instances, outlets were unintentionally sealed, leading to pressure build-up within the microchannel. This internal pressure likely exceeded the mechanical strength of the weld seam, resulting in crack formation and fluid leakage (figure 4.32).

The properties of the hot embossed components themselves also posed unexpected challenges. Although the raw polycarbonate substrates exhibited quite predictable welding behaviour, the hot embossed chip halves deviated notably. One reason for this was the compromised surface quality after demoulding and post-processing. The removal of flash and excess material by milling left the surfaces rough and optically non-uniform. While subsequent sanding and polishing steps improved the surface finish to some extent, they could not fully restore the original quality of the raw stock material (cf. figure 4.23). This reduction in surface quality likely led to increased scattering and localised absorption during welding, contributing to weld irregularities.

Moreover, an unexpectedly high number of localised impurities were observed in the hot embossed parts. These appeared as optically intransparent inclusions within the polycarbonate and were not present during the fabrication of the MBR, despite the use of similar process parameters and materials. Such inclusions can act as local absorption hotspots under laser irradiation, leading to the formation of charred regions and local degradation of the weld seam. Their presence represents a new variable that must be controlled in future optimisation of the process.

Although these manufacturing challenges prevented the successful fabrication of leak-tight PC-RC chips in the current setup, the underlying laser transmission welding process was systematically investigated. Key parameters affecting absorber-free LTW of PC were identified, characterised, and their interactions analysed. Moreover, a parameter set suitable for bonding the final chip geometry was successfully established (see figure 4.32, parameter set 6). These results form a valuable foundation for further development and optimisation, and conclude this chapter.

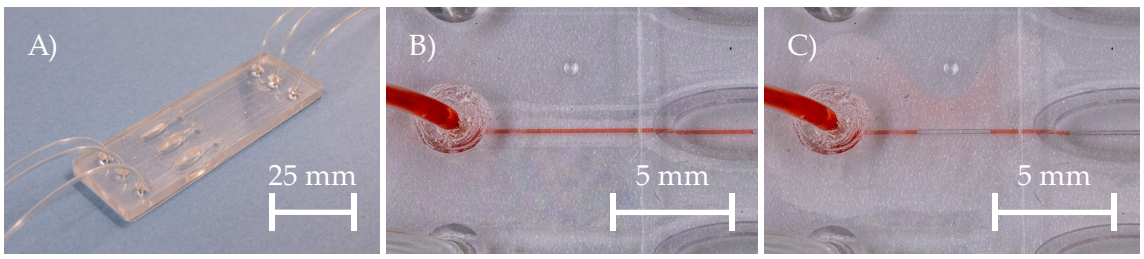

Figure 4.32: A) Completed Root Chip manufactured from PC using hot embossing to mould the chip halves, which were subsequently bonded via absorber-free laser transmission welding. **B)** Root Chip in which an outlet was inadvertently sealed during the glueing process. Initially, the fluid enters and fills the channels successfully. **C)** After 3 s, the internal pressure surpasses the weld seam's mechanical strength, leading to a rupture and leakage between the bonded chip halves.

5. Application of the microfluidic chips

Both, the Microfluidic Bioreactor and the Root Chip have been widely applied for experiments in the DialogProTec project. The JKIP (KIT, Karlsruhe, Germany) and IBMP (CNRS, Strasbourg, France) have been the collaborating institutes, where the MBR and RC have been used respectively. The following sections provide a summary of the work done at these institutes with the according MFCs. First, the application of the MBR for plant cell and fungi cultivations and experiments will be covered (section 5.1), followed by a summary of the application of the RC (section 5.2).

5.1 Application of the Microfluidic Bioreactor

The Microfluidic Bioreactor was used for several analyses and experiments in cooperation with Christian Metzger at the JKIP (KIT, Karlsruhe, Germany). The MBR served as a central experimental platform in his dissertation to investigate controlled biological interactions between plant and fungal systems. The following subsections will provide an overview of the completed work. More details are found in his dissertation [48]. The system was applied for continuous cultivation, real-time physiological measurement, and co-cultivation assays, demonstrating its utility for dynamic studies in plant-aggressor interaction research. Together, these results establish the MBR as a reliable platform for reproducible and high-resolution analysis of plant-fungal interactions. The chip enabled simultaneous cultivation, stimulation, and monitoring of living plant cells under physiologically relevant conditions, providing a valuable tool for advancing the field of ecological and phytopathological microfluidics.

5.1.1 Plant cell cultivation and viability monitoring

To assess the compatibility of plant cell cultures with the Microfluidic Bioreactor, cell mortality was quantified using a selective Evans Blue staining protocol. Only dead or dying cells absorb the dye due to compromised plasma membranes, allowing precise viability assessments. Four plant cell lines – *Nicotiana tabacum* Bright Yellow 2 (BY-2), Chardonnay, *Vitis vinifera sylvestris Ke15*, and *Vitis rupestris* – were introduced into the MBR and continuously perfused with Murashige- and Skoog (MS) medium (table 5.1) at a flow rate of 30 µL/min for seven days. Among these, only BY-2 cells maintained visual stability throughout the cultivation period, while the other three cell lines deteriorated within a few days, and thus, were terminated prematurely. The cell mortality was not quantified for these lines. For the BY-2 line, samples were retrieved after seven days and mortality was quantified. Cells cultivated in the MBR exhibited a mean mortality of 16.09 % (standard error (SE) ± 1.23), substantially higher than the Erlenmeyer flask-based control, which showed a mortality of 3.19 % (SE ± 0.56). Still, this was in a reasonable range for experiments and the MBR was therefore further tested with BY-2.

To investigate whether the MBR could support bioassays involving chemical elicitors, BY-2 cells were exposed to harpin – an elicitor known to induce programmed cell death – at a

Compound	Amount [mg/L]
Murashige-Skoog salts	4300
D(+)-Sucrose	30.000
KH_2PO_4	200
Myo-Inositol	100
Thiamine	1
2,4 Dichlorophenoxyacetic acid	0.2

Table 5.1: Composition of the standard Murashige- and Skoog medium used for plant cell cultivations in the MBR.

concentration of 27 µg/mL for two days. Cell mortality consistently increased under these conditions, reaching 40.31 %, 26.59 %, and 23.43 % across three independent experimental runs, compared to the corresponding untreated controls, which ranged from 8.36 % to 14.13 %. Overall these results were judged that the MBR allows for reliable plant cell culture and can be used to detect biologically meaningful responses to external stimuli, including mortality-inducing compounds, if the higher cell mortality in the MBR is taken into account.

5.1.2 Fungal cultivation and co-cultivation assays

Furthermore, the MBR was employed to explore the potential for interkingdom co-cultivation of plant and fungal cells. To this end, a suspension of *N. parvum* was loaded into MBRs equipped with either 1 µm or 3 µm pore membranes and perfused with MS medium at a flow rate of 137 µL/min. Fungal growth was successful and hyphae densely filled the cell chamber within three days. However, it was found that the hyphae were able to still penetrate the membrane and grow towards the inlet. The growth direction was most likely motivated by the higher nutrient density in the inlet area and the penetration facilitated by the overlay of several pores resulting from the membrane-manufacturing method (track etching). The resulting pressure buildup at the inlet led to failure of the tubing, terminating all long-term cultivations prematurely.

Subsequently, a co-cultivation setup was established with a BY-2 wild-type suspension cultivated downstream of *N. parvum* (general introduction in appendix A.5.7) in sequentially connected MBRs. Control and co-cultivation systems received medium from a common source and were cultivated for two days at 30 µL/min. Cell mortality in the BY-2 cultures was assessed via Evans Blue staining. Elevated mortality in co-cultivated samples (83.36 % (SE ± 5.98) compared to 10.6 % (SE ± 2.67) in control cultivation) indicated a physiological response of the plant cells to the downstream presence of compounds from the upstream fungal cultivation, showing that the MBR platform can facilitate chemical communication studies between distinct cell types. The findings support the suitability of MBR-based modular co-cultivation for studying complex cellular interactions under controlled flow conditions. These findings were published in [140].

5.1.3 pH dynamics and chitosan-induced acidification

To investigate chitosan-induced immune responses in plant cells, the extracellular pH of BY-2 cell cultures was monitored during treatment within the MBR in combination with the sensor screw introduced in 3.3.2. Chitosan is known to trigger defence signalling in plant cells, including an alkalinisation of the extracellular medium. BY-2 cells were

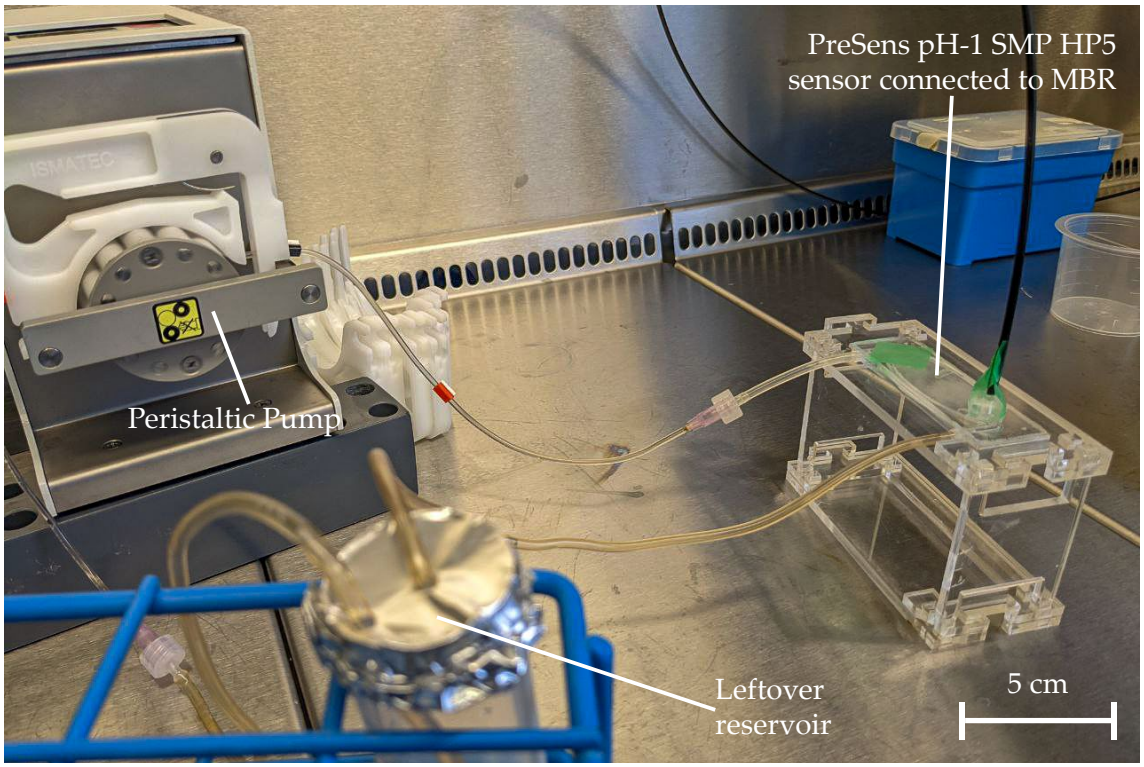

Figure 5.1: Setup of the pump and chip: The MBR is placed in scaffolding for easier tube management. 15 ml of MS medium is pumped via a peristaltic pump in a unidirectional circular medium flow. The pH value is measured continuously every 30 seconds.

cultivated in the MBR under continuous perfusion with fresh MS medium at a flow rate of 134 µL/min, using a the standard unidirectional setup (figure 5.1). 800 µL of seven-day-old cell suspension was inserted into the cultivation chamber, and the MBR was positioned horizontally after air displacement to ensure consistent flow. A pH-sensitive sensor spot integrated into the sensor-screw enabled non-invasive, real-time pH monitoring with measurements taken every 30 s using the PreSens pH-1 SMA HP5 system (PreSens Precision Sensing GmbH, Regensburg, Germany).

Before introducing the substance of interest (SoI, here: Chitosan), the system was equilibrated for 90 min, followed by a 30 min baseline recording. Treatments consisted of either 25 µg/mL chitosan or a solvent control containing 0.0025 % acetic acid and their addition to the setup were defined as timepoint 0:00. After treatment, the pH is continuously measured every 30 s for two hours. Each treatment was conducted in biological triplicates. The pH response was quantified by calculating the deviation from the baseline (ΔpH), and the effect of the substance was corrected for solvent-induced changes by computing the differential response ($\Delta\Delta pH_{chitosan}$).

The solvent control induced a sustained drop in pH beginning around 15 min post-application. In contrast, chitosan-treated samples initially mirrored this trend but then recovered to near-baseline values. After correcting for solvent effects, a significant positive ΔΔpH became apparent, indicating a chitosan-specific alkalinisation. This shift was reproducibly observed across biological replicates and was statistically validated using a two-tailed T-test ($p < 0.05$), visualised as a heatmap in figure 5.2.

These results confirm that the combination of MBR, sensor screw and optical pH sensing is capable of detecting dynamic extracellular pH responses in real time. Compared to earlier experiments using conventional benchtop pH meters, this setup reduces sample handling and enables high-temporal-resolution data acquisition. The observed pH shift supports the

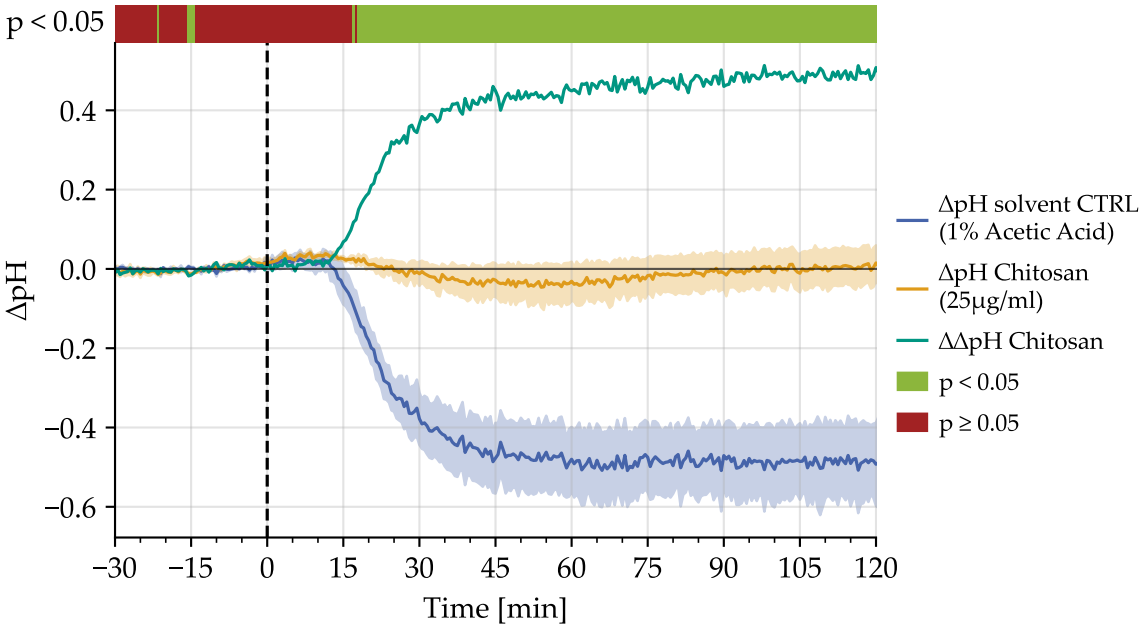

Figure 5.2: pH shift induced by chitosan: The baseline pH value is measured for 30 min before the SoI is added at $t = 0$ min. Subsequently, the pH value is observed every 30 s for two hours. ΔpH and ΔΔpH values are displayed with the respective standard error, if applicable. The significance of the difference between $\Delta pH_{chitosan}$ and $\Delta pH_{solvent\ CTRL}$ is displayed via a colour-bar on top of the graph, with the T-Test significance level being $p < 0.05$.

use of chitosan as a reference compound for plant immune elicitation and demonstrates the suitability of this microfluidic method for future screening of immunoactive substances under controlled flow conditions.

5.1.4 Quantification of hydrogen peroxide production

The generation of reactive oxygen species (ROS) is a known response of plant cells to biotic and abiotic stress (cf. appendix A.4 and appendix A.6.2), with H_2O_2 acting as both signal and defence molecule. To evaluate whether ROS induction is detectable in the runoff of cells cultivated in an MBR, BY-2 wild-type cells were cultivated in two MBRs perfused with MS medium at 137 µL/min. One cultivation was kept as a control under these standard conditions. The source tubing for the second MBR was placed in MS medium which was treated with 150 mM NaCl, to induce salinity associated stress. Following treatment with NaCl-containing medium for 60 min, runoff was collected in technical triplicates from both MBRs and further analysed.

H_2O_2 levels were quantified using the Amplex™ Red Hydrogen Peroxide/Peroxidase Assay (Thermo Fisher Scientific Inc., Waltham, MA, USA) and a microplate reader. A standard curve enabled determination of absolute concentrations: control samples contained 194.11 nM (SE ± 10.64 nM) H_2O_2, while NaCl-treated samples reached 502.06 nM (SE ± 34.22 nM). These results confirm that the MBR permits reliable quantification of ROS signals in response to abiotic stress.

This concludes the brief reports on the applications of the MBR by our partners at JKIP (KIT, Karlsruhe, Germany). The cell viability tests confirmed the suitability of the MBR for plant cell cultivation, and it was further demonstrated that fungi such as *N. parvum* could also be cultivated within the cultivation chamber. Through such fungal cultivation, the modular concept of the MBR for studying interkingdom interactions was successfully validated. Moreover, it was possible to analyse stress indicators in plant cell cultures

within the MBR. A pH shift was monitored using an optical sensor inserted via the sensor screw, and the reactive oxygen species H_2O_2 was quantified with the Amplex™Red Hydrogen Peroxide/Peroxidase Assay (Thermo Fisher Scientific Inc., Waltham, MA, USA). These reports clearly demonstrate both the wide range of potential applications and the strong interest of our partners at JKIP in employing the MBR for plant cell studies and investigations of interkingdom communication.

5.2 Root growth analysis using the Root Chip

The Root Chip and its various versions were applied at the IBMP (CNRS, Strasbourg, France) beginning with the DialogProTec project. Several designs were evaluated or are currently awaiting testing. The standard design with straight channels was initially used to examine the suitability of *Arabidopsis thaliana (A. thaliana)* as a model plant. Results indicated that while *A. thaliana* is appropriate for initial testing, further assays should incorporate additional models such as grapevine or BY-2 cultures to capture a broader range of responses.

Next and as well during the DialogProTec research, experiments focused on the cultivation of *A. thaliana* seedlings in the RC and their response to fungal extracts such as Sclerodin and Aceton-Adduct of Ent-Atrovenetinone. Exposure to Aceton-Adduct of Ent-Atrovenetinone at concentrations of 1×10^{-5} M or higher reduced root growth rates by approximately 2 mm/d and disrupted microtubule organisation. Essential oils from *Mentha spicata* – Spearmint – and *Mentha aquatica* – Watermint – were also tested for their allelopathic effects, which was measured by root elongation under continuous perfusion.

The influence of specific monoterpenoids, including (-)-carvone and (+)-menthofuran, on the cytoskeleton of *A. thaliana* and BY-2 was investigated in detail and jointly published in Hering *et al.* [141]. The study aimed to identify volatile plant-derived compounds that selectively target the cytoskeleton and might be leveraged for crop protection. Using biochemical, microscopic, and phenotypic methods, the compounds were screened for microtubule-destabilising effects in both callus cultures and intact seedlings.

The standard PDMS-based Root Chip was instrumental in these experiments, offering a microfluidic platform for the sterile, controlled cultivation of *A. thaliana* seedlings and their exposure to volatile compounds. As usual, seedlings were pre-germinated in transfer tips and then inserted into the angled inlets of the RC, allowing roots to grow along the perfused channels for real-time observation and comparative screening.

Compounds tested in this publication included the extracted essential oils of *Mentha spicata*, *Mentha aquatica*, and *Mentha piperita* – Peppermint. While some compounds – such as (+)-menthofuran or (-)-limonene – had only mild effects, (*R*)-*carvone* caused pronounced spindle elongation and mitotic inhibition in roots, phenotypes clearly observable within the RC. Interestingly, *Mentha piperita* oil, despite containing (-)-carvone, did not induce similar effects, likely due to counteracting components or reduced (-)-carvone content.

By bridging cellular-level observations in callus with whole-plant phenotypes, the RC demonstrated its value as a robust and reproducible tool for compound screening. It enabled high-resolution analysis of root development and was central to the identification of (-)-carvone as a candidate compound affecting the plant cytoskeleton. The RC thus contributed significantly to the experimental pipeline and to phytochemical research strategies in this context. These findings are published in detail in [141].

6. Conclusion

The DialogProTec project – from which this thesis originated – sought sustainable approaches to plant protection by analysing communication between plants and their aggressors, such as fungi. In this context, this thesis set out to develop, refine, and apply two microfluidic chips: the Microfluidic Bioreactor for plant cell cultivation and the Root Chip for seedling analysis. Addressing key technological gaps was essential for manufacturing both systems. For the MBR, the challenges were to adapt the initial design for successful fungal cultivation and to install ultra-thin membranes in an USW-bonded MFC without wrinkling or tearing the membrane. For the RC, the central requirement was a design that could be sterilised by autoclaving. Once PC was selected as the material and USW ruled out for bonding the chip halves, this exposed the remaining gap: absorber-free LTW of PC is scarcely documented – and, to my knowledge, entirely unreported for unevenly thick welding partners like a foil joined to a bulk substrate – necessitating the establishment of a viable absorber-free LTW process for bonding the thermoplastic RC.

The adaptation of the Microfluidic Bioreactor for fungal cultivation was driven by the DialogProTec objective to analyse interactions between grapevines such as Chardonnay, *Vitis vinifera sylvestris Ke15*, and *Vitis rupestris* and fungal pathogens such as *Neofusicoccum parvum*. Because hyphae can be thinner than plant cells, the previously used track-etched membrane with 5 µm pores and 19 µm thickness was replaced by membranes with smaller pore sizes (3 µm and 1 µm).

The installation of ultra-thin membranes via ultrasonic welding posed a practical challenge, as the alternative membranes necessary for the MBR's adaption for fungal cultivation were only about half as thick (pore size: 3 µm, thickness: 9 µm, and pore size: 1 µm, thickness: 11 µm). This reduced thickness led to pronounced wrinkling and occasional tearing during USW. Parameter sweeps eliminated tearing but not wrinkling, and the latter disrupted even flow profile in the MBR, necessitating a redesign of the membrane installation and bonding strategy. Adhesive bonding was rejected because potential leachates could alter cultivations; laser welding was unsuitable because the membrane absorbed strongly and frequently charred; and mechanical clamping (screwing) would have added unacceptable bulk for microscopy and routine handling. USW was therefore retained as the bonding process, but the membrane was no longer imprinted and then welded in place. Instead, the membrane was spanned taut across a sealing ring running along the ovally shaped chambers. At the edges, the membrane was fixed by ten discrete pillars which replaced the previous continuous energy director (ED) around the oval chambers. Matching holes for the pins in the opposing half created a tongue-and-groove ED, which are used to bond the chip halves together. During welding the membrane tightened further across the then compressed sealing ring – analogous to tensioning a drumhead – without rupturing or wrinkling it. This approach yielded several leak-tight MBRs of the

revised design within the scope of this work, however, due to time constraints, they could not be tested for their suitability for cultivating fungi any more.

A preliminary test using the new membrane (pore diameter 1 µm) with the previous MBR design was partially successful: cultivation of *N. parvum* could not be maintained beyond three days because hyphal growth clogged the inlet, overpressure developed, and tubing disconnected [48]. This is plausibly attributable to the statistical nature of track etching, which can locally superimpose pores and create larger openings that permit hyphal ingress. The revised MBR simplifies membrane exchange and thus supports rapid iteration toward pore architectures more robust to hyphal penetration. C. Metzger however, demonstrated successful cultivation of *N. parvum* for a two-day period in the MBR. Furthermore, a modular two-stage setup in which *N. parvum* and BY-2 were perfused sequentially under unidirectional flow was set up. Here, BY-2 mortality was significantly higher downstream of *N. parvum* than in control cultivations supplied from the same medium source but unconnected to the fungal reactor [48].

A review of the MBR and its applications was conducted in discussions with the DialogProTec partners at JKIP, Karlsruhe, Germany. Drawing on their experience with the MBR and its refined versions, they reported that the MBR is a promising microfluidic chip for cultivating plant cells, both as a stand-alone device and in a modular configuration combining several individual cultivation units. They recommended expanding, improving, and simplifying the optical measurements of stress indicators such as pH and ROS (e.g., H_2O_2). Detecting biotic and abiotic stress responses in plant cells cultivated in the MBR has already provided the partners at JKIP with valuable insights. However, they emphasised that further simplification of handling would be valuable – among other reasons – for solidifying research findings and speeding up equipment handling in the laboratory. The partners were pleased with the initial adaptations of the MBR membrane to accommodate the smaller diameter of fungal hyphae and welcomed the refined design of the MBR, which allows easier membrane exchange, is more versatile, and is less constrained by the materials of new membranes. They noted that cultivation conditions and the retention of fungi in the MBR cultivation chamber can and should be further improved. Finally, the modularity enabling co-cultivation of different specimens in individual MBRs sparked strong interest at JKIP, owing to the potential to harness these features for high-throughput screening of compounds acting on interacting specimens. Overall, the MBR is viewed as a promising and adaptable platform with clear avenues for practical enhancement.

Refinements of the Root Chip in this work included, among others, exploring new methods for fabricating PDMS-moulds and developing more versatile strategies for administering and exchanging compounds within the RC. However, the key goal for the RC was to transfer the design from the prototyping material PDMS to a sturdier and, above all, autoclave-sterilisable RC design made from PC. Bonding by USW was evaluated first – by analogy to the MBR – but the 200 µm × 200 µm analysis channel was unacceptably altered, yielding either a T-shaped channel or intrusions of flash from the ED. As with the MBR, glueing was rejected due to potential leachates into the cultivation at later stages, and mechanical screwing was dismissed because it would add excessive bulk incompatible with microscopic analysis. LTW was therefore selected as the bonding method.

Absorber-free laser transmission welding of PC scarcely represented in the published literature, and no studies address the welding of a thin foil to a bulk substrate. In most reported cases, PC is laser welded either with an absorbing welding partner or with added absorbers. The former approach is incompatible with the requirement for optical

transparency, while the latter carries the risk of leachates. Consequently, several parameters influencing the weld quality of absorber-free LTW were identified and studied in this thesis, like the material preparation and environmental influences, the focal-plane positioning, the applied laser power, and the specific effects of unevenly thick welding partners. The underlying LTW process was investigated systematically and substantially improved for the foil-on-bulk case. A suitable parameter set was established for welding the hot-embossed chip halves together, from which an approach for bonding the thin, channel-embossed foil to the bulk seedling-inlet half was derived. Despite these advances, no device passed the final leak test. The failures were attributable to coupled factors: suboptimal HE quality of the chip halves, a laser welding system likely not designed for a contour welding strategy, and imperfect installation of the connecting tubes.

Assessment of the Root Chip and its application possibilities was carried out in discussion with the DialogProTec partners at IBMP (CNRS, Strasbourg, France), Strasbourg, France. Based on their experience with the RC and their expertise in seedling analyses in standard setups like Petri-dish, etc., they reported that the RC was easy to handle both during cultivation setup and during microscopy, owing to its conveniently standardised slide-like size. However, they noted that the compound volume required to fill the syringes for the syringe pump feeding the RC, as well as the associated tubing, is several orders of magnitude larger than in a setup where a seedling is sandwiched between a microscope slide and a thin cover slip, which is one of their standard analysis configurations. This makes the RC unusable for experiments in which the compound to be applied is available only in very limited volume, even though the MFC-based analysis could provide deeper insights over a longer cultivation period. Furthermore, a root chip can currently hold up to three seedlings – depending on the design – and the pre-germination and transfer to the RC are time-consuming compared with a Petri-dish-based analysis, where the entire process remains in the same dish and no transfer is required. Our partners again emphasised how impractical leaking MFCs are in the laboratory, making a thorough leak-test at the end of manufacturing essential, as shown in 4.1.3. Nevertheless, our partners at IBMP (CNRS, Strasbourg, France) highly appreciated that the RC enables easy and rapid replacement of the liquid culture medium feeding the seedlings. This created the possibility, for example, to image the very first instants of a treatment on the primary root, or to record the recovery of seedlings that had been exposed to an SoI and were then fed with standard nutritional medium, down to the cellular level. In addition to such analyses, the RC provides access to growth information and behaviour in *in planta* experiments and thus allows kinetic analyses over longer periods, of up to a week. Thus, the RC already constitutes a strong yet versatile platform for future research on root development – although there remains ample scope for improvements, such as reducing compound consumption.

Avenues for future research emerge from this work in several directions. For the MBR, an obvious next step is to replace the current track-etched membrane with one featuring a regular pore lattice and tightly controlled diameters, thereby reducing variability in hydraulic performance and hyphae breakouts. This should be reasonably easy in the revised design of the MBR. In parallel, the revised MBR design should be transferred into a mould for hot embossing to streamline fabrication and standardise chip-half dimensions across batches. Beyond this, the mini-luer connector could be directly incorporated into the hot-embossed chip halves by integrating it into the design of both the upper and lower chip halves and extending the continuous ED along the channel and into the connector. The MBR design could also be adapted further to enable faster perfusion. A possible approach would be to connect the inlet channel directly to the cultivation chamber while keeping the outlet channel linked to the supply chamber, thereby ensuring a crossover of the

nutrient medium – potentially spiked with SoI or compounds from upstream cultivations – through the cultivation chamber. To ensure the viability of the cultivated plant cells and thus, the suitability of the further revised MBR, this approach should include close collaboration with biologists to test several, potentially faster, flow rates and evaluate their effects on BY-2 cell cultivations within the MBR, with particular attention to changes in cell mortality. Continued cooperation with PreSens Precision Sensing GmbH, Regensburg, Germany, is likewise recommended to assess the applicability of their VisiSense TD foils in the MBR. These are foils that can be attached to surfaces and together with the according readout system provide an area overview of one or more parameter changes. This would enable a spatial analysis of these parameters and their change over time. On the topic of sensing in the MBR, of course, the sensor screw design holds great potential as well and thus, should be further refined to offer greater flexibility for integrating different sensors and measuring additional parameters of interest to biological studies.

For the RC, efforts should focus first on refining the HE process for the chip halves to improve surface quality. In addition, transferring the channel-embossed foil from a standard HE process to a roll-to-roll hot embossing process, which is specifically developed for foils, could increase throughput and uniformity. On the design side, seedling behaviour in labyrinthine channels is a promising topic as was shown by Held *et al.* [24], who investigated fungal cultivation in labyrinthine microstructures, and Aufrecht *et al.* [74], who developed microfluidic systems mimicking sandy soil environments. To adapt the RC for such experiments, a pre-test was conducted together with E. Herzog (IBMP, CNRS, Strasbourg, France), in which zigzag-RC devices derived from the zigzag-mixer layout were opened to allow seedlings' roots to grow backwards through the zigzag structure. The seedlings' primary roots established well and consistently formed secondary roots at each 90° turn (see figure 6.1). These observations are promising and provide a clear basis for targeted follow-up studies. Furthermore, a major challenge for biologists with most microfluidic chips is that, although overall liquid volumes are greatly reduced compared to macro-scale analyses, the required amounts of specific compounds or substance of interests often remain difficult for biologists to obtain due to complex distillation and extraction procedures. The RC is not yet exempt from this issue, as its analysis channel must be large enough to accommodate a seedling's primary root which so far has been contradicting to minimising compound consumption during perfusion further. Consequently, future research should focus on finding different ways to apply compounds to the analysis channel in the RC to reduce the required volumes of such difficult to separate SoIs. A promising approach could be to integrate a small reservoir upstream of the analysis channel and mixer structures that can be selectively activated for compound delivery. Through the use of the mixer layouts – like the ones tested in this work – this could enable a reduction in the required SoI because the preparation of a prefilled syringe of compound mixture would no longer be necessary for an experiment. Additionally, this could avoid the unnecessary preparation of the such compounds, in case a seedling does not successfully establish in the device.

In conclusion it is to note that this thesis has filled significant gaps in publicly available research (cf. sections 2.4 and 2.5), especially in the areas of installing ultra-thin membranes using ultrasonic welding and absorber-free laser transmission welding. The revised design of the MBR is well prepared to aid biologists in their future experiments to dissect the communication between different intra- and interkingdom cultivations. With some further improvements the PC-RC should be ready for its application in seedling experiments and will simplify handling and sterilizing compared to its predecessor PDMS-versions.

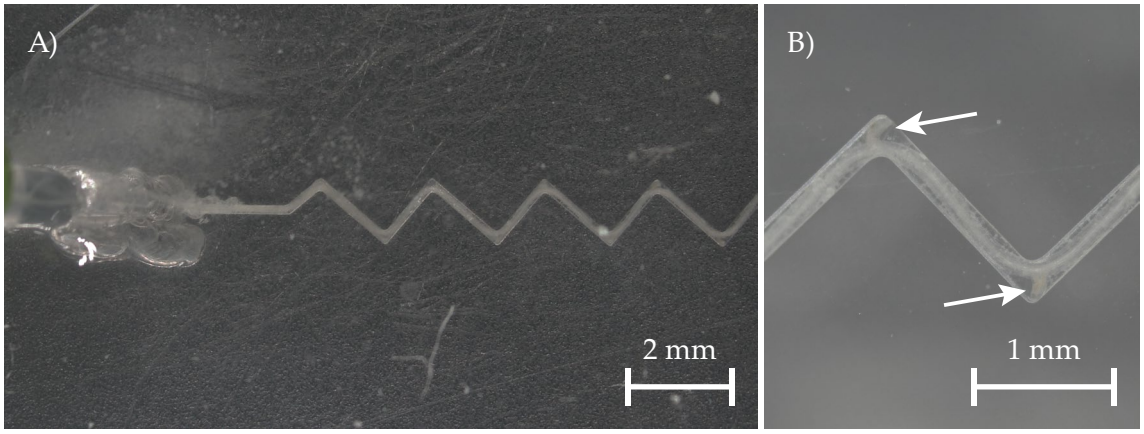

Figure 6.1: A) Seedling growing through a zigzag-mixer RC backwards so that the zigzag-structure forms a labyrinth that forces the root to make multiple 90° turns. **B)** Detail picture which shows the developed secondary roots when the primary root turns 90°. Pictures courtesy of E. Herzog, IBMP, CNRS, Strasbourg, France.

Scientific and Technical Background

A Fundamentals

The following sections provide the essential background for this thesis, covering key aspects of manufacturing, biology, and sensor technology necessary for understanding and replicating the presented work.

The mechanical fundamentals will be introduced first, following the logical flow of the manufacturing process: First, covering the replication and some mould materials (appendix A.1), followed by methods for shaping and moulding chip components (appendix A.2), and concluding with bonding techniques used to assemble the MFC[1] (appendix A.3).

Next, the biological basics relevant to this study will be covered. This section begins with an introduction to plant cell's cellular structure and cultivation (appendix A.5.1) – analysed later using the MBR –, followed by a discussion on plant roots (appendix A.5.2), which are examined using the Root Chip. Additionally, the role of fungi – an often overlooked but essential factor in natural ecosystems – will, be explored in appendix A.5.3. The section concludes with an overview of the model plants used in this research (appendix A.5.4).

Following this, stress indicators in plant cell cultures will be introduced in appendix A.4. The focus will be on physiological markers relevant to plant health and stress responses, providing a basis for understanding the need for continuous monitoring within the MBR.

Finally, sensor systems and measurement approaches for key stress indicators pH value (appendix A.6.1) and ROS (appendix A.6.2) will be outlined. These two parameters were selected for analysis in plant cell cultures within the MBR, and their detection methods will therefore be discussed in detail.

A.1 Materials for chip replication and mould manufacturing

This section focuses on the material properties relevant to microfluidic chip fabrication and functionality. The first two subsections cover materials for manufacturing and replication: PC (appendix A.1.1), and a silicone called PDMS (appendix A.1.2). The section concludes with PMMA as a mould material for (appendix A.1.3).

A.1.1 PC for replicating microfluidic chips

PC is used for replicating the chip halves of the MBR and the hot-embossed version of the Root Chip. Its transparency and biocompatibility [131], [142]–[144] are critical for this work, as the MBR is employed for monitoring plant cell cultivations using microscopy, among other techniques. Transparency is essential for such optical analysis, while biocompatibility is necessary for sustaining cell cultures. Additionally, PC can be sterilised via autoclaving;

[1] All microfluidic setups discussed in this thesis fall under the category of MFCs, including the MBR and Root Chip developed in this work as specialised types. For further details on this terminology, see chapter 1.

however, repeated autoclaving weakens its mechanical integrity. Parts should be inspected for signs of plastic ageing, such as stress cracks, discolouration, or clouding [142], [143].

PC is a high-performance technical polymer available in chemically modified variants and various blends tailored to specific properties. The most common type is Bisphenol A-PC, which is also used in this work. PC exhibits excellent mechanical strength (Young's modulus: 2400 MPa), hardness, and rigidity, while also offering exceptional impact resistance [131], [142]–[146]. Its high impact resistance makes it shatter-resistant, a crucial property for laboratory environments where space constraints increase the likelihood of accidental drops. In cases where an MFC contains genetically modified samples, preventing breakage is particularly important to avoid unintended release into the surroundings.

As a thermoplastic, PC can be reprocessed using methods such as injection moulding and hot embossing [131], [147], with the latter applied in 3.1.1 and section 4.4. These processes require knowledge of its glass transition temperature (T_g) of 148 °C. Additionally, its functional range of −100 °C to 130 °C is relevant for applications involving heating or sterilisation [131], [145].

During reshaping processes such as welding (4.4.3.6), it may be necessary to pre-dry the generally hygroscopic material to prevent hydrolytic degradation. At higher temperatures necessary for these processes, water molecules can attack the carbonate linkages connecting the dihydric phenols, leading to structural weakening. Maintaining the material's moisture content below 0.02 % prevents this issue [131], [142].

A.1.2 PDMS as replication material

PDMS is used for replicating several designs of the Root Chip (cf. 4.1.1 and sections 4.2 and 4.3). It is a solvent-free silicone initially developed for encapsulating electronic components [148]. However, due to its straightforward processing (see appendix A.2.2), ease of replicating 2.5-D structures, and favourable material properties such as transparency and chemical inertness, it is widely used in microfluidics. Additionally, PDMS is comparatively inexpensive [15], [149]–[153], which is another reason why it is often used for prototyping of MFCs like in this thesis. PDMS-structures can be permanently or reversibly bonded to themselves or other materials, such as glass, or, in microfluidic applications, used as capping layers [154], [155]. A detailed description of PDMS-bonding and the underlying processes is provided in appendix A.3.1.

The material is available as either a one-component or two-component system, the latter comprising a base and a hardener. Depending on the formulation, curing occurs at room temperature or under heat, typically in an oven. Transparent PDMS is commonly used for fabricating microfluidic chips, although opaque variants also exist [148], [154].

PDMS is non-toxic to plant cells. However, as with any material used in biological applications, its potential influence on cell behaviour must be considered [149], [150]. A key limitation is its intrinsic hydrophobicity, which can pose challenges in microfluidic and biological applications. Surface plasma treatment can temporarily or permanently modify this property, depending on the plasma parameters and post-treatment process (see appendix A.3.1) [149], [156], [157].

PDMS is also gas-permeable, which can be disadvantageous in applications requiring pressure retention, but beneficial for aqueous cell cultures where gas exchange is necessary [15], [150], [151].

The mechanical and chemical resistance of PDMS is decent, but not overly good. Additionally, it exhibits significant, temperature-dependent shrinkage during moulding (at 60 °C curing temperature on average 1.4 %), which can affect structural precision. As a result,

PDMS is less suited for long-term applications (>1 day) or large-scale production [158]–[160]. Furthermore, the material is highly susceptible to contamination like impurities incorporated into the bulk material inevitably appear in the final moulded parts [148].

A.1.3 PMMA as mould-material

PMMA is primarily used in this thesis as a bulk material for micro-milled moulds. It is an amorphous thermoplastic with high hardness and stiffness but is brittle and less impact-resistant than PC (see appendix A.1.1). To prevent damage during mould-fabrication and its later use in an oven, it is essential to consider its glass transition temperature of 105 °C and working range between −40 °C and 75 °C [131], [145], [161]. PMMA is well-suited for (micro-)milling and produces short, manageable shavings, unlike PC, which generates longer, more difficult-to-handle debris. It also exhibits moderate chemical resistance, which is sufficient for casting the chemically inert PDMS [161]–[163].

Due to its suitable working temperature, adequate chemical resistance to PDMS, and good machinability, PMMA is an appropriate material for fabricating the PDMS-moulds used in this thesis. These moulds are milled and then used to cure PDMS at 65 °C in an oven. During the casting process, PDMS must completely fill the mould's cavities and corners while allowing for easy demoulding after curing: Requirements that PMMA fully meets.

A.2 Replication and casting processes

The following subsections cover approaches to mould fabrication, prototyping, and the replication of MFC components. First, the micro-milling process (appendix A.2.1) is described, which was employed for prototyping with hard polymers such as PMMA and PC, as well as for fabricating metal and polymer moulds used in casting. Next, the casting process of PDMS (figure A.1) is outlined, along with fundamental replication principles that must be adhered to when working with this material. The section concludes with a description of the hot embossing process (appendix A.2.3), which was used for semi-mass replication of MBR components and later, the redesigned Root Chip. This term is used as the number of replicated parts was substantial for research and development but remains low compared to industrial standards for mass production.

A.2.1 Micro Milling and Machining

Prototypes and chip halves were milled from PC (cf. 3.2.3.3), as well as moulds manufactured from PMMA (4.1.1, 4.2.2 and 4.2.3 and section 4.3) and brass (4.4.1). This text provides a comprehensive overview of key terms and principles of this machining technique and concludes with two paragraphs addressing aspects specific to the work presented in chapters 3 and 4.

Milling is a subtractive manufacturing process in which a rotating milling tool removes material in a discontinuous manner. It is well suited for shaping, refining dimensions, and surface finishing [164]–[167]. Standard milling machines operate with three linear feed axes, controlled simultaneously to enable complex spatial paths. Advanced five-axis milling machines incorporate two additional rotational axes, expanding the range of possible tool orientations. These machines are typically controlled via computerized numerical control software [166]–[168].

To achieve high dimensional accuracy and surface quality, milling is performed in multiple stages. Roughing removes material rapidly, while finishing refines surfaces with reduced material removal to improve precision [164], [166]–[169]. The following paragraphs describe key control parameters – rotational speed, feed, cutting width, and cutting depth – which are essential for optimising the milling process.

Rotational speed refers to the number of spindle rotations per minute (revolutions per minute), which determines the cutting speed of the tool. Cutting speed is calculated as the product of rotational speed, tool diameter, and Π, representing the circumferential speed of the tool [164], [166]–[169]. Excessive rotational or cutting speeds generate heat, accelerating tool wear. In general, lower speeds are used for roughing, while higher speeds are preferred for a smooth finishing [165], [166], [168], [169].

Feed corresponds to the movement of the milling tool along the workpiece axes, measured as movement per revolution. In multi-toothed tools, the overall feed is distributed across each cutting edge, known as tooth feed. The corresponding velocity, or feed speed, is given in millimetres per minute (mm/min). Roughing operations typically use higher feed speeds, limited by material properties and machine capabilities, whereas finishing requires reduced speeds to achieve high surface quality [164], [166]–[169].

Cutting width and depth define the tool's material engagement. Cutting depth measures how far the tool penetrates the material in the perpendicular direction, while cutting width describes the lateral engagement within the workpiece [164], [168].

PC and PMMA, the polymers milled to create parts and moulds in this thesis, heat rapidly and melt if excessive energy is applied during machining due to their comparatively low melting temperature and limited thermal conductivity [161], [170]. Efficient chip removal and cooling are therefore essential during standard milling procedures. Without them, fused chips[2] can clog the milling tool and damage machined structures. Compressed air is effective for chip evacuation and cooling of both the tool and workpiece, while cutting fluids, such as cutting oil, also provide suitable cooling [169]. Furthermore, this thesis dealt with micro milling of PC (3.2.3.3). For this milling subtype special and highly precise machines are used. These CNC-driven setups can produce structures with error tolerances below 2 µm. Accuracy depends on the precision of axis movements and spindle performance, while temperature fluctuations and vibrations can negatively affect results. Although these factors are relevant in macro-milling, their impact becomes significantly more pronounced at the microscale [165].

A.2.2 Casting with PDMS

The fabrication of microfluidic chips from PDMS requires minimal equipment, can be completed relatively quickly, and is cost-effective. Combined with the material properties outlined in appendix A.1.2, which make it suitable for various microfluidic applications, PDMS is commonly used for prototyping MFCs, as seen in Berthier, Young and Beebe [149], Whitesides [153], Eddings, Johnson and Gale [156], and Yeong-Eun Yoo [158]. The manufacturing process consists of three main steps: mould fabrication, typically via photolithography or micro-milling; casting; and assembly of the microfluidic chip. Figure A.1 illustrates this process.

The moulds used in this work were manufactured by micro-milling (see appendix A.2.1 for more details); therefore, mould production via photolithography is not further discussed. The general design principles for casting liquids or melts with medium to high viscosity apply to the micro-milled moulds. They should be free of undercuts to facilitate demoulding, and avoid narrow-angled structures where air bubbles could accumulate. If undercuts are required, a multipart mould is recommended to allow disassembly before demoulding.

For successful casting, the mould must be free of grease, dust, or other impurities [152]. In the case of two-component PDMS, the base and hardener are thoroughly mixed, typically in a 10:1 mass ratio [148], [154], [157]. During mixing, air bubbles become trapped in the

[2] In terms of material shavings.

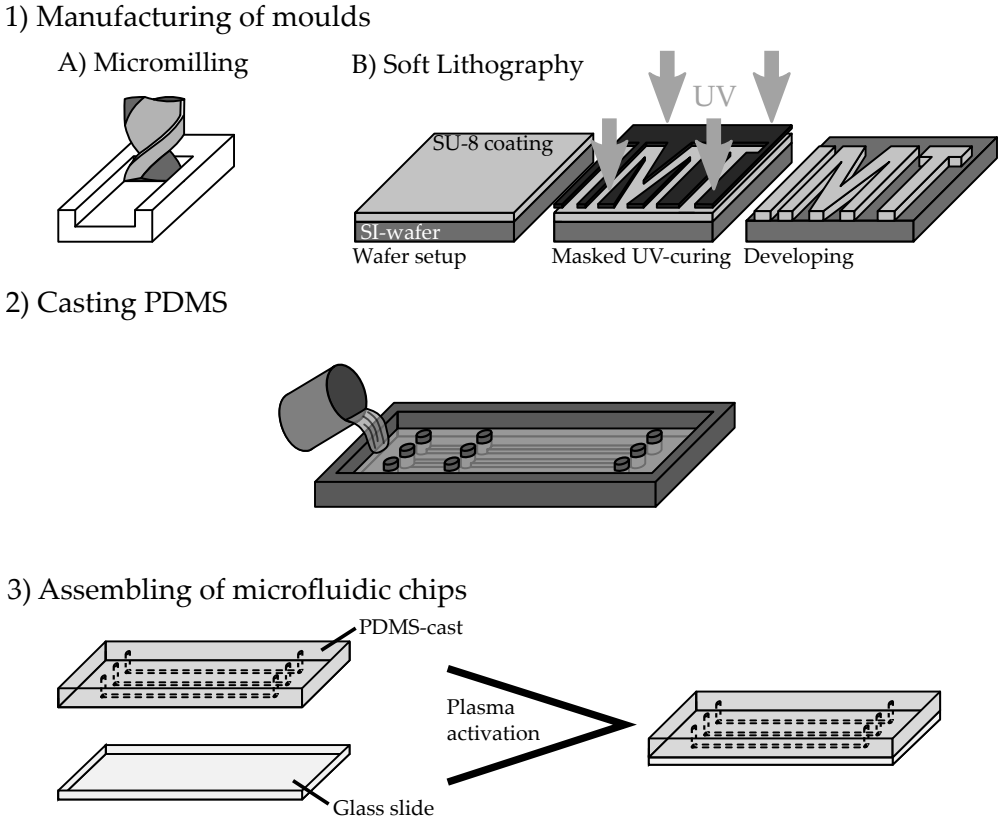

Figure A.1: The fabrication of PDMS-based microfluidic chips begins with mould production, which is typically achieved by micromilling a suitable polymer, such as PMMA, or by etching using protocols like the well-established SU-8 process. Once the mould is created, the PDMS chip halves are cast. The final step involves chip assembly, often performed via plasma activation. For details on PDMS-bonding methods, see appendix A.3.1.

material. These must be removed by placing the PDMS container in a desiccator and applying vacuum, as trapped air could obscure critical details such as channels or reservoirs or adhere to structures in the mould, leading to unwanted cavities in the final casting [148], [152], [157]. If air bubbles form again during pouring, additional degassing before curing may be necessary [152], [157]. As cross-linking begins during mixing, the material's pot life is limited, typically to 1.5 h. Final curing occurs at either room temperature or an elevated temperature, depending on the material. In some cases curing times can be sped up additionally through higher temperature. The curing time also depends on the polymer formulation and mould cavity depth, which determines the final chip thickness [152].

Once curing is complete, the PDMS can be carefully removed from the mould. Although elastic, excessive deformation may cause it to break.

After demoulding, the PDMS-chip can be bonded or capped with materials such as glass, PDMS itself, or other polymers like PS [154]. Bonding methods are detailed in appendix A.3.1.

A.2.3 Hot embossing

In this work, hot embossing is used to replicate chip components for the standard MBR (3.1.1) and the PC-RC (4.4.1). This method is better suited for laboratory-scale production and small series than micro-injection moulding, as it requires lower investment, simpler, more cost-effective tooling, and shorter machine setup times [171]. However, moulding cycles are significantly longer than in micro-injection moulding [147]. The extended process times and shorter polymer flow distances result in lower internal stresses within the moulded components compared to micro-injection moulded parts [172].

Hot embossing is primarily used to replicate moulds in polymers, including thermoplastic elastomers, non-cross-linked thermosets, and amorphous and semi-crystalline thermoplastics [171]. However, its application to amorphous materials such as glass has also been reported [173].

The machine setup consists out of a baseplate and a mould which are mounted in a vaccuum chamber and can can be heated or cooled, depending on the process step. The thermoplastic is placed on the baseplate at the beginning of the process (process and basic setup are illustrated in figure A.2). Once the vacuum chamber is sealed, the hot embossing process consists of three main steps:

1. Heating the mould and substrate above the glass transition temperature of the substrate.
2. Forming the substrate by impressing the mould.
3. Cooling the mould and thermoformed substrate below the glass transition temperature T_g, followed by demoulding[147], [171], [172].

Hot embossing can be performed using path control, force control, or a combined force-path control. In path-controlled embossing, the tool is moved into the substrate by a defined distance. In force-controlled embossing, the tool moves at a set speed until the predefined embossing force is reached. The force-path-controlled process first moves the tool by a defined distance before applying the set force. This mode was applied for manufacturing the chip halves for this thesis.

Following the forming step, a post-pressing phase ensures complete structure formation and further reduces internal stresses. During this phase, embossing force and temperature are maintained, allowing the material sufficient time to flow and fully conform to the mould and reduce internal stress [147], [172].

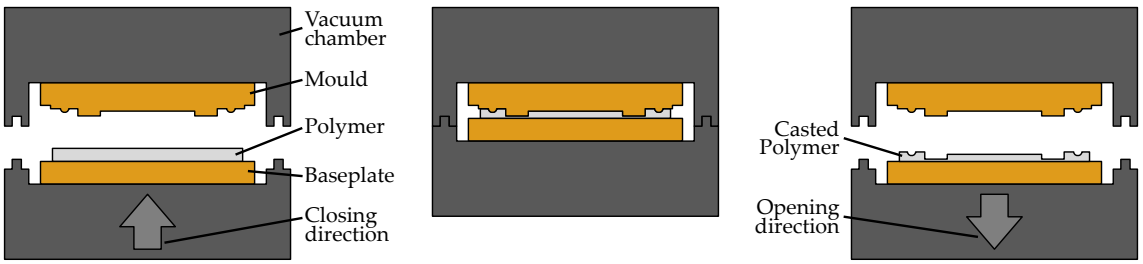

Figure A.2: Visualisation of the hot embossing process. After positioning the polymer on the baseplate, the vacuum chamber is sealed. Next, mould, baseplate, and polymer are heated above the polymer's glass transition temperature. Once, the material is molten, the mould is pressed into the mass to cast it. Finally, the setup is cooled below the polymer's glass transition temperature and the vacuum chamber is opened so that the cast polymer can be demoulded.

The post-pressing phase is followed by the critical demoulding step. While release agents can facilitate demoulding, they are rarely suitable for microsystems technology due to the required layer thickness in relation to the micro- or nanostructures being replicated [147], [174].

Process temperature selection is crucial, as it affects both replication accuracy and cycle times. Higher embossing temperatures, provided they remain below the decomposition temperature, reduce the viscosity of the substrate melt, enabling more precise reproduction of fine structures. Demoulding temperatures, in contrast, must be low enough to prevent excessive polymer shrinkage onto the mould while ensuring sufficient structural stability to prevent tearing or deformation during demoulding [172].

Precision tool movement is essential in hot embossing. For this reason, hot embossing systems for microsystems technology are often based on tensile testing machines, which provide the required precision guidance [171]. This is also the case with IMT's WUM 02, used in this work.

Additionally, embossing tools must be fabricated with high precision. Manufacturing methods include ultra-precision machining and micro-spark erosion [147], [171]. As mould wall roughness significantly influences demoulding forces, the Lithographie, Galvanik, Abformung process is particularly well suited for complex structures and high aspect ratio features [171], [172]. However, due to long scheduling times, it was not employed in this work. The relatively low process pressures in hot embossing allow for a broader selection of machinable materials for mould fabrication. In this thesis, a special brass alloy (CuZn40Pb2) was used, as it provided the right parameters for milling and later hot embossing, and was readily available at the IMT [147].

A.3 Bonding methods

PDMS bonding (appendix A.3.1) was used for prototyping the RC (4.1.2 and sections 4.2 and 4.3), while the further developed RC, composed of PC chip halves, was sealed using LTW (see appendix A.3.3) to bond the cover foil to the base plate. For the MBR, USW (see appendix A.3.2 for the general introduction, 3.1.2 for the later applications) was applied, enabling a rapid, purely mechanical bonding process. The following sections describe these methods, their underlying principles, and key process considerations.

A.3.1 Bonding of PDMS

After casting PDMS-parts to be included in different versions of the Root Chip (cf. (4.1.2 and sections 4.2 and 4.3) they have to be covered. Various methods exist for covering or bonding PDMS-based microfluidic channel structures or MFCs to themselves or other materials. These methods generally follow one of two principles: Either by chemically activating the surfaces to be bonded, creating a molecular bond, or through using an adhesive, which may also consist of the same material, such as PDMS. In all cases, the bonding surfaces must be free of impurities, including grease, dust, or other particles [152].

Bonding by glueing has been reported using ready-mixed PDMS [175] or UV-curable adhesives [176]. If the hardener of a two-component PDMS is used, as in [177], the bonding process is influenced by both the additive and surface activation, as both mechanisms contribute to adhesion. To avoid introducing additional material, oxygen plasma activation can be applied to the PDMS-surface. This process exposes silanol groups (Si−OH), which form covalent siloxane bonds (Si−O−Si) upon contact with PDMS, typically under pressure [155], [156], [178]. Plasma activation can be performed in a vacuum process [155], [156] or using a handheld corona discharge device [178]. In this work, the bonding was conducted through vacuum assisted oxygen plasma activation as detailed in 4.1.2.

A.3.2 Ultrasonic welding

Ultrasonic welding is used to seal the MBR in 3.1.2 and 3.2.3. It is a purely mechanical joining method for thermoplastics, where mechanical vibrations in the ultrasonic range generate heat in the joining zone. This is particularly advantageous for bonding MFCs like the MBR, as it eliminates the need for additives that could introduce unwanted and unmonitored side effects in subsequent cell culture experiments.

The primary process parameter in ultrasonic welding is the amplitude of the induced vibrations. The welding process begins in the generator, where electrical oscillations are generated. These oscillations, typically ranging from 15 kHz to 70 kHz, are then converted into mechanical vibrations of the same frequency by a converter, either through magnetostrictive or piezoelectric mechanisms.

In general, higher vibrational frequencies result in gentler welding processes, but generating very high frequencies requires costly equipment. At the IMT, an USW setup with an initial frequency of 35 kHz is available, which exceeds the industrial standard of 20 kHz [179]–[181]. However, the amplitude introduced into the welding partners requires further adjustment, which is achieved by interposing a booster. The booster modifies the oscillation amplitude by altering the cross-section of the wave-propagating structure: a tapered section increases amplitude, while a widened section reduces it [139], [180], [182].

The mechanical vibrations are transmitted via the booster and sonotrode to the component fixed on the anvil. Together, these components form the "stack" [139], [180], [182]. Achieving the correct amplitude for welding is crucial, and the overall stack amplitude is determined by selecting the appropriate components. It can be estimated using the equation:

$$A_{Output} = \%_{Amplitude} \cdot A_{Converter} \cdot G_{Booster} \cdot G_{Sonotrode} \tag{A.1}$$

where $A_{Converter}$ is the converter amplitude, specified by the manufacturer; $G_{Booster}$ is the booster gain, determined by its tapering; $G_{Sonotrode}$ is the horn gain, also typically provided by the manufacturer; and A_{Output} is the amplitude at the horn-part interface [82]. The amplitude of the vibrations used in this work is calculated in 3.1.2.

Figure A.3 illustrates the setup of an USW-machine and ongoing process graphically. The individual parts of the stack are coloured in different shades of green (converter and booster) and blue (sonotrode, sometimes called horn), while the components fixing the welding partners in place for the weld are dyed in orange colours. The welding partners are marked with red. They absorb the introduced high-frequency vibrations, and local heating occurs above the melting temperature of the contact surfaces due to molecular and interfacial friction [139], [182]–[184].

The distance between the coupling point of the sonotrode onto the welding partner as the source of the mechanical vibrations and the weld seam is a critical factor in USW. In industrial 20 kHz systems, welding is classified as near-field when the seam-to-sonotrode distance is 6 mm or less, while distances exceeding 6 mm are considered far-field welding [179]–[181]. Near-field welding generally achieves higher seam quality, as ultrasonic waves travel a shorter distance and experience less attenuation due to material damping. In near-field welding, the oscillation frequency of the sonotrode closely matches that at the joining surface. Far-field welding, by contrast, is suitable only for sound-hard thermoplastics with low damping coefficients, ensuring sufficient wave transmission to the joint [179], [181], [186]. As this work focuses on microstructures and small welding components, far-field welding is not considered further.

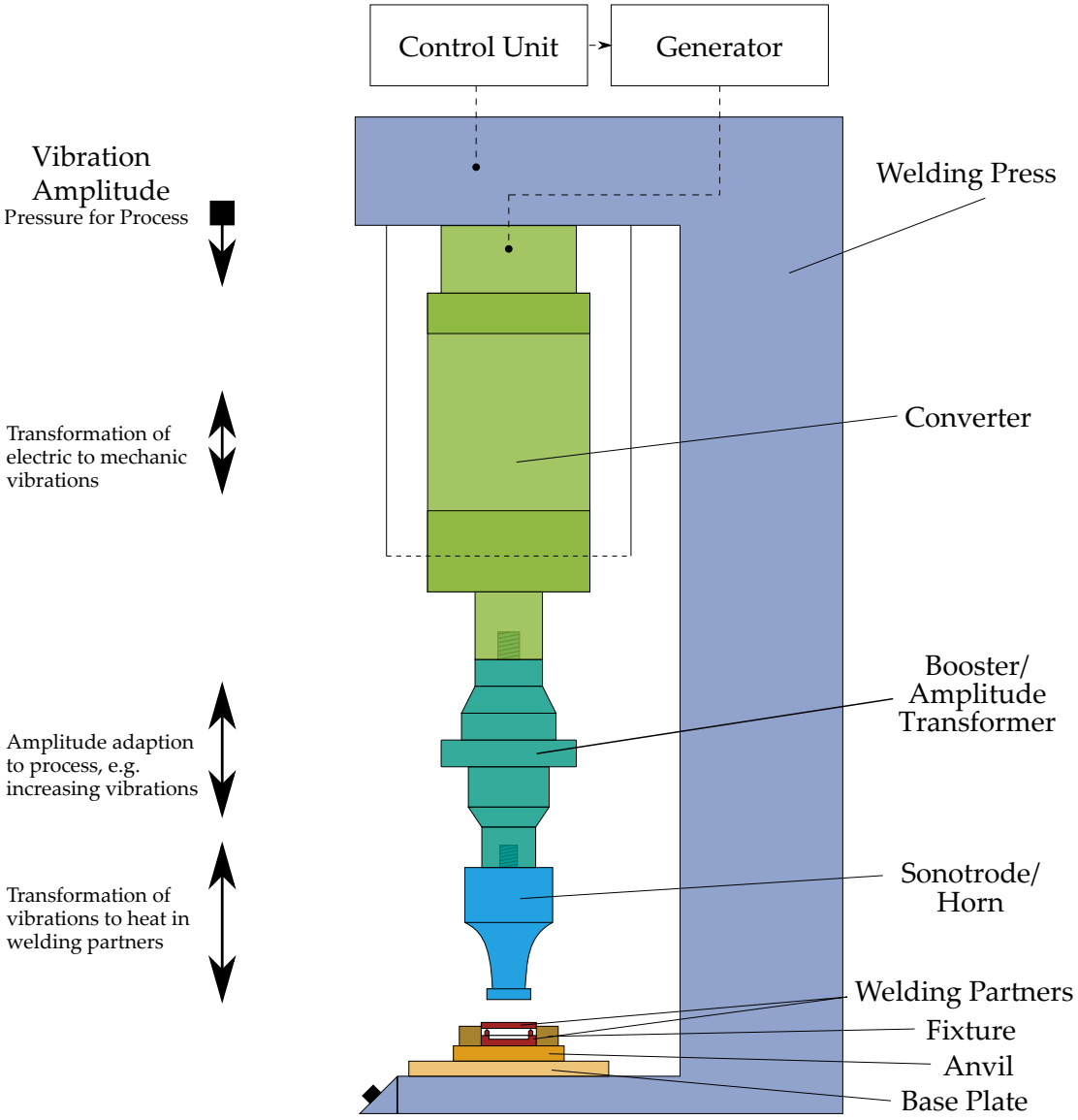

Figure A.3: The left-hand side of the diagram illustrates the vibrational amplitudes and their variations throughout the stack. The stack consists of the converter (light green), the booster (teal), and the sonotrode (light blue). It converts the electrical vibrations generated by the converter into mechanical vibrations, which are transmitted through the stack to the contact point between the sonotrode and the welding partners. The vibrational amplitude is influenced by the booster and sonotrode geometry. A transition from a wider to a narrower cross-section increases the amplitude, while a narrow-to-wide transition reduces it. After [82], [139], [179], [184], [185] and the USW-setup PS DIALOG digital control (Herrmann Ultraschalltechnik GmbH & Co. KG, Germany) available at the IMT.

From the component perspective, the ultrasonic welding process consists of four distinct phases which are visualised in the welding diagrams in 3.1.2:

1. Initial Melting: The sonotrode presses the components together, and once the trigger force (F_T) is reached, ultrasonic vibrations are activated. Dissipation of the mechanical vibration energy heats the interface, melting the material, which is displaced laterally and initially solidifies under pressure. Contact pressure continues to rise until the welding force (F_W) is reached.
2. Continued application of mechanical vibrations and pressure sustains heating, further melting the material or re-melting any previously solidified regions, effectively joining the upper and lower parts.
3. Stationary melting: In this phase, the material is melted at a constant speed and a constant melt layer thickness is formed in the seam. The joining path increases at a uniform speed, reaching the maximum weld area.
4. The sonotrode ceases vibration, and no further energy input occurs. A holding force (F_H) is applied for the duration of the preset holding time, allowing compression of the molten material and further stress relaxation within the weld seam while the material cools down and hardens [179], [183], [184].

Several of these parameters are used for process monitoring and control. A primary control parameter is selected to regulate the process, while secondary parameters serve as constraints to maintain weld quality. Process control can be categorised as follows:

1. Time-controlled: Ultrasonic energy is applied for a fixed duration t_W.
2. Energy-controlled: Welding continues until a predefined energy level (E_W) is introduced into the components, requiring measurement of input sound power and subsequent calculation of the corresponding energy.
3. Reference Point Numeric (RPN)/Displacement-controlled: Welding is carried out until a defined welding path - i.e. a certain compression height after the start of fusion - is reached.
4. Power-controlled: Ultrasonic energy is applied until the peak power is achieved.
5. Position mode: Welding is carried out independently of the components until a defined distance has been covered and a reference point was contacted. Typically, it is set as the contact between sonotrode and the components fixing plate [179].

For the MBR, energy-controlled and RPN-controlled welding were employed for membrane imprinting and chip half bonding (see 3.1.2.1, 3.1.2.2 and 3.2.3.4).

Ultrasonic welding was originally developed for joining plastic components. In principle, all thermoplastics can be welded, as they melt and solidify reversibly [184]. However, the material must also transmit ultrasonic waves from the sonotrode contact point to the weld zone, where they are converted into thermal energy [179], [184]. A material's attenuation and energy transfer properties significantly influence weldability [139], [181], [186].

Amorphous polymers exhibit a gradual phase transition from solid to molten states, resulting in slower, more controlled welding processes. In contrast, crystalline polymers maintain rigidity until reaching their melting point, after which they rapidly transition to a molten state. This leads to more abrupt weld formation, requiring greater process control [139],

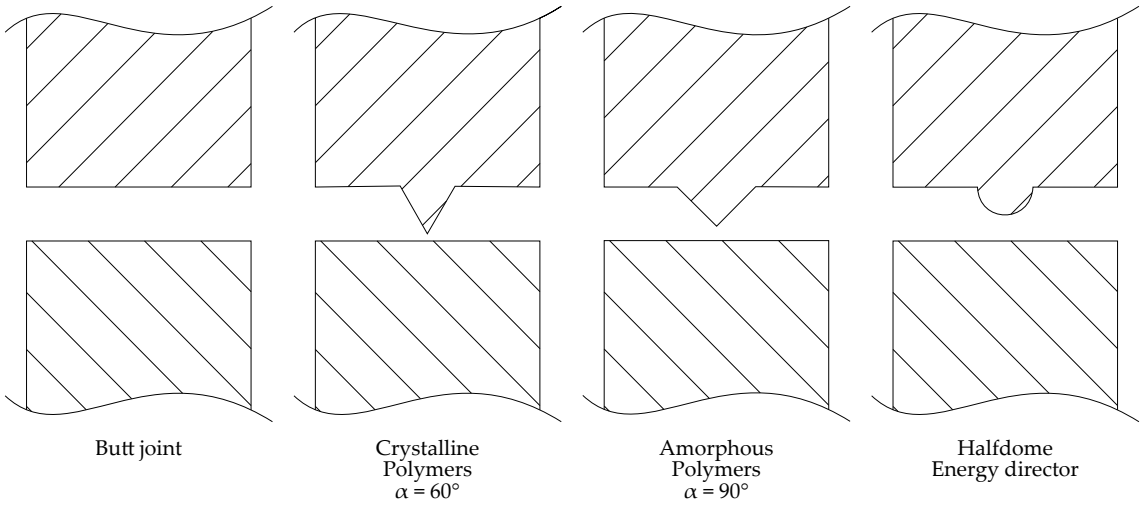

Figure A.4: Energy director types. A butt joint is often criticised for failing to define both the initial contact point and the weld origin. Consequently, EDs are commonly used. Triangular EDs provide the smallest initial contact point, enabling precise energy concentration, but are more challenging to manufacture. In contrast, half-dome EDs still create a small contact area while being easier to fabricate. They also provide a softer contact point compared to the triangular EDs. Regardless of the specific type, EDs align with the fundamental principle of USW: progressing from small to large weld areas. After [139], [179]–[181], [186].

[181], [186]. Since, the MBR chip halves manufactured from PC are amorphous, process control was easier than it would have been for a polyethylene (PE) or polyester part.

In designing an ultrasonic welding process, several considerations are essential. Welding should progress from small to large areas, component halves should be precisely aligned (e.g., using locating pins), and efficient energy transfer should be ensured, typically by maximising the contact area between the sonotrode and the component [179], [184], [186].

Additionally, seam design plays a crucial role in weld success, particularly for challenging materials. energy director (ED) help focus ultrasonic energy at the contact point and facilitate sequential melting from small to large areas. As shown in figure A.4, an ED is typically a protruding triangular or semi-rounded feature, providing a defined initial contact point between components during welding [139], [180], [181].

Ultrasonic welding is particularly well suited for series production due to its extremely short welding times of 1 s or less [139], [180], [187]. However, the process is limited to components with relatively short weld seam lengths. Seam lengths of up to 500 mm can typically be achieved, while for round and square seams, the maximum length is between 150 mm and 300 mm [184]. These limitations arise from physical constraints on the maximum size of the welding tool [139], [184].

Considering these constraints and the practical handling requirements, ultrasonic welding is most commonly used for small to medium-sized components, making it well suited for the applications around the manufacturing of the MBR [139], [180], [183].

A.3.3 Laser transmission welding

The third bonding method applied in this thesis is laser welding, specifically laser transmission welding of thermoplastics like PC (4.4.3). This introduction follows a three-part structure. First, the laser source used for bonding the RC – a thulium fibre laser – is introduced, including a general overview of solid-state lasers, and the fundamental setup of

such laser welding systems. Second, the basics of laser welding are discussed, covering heat generation and dissipation – key factors that historically made polymer welding challenging – along with the fusion process and material compatibility. The first two sections provide the foundation for understanding LTW process types, how laser absorption can be optimised, and critical considerations for weld joint design.

Building on these fundamentals, section 2.5 examines recent advancements in welding transparent thermoplastics, a crucial process for bonding the revised RC design (section 4.4). As PC is the primary material used for microfluidic chips in this work, studies on PC welding are specifically reviewed in 2.5.1. Additionally, the development of absorber-free LTW processes, a key focus of this thesis, is detailed.

In general, the laser active medium determines the type, name, and characteristic wavelength of a laser and can be a gas, liquid, or solid. Typical laser media for welding include carbon dioxide (CO_2) gas mixtures, neodyniumyttrium-aluminum-garnet crystal rods, and diode lasers [186], [188]–[191].

CO_2 gas lasers, often associated with working with polymers, were not used in this work, as they are typically employed for cutting applications due to their high power output [192], [193]. They are therefore not covered here. Instead, a solid-state laser was utilised, specifically a thulium fibre laser.

Fibre lasers offer improved heat dissipation due to their geometry. They incorporate a glass fibre with a doped fibre core, where laser-active ions such as Nd, Yb, or Er determine the wavelength characteristics. The core is surrounded by a silica cladding, which functions as a waveguide for the pumping radiation, and a secondary outer cladding ensures total reflection of the applied radiation. The laser resonator is formed by special coatings at both fibre ends, and diode lasers provide the pumping radiation at the required activation wavelengths. Due to the thin and elongated active medium, local heat generation is minimised and efficiently dissipated, eliminating previous thermal management challenges [188]–[190], [194].

The thulium fibre laser used in this thesis is a rare-earth-doped laser. Rare-earth ions in the host material exhibit well-shielded electronic structures, resulting in narrow absorption and emission spectra [195]. Thulium-doped silica can lase at wavelengths between 1700 nm and 2050 nm [196]. The first thulium fibre laser was introduced in 1989 by Hanna *et al.* [197]. The EvoSYS GmbH welding setup used in this thesis was configured for a wavelength of 1940 nm.

The following sections detail laser beam focusing and guidance, followed by the principle setup of an LTW system.

To harness the laser beam for welding, its characteristics must be adapted to the specific requirements of the weld, such as spot geometry and radiation intensity distribution. This is achieved through beam-shaping optics, lenses, or mirrors. Focusing systems are categorised as static or dynamic [189], [190], [194].

A static focusing system maintains a fixed distance between the laser beam and the focusing device, while the workpiece moves relative to the beam. This setup is commonly used for fibre-guided diode lasers. In contrast, a dynamic focusing system keeps the workpiece and focus point stationary, while the laser beam moves along the welding contour, typically using a scanner head [189], [190], [194].

For certain applications, it may be beneficial to generate specific beam geometries such as circles, lines, or complex contours, requiring specialised beam-shaping optics. In this case, special beam shaping optics are applied [189], [190], [194]. However, these setups are not discussed here as they are out of scope for the work on the RC and MBR.

Laser radiation can be guided using either a glass fibre or a mirror system. Mirror-based systems can handle high-power lasers, such as CO_2 lasers, but require precise alignment of the beam path and optical axis. Additionally, mirrors must be made of high-energy-resistant materials, such as copper or silicon for CO_2 lasers, or fused silica with highly reflective coatings for near-infrared lasers.

Glass fibre-based guides offer simpler handling and maintenance but are less effective at transmitting high characteristic wavelengths, such as those from CO_2 lasers, due to power losses associated with available fibre materials. In these systems, a focusing optic couples the laser beam into the glass fibre, which consists of a core with a diameter of 100 µm to 1000 µm, a first cladding (100 µm), where total internal reflection confines the beam within the fibre, and a second, outer cladding, ensuring fibre flexibility. Over the length of the fibre, internal reflections alter the beam profile, resulting in a wider intensity distribution. To restore the original beam shape, collimating optics are positioned at the fibre's exit. paralleling the beam shape [189], [190], [193], [194]. A functional laser welding system consists of the following components: A laser source, a focusing unit, and a beam delivery system. These elements, combined within an appropriate housing, form a basic welding system. However, industrial laser welding systems typically include additional components, such as a controller unit, cooling system, and workpiece handling system for clamping and positioning [189], [194].

The fundamental concept of LTW for thermoplastics is based on selective laser transmission and absorption. The laser beam passes through the transparent upper material, reaching the lower welding partner, which absorbs the radiation, converting it into heat. This process first melts the lower component, and then, through heat convection and direct contact, the upper component also melts. Applied pressure ensures proper bonding and weld formation [186], [188]–[191], [194], [198]–[201]. This principle is illustrated in figure A.5.

Heat generation during laser welding of thermoplastics depends on the interaction between the material and the laser beam. This interaction occurs through three primary mechanisms: absorption (A), transmission (T), and reflection (R), that are connected through the relation $A + T + R = 1$ [188], [189], [194], [198].

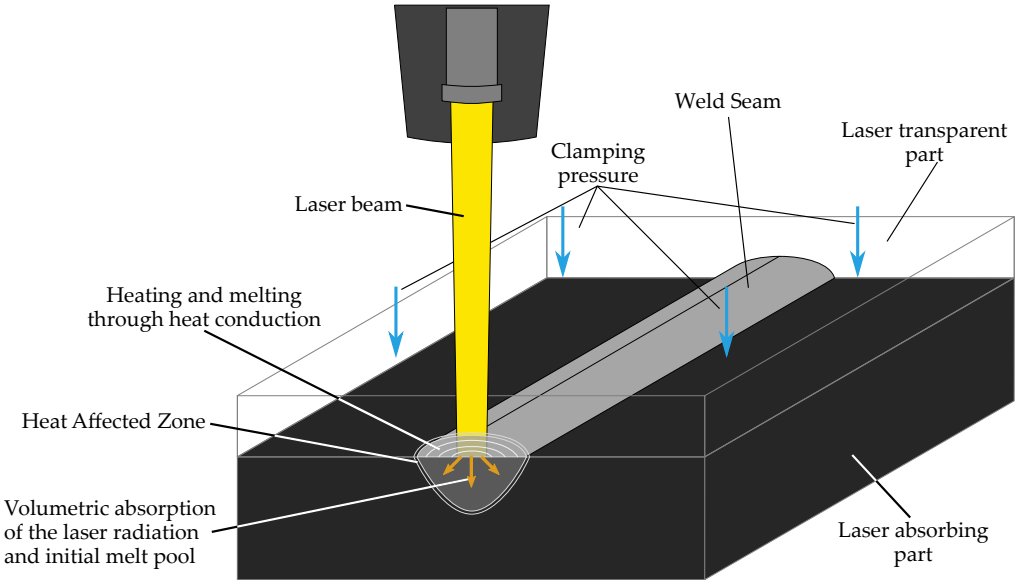

Figure A.5: Principle of absorber-based laser welding. The laser light is absorbed by the lower welding partner which is doped with absorbing additives. The absorbed heat is then conducted to the upper, laser-transparent welding partner and melts the material here. The workpieces are pressed together, which aides the forming of the weld. Adapted after [106], [190], [194], [202]

Reflection generally has negligible effects when welding homogeneous thermoplastics, as these materials reflect only an insignificant portion of the incident radiation. However, if the workpiece is coated, for instance with a metallic layer, reflectivity may increase and alter the welding process [186], [198]. Since this work focuses on uncoated materials, such cases are not further considered.

Absorption is the primary factor influencing heat generation, as it determines the amount of incident laser radiation converted into heat and subsequently dissipated through thermal conduction within the polymer matrix. This defines the maximum energy available for melting the material and forming the weld.

Absorption occurs via two mechanisms: Direct absorption, where the laser radiation interacts with the macromolecular bonds of the polymer and indirect absorption, where added laser absorbers convert the radiation into heat and transfer it to the surrounding resin [189], [194].

The chemical structure of a polymer dictates its direct absorption capacity, as different molecular bonds absorb different wavelengths by initiating vibrational excitation [188], [189], [194], [198]. For example, C−O, S−H, O−H, and N−H bonds exhibit fundamental oscillations within the mid-infrared range, between 2500 nm and 25 µm.

Indirect absorption, facilitated by the addition of special absorbers, relies on heat exchange between the absorber and the polymer matrix. The most common absorber is carbon black, an inorganic pigment widely used for this purpose. Modern approaches utilise dyes and alternative pigments, enabling colour variation while maintaining effective laser absorption [188], [190], [194], [198]. Further discussion on optimising absorption and recent advances in absorber-based LTW is presented in appendix D.2.

The third parameter influencing the laser's interaction with a material – transmission – is critical in through-transmission welding, as the upper workpiece must allow the laser beam to reach the welding interface [194]. The degree of crystallinity in a polymer significantly affects its laser transparency. Partially crystalline materials exhibit internal reflection due to their lamellar structures, which reduces laser penetration and limits the maximum thickness of the transparent upper layer [186], [189], [190], [194], [198].

When the polymer is heated above its melting temperature (t_M), it transitions from a solid to a liquid state, allowing macromolecular interdiffusion and entanglement between the welding partners. Clamping the parts during this process enhances molecular penetration. As the polymer melts, its specific volume expands, generating internal pressure in the molten zone, which facilitates diffusion across the interface. Upon cooling and resolidification, a permanent weld joint is formed. However, it is critical to ensure that the degradation temperature (t_D) is not exceeded, as this can cause irreversible defects [186], [188], [194], [203].

As with any welding process, a heat-affected zone (HAZ) forms during bonding. Analysing the HAZ morphology provides deeper insights into the welding process mechanics, which will be discussed further in section 2.5 [189], [194], [204].

The diffusion time available for weld formation depends on the polymer properties. Generally, any material suitable for ultrasonic welding is also compatible with LTW as long as one welding partner is transparent to the applied laser light. The weldability improves when the welding partners have similar material properties, including melting temperature, melt flow rate, and collapse behaviour. Additionally, chemical structure, thermal properties, surface characteristics, and rheological behaviour all influence the welding process [139], [190], [194].

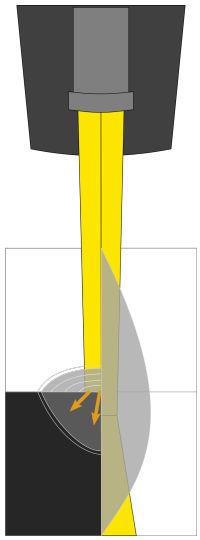

Figure A.6: Comparison of the two types of developing heat-affected zones if the weld is done either absorber-based (left side) or absorber-free (right side). It is important to note that for absorber-free LTW (right side), the focus of the laser beam should be slightly underneath the contact plane of the welding partners to achieve an ideal shape of the heat-affected zone and thus a strong weld. For absorber-based laser transmission welding (left side) the laser beam is typically focused right onto the contact plane of the welding partners. Adapted from [109] and [106].

In conventional LTW, the welding partners consist of a laser-absorbing and a laser-transmitting material. The laser beam passes through the upper, transparent partner and is absorbed by the lower partner, which converts the radiation into heat. This localized heat transfer melts the lower partner first, followed by melting of the upper partner via thermal conduction and contact. Applying clamping pressure during melting ensures intimate contact and material interdiffusion, forming a solid weld upon cooling [186], [189]–[191], [194], [198], [203], [205]. Along with the weld seam, which consists of a core zone and a melt zone, an HAZ is formed [206]. Its shape and size are influenced by laser power, interaction time, and optical penetration depth. In "classical" LTW – thus the material combination of a laser-transmitting and an -absorbing material just mentioned – the HAZ originates in the lower, absorbing partner, where radiation is converted into heat. It extends outwards in an elliptical shape, but its geometry may be distorted if an unbridgeable gap exists between the welding partners [106], [201], [205], [207], [208].

In absorber-free LTW, the laser beam is absorbed by both welding partners, creating an elongated weld seam and an HAZ spanning the entire weld cross-section. The absorption follows the Lambert-Beer law:

$$I(z) = I_0 + exp(-\alpha + z) \tag{A.2}$$

where $I(z)$ is the absorption intensity in the z-direction, I_0 is the incident laser intensity, and α is the absorption coefficient [106], [201], [207], [208]. Figure A.6 illustrates the differences in HAZ formation between classical and absorber-free LTW. The size and shape of the HAZ are commonly used to assess weld quality and strength [106], [201], [205], [207]. This topic is further explored in 2.5.1 and 2.5.2.

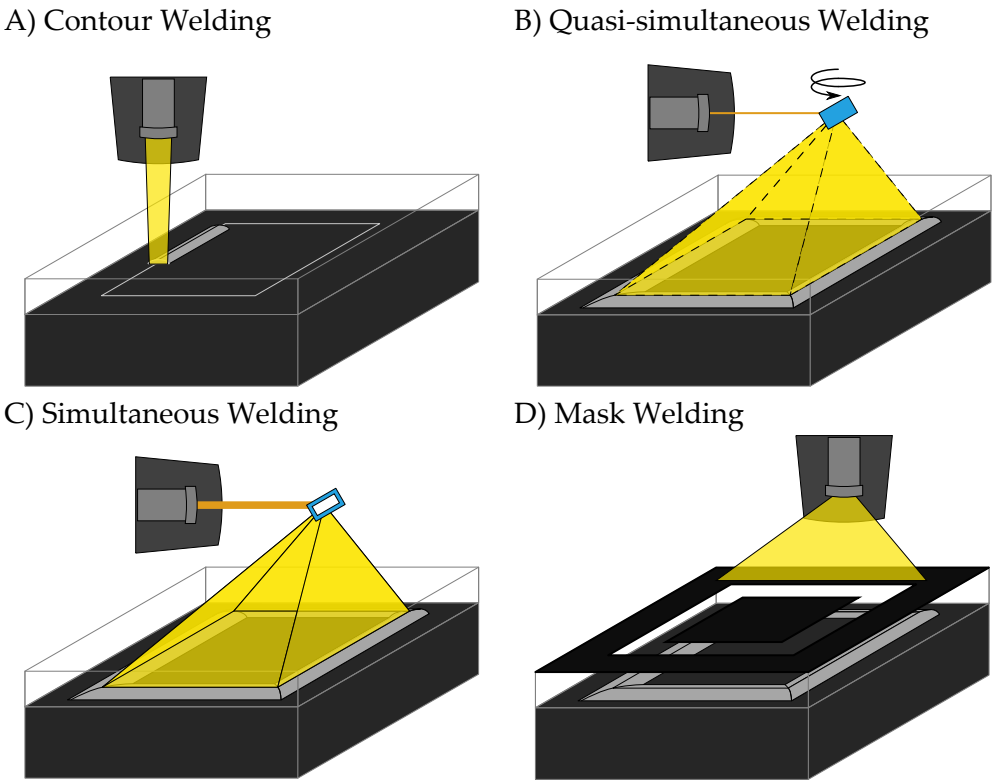

Figure A.7: The four major irradiation strategies for laser transmission welding: Contour welding, quasi-simultaneous welding, simultaneous welding, and mask welding.

Laser welding can be performed using one of four primary process strategies: CW, simultaneous welding (SW), quasi-simultaneous welding (QSW), and mask welding [186], [189]–[191], [194], [198], [203], [205]. Figure A.7 illustrates the working principles of these strategies. Out of these strategies, CW and QSW were applied for covering the hard plastic versions of the RC (cf. section 4.4)

In CW welding, a focused laser beam follows the weld joint contour, making it a highly flexible method as any path can be programmed [139], [186], [194]. The line energy, defined as

$$E_L = P/v \tag{A.3}$$

where P is the laser power and v is the beam travel speed, provides a general guideline for process optimisation. However, efficiency losses due to lens imperfections, material coupling, and impurities may lead to variation in weld quality, even for identical line energy values [104], [139], [186], [194]. When optimising parameters for a new weld, as in 4.4.3.6, the line energy serves as a key reference, providing a structured approach to identifying adjustable parameters while maintaining consistency in others. The advantages of this welding strategy are the easy machine setup because any beam guiding system can be applied, and thus, low investment costs as well as the high flexibility of the process due to the possibility to individually program the contour. However, as only small parts of the weld path are melted at the same time, only minor gaps between the welding partners can be bridged and manufacturing tolerances for the workpieces are very small [188], [194], [198], [209], [210]. In addition, parts of the weld seam might have already re-solidified when other parts of the weld path were not activated yet, resulting in strong residual stresses, as Kreimeier Sooriyapiragasam and Hopmann [209] and Hopmann, Bölle and Kreimeier [210] have shown in their work.

Simultaneous welding is the inverse of CW, as the entire weld path is irradiated simultaneously, resulting in uniform melting and welding along the entire contour. This approach offers several advantages like a higher tolerance for part positioning, as settling can compensate for minor misalignments, lower residual stresses, as simultaneous melting and solidification prevent localised shrinkage, and faster welding cycles. However, beam guidance and shaping must be precisely matched to the weld contour, making SW setups costly. As a result, this method is generally used for high-volume production, where the weld contour remains unchanged [139], [186], [188], [190], [194], [198].

In mask welding, a mask defines the weld pattern, and a wide laser beam irradiates the entire surface. If the weld width exceeds the beam curtain, multiple passes with slight overlap can be performed. Key advantages of this approach include the possibility to create highly precise weld seams, which can be simultaneous formed at multiple weld widths within a single beam pass. However, accurate positioning of the mask above the welding partners is essential. Photolithographic processing is commonly used to fabricate these masks, where a metallic coating on a glass plate is selectively removed, allowing targeted laser transmission while the coating reflects or absorbs unwanted radiation [186], [191], [194].

A more recent approach, QSW welding, combines aspects of CW and SW, offering both flexibility and improved gap-bridging capability. This method employs a fast galvanometer scanner to direct a single laser beam along the weld path at high speeds, leveraging the heat accumulation effect inherent to polymers. Due to their low thermal conductivity, polymers retain heat along the scanned path, enabling near-simultaneous melting of the entire weld seam. The resulting process facilitates the bridging of larger gaps between welding partners caused by imperfections or minor misalignments [109], [186], [188], [190], [191], [194], [200], [211]. Furthermore, the selective and contactless energy deposition minimises both thermal and mechanical stress. Since the material is heated more gradually than in CW welding, thermal stresses are further reduced [109], [194], [200], [201], [211]. However, due to the multiple cooling intervals between successive passes, even if brief, the maximum achievable weld length is inherently limited. Additionally, the required scanner system increases overall complexity and cost [109], [201].

Optimisation of QSW welding requires careful control of several parameters, including joint path length, scanning speed, number of passes, and laser power [109], [186], [194], [211]. Specialised focusing optics, such as fisheye lenses, are typically employed to equalise the laser scanning field. Among them, f-theta lenses, a subset of fisheye optics, are widely used in LTW applications to maintain a constant focal length across a planar work area [207], [211]. An f-theta lens is also incorporated into the LTW setup used in this work.

As discussed earlier, the absorption of a material can be enhanced to improve laser welding efficiency. The most common approaches include the use of absorbing additives such as carbon black or titanium dioxide, absorbing dyes like Clearweld [105] or Lumogen™ [212], and surface coatings applied to the material [186], [190], [194], [201]. Surface coatings can be applied by spraying, allowing coverage of large areas, or by using needle-tip dispensers, which deposit coatings in precise widths ranging from 1 mm to 5 mm. In most cases, the absorber is dispersed or dissolved in a carrier solvent, such as ethanol or acetone, to ensure uniform application [190], [194], [213].

The effectiveness of absorbing dyes is dictated by their specific absorption bands, which can be precisely matched to a laser's wavelength [190], [194]. These dyes generally require low concentrations, typically ranging from 0.1 % to 0.01 % in the polymer matrix [194]. In contrast, absorbing pigments require higher concentrations, typically 2 % to 0.5 %, to achieve sufficient absorption [194], [213]. Among absorbing additives, carbon black remains the most widely used due to its strong absorption properties in the near-infrared range,

low cost, and good processability, allowing its integration into resins without significantly affecting their extrusion or moulding behaviour [190], [194].

Despite these benefits, the use of absorbing additives presents several challenges. One of the primary concerns is concentration control. An excessive concentration can result in excessive localised heating, potentially leading to polymer degradation. Conversely, insufficient absorber concentration may result in insufficient heat generation, leading to incomplete fusion and weak welds [190], [194], [205], [214]. Another major limitation, particularly relevant to this thesis, is the impact on optical transparency. Many microfluidic applications require clear materials to enable standard and fluorescent microscopy for cell culture and root system analysis. The incorporation of absorbers, such as carbon black, inherently reduces transparency, making it unsuitable for these applications [190], [194], [215].

Beyond optical considerations, biocompatibility is another critical factor. The introduction of absorbing additives can alter surface properties, affecting cell adhesion, growth conditions, and measurement accuracy within microfluidic devices [109], [191]. Even commonly used polymers such as PMMA, cyclic olefin copolymer, PS, and PC may exhibit undesirable changes in biocompatibility when combined with absorbers, potentially compromising experimental conditions for plant cells and roots [190], [191], [194], [216]. Furthermore, while certain absorbers can be engineered to maintain transparency and biocompatibility, they are often costly, making them economically unfeasible for large-scale applications [194], [201], [216], [217].

Given these limitations, research has focused on developing absorber-free LTW, allowing the bonding of thermoplastics without the need for additional absorbers. This approach is of key importance to this thesis, and an overview of recent advancements in absorber-free LTW for PC and other thermoplastics is provided in 2.5.1 and appendix D.1.

A.4 Stress indicators in plant cells

Analysing stress indicators and their link to plant behaviour is a key application of the MBR as well as the RC. To put the application of the MFCs in chapter 5 into perspective a short introduction on stress indicators in plant cells is given in the following paragraphs. First, a general introduction and in the last two paragraphs of the text a more detailed introduction of the two parameters analysed within this work as a proof-of-concept test for the MBR. Plant cells are continuously exposed to environmental stressors that significantly affect their physiology and development. These stressors are broadly classified into abiotic and biotic factors. Abiotic stressors include extreme temperature fluctuations, drought, flooding, salinity, metal toxicity, and nutrient imbalances, whereas biotic stressors arise from living organisms such as pathogens, herbivores, or competing plants, which negatively impact plant health, growth, or reproduction. Each type of stress elicits specific cellular responses as plants attempt to mitigate damage and adapt to adverse conditions [45], [218]–[223].

Among abiotic stressors, drought stress restricts water availability, prompting stomatal[3] closure to reduce water loss. While this conserves moisture, it also limits CO_2 uptake, leading to reduced photosynthesis and increased reactive oxygen species (ROS) accumulation. Elevated ROS levels can damage cellular components, necessitating the activation of antioxidant defence mechanisms to maintain cellular integrity [45], [219], [222], [224]–[227].

Similarly, high salinity disrupts ionic balance, particularly the Na^+/K^+ ratio, impairing enzyme function and water uptake, ultimately leading to osmotic stress. In response, plants

[3]Stomata, microscopic pores on the leaf surface that regulate gas exchange and water loss [45], [219].

accumulate osmolytes and activate ion transporters to restore homeostasis [45], [219], [222], [224], [227].

Temperature extremes also impose significant stress. Heat stress denatures proteins and disrupts membrane stability, triggering the synthesis of heat shock proteins to assist protein refolding and modifications in membrane lipid composition to maintain stability. Conversely, cold stress induces the expression of cold-responsive genes, which help protect cellular structures and enhance resilience under low temperatures [45], [218]–[222], [224].

In addition to abiotic challenges, biotic stressors such as pathogen infections and herbivory further complicate plant responses. Pathogen attacks activate signalling cascades, including mitogen-activated protein kinases (MAPKs) and transcription factors like WRKYs, which regulate the expression of defence-related genes and stimulate antimicrobial compound production [45], [218], [220]–[222]. Herbivory, on the other hand, triggers the jasmonic acid pathway, leading to the synthesis of protease inhibitors that deter further feeding. Additionally, mechanical damage caused by herbivores induces cell wall reinforcement and stimulates the production of secondary metabolites, reducing the plant's palatability [45], [218]–[222], [228].

This thesis focuses on stress factors relevant to plant cell cultivations and their respective biomarkers. The five most commonly measured stress indicators in plant cell cultures include:

1. Reactive oxygen species accumulation, a primary marker of oxidative stress.
2. Expression Profiles of stress-responsive genes, such as those encoding heat shock proteins and antioxidant enzymes.
3. Fluctuations in stress-related hormones, including increased abscisic acid under drought stress and jasmonic acid following herbivory.
4. Fluctuations in intracellular and extracellular pH levels influenced by stress conditions such as salinity, drought, or ammonium toxicity.
5. Membrane Integrity and Electrolyte Leakage indicating stress-induced membrane destabilisation and cell damage.

Two key indicators, pH fluctuations and ROS accumulation, were specifically analysed using the MBR developed in this thesis.

The pH of plant cell cultivations, which influences both intracellular metabolism and the extracellular environment, can increase or decrease depending on stress conditions. Oxidative stress, triggered by factors such as drought or salinity, often leads to the excretion of organic acids, including malate and citrate, which lower the pH of the medium. Similarly, pathogen-induced stress can cause acidification through increased respiration and carbonic acid production. In contrast, ammonium toxicity can lead to alkalisation of the cultivation medium, as excessive ammonium uptake without sufficient counterbalancing anions such as nitrate results in proton exchange processes that increase the pH [45], [218]–[220], [222], [223], [226].

A common hallmark of plant cell stress is the accumulation of ROS, which serves as both a stress marker and a signalling molecule in plant defence mechanisms. ROS production increases under oxidative stress, drought, and exposure to pathogens, leading to potential oxidative damage if the antioxidant defence system is insufficient. The interplay between hormone regulation, gene expression, and metabolic adjustments determines how effectively the plant cell mitigates damage and adapts to stress conditions [45], [218], [219], [222], [225], [227].

A.5 Basic biology

The following section provides an overview of the biological fundamentals relevant to this thesis. It begins with a brief introduction to plant cell cultivations and their structural characteristics (appendix A.5.1). This is followed by appendix A.5.2, which explores plant roots, examined using the Root Chip. Next, an overview of fungi (appendix A.5.3) – an often overlooked but essential component of natural ecosystems – is presented. The chapter concludes with a summary and description of the model plants used in this research (BY-2 in appendix A.5.5 and *Arabidopsis thaliana* (*A. thaliana*) in appendix A.5.6).

A.5.1 Plant cells

Plant cell cultures are central to the analysis conducted using the MBR. The following section provides an overview of plant cell structure and function to establish a foundation for later design decisions and experiments. While plant cells exhibit considerable variability, fully differentiated cells share several essential characteristics. They contain distinct organelles that perform critical roles in metabolism, energy conversion, and structural integrity. Key components include the cell wall, vacuole, nucleus, mitochondria, plastids, and plasma membrane, each contributing to the cell's overall function and survival [47], [218], [222]. Figure A.8 displays this structure schematically.

The cell wall is the outermost structure of a plant cell, providing shape and mechanical protection. It functions as an exoskeleton, defining the cell's size, form, and mechanical properties [222]. Primarily composed of cellulose, the cell wall contains highly durable fibrils that are both flexible and resistant to tearing, ensuring structural integrity under various environmental conditions [230]. In addition to cellulose, the wall can undergo lignification, a process that caused cell death alongside with the deposition of lignin, converting the cell into a structural support element [218]. The mechanical properties of the cell wall allow it to stretch, accommodating changes in cell volume [230].

Beneath the cell wall, the plasma membrane (cell membrane) is a selectively permeable barrier that regulates material exchange between the cell and its environment [222], [230]. While water and small molecules diffuse freely, larger molecules and ions require translocators – specific transport proteins that facilitate controlled movement [222], [231]. Inside the membrane, the cytoplasm consists of the cytosol and a network of fibre proteins, including microtubules, which form the cytoskeleton. The cytoplasm hosts essential metabolic reactions and contains organelles such as mitochondria and plastids, which are crucial for cellular energy production and biosynthesis [218].

The nucleus, enclosed by a nuclear membrane, contains the cell's genetic material in the form of DNA organized into chromosomes [218], [222]. The nuclear pores facilitate controlled exchange between the nucleus and cytoplasm, allowing messenger RNA to exit for protein synthesis [218], [231]. The nucleus governs gene expression, protein synthesis, and DNA replication, playing a central role in cellular regulation and heredity [218].

Mitochondria, often referred to as the powerhouses of the cell, drive cellular respiration by converting chemical energy from nutrients into adenosine triphosphate via oxidative phosphorylation [218]. Mitochondria possess their own DNA and ribosomes, allowing them to replicate independently of the nucleus [230], [231]. This autonomy enables them to adapt to cellular energy demands by increasing their numbers as needed.

Plastids, including chloroplasts, play fundamental roles in photosynthesis. Chloroplasts capture solar energy and convert it into chemical energy stored as adenosine triphosphate, which is subsequently used to synthesize glucose [232]. This process occurs in the thylakoid membranes, which contain chlorophyll, the primary pigment responsible for light absorption.

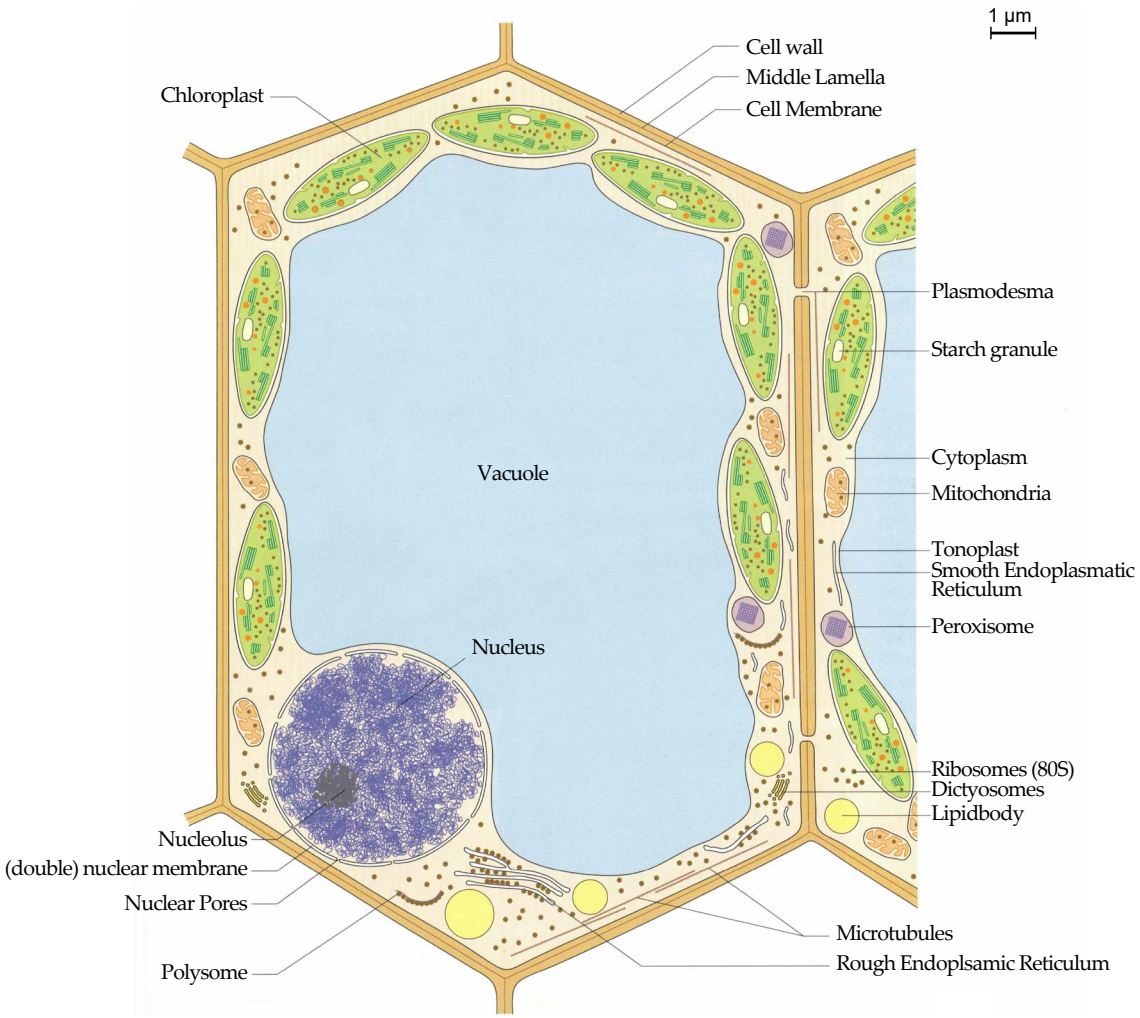

Figure A.8: Schematic illustration of a plant cell, specifically a mesophyll-cell. It can be seen clearly that the vacuole takes up the majority of the plant cell's volume. Since this is a mesophyll cell, which is the cell type located closest to the plant leaf's surface and thus, plays a key role in the photosynthesis process, only chloroplasts are displayed for the plastids category. Taken from [229] and translated to English.

In non-photosynthetic tissues such as roots, plastids differentiate into chromoplasts, which store pigments, or leucoplasts, which store starch [47], [231]. All plastids share common structural features, including a double membrane and the ability to self-replicate, similar to mitochondria [230].

The vacuole is a defining feature of plant cells, often occupying up to 90 % of the cell's volume in fully differentiated cells [230]. It is a fluid-filled compartment enclosed by the tonoplast, a membrane that controls the transport of ions and molecules between the vacuole and cytoplasm [233]. The vacuole maintains turgor pressure, which stabilizes the cell and supports the plant's overall structure by absorbing water [234]. Additionally, it serves as a storage reservoir for nutrients such as nitrate and phosphate, as well as for waste products and potentially harmful compounds [218], [231].

The Golgi apparatus is essential for protein modification and transport. It also plays a key role in cellulose synthesis, which is critical for cell wall formation [230]. The endoplasmic reticulum (ER) contributes to protein synthesis and calcium storage, with the rough ER (studded with ribosomes) functioning in protein translation, while the smooth ER is involved in lipid biosynthesis and detoxification [235].

Plasmodesmata (singular: plasmodesma) are microscopic channels that traverse the cell walls, linking the cytoplasm of adjacent cells and enabling intercellular communication and material transport [236]. These structures are vital for coordinating plant tissue functions, though they also serve as potential entry points for pathogens [237]. By facilitating direct cytoplasmic connectivity, plasmodesmata establish a symplastic transport network that allows water and solute movement throughout the plant [231].

In summary, plant cells are highly specialized, integrating various organelles to coordinate metabolic processes, energy production, structural support, and communication. The interactions between the cell wall, membrane, nucleus, mitochondria, plastids, vacuole, and other organelles enable plant cells to sustain life and adapt to environmental conditions efficiently.

A.5.2 Plant roots: Structure and basic functions

Plant roots, alongside the shoot system, constitute one of the two major tissue systems in plants. In this work, their growth behaviour was analysed using the RC. The following paragraphs provide an overview of these essential plant tissues to establish context for the application examples in chapter 5.

Roots fulfil three primary functions: anchoring the plant in the soil, absorbing water and nutrients, and storing products of photosynthesis. Their extensive branching and high surface area-to-volume ratio enable highly efficient water and nutrient uptake [45], [46], [221]. Additionally, roots engage in essential symbiotic interactions with microorganisms, which enhance nutrient acquisition and contribute to overall plant health [221], [238]–[241].

At the cellular level, roots are organised into distinct developmental zones, though their transitions are gradual [45], [221]. The root tip is protected by the root cap (calyptra), which serves two critical functions. First, it shields the delicate meristematic tissue at the tip by secreting mucilage, a lubricant that facilitates root penetration into the soil [47], [239]. Second, the root cap contains specialised statocyte cells, which detect gravitational forces via starch granules, enabling the root to orient itself through gravitropism [47], [242].

Directly behind the root cap lies the cell division zone, known as the Root Apical Meristem. This region consists of rapidly dividing initial cells, functionally similar to stem cells in animals. These cells divide at high rates, with division cycles ranging from 4 h to 12 h, depending on the plant species [45], [46], [220], [221]. Centrally located within the Root Apical Meristem is the quiescent centre, a group of cells that divide much more slowly, approximately every 170 h, depending on the species [46], [220]. This region is believed to act as a reservoir of initial cells and play a regulatory role in root growth [45], [46], [220]. Figure A.9 provides a schematic representation of these zones in relation to one another.

The newly formed cells differentiate into three primary tissue types. The protoderm develops into the epidermis, providing a protective outer layer. The ground meristem gives rise to the cortex, which serves as a storage site for nutrients. The procambium differentiates into vascular tissues, facilitating the transport of water and nutrients throughout the plant [45], [244].

Above the cell division zone lies the elongation zone, where newly formed cells expand, driving root growth by pushing the root tip forward. This region is crucial for increasing root length, and it is here that cells begin to specialise [45], [244]. Further up, the differentiation zone is where cells fully mature and assume their final functions. In this region, the xylem and phloem develop into the vascular system, which facilitates the transport of water, nutrients, and photosynthates throughout the plant [46], [47], [221]. The cortex also forms in this zone, serving as a storage site and regulating water and nutrient flow within the

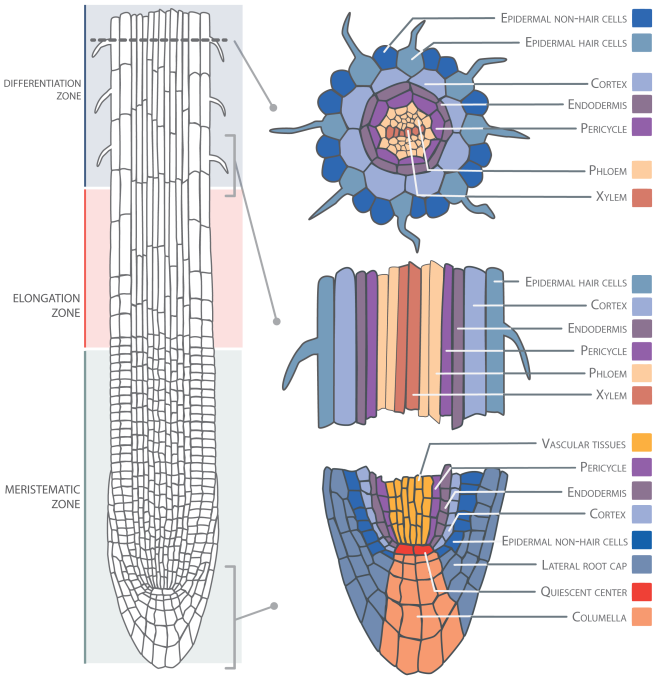

Figure A.9: Schematic illustration of an *A. thaliana* plant root. From [243]

root [220], [221], [242]. The outermost layer, the epidermis, gives rise to root hairs, which significantly enhance the root's surface area and efficiency in water absorption [46], [47].

Root tips play a crucial role in symbiotic interactions with soil fungi and bacteria. Approximately 95 % of plants establish mycorrhizal associations, in which fungal partners extend the root's absorptive capacity by facilitating access to essential nutrients, such as nitrogen and phosphorus, in exchange for carbohydrates from the plant [221], [238], [241]. Additionally, certain bacteria colonise plant roots and induce the formation of root nodules, where nitrogen fixation occurs, making atmospheric nitrogen bioavailable to the plant [47], [221], [238], [240]. These symbiotic relationships enhance nutrient acquisition and significantly improve plant adaptation to diverse environmental conditions [221], [222], [238].

A.5.3 Introduction on fungi

Fungi (Mycota) are a diverse kingdom, with forms ranging from unicellular to multicellular, and they play vital ecological roles in both terrestrial and aquatic ecosystems. Unlike plants, fungi lack the ability to perform photosynthesis, and their cell walls are composed of chitin rather than cellulose. Fungi are heterotrophic organisms, meaning they acquire nutrients by breaking down organic matter or living as parasites or symbionts with other organisms. They are one of the five major groups of Eukaryotes: the Amorphae. The other groups are: Plantae (plants), Chromalveolata, Rhizaria, and Excavata. Despite their morphological diversity, fungi generally do not form true tissues, distinguishing them from animals and plants [47], [245].

In terms of their evolutionary history, fungi were historically classified based on their reproductive structures and morphological characteristics, such as the types of spores they produce and their developmental cycles. However, advances in molecular biology, particularly DNA sequencing, have revolutionised fungal taxonomy. Modern classifications now rely on phylogenetic relationships, which reflect the evolutionary history of the species more accurately. This shift has led to significant changes in the understanding of fungal diversity [45], [245].

Fungi are broadly classified into the groups of slime moulds (Acrasiobionta and Myxobionta), Heterokontobionta (Oomycota – cellulose-based fungi), and Mycobionta (chitin-based fungi). The latter group is subdivided into five additional groups called: Chytridiomycota (chytrids), Zygomycota, Glomeromycota (arbuscular mycorrhizal fungi), Basidiomycota (club fungi), and Ascomycota (sac fungi) [45], [47], [221]. These divisions differ in their modes of reproduction, with some fungi producing spores asexually and others through sexual reproduction. Fungi are critical for nutrient cycling as decomposers, breaking down dead organic material and recycling nutrients back into the ecosystem. Additionally, they form important symbiotic relationships, such as mycorrhizae with plants, and contribute to human industries through fermentation and antibiotic production [46], [47], [245].

A key group for this thesis is the Ascomycota, commonly referred to as sac fungi. Because the target fungi of this thesis *N. parvum* (see appendix A.5.7 is part of this group, it will be introduced in more detail: Ascomycota are characterised by their production of sexual spores within a specialised sac-like structure called an ascus, from which they derive their name. These fungi are a highly diverse group, containing both unicellular yeasts and complex multicellular fungi that form fleshy fruiting bodies, such as morels and truffles [45], [221], [245]. The majority of Ascomycota exhibit septate hyphae, which are thread-like structures that form the vegetative body of the fungus. The hyphae are divided by cross-walls, known as septa, that allow the flow of cytoplasm and organelles between compartments [45], [47].

Ascomycota are ecologically significant, inhabiting a wide range of environments, including terrestrial, freshwater, and marine ecosystems. They act as decomposers, pathogens, and symbionts. Notably, many Ascomycota species engage in mutualistic relationships with plants, forming lichens or ectomycorrhizal associations that are essential for plant nutrition. Additionally, several Ascomycota species are notable plant pathogens, such as those causing powdery mildew and Dutch elm disease. Approximately 60,000 species of Ascomycota have been described, making them one of the most diverse fungal groups [47], [240], [245].

A.5.4 Model organisms in plant sciences

Within the scope of this thesis, several experiments using plant cells or seedlings were conducted. In the following, they are briefly introduced. As this work focuses on the microsystems and manufacturing aspects, the according model organisms are introduced only as far as it is necessary for a solid understanding of text and conducted experiments.

A.5.5 BY-2 cells

Nicotiana tabacum (N. tabacum) is a widely known model plant [246], [247]. If an introductory book on biology is opened, it is likely that one will find pictures of *N. tabacum*-cells in there, for example in [46], [219]–[222], [228], [240]. According to publications, the line was created from a *N. tabacum* seedling which was put on a callus-inductive agar medium [248]. After subcultivation in callus-form, it was carried over into a liquid culture and further refined. From there, several Bright Yellow cultivars (no. 1 – 4) were bred. BY-2 was distributed in the beginning partly officially, but as well partly secretly because Japan Tobacco & Salt Monopoly Public Corp., the company that created the cell lines, pursued them as a filler material for cigarette production. However, this did not work out [249]. Meanwhile, BY-2-cells show a very high synchrony (up to 95 %), and – if maintained properly – can be recultivated with only 2 % of inoculum volume in fresh medium once a week [246], [249]. Today, BY-2 is a prominent model organism in plant cell research and work on its basis has been published countless times [247], [249], [250]. In this thesis, BY-2-cells were used for experiments in the MBR. Further information can be found in chapter 5.

A.5.6 Arabidopsis thaliana

A. thaliana is the model plant used in this thesis for testing the functionality of the Root Chip. In addition, it was used to run experiments in the Root Chip, e.g. concerning root growth under drought conditions. *A. thaliana* is a small weed (see figure A.10 for a depiction), and its plant genome is one of the genomes completely sequenced so far [222], [240], [251], [252]. Due to several of its attributes, this plant is especially suitable, to be a model plant. The most important of these characteristics are:

- The comparably small genome: As mentioned, *A. thaliana* has a small, relatively small genome with 25,706 genes comprised out of five chromosomes. The genome is one of the shortest in plants and has been completely sequenced [222], [240], [251], [252].
- Known mutations: Because *A. thaliana* self-fertilises, new homozygous mutants of the plant can be created well and be reproduced easily. Due to this, large collections of well-documented mutants are available to researchers [240], [251], [252].
- The small size: *A. thaliana* reaches a height of about 40 cm to 60 cm when fully grown. It is one of the smaller plants displaying all parts of higher plants like shoot, leaves, flowers, fruits, and seeds. Due to its small growth, it is suitable for lab cultivation [240], [251], [252].
- The short generation time: Within six weeks *A. thaliana* undergoes all passages of a plant from germination via a vegetative state all the way to the reproductive phase [240], [251], [252].
- Its robust nature: In nature *A. thaliana* is found growing in harsh conditions. Because of this, *A. thaliana* can adapt to not ideal growth conditions, which makes it easier to cultivate in labs [240], [251], [252].

For these reasons, *A. thaliana* is so well suited as a model plant.

Figure A.10: Full grown *Arabidopsis thaliana*. Leaves, shoot, and flowers are well distinguishable [251]

.

A.5.7 Neofusicoccum parvum

N. parvum is a fungus of the division Ascomycota and belongs to the family Botryosphaeriaceae. Due to climate change and the resulting more extreme weather conditions like heat or drought, the economic impact of *N. parvum* has risen. This is because it is one of the known agents of Grapevine Trunk Disease, which in turn can significantly affect viticulture [253], [254]. *N. parvum* primarily inhabits the grapevine (*Vitis vinifera*) as an endophyte, residing within the plant tissues without causing immediate significant harm [255]. However, *N. parvum* can switch from a benign to a pathogenic state under certain conditions, such as environmental stress or physical damage to the plant, particularly drought or heat. This switch is triggered by the accumulation of certain compounds in the grapevine, such as trans-ferulic acid, which acts as a stress signal to the fungus. In response, *N. parvum* produces the phytotoxin fusicoccin A, which accelerates the death of host tissue, enabling the fungus to complete its life cycle by producing spores for dispersal [256].

A.6 Sensor systems

The following two chapters outline the methodologies for measuring the two stress indicators investigated in the proof-of-concept experiments conducted in the MBR. Appendix A.6.1 discusses optical techniques for pH measurement, while appendix A.6.2 focuses on the detection of H_2O_2 in plant cell cultivations. These sections align with the corresponding proof-of-concept application chapters: 5.1.3 for pH measurement and 5.1.4 for the quantification of ROS, specifically H_2O_2.

A.6.1 Optical measurement of pH

As established in appendix A.4, pH fluctuations are a key indicator of cultivation conditions. While glass pH electrodes remain the gold standard for pH measurement [257], their invasive nature can disrupt or influence the cultivation process [258]. To facilitate the analysis of communication between plants and their aggressors in the MBR, it is essential to employ minimally invasive techniques, such as optical pH sensing. Furthermore, real-time monitoring is crucial for establishing causal relationships in plant cell cultivations [258] and is particularly relevant within the MBR. The integration of an optical pH readout into the MBR is detailed in 5.1.3. The following section provides an overview of the fundamentals of optical pH measurement in this context.

The fundamental distinction between potentiometric and optical pH measurement techniques is in their underlying principles. Potentiometric methods rely on the activity of hydrogen ions, whereas optical methods determine the concentration of a dye species that correlates with pH [257]–[259]. Consequently, potentiometric measurements align more closely with the mathematical definition of pH, introduced by Sørensen in 1909 as the negative logarithm of the hydrogen ion concentration: $pH = -\log[H+]$ [260]. In contrast, optical chemical sensors function by allowing the sensor material to chemically equilibrate with the local pH of the sample, after which the resulting reaction is read optically [257]–[259].

To ensure their effective application, the limitations of optical pH sensors must be carefully considered. These include their restricted measurement range – many sensors are limited to approximately three pH units – their slower response time, which results from the necessary phase change between the aqueous indicator dye and the solid phase of the probe, as well as potential interferences from ambient light or photobleaching [257]–[259], [261]. However, optical pH measurement offers significant advantages, including a wide variety of implementable probe sizes –ranging from planar, film- or foil-based sensors to fibre-optic devices with reported tip sizes between 1 mm and less than 50 µm – and even

nanoparticle-based configurations. Additionally, optical methods enable the separation of the probe and the sensor (i.e., the readout system), which minimises interference with the sample, while also providing electrical isolation and chemical inertness [257]–[259], [262]–[266].

A variety of methods are employed for optically analysing pH changes, including absorptiometry, luminescence-based sensing, refractive index-based approaches, photonic crystal-based sensing, infrared and Raman spectroscopy, and interferometric sensing. Among these, luminescence-based techniques – particularly fluorescence-based methods – are among the most widely applied. This category can be further subdivided based on the applied readout mechanism, including luminescence intensity analysis, luminescence decay time measurement, Förster resonance energy transfer (FRET), quenching, and dual-lifetime referencing (DLR). The latter involves comparing the fluorescence lifetimes of a reference fluorophore, which remains inert to pH variations, with those of a pH-sensitive fluorophore [258], [267]–[273]. Overall, the extensive range of optical pH-sensing techniques, particularly those based on luminescence, underscores their versatility and precision, making them indispensable across various scientific and industrial applications.

A.6.2 ROS: Measuring H_2O_2 in plant cells

For a proof-of-concept experiment, H_2O_2 concentrations in plant cell cultivations were measured within the MBR. Details of this experiment are provided in 5.1.4. The following section introduces ROS measurement principles, highlighting key approaches and challenges for better understanding of the later work.

ROS are partially reduced derivatives of molecular oxygen, generated as by-products of aerobic metabolism in plant cells. While excessive ROS accumulation can be damaging, these molecules play essential roles in cellular signalling, stress response, and metabolic regulation [274]–[277]. They are involved in key physiological processes, including cell proliferation, differentiation, programmed cell death, and defence mechanisms against environmental stressors such as pathogen attacks, drought, and extreme temperatures [276], [278], [279].

Among the different ROS, hydrogen peroxide (H_2O_2), superoxide anion (O_2^-), hydroxyl radicals ($^{\cdot}OH$), and singlet oxygen ($^1O_2$) are the most significant [275]–[277]. Each exhibits distinct chemical properties and reactivity, with H_2O_2 being particularly important due to its stability and role as a diffusible signalling molecule [274], [275], [280]. While uncontrolled ROS accumulation leads to oxidative stress and cellular damage, controlled ROS production is essential for cellular communication and adaptation to environmental changes [276]–[279].

Detecting and quantifying ROS in plant cells is inherently challenging due to their high reactivity and short lifespan [274], [275], [277], [278]. Several analytical techniques have been developed, including fluorescence-based detection, electrochemical sensors, chemiluminescence, and electron paramagnetic resonance spectroscopy [274], [275], [277], [280].

Fluorescent and luminescent probes, particularly those utilising metal-coordinated systems, offer enhanced specificity for ROS detection in biological samples [279], [280]. Further advancements, such as genetically encoded ROS reporters and nanoparticle-based sensing technologies, have improved the precision of ROS measurements, allowing for real-time intracellular tracking [274], [275], [277].

Among the various ROS, H_2O_2 is the most frequently measured due to its relatively long half-life and central role in redox signalling [274]–[278]. Electrochemical sensors have proven highly effective for H_2O_2 quantification, offering high sensitivity, rapid response times, and real-time monitoring capabilities [275], [277], [280]–[283]. The integration of

microfluidic systems with electrochemical detection has further enhanced precision in H_2O_2 measurements within plant tissues [275], [277], [281], [282].

While H_2O_2 is commonly measured due to its stability, more reactive species, such as hydroxyl radicals ($^{\cdot}OH$) and singlet oxygen ($^1O_2$), remain critical in oxidative stress research. However, their detection is significantly more complex, often requiring indirect measurement techniques [277], [280], [283].

In conclusion, ROS are central regulators of plant physiology, balancing between beneficial signalling roles and detrimental oxidative stress effects. Advances in ROS detection technologies continue to refine measurement accuracy, particularly for H_2O_2, offering deeper insights into plant responses to environmental challenges [275]–[277], [279].

B Historical overview of publications on MFCs for plant related research

In the following paragraphs, key publications in the field of microfluidic chips (MFC) for plant research are presented in greater detail. These publications – which supplement the information in section 2.1 – are organised chronologically, with each paragraph indicating the corresponding subtopic: cultivation setups, cell fusion, single-cell analysis, pollen tube analysis, phloem analysis, droplet-based analysis, or fungi cultivation. Publications on MFCs related to plant root analysis are summarized separately in appendix C due to their distinct relevance to the development of the RC. For further details, see chapter 4. Figure B.1 provides a historical overview of the field. While numerous other publications on plant-related research in Microfluidic Bioreactors exist, this selection offers a comprehensive overview, ensuring conciseness while maintaining depth.

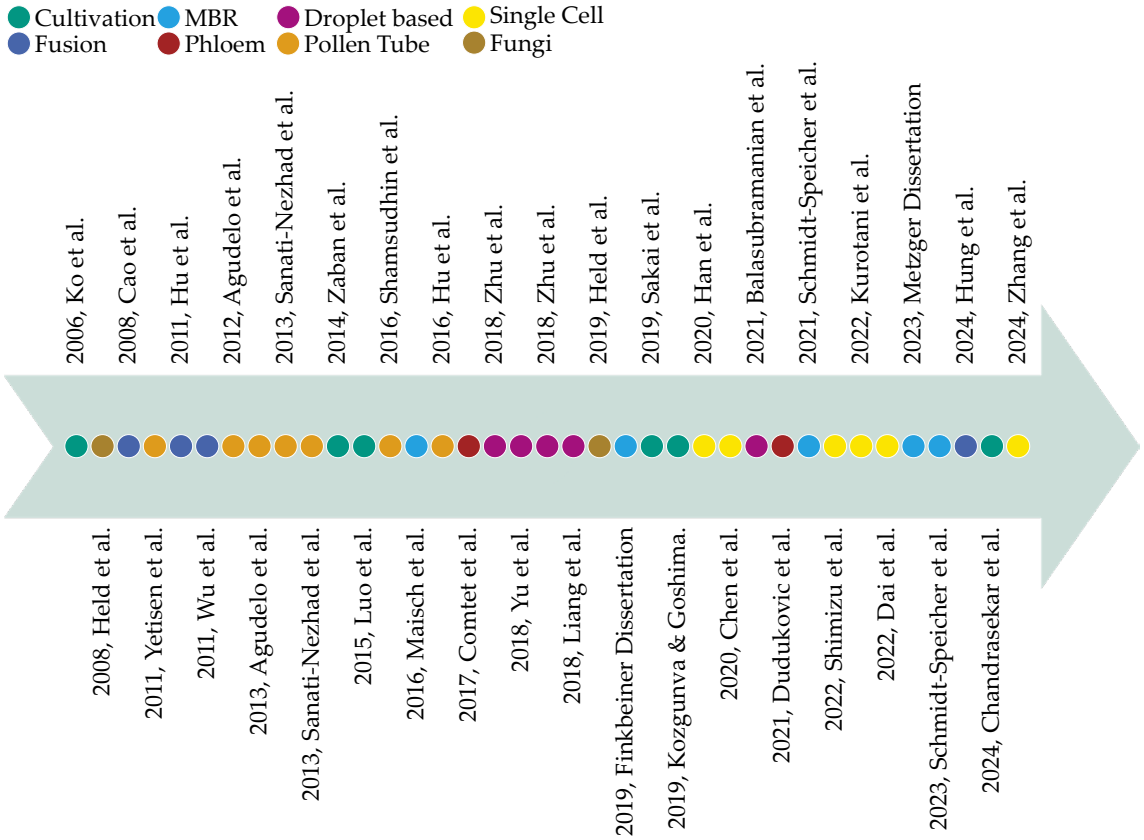

Figure B.1: Overview of literature in the field of MFC for plant-related research (except plant root analysis setups). The development of MFCs supporting plant studies began approximately two decades ago with a proof-of-concept paper by Ko *et al.* [15], demonstrating that plant protoplasts can be successfully cultivated in a microfluidic setup.

In May 2006, Ko *et al.* [15] published their baseline paper, introducing the first MFC designed for cultivating plant protoplasts. The chip featured a cultivation channel where a comb of micropillars retained the flushed-in *N. tabacum* protoplasts while the channel was continuously perfused with nutritional medium throughout the experiment (see figure B.2). The channel measured 1 mm in width and 100 µm in height, with 12 µm-wide gaps between the pillar combs. Fabrication was carried out using the standard soft-lithography process, where PDMS-casts of the channel structures were plasma-bonded to glass slides, sealing the channels (see appendices A.2.2 and A.3.1). As a proof-of-concept experiment, the authors cultivated *N. tabacum* protoplasts in the chip for up to four weeks, assessed their viability, and found it to be high [15].

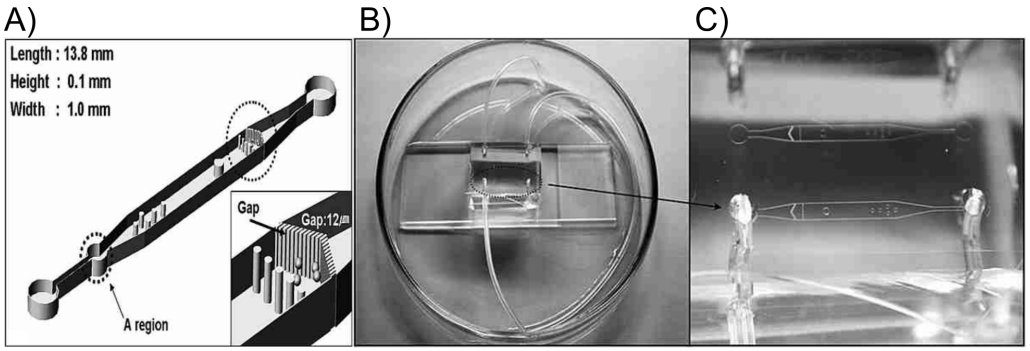

Figure B.2: A) Design concept of the MFC for protoplast cultivation. The protoplasts are flushed in from the left side and are kept from flowing through the setup by the comb-structure out of pillars. **B)** Photograph of the finished MFC kept in a petri-dish to maintain outside influences low. **C)** Zoomed in picture of the observation channel for the protoplast-cultivation. Adapted from [15].

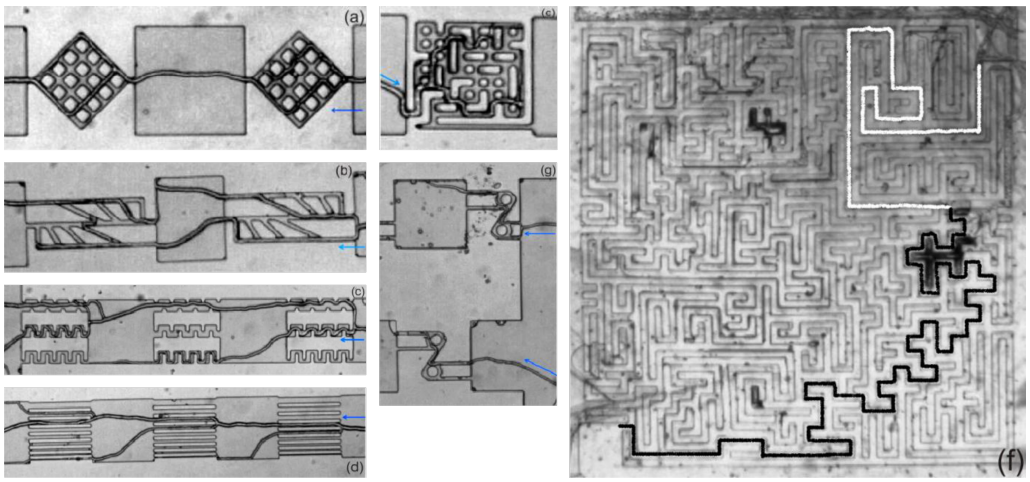

Figure B.3: Mazelike structures for analysing fungi hyphae growth behaviour. Blue arrows indicate the initial growth direction. Realized structures were a (a) diamond, (b) cellular, (c) comb, (d) stripes, (e) small maze, (f) big maze (white line shows how far the hyphae explored the black-lined solution path), (g) roundabout structure. Presented by [16]

In February 2008, Held, Edwards and Nicolau [16] introduced microfluidic setups for fungi cultivation, demonstrating the feasibility of fungi cultivation in such systems, which is relevant to this thesis. Their publication served as both a baseline paper, as it presented a novel MFC design, and an application paper, as biological experiments were a key focus. The study featured seven maze-like microfluidic structures – diamond, cellular, comb, stripes, small maze, big maze, and roundabout (see figure B.3) – which were replicated from moulds into PDMS using soft lithography and sealed with a plain PDMS-slip. The setups facilitated the cultivation and continuous microscopic analysis of *N. crassa*, a filamentous red bread mould. The authors investigated fungal growth patterns, including branch formation, factors influencing branching behaviour, and the extent to which a single hypha could grow along a channel, thus indicating how far the colony could support exploratory hyphae. They observed that the fungus displayed a strong memory of its initial growth direction, reverting to it after manoeuvring around obstacles. Additionally, they found that hyphae typically adhered to one side of the channel walls while branching on the opposite side and that fungal growth favoured edges and corners, potentially using them as guides [16].

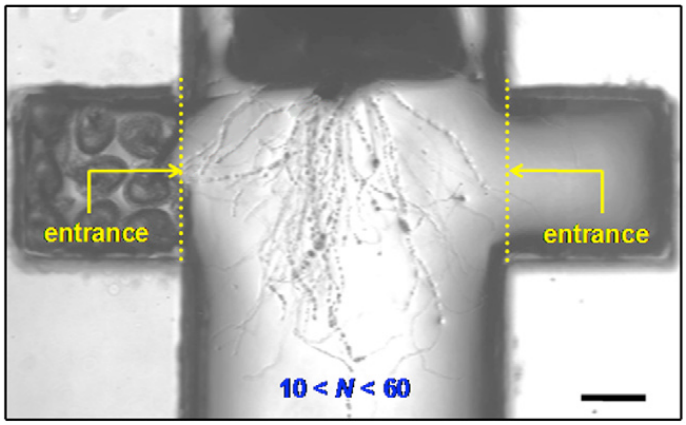

Figure B.4: Pollen tubes clearly favour the chamber full of unfertilised ovules over the empty chamber by growing pre-dominantly in the direction of the full chamber. Scale bar, 200 µm. Adapted from [18].

In April 2008, Cao *et al.* [17] published their baseline paper on electrofusion of protoplasts. Electric fusion setups benefit from MFCs due to the short distance between counter-electrodes, because smaller electrode gaps require lower voltages to generate the necessary pulses. The fusion process consists of two steps: first, a low-amplitude high-frequency alternating current field positions the individual cells for fusion; then, short high-strength pulses induce fusion by electroporating the cell membranes. The authors designed an MFC containing six microchambers, each equipped with 228 microelectrode pairs arranged in different configurations (see figure B.5A). Electrode spacing varied across microchambers from 50 µm to 100 µm in 10 µm increments, allowing for compatibility with different cell sizes. Fabrication involved sequential etching and oxidation of a silicon wafer, followed by deposition and etching of Ti and Au electrodes. The channels were sealed by plasma bonding a plain PDMS-slab with inlets and outlets for fluid handling. As a proof of concept, the authors tested the alignment and fusion of cucumber mesophyll protoplasts, yeast cells, pigeon red blood cells, and human embryonic kidney cells (HEK-293) cells, with the cucumber protoplast experiments being the most detailed. They found that while cell alignment functioned effectively, fusion efficiency depended on a balance between pulse strength, fusion rate, and cell viability, low pulse strengths failed to perforate membranes sufficiently, while excessive pulses compromised cell viability [17].

In April 2011, Yetisen *et al.* [18] introduced the first microdevice designed to monitor the growth behaviour of *A. thaliana* pollen tubes in the presence of fertilised and unfertilised ovules. The authors developed a PDMS-based device featuring a main channel connected to side chambers and sealed with a plasma-bonded glass slide. The chambers were filled with pollen growth medium, and a pistil with pollinated pollen tubes was placed at the centre of the main channel. Growth patterns were analysed by comparing pollen tube responses when the side chambers contained unfertilised ovules versus when they were empty. As shown in figure B.4, pollen tubes preferentially grew toward unfertilised ovules, whereas no specific directional growth was observed when both chambers were either empty or contained unfertilised ovules. While the authors did not analyse the specific chemoattractants responsible for directing pollen tube growth, they concluded that their microdevice provided a more controlled and suitable environment for such studies than conventional petri-dish-based methods [18].

Hu *et al.* [19] built on the work of Cao *et al.* [17] and presented their updated work on fusing cells like mammal cells or protoplasts in microfluidic setups in 2011. Instead of a serpentine microchannel – which caused cells to accumulate at the turns, causing malfunctions in the fusion process [17] –, the authors applied a straight channel design with protruding

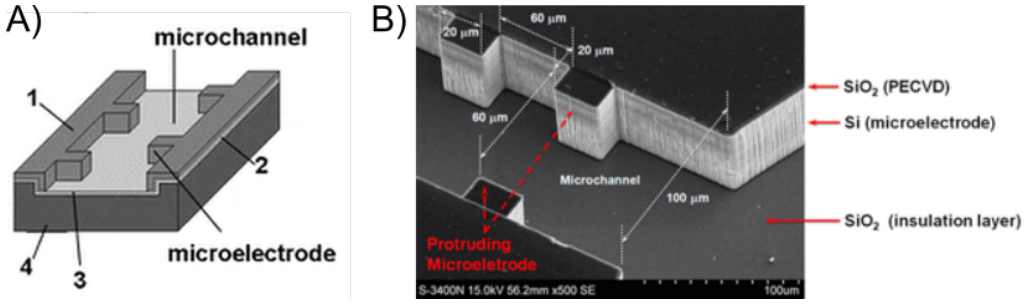

Figure B.5: Setup of microchannels with protruding microelectrodes for protoplast fusion. **A)** Concept sketch of microchannel with protruding microelectrodes arranged in a serpentine layout. Adapted from [17]. **B)** scanning electron microscopy-recording of the microchannel with evenly paired micro-electrodes as presented by Hu *et al.* [19]. Adapted from [19].

electrode pairs (see figure B.5B). Furthermore, the authors now chose a fixed distance of 60 µm between the counter-electrodes. To test the average fusion efficiency HEK-293 as well as tobacco protoplasts were fused in the created device. In addition, the authors simulated the influence of a continuous Al film along the bottom of fusion channel. They found that such a conductive film enhanced the consistency of the electric field during the positioning and fusion phase and that it would be recommendable to install one in the future. Overall, a fusion efficiency of 33.3 % (HEK-293-cells) and 41.7 % (tobacco protoplasts) was reached in the experiments. [19]

In October of 2011, Wu *et al.* [20] presented their work on chemically induced protoplast fusion in a microfluidic device. This is a baseline-paper because a new MFC design was presented: The device was set up with five individual culture channels originating in a single central sample input. Each channel was equipped with a micro-column array (columns spaced 20 µm apart) to trap the oncoming tobacco mesophyll protoplasts [20]. Using polyethylene glycol, which can cause pore formation in membranes, thus facilitating the fusion of cells [284], the authors induced the fusion of the trapped protoplasts. In addition, the fusion efficiency was calculated to be 28.8 % in 3-5 min [20]. That is much higher than the efficiency of the traditional polyethylene glycol-induced approach, which was about 5 % at that time [285]. To proof the suitability for cultivating and fusing protoplasts of their microfluidic setup, the authors analysed the viability of the newly created protoplasts and found it to be well [20].

In September 2012, Agudelo *et al.* [21] introduced a microfluidic platform for studying pollen tube growth behaviour in response to mechanical obstacles (see figure B.6A). This baseline paper demonstrated that the observed growth behaviour closely resembled previous in vitro studies, with pollen tubes achieving total lengths exceeding 1 mm to reach pollen grains for germination [21].

In March 2013, Agudelo *et al.* [286] published their TipChip platform (see figure B.6B), a microfluidic device designed for cultivating pollen tubes, filamentous yeast, and fungal hyphae to analyse their growth behaviour. Building on their previous work [21], the authors demonstrated that pollen tubes do not exhibit directional memory, once diverted from their initial growth direction, they are unable to revert. Furthermore, the TipChip experiments revealed that pollen tubes could grow in and through air, suggesting a greater flexibility in water uptake than previously assumed [286]. As the primary focus of this study was biological experimentation, it is classified as an application paper.

In May 2013, Sanati Nezhad *et al.* [43] expanded on pollen tube studies by investigating their ability to exert penetrative force and pass through microscopic openings cast from PDMS. They observed that, where possible, an elastic opening was forced open to allow

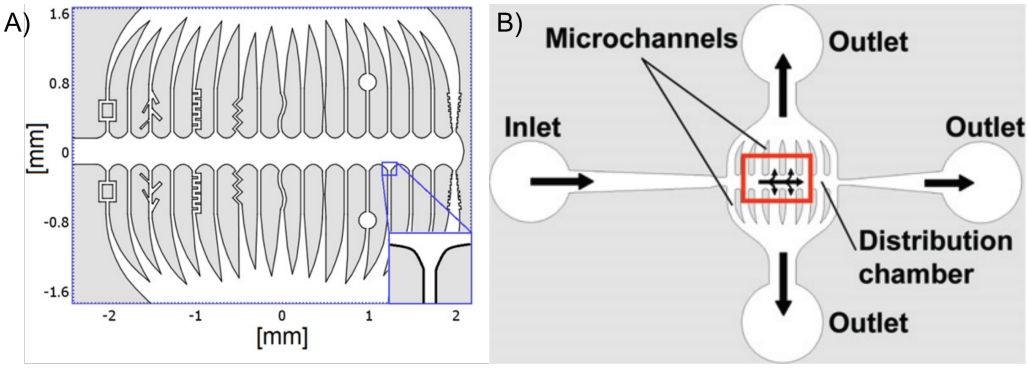

Figure B.6: A) Obstacle course for pollen tubes. The study provided deeper insights into how a pollen grain can attract the growth of a pollen tube, even when confronted with obstacles such as labyrinth-like deflections or extremely narrow channels. Adapted from [21]. **B)** Concept of the TipChip by Agudelo *et al.* [286]. The microfluidic chip was designed similarly to other chips of that time, with perfusion from inlet to outlet (left to right). The obstacle course for the pollen tubes was positioned at the centre of the chip. Adapted from [286].

passage. When this was not feasible, the pollen tube adapted by reducing its diameter to squeeze through the gap. If the opening was too small, the tube was unable to pass [43].

In September 2013, Sanati Nezhad *et al.* [287] introduced an optimised method for evenly distributing pollen grains at the openings of eight individual side channels within an observation chamber. Their improvements addressed limitations in earlier designs, such as those by Agudelo *et al.* [21] and Agudelo *et al.* [286], where pollen grains were simply flushed into the main channel and often accumulated at one end. Sanati Nezhad *et al.* [287] demonstrated that their approach enabled the reproducible positioning of single pollen grains. The manufacturing process remained unchanged, using a PDMS-cast plasma-bonded to a glass slide [287]. As this study primarily introduced design modifications, it is considered a baseline paper.

In July 2014, Zaban *et al.* [22] published a baseline paper showcasing an MFC for orienting plant cells along a specific axis. Notably, this was the first instance in which entire plant cells were cultivated in an MFC, rather than protoplasts, which are easier to handle. The authors designed a PDMS-cast featuring a main channel with embedded microvessels (72.8 µm by 52.5 µm, see figure B.7), which was plasma-bonded to a glass slide. Initially, the outer cell wall was lysed to generate protoplasts, which were then introduced into the microvessels (one per vessel). After approximately one day, the protoplasts aligned their axes with the rectangular microvessels. Auxin – a phytohormone that triggers primary cell wall (PCW) regeneration – was then introduced from one side of the MFC, prompting the protoplasts to regenerate their cell walls while maintaining their aligned orientation. The feasibility of the chip was demonstrated through the successful cultivation of BY-2 plant cells [22].

In August 2015, Luo *et al.* [37] presented their baseline paper on cultivating plant cells on shear-spun fibrous scaffolds composed of PLA- and PET-fibres (see figure B.8). The study aimed to assess whether plant cells could adapt to this unconventional environment. The authors found that cells previously cultured in liquid media successfully adapted to the scaffold, exhibiting novel, previously undocumented morphologies, such as double-spiral growth around a filament and polygonal cell shapes conforming to the spaces between fibres [37].

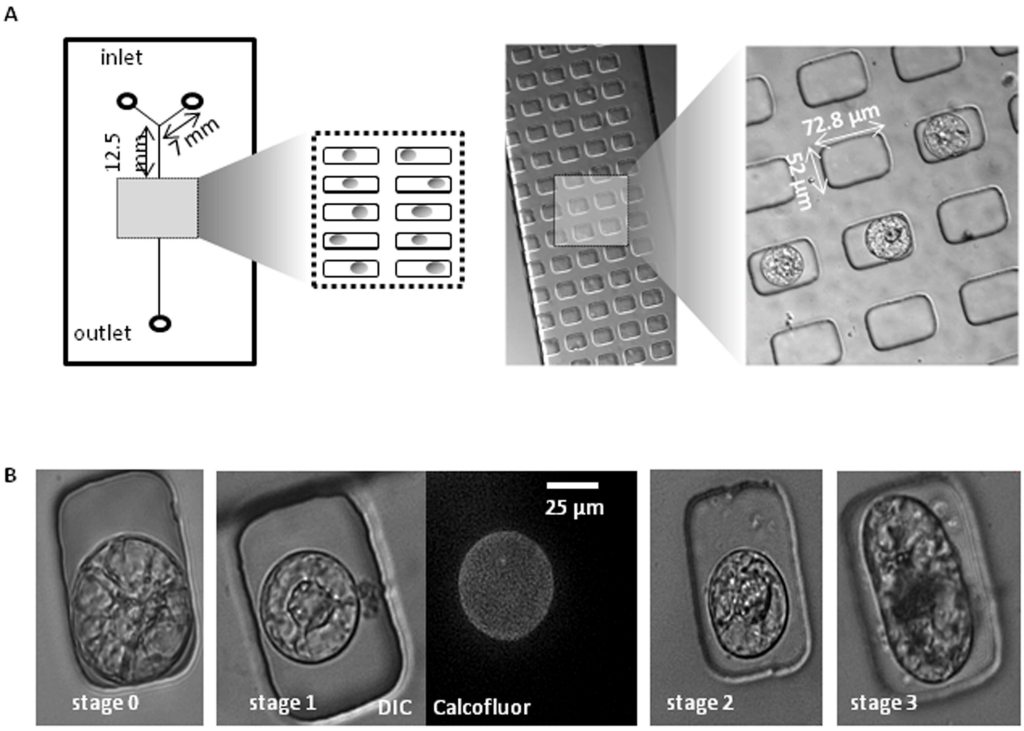

Figure B.7: A) Setup of the MFC for plant cell cultivation and cell axes orientation. **B)** Stages of the protoplast orientation and cell wall regeneration. Stage 0 shows the initial stage after the protoplast was flushed into the microvessel. Stage 1 depicts the protoplast after the initial orientation phase, when a cellulosic wall has formed again. This happens after about 1 day of cultivation. Stage 2 features the the plant cell with a manifested cell axis after two days of cultivation. Stage 3 shows the cell expansion after three days of cultivation along the newly positioned cell axis. Adapted from [22].

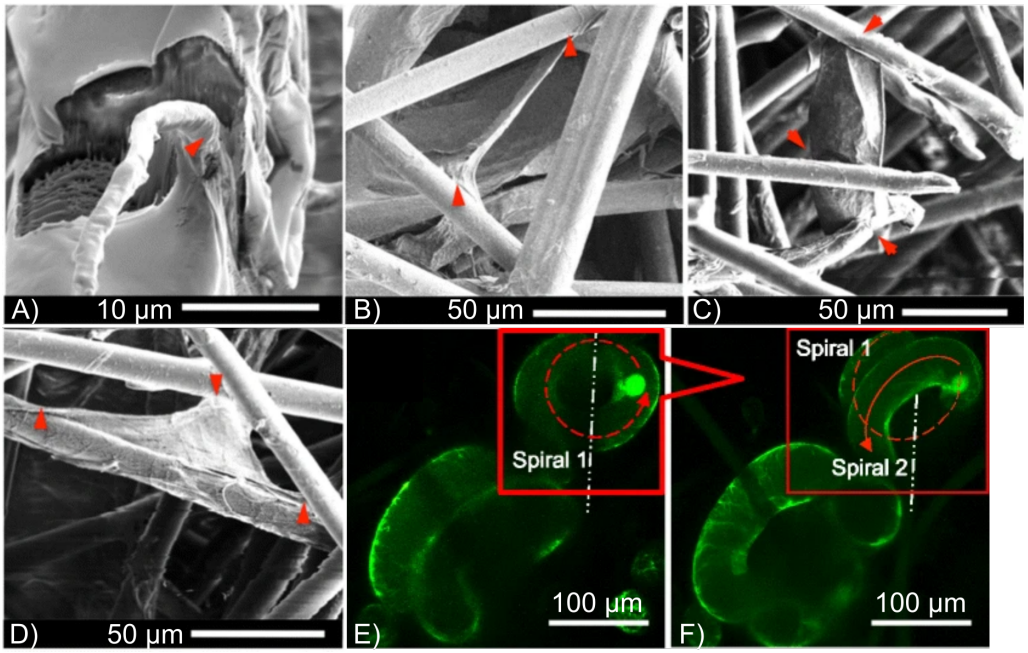

Figure B.8: Plant cells cultivated on shear-spun scaffolding. The red arrows show spots were the plant cells attached to the scaffolding. Picture **E)** and **F)** show the same plant cell spiralling twice around a fibre whose axis is marked by the dotted line. Adapted from [37]

In August of 2016 Shamsudhin *et al.* [40] published their baseline-work on a microfluidic device with which the cell wall and its mechanical properties could be analysed. For this, they mounted a tip with a tip diameter of 800 nm (Picoprobe® tungsten probe tip) onto a micro electro mechanical system force sensor (FT-S100, FemtoTools AG, Switzerland). The tip was positioned through a 3-axis piezo-positioner above a pollen tube guided within an MFC and micro-identations could be created through engaging the tip with the pollen tube. The resulting behaviour was analysed via measuring the stiffness fed back by the actuator as well as fluorescent and brightfield microscopy. In a proof-of-concept test, the authors showed that they could cultivate pollen tubes and pollen grains of Easter lily in their MFCs and investigate the growth behaviour via microscopy and stiffness measuring [40].

In August 2016, Maisch *et al.* [38] introduced a baseline paper that laid the foundation for the MBR developed in this thesis. The MFC design was adapted from a stem cell cultivation setup developed by Kreppenhofer [13]. Unlike most MFCs, which are fabricated from PDMS, this device was manufactured from PC via hot embossing and sealed using thermal bonding. The design featured a main chamber divided by an ion track-etched PC membrane, with the upper chamber designated for plant cell cultivation and the lower chamber facilitating nutrient perfusion (see figure B.9). Following Zaban *et al.* [22], this study was only the second to cultivate whole plant cells in an MFC. As a proof of concept, BY-2 cells were cultured in the device for up to seven days. The authors assessed cell viability, mitotic index, and division synchrony, while also collecting and analysing perfusate samples using nuclear magnetic resonance spectroscopy. They reported high viability, stable mitotic indices, and synchronised cell division, with nuclear magnetic resonance analysis providing metabolic insights over time [38].

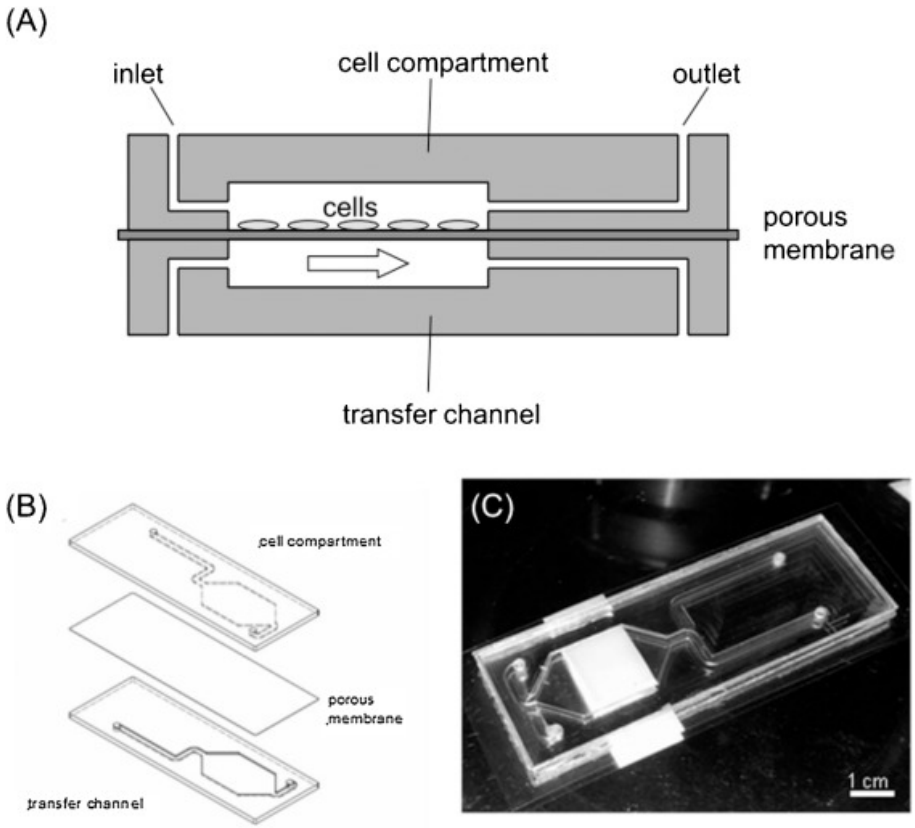

Figure B.9: Baseline paper for MBR development. **A)** Schematic sketch of the MFC for cultivating plant cells. **B)** Individual layers of the MFC for plant cell cultivation. **C)** The finished MFC for plant cell cultivation. It is manufactured from PC via hot embossing and sealed via thermal bonding. Adapted from [38].

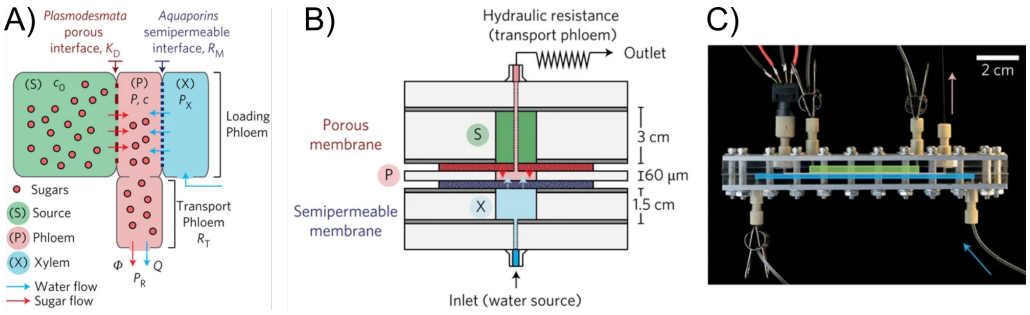

Figure B.10: Tree-on-a-chip: **A)** Schematic model of the tree-on-a-chip showing the passive transportation of sugars and water through the phloem (red) and xylem (blue). The source compartment is marked in green. **B)** Conceptual design of the tree-on-a-chip setup. **C)** Photograph of the tree-on-a-chip. Adapted from [39].

In November 2016, Hu *et al.* [44] introduced a system for measuring the biomechanical properties of *Lilium longiflorum* (lily) in a baseline-paper. Their MFC incorporated a soft membrane to apply a preset load on in-chip cultivated pollen tubes. Combined with the inherent turgor pressure, the authors found that pollen tube wall stiffness significantly decreased with increasing initial diameter, supporting the broader observation that wall stiffness and turgor pressure are intrinsically linked. The chip layers were fabricated from PDMS and bonded using oxygen plasma treatment [44].

In March 2017, Comtet *et al.* [39] presented a baseline paper introducing a tree-on-a-chip setup to investigate phloem loading mechanics. Their microfluidic device was constructed from soft polyvinyl chloride, PET, and acrylic sheets, sandwiched between aluminium plates and held together by screws. The chip featured a main channel mimicking the phloem, separated by a porous membrane on one side and a semipermeable membrane on the other, replicating the xylem (see figure B.10). With this setup – capable of withstanding pressures up to 1 MPa – the authors analysed passive phloem loading via osmosis. Their experiments demonstrated how sugar and water transport could be studied across different plant sizes, and in a proof of concept, they successfully examined the fundamental principles of passive phloem loading and long-distance transport in plants [39].

In 2018, Zhu *et al.* [33] introduced their nano-droplet microfluidic chip, nanoPOTS. The chip was fabricated from multiple patterned and photolithographically processed glass slides (see figure B.11). Hydrophilic pedestals were designed on an otherwise hydrophobic surface to act as sample vessels, with nano-droplets (200 µL or smaller) deposited via a robotic system. Following deposition, standard microscopy was used to determine parameters such as cell count and dimensions, followed by a multi-step protocol (see figure B.11). In a proof-of-concept study, the authors demonstrated that with only ten cells per droplet, approximately 1,500 proteins could be identified. When the Match Between Runs algorithm (MaxQuant [288]) was applied, this number increased to approximately 3,000 proteins per ten-cell droplet [33].

In May 2018, Yu *et al.* [23] published a baseline paper presenting a droplet-based microfluidic platform. The chip was fabricated from a PDMS-cast plasma-bonded onto a glass slide, with the mould created via a standard SU-8-based soft lithography process. The chip featured a flow-focusing microfluidic design (see figure B.12A) that enabled the encapsulation of individual protoplasts within fluorinated carrier oil droplets. These droplets could then be sorted using electrodes (see concept in figure B.12B). As a proof of concept, the authors demonstrated high-throughput *Marchantia polymorpha* protoplast encapsulation and sorting at rates exceeding 100,000 protoplasts per hour.

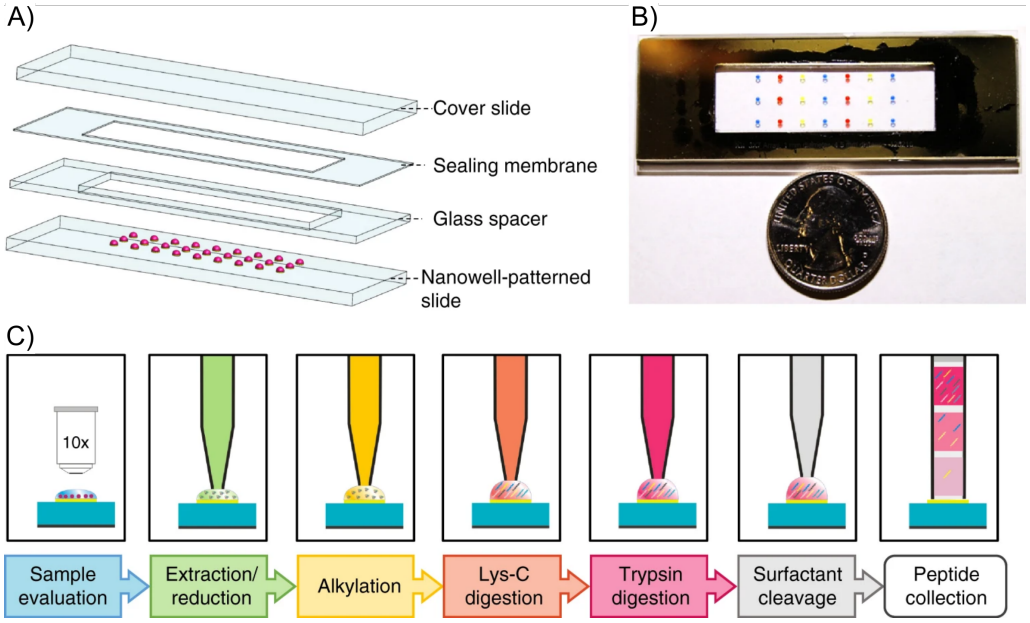

Figure B.11: Nano-droplet microfluidic chip: nanodroplet processing in one pot for trace samples.**A)** The individual layers of the nanoPOTS-setup in a concept-sketch. **B)** Picture of the nanoPOTS next to an U.S. Quarter for size. **C)** Seven step protocol conducted on the nanoPOTS. Adapted from [33].

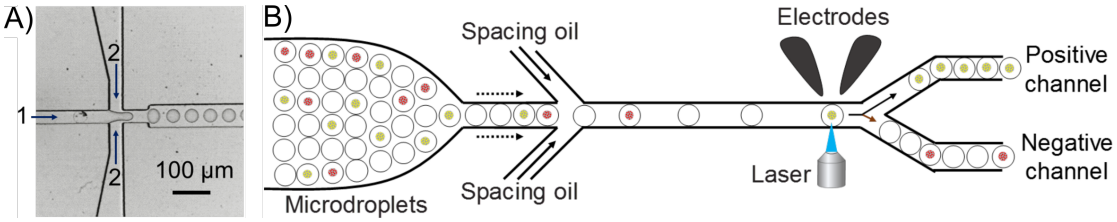

Figure B.12: Baseline paper of a droplet-based microfluidic platform. **A)** Flow-focusing microfluidic device used for isolating samples (e.g., protoplasts). Carrier oil flows in from direction 1 and is formed to a droplet and broken away from the main stream by an aqueous stream coming from direction 2. **B)** Schematic of the sorting setup applied to distinguish between different protoplasts in the carrier oil droplets. Adapted from [23]

In July 2018, Zhu *et al.* [35] extended their earlier nanoPOTS research [33] in an application paper, focusing on rat brain tissue. The authors demonstrated the integration of laser-capture microdissection (LCM), which enables the dissection of tissue into small samples (e.g., 20 µm), with their nanoPOTS system. Additionally, the setup was enhanced by pre-filling the sample wells with dimethyl sulfoxide, which improved proteome analysis by facilitating sample capture and lipid dissolution. Using this approach, the authors successfully analysed and correlated proteins from 100 µm diameter samples of three distinct rat brain regions, identifying approximately 1,000 proteins per sample. Their findings highlighted the potential for conducting localised tissue-specific proteomic analyses using LCM in combination with nanoPOTS [35].

In August 2018, Liang *et al.* [34] published an application paper demonstrating the use of the droplet-based nanoPOTS platform for plant tissue proteomics. The authors analysed the proteome of tomato pericarp cells using LCM to deposit samples into nanoPOTS wells. They examined cells from different pericarp regions (parenchyma, collenchyma, and outer epidermis), identifying tissue-specific enzymes involved in carbohydrate transport and the source-sink relationship. This study marked the first application of droplet-based microfluidics in plant tissue proteomics [34].

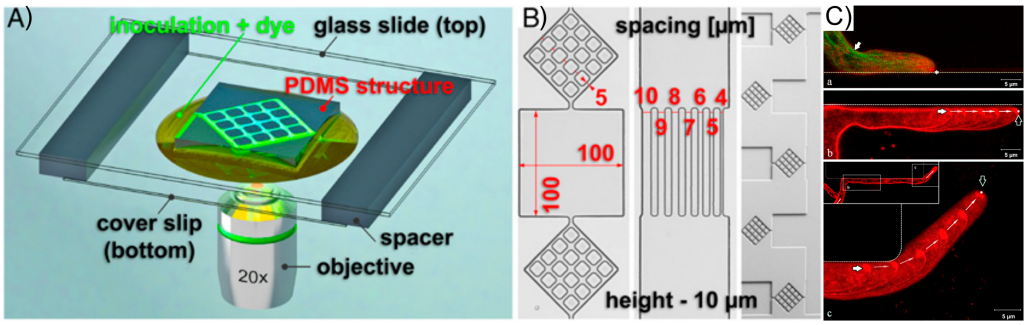

Figure B.13: Analysis of Spitzenkörper growth and fungal growth direction. **A)** Principal sketch of the MFC and analysis setup for experiments on *N. crassa* fungal growth. **B)** Microfluidic channels casted from PDMS. Left: Connected chambers for examining constrained and free growth behaviour. Centre: Microchannels with different widths. Right: Image of the complete chip for constrained growth analysis. **C)** Growth behaviour of a hypha nestling against a wall and its behaviour after the wall ends. The Spitzenkörper (labeled with fluorescent marker FM4-64) is pseudocolored red. Through the nestling phase along the wall the Spitzenkörper is facing towards the obstacle. Once it reaches the end, it resumes its central position in the hypha tip. Published by [24]

In July 2019, Held *et al.* [24] published an application paper expanding on their earlier work [16] on fungal orientation in microfluidic environments. The authors examined the Spitzenkörper – a dynamic structure in fungal hyphae responsible for vesicle delivery and tip growth – and its role in directing hyphal growth. The study utilised PDMS-cast labyrinthine microchannels, sealed with a plain PDMS-slab. Using an inverted laser-scanning microscope (Zeiss Axio Observer Z1 with LSM Exciter RGB, Carl Zeiss), they conducted bright-field and fluorescence time-lapse imaging (results shown in figure B.13). The authors found that the Spitzenkörper plays a critical role in hyphal exploration. When absent from the hyphal tip, orientation was lost, leaving growth direction to be determined by isotropic turgor pressure [24].

Also in July 2019, Finkbeiner [14] defended his dissertation on the development of the MBR, representing a baseline paper focused on manufacturing techniques and design improvements. Key modifications included the introduction of ultrasonic welding for bonding and a transition from a chamber with corners (cf. [13]) to an oval-shaped cultivation chamber. Two MBR configurations were presented: a smaller 200 µL volume device for pre-screening and a larger 800 µL setup [14].

In October of 2019 Kozgunova and Goshima [26] presented their baseline-publication on cultivating and monitoring moss (*Physcomitrella patens*) in an MFC using highly inclined and laminated optical sheet microscopy. Plant cells are cultivated in suspension making it difficult to view inner parts of them with standard light microscopy, as not enough light reaches the inner layers of the cells. To improve the visibility, cells have to be pressed against the light transmitting boundary, e.g., a cover slip. Kozgunova and Goshima [26] presented an MFC with a sample channel thin enough that the plant samples were automatically flattened against the channel-covering thus ensuring improved light transmission. In their baseline-paper the authors tested the effect of three different channel heights: 4.5 µm, 8.5 µm, and 15 µm for an on average 21.5 µm high moss-filament. They found, that the viability of the moss filaments was not significantly hampered in any of the three channels compared to a control cultivation under standard conditions. The authors did not find it advantageous to use the thinner channels and thus opted for the 15 µm for future MFCs. The setup was manufactured from PDMS using the standard soft-lithography process (see appendices A.2.2 and A.3.1). To close the chip the PDMS-cast was covered with either a cover-slip (glass) or bonded to a glass-bottom dish [26].

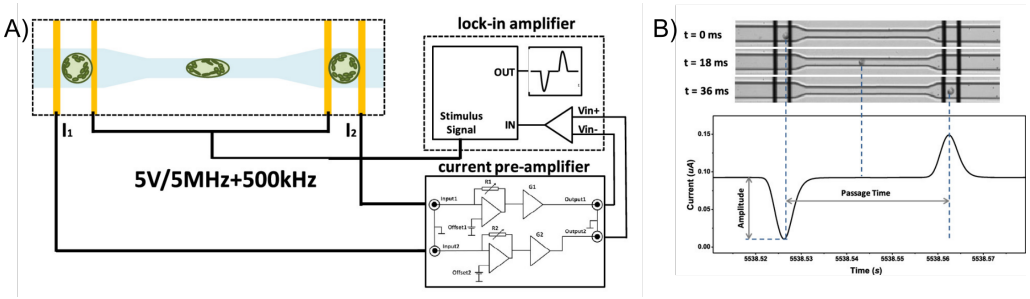

Figure B.14: MFC for single cell analysis. **A)** Setup of the MFC for analysing individual protoplasts. The passage time of a protoplast – determined by the two impedance peaks measured by the microelectrode pairs – different kinds of protoplasts can be distinguished. **B)** Picture of a protoplast passing through the analysis channel and the according impedance measurings. Adapted from [27].

In September 2020, Han *et al.* [27] introduced an MFC for the mechanical and electrical characterisation of single plant cells in a baseline paper. The chip contained two microelectrode pairs positioned at each end of a microfluidic channel, which was thinned between the electrodes (see figure B.14). The microelectrodes were fabricated by depositing 50 nm Ti and 200 nm Au onto a glass substrate using a standard lift-off process. The microchannels were cast from PDMS via a standard soft lithography process, with the glass slide plasma-bonded onto the PDMS to seal the microchannel and enclose the microelectrodes (see appendix A.3.1). After establishing an electrical connection, the authors conducted experiments with *A. thaliana* and *Populus trichocarpa* protoplasts. The microfluidic setup allowed for the differentiation between the two protoplast types by measuring their electrical impedance. Each protoplast type exhibited distinct impedance values when its plasma membrane was exposed to a red fluorescent protein. Additionally, mechanical properties were characterised by measuring the passage time of individual protoplasts through the narrow channel and correlating these values with cellular deformability. The authors also examined the effect of the phytohormone auxin on PCW regeneration, demonstrating that – as expected from conventional petri-dish experiments – auxin promoted PCW regeneration. This was evident through an increase in electrical impedance opacity and prolonged passage times compared to untreated cells [27].

In October 2020, Chen *et al.* [28] reported their findings on PCW regeneration in a microfluidic device. The setup, again designed for single-cell analysis based on electrical impedance spectroscopy, was built on the work of Han *et al.* [27] and, due to its strong biological focus, is classified as an application paper. The device consisted of two interconnected channels cast from PDMS. One channel closely resembled the previous setup, featuring a narrowed centre section with three microelectrodes for protoplast analysis. The second channel served as a bypass, directing protoplasts along an alternative route if the main observation channel was already occupied (see figure B.15). Using their device, the authors demonstrated that different trapped protoplasts could be clearly distinguished based on their impedance values. Additionally, they showed that auxin facilitated PCW regeneration, with different cell walls producing distinguishable impedance readouts [28].

In May 2021, Balasubramanian *et al.* [36] conducted another experiment using the nanoPOTS platform, marking the second application of this droplet-based setup for plant tissue analysis. The authors described detailed protocols for collecting and preparing poplar root and leaf samples using LCM, examining them with nanoPOTS, and analysing the resulting proteomic data. In these proof-of-concept experiments, the authors demonstrated that it is possible to gather localised proteomic information from plant tissues. Specifically, they confirmed the expected result that leaf palisade cells – photosynthetic cells located beneath

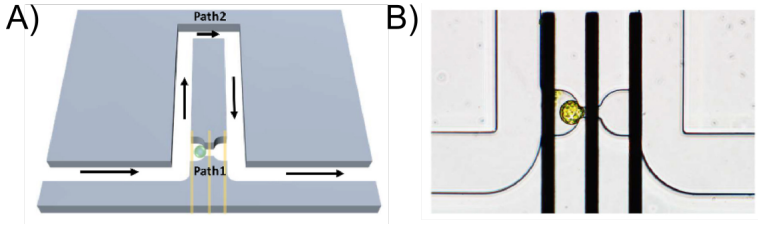

Figure B.15: MFC for single cell analysis. **A)** Design of the MFC aimed to either trap protoplasts within path 1 or circumvent them further down the line through path 2 if path 1 is already trapped. **B)** The created MFC with a protoplast trapped in path 1. The microelectrodes (black vertical bars) are used to analyse the protoplast via its impedance readout. Adapted from [28].

the epidermis of leaves – exhibit a protein profile primarily related to photosynthesis, while vascular leaf cells – responsible for nutrient and water transport – predominantly express proteins involved in sugar and carbohydrate synthesis [36].

In June 2021, Dudukovic *et al.* [32] contributed a notable baseline paper to the field of phloem analysis using MFCs. The authors employed stereolithographic additive manufacturing to fabricate structures composed of individual unit cells, allowing them to examine the corresponding fluidic behaviour. This approach enabled the study of capillary rise within open and complex geometries, providing insights into fluid transport mechanisms in biomimetic systems [32].

In April 2022, Shimizu *et al.* [29] introduced a baseline paper on the trapping of individual cells in an MFC for cultivation and analysis. Unlike previous studies in this area, which focused on protoplasts, the authors targeted BY-2 cells. Their preparation method typically yielded small cell strands (two to four cells, occasionally more) rather than single cells. The microfluidic device was designed to individually trap multiple cell strands (112 trap zones were implemented, see figure B.16A). As a proof of concept, mitotic (cell division) behaviour was monitored over four days, revealing that propagation patterns remained consistent with standard beaker cultivations. However, the immobilisation of cell strands in the microfluidic setup allowed for prolonged observation without drift (see figure B.16B). The device was manufactured using the soft lithography replication process in PDMS [29].

In July 2022, Kurotani *et al.* [41] presented an application study building on Shimizu *et al.* [29]. The authors used immobilised BY-2 cell strands to investigate the role of plasmodesmata – microscopic channels that connect plant cell walls – in cell-to-cell communication. To test this, they photobleached a single cell in a strand, eliminating the H2B-GFP protein. After 200 min, the bleached cell regained the H2B-GFP protein if left undisturbed. However, when the entire immobilised cell strand was bleached, protein recovery did not occur. Additionally, no recovery was observed when sodium chloride, which induces plasmodesmata closure, was introduced. These findings led the authors to conclude that protein exchange between cells in a strand relies on open plasmodesmata and protein availability [41].

In August of 2022, Dai *et al.* [289] from the groups of Jiehua Wang, and Xuexin Duan – the same groups as Chen *et al.* [28] and Han *et al.* [27] – published an application paper on the phenotypic characterisation of plant protoplasts using an MFC. The channel design was similar to that of Han *et al.* [27] and was fabricated from PDMS via standard soft lithography. However, in contrast to previous approaches, Dai *et al.* [289] employed fluorescence markers for measurement. Two low-power lasers (488 nm, 50 mW, and 360 nm, 50 mW) were used to excite different fluorescent markers, enabling simultaneous detection of ROS and PCW regeneration. As a proof of concept, different *A. thaliana* genotypes were analysed, and the system successfully distinguished between various cell lines [289].

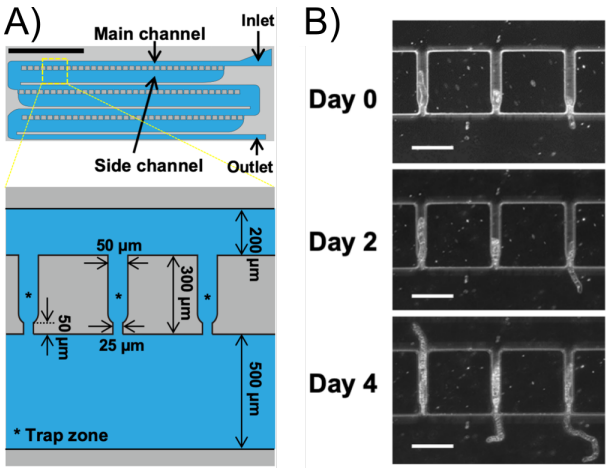

Figure B.16: A) Design of the MFC for trapping strands of a few cells in individual zones. 112 trapping zones were created on each chip. The width of 50 µm corresponds to the width of a cell strand. Black scale bar up top is 5 mm long **B)** Cultivation of individual cell strands over four days in the MFC. Cell division and thus, the elongation of the individual cell strands, can be observed well in the chip. White scale bars are 200 µm. Adapted from [29].

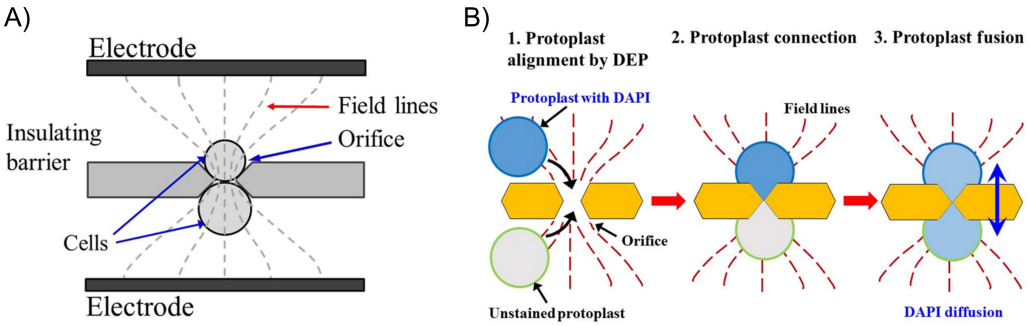

Figure B.17: A) Concept of electrofusing two protoplasts by positioning them at an insulating barrier. **B)** Process of positioning, membrane punctuation, and fusion of two protoplasts [31].

More than a decade after the last cell fusion publication in plant-related research, Hung *et al.* [31] released their baseline paper in February 2024, detailing advancements in electrofusion of protoplasts. The authors refined previous research and significantly improved fusion efficiency, achieving 76 % for *Phalaenopsis* protoplasts and 80 % for *R. raphanistrum* subsp. *sativus* protoplasts. Their work builds on the foundation established by Washizu et al., who published a series of studies on electrofusion, beginning with plant protoplasts and human cells in 2008 [290], extending to human cells and human stem cells [291]–[293], and later addressing the fusion of mouse cells [294]. The microfluidic electrofusion system consists of two indium tin oxide glass electrodes, each laminated within PDMS. A thin Kapton sheet, positioned between the PDMS-layers, contains regularly spaced orifices adjusted to the size of the cells targeted for fusion (5 µm for protoplast fusion). To initiate the process, protoplasts are flushed into the upper and lower chambers and positioned at the orifices using a high-frequency alternating current electric field (1 MHz, 10 kV/m). A voltage pulse then generates a localized drop in voltage around the orifices, disrupting the membrane at the contact points and facilitating fusion. Figure B.17 illustrates this process. The authors conducted proof-of-concept experiments with *Phalaenopsis* and *R. raphanistrum* subsp. *sativus* protoplasts, demonstrating a notable improvement in fusion efficiency compared to the work of Hu *et al.* [19] [31].

In February 2024, Chandrasekar *et al.* [30] published their baseline paper introducing an MFC designed to analyse thin sections of a corn stem (60 µm). The authors fabricated a PDMS-cast with a single cavity (250 µm high) and perforated it with inlets and outlets. A cryo-sectioned corn stem sample was placed on a 25 mm diameter cover glass and enclosed using a super glue bond (Gorilla Catalog No. 721195) to adhere the PDMS-structure onto the glass. With this setup, the authors validated the expected finding that the walls of parenchyma cells – essential for photosynthesis and predominantly found in leaves – are more digestible than the structurally robust cell walls of vascular bundle cells, which form part of the plant's vascular system, including xylem and phloem [30].

In July 2024, Zhang *et al.* [42] advanced the field of single plant cell analysis in microfluidic systems. Their work built upon the MFC designs established by Han *et al.* [27], Chen *et al.* [28], and Dai *et al.* [289]. In their application paper, Zhang *et al.* [42] introduced a refined MFC and conducted multiple experimental applications using the new setup of the MFC developed by the group of Jiehua Wang, and Xuexin Duan. The updated microfluidic design is similar to that of Chen *et al.* [28], featuring a channel with a central section of reduced width. At the inlet and outlet of this constricted section, electrode pairs are positioned to detect impedance signals when a protoplast enters or exits the observation region. Fluorescent microscopy was incorporated to assess the presence of ROS in the examined protoplasts. The device was fabricated from PDMS via standard soft lithography and sealed with a glass slide bonded through plasma treatment. With this setup, the authors investigated the effects of three phytohormones – gibberellin, cytokinin, and auxin – on PCW development. Additionally, they examined ROS generation in response to heavy metal-induced stress and analysed the mechanical and electrical properties of different protoplast types [42].

This concludes the historical overview of MFCs in plant-related research. Although the past fifteen years have seen a considerable number of contributions in this field, it is important to recognize that these publications cover a broad spectrum of research areas. When focusing on any single domain, the use of MFCs remains the exception rather than the standard.

C Historical overview of publications on RCs for plant related research

Root analysis is a critical research area for understanding and improving crop performance. However, it is often underrepresented in microfluidic studies. The following sections provide a chronological review of microfluidic Root Chips that have significantly advanced research in this field.

In 2010, Meier, Lucchetta and Ismagilov [68] demonstrated for the first time that *A. thaliana* could be cultivated in an MFC for root analysis and that its root development could be influenced by phytohormones and chemical compounds. The chip consisted of two structured PDMS-layers positioned between two 0.2 mm thick glass slides, which served as top and bottom enclosures. Alignment pins and holes ensured precise positioning of the layers, which were bonded using plasma treatment (see appendix A.3.1). Figure C.1 illustrates the chip's layout. The *A. thaliana* seedlings were germinated externally before being inserted laterally into the chip, exposing the root to the flow of nutrient medium. Micropillars within the analysis channel helped to stabilize the root. Upstream, the main channel split into three branches: the central channel delivered the test compound, while the left and right channels provided standard nutrient medium. Due to laminar flow conditions, only a small, localized section of the root was exposed to the test compound, while the remaining root sections served as a baseline for comparison. As a proof of concept, the authors demonstrated that synthetic auxin (2,4-Dichlorophenoxyacetic acid) promoted the growth of epidermal root hairs. The experiment was monitored over several days using fluorescence microscopy [68].

In June 2011, Parashar and Pandey [69] introduced the Plant-on-Chip, another PDMS-based MFC bonded onto glass slides. This chip featured eight parallel channels, each with dedicated inlets and outlets, enabling the simultaneous monitoring of multiple roots. Seedlings were pre-germinated before being transferred into the chip for experimentation, where they were observed over several days under a microscope. To validate the platform's functionality, the authors examined how different concentrations of Murashige- and Skoog (MS) medium affected *A. thaliana* root development, as well as the impact of sugar beet nematodes and *Phytophthora sojae*. The results demonstrated that this system allowed for detailed morphological analysis of root responses. For example, higher nutrient concentrations led to a denser root hair network, while lower nutrient levels resulted in sparser, elongated root hairs [69].

A few months later, in December 2011, Grossmann *et al.* [59] expanded on the work of Meier, Lucchetta and Ismagilov [68] and introduced an MFC designed for parallel cultivation of eight roots, naming it the RootChip. Similar to previous designs, it was fabricated from PDMS, with two chip halves plasma-bonded together and sealed to a glass slide as the base. The device featured eight analysis chambers, each accessible via angled inlets (30°). By integrating pneumatically controlled valves, the authors established a computer-operated

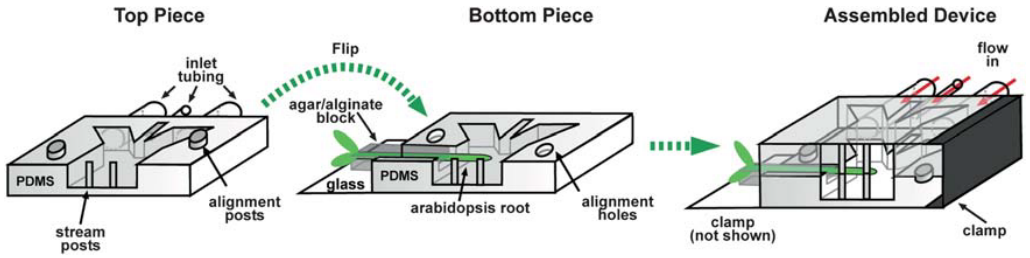

Figure C.1: First MFC for root analysis by Meier, Lucchetta and Ismagilov [68]. The *A. thaliana* root is perfused sideways and can be exposed to phytohormones or other chemical compounds [68].

flow management system, allowing the application of three different media to individual root chambers. The system enabled real-time observation of root responses via fluorescence and light microscopy. The proof-of-concept experiment investigated root responses to galactose exposure, revealing that galactose induced cellular deformation and cell death [59], [295].

In 2012, Busch *et al.* [60] introduced an MFC designed for high-throughput root analysis, accommodating up to 64 pre-germinated *A. thaliana* seedlings arranged in four rows. The chip featured a lower root chamber filled with MS medium and an upper chamber providing fresh air to the shoots. A key innovation of this study was the chip's fabrication: rather than relying on soft lithography, the chip halves were 3D-printed using stereolithography with a high-resolution resin (Somos® WaterShed® XC 11122, Stratasys Inc., Eden Prairie, MN, USA). According to the authors, the material choice enabled sterilization and reuse of the chips. As a proof of concept, they analysed gene expression in 12 transgenic reporter lines, assessing how specific genes influenced root growth. Imaging-based segmentation models were trained to reconstruct three-dimensional root scans from collected data. By leveraging machine-learning-based segmentation and the high sample capacity, the authors developed a high-throughput screening platform [60].

Continuing the trend of high-throughput root analysis, Jiang *et al.* [61] presented a vertical MFC for plant phenotyping in 2014. This design featured an automated seed distribution system that guided seeds into individual funnel-like compartments, allowing in-chip germination – a departure from previous studies that required external germination. The system enabled long-term observation of seedling development for up to four weeks, facilitating detailed phenotypic analysis. The chip was fabricated from PDMS using soft lithography and bonded to a glass slide via plasma treatment. To demonstrate its capabilities, the authors cultivated *A. thaliana* seedlings and assessed their response to varying nutrient concentrations in the growth medium as well as exposure to *Phytophthora sojae* spores. Their findings confirmed that seedlings in low-nutrient conditions developed longer primary roots at a faster rate. Additionally, fungal spores successfully located the root within 5 h to 10 h and subsequently initiated plant invasion [61].

In 2017, three contributions were made to the field of Root Chip research, all of which were PDMS-based [62], [63], [70].

In April 2017, Massalha *et al.* [62] introduced their Tracking Root Interactions System, a microfluidic chip designed to study interactions between plant roots and bacteria. The MFC consisted of a PDMS-cast bonded to a glass slide. Each cast contained nine channels with hexagonal cross-sections, each equipped with individual inlets and outlets, as well as a separate angled inlet for seedling insertion. Nutrient medium was perfused through each channel via inlets and outlets connected to PE tubing and corresponding reservoirs. The inlets also served as entry points for bacterial administration to study root-microbe interactions. As a proof of concept, the authors conducted multiple experiments: first, they monitored *Bacillus subtilis* colonization on the root surface. This was followed by an experiment comparing the competitive colonization between *Bacillus subtilis* and *Escherichia coli*. Finally, they examined different genotypes of *A. thaliana* seedlings, using fluorescently labeled *Bacillus subtilis* to identify bacterial colonization preferences for specific root regions and mutant lines [62].

Later that year, Park *et al.* [63] presented their MFC, designed to investigate how varying nutrient concentrations in solid MS medium affected *A. thaliana* seedling growth. Their findings confirmed that higher nutrient concentrations led to faster seedling development. The chip was composed of a PDMS-cast forming the bottom plate, which contained 20 individual channels filled with solid MS medium. The top plate was a square PMMA sheet

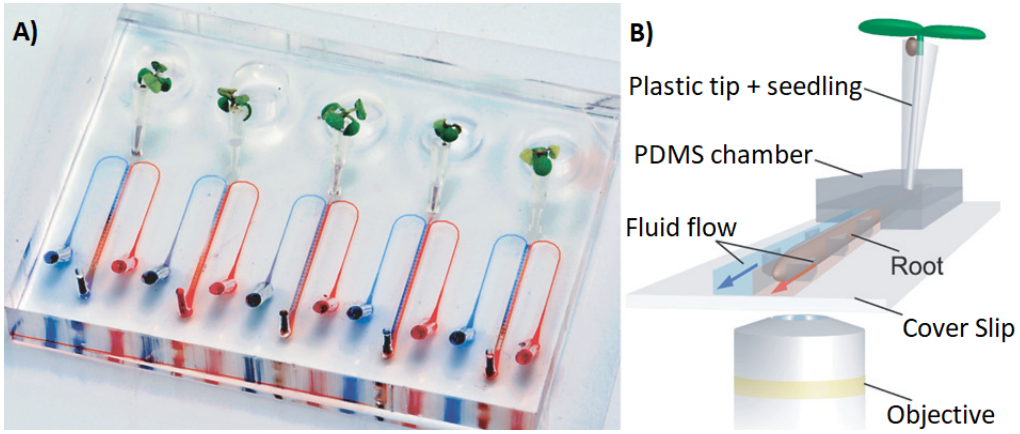

Figure C.2: Dual-flow-RootChip presented by Stanley *et al.* [64]. **A)** shows the manufactured chip made from a PDMS-cast and glass slide perfused with two coloured dyes. **B)** shows the schematic sketch of the setup, highlighting the laminar flow that allows for the application of two almost completely unmixed fluids to two sides of a root [64].

featuring 400 evenly spaced openings for seed placement. Seed germination and subsequent seedling growth were monitored using stereo microscopy [63].

Around the same time, Aufrecht *et al.* [70] published their work on studying epidermal root hairs using an MFC. Their setup was fabricated from a PDMS-cast placed inside a Petri dish, which acted as the bottom plate, with agar used to secure the cast in place. While PDMS is autoclavable, its adhesion to glass is often compromised during autoclaving due to the heat and pressure. By positioning the PDMS-cast after sterilization and securing it with agar rather than bonding it to a glass surface, the authors ensured that autoclaving remained a viable sterilization method. Additionally, after completing the growth experiments, the PDMS-cast could be peeled from the Petri dish, allowing further analysis of root hairs using techniques such as atomic force microscopy or scanning electron microscopy [70].

In 2018, Stanley *et al.* [64] introduced the Dual-Flow RootChip, an MFC designed to exploit laminar flow conditions, enabling the combination of two fluids in the root examination channel with minimal mixing (as illustrated in figure C.2). This approach allowed researchers to observe root responses to different environmental conditions within the same experiment. To facilitate root hair analysis, triangular micro-pillars were integrated into the examination channel, ensuring the root remained centred while also guiding its forward growth. The chip was fabricated from a PDMS-cast containing the microchannel structure, which was plasma bonded to a glass plate. As a proof of concept, the authors conducted experiments on *A. thaliana* seedlings, exposing them to phosphate stress. Their results demonstrated that *A. thaliana* locally adapts to heterogeneous environmental conditions [64].

In 2019, three papers were published on the topic of Root Chips. In June, Chai *et al.* [65] introduced a Petaloid root-growth microfluidic chip (PRGM-Chip) designed for studying *Oryza sativa (O. sativa)* (rice) rather than the more commonly used *A. thaliana*. The chip was fabricated from a PDMS-cast containing the channel structures, which was plasma-bonded to a glass slide serving as the bottom plate. The design featured five petaloid-like cavities arranged around and connected to a central germination chamber (see figure C.3). The authors pursued a similar research goal to Stanley *et al.* [64], aiming to examine how a single plant responds to varying growth conditions. In their proof-of-concept experiments, Chai *et al.* [65] subjected rice seedlings to different levels of drought stress by

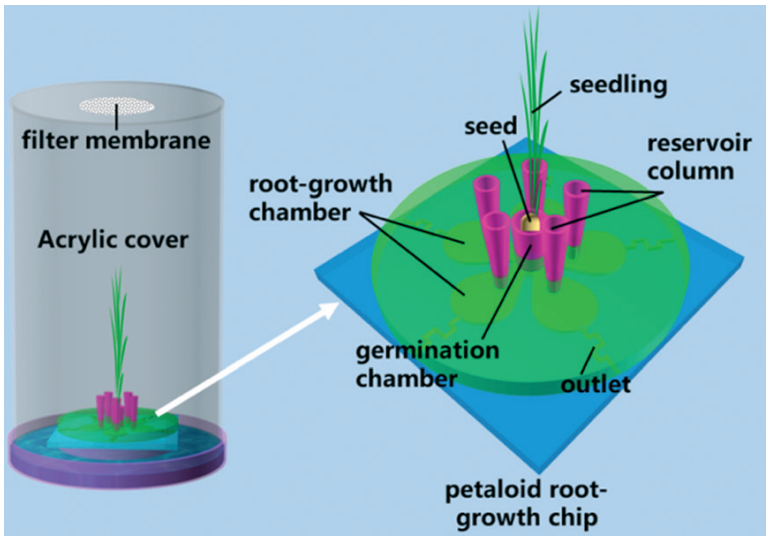

Figure C.3: Schematic sketch of the PRGM-Chip presented by Chai *et al.* [65]. To achieve ideal cultivation conditions, the MFC is housed in an acrylic cover. The chip itself is constructed out of a PDMS-cast bonded onto a glass slide. Five petaloid-like chambers are positioned around a central seed germination chamber [65].

modulating water availability in the five petaloid root cavities using polyethylene glycol 6000, a non-toxic, water-soluble polymer. By adding this polymer, a controlled amount of water was displaced from the cavities. Their findings demonstrated that root growth slowed when water availability decreased, while the density of root hairs increased [65].

In July, Patabadige *et al.* [72] introduced an MFC designed to analyse the chemical composition of the microenvironment surrounding wheat seedling roots. The chip consisted of two PDMS-halves: a bottom half forming two separate sampling channels and a top half holding the germinated seedling. A key aspect of this work was the integration of a nano-porous polyester membrane, which separated the bottom and top halves. Two PDMS-based approaches for membrane adaptation were explored: applying an approximately 6 µm thin layer of still-wet PDMS using a stamping technique to selectively seal unwanted pores, or soaking the membrane in a PDMS-solution using a mould to block specific areas. Once assembled, the chip was used to analyse root exudates at two different points along the root [72].

Walczak, Kawa and Adamski [76] focused on measuring the mechanical force exerted by growing roots. The authors utilised inkjet 3D printing to fabricate an MFC consisting of two halves, using VisiJet M3 Crystal as the printing material. The lower half contained a seed chamber, a water supply channel, and a deflection beam positioned beneath the chamber to measure the force exerted by the root during growth. Seeds were placed directly into the chamber without pre-germination, and the setup was then sealed with the top half, which featured a second deflection beam for measuring the growth force of the developing seedling's stalk. Their experiments showed that *Lepidium sativum* seedlings exerted a maximum growth force of 58 mN with their roots, while the stalks generated approximately 501 mN, meaning the root's force was about 10 % of that of the stalk [76].

In December, Song *et al.* [66] introduced a foldable MFC designed for continuous monitoring of the germination process. The study used *N. tabacum* as a model plant, marking the first time this species had been used for root analysis in a microfluidic device. The chip consisted of modular components, each containing two glass slides as bottom plates and a PDMS-cast with two independent channel structures. The PDMS-cast was plasma-bonded to the glass slides at the structured regions, while the unstructured PDMS between the

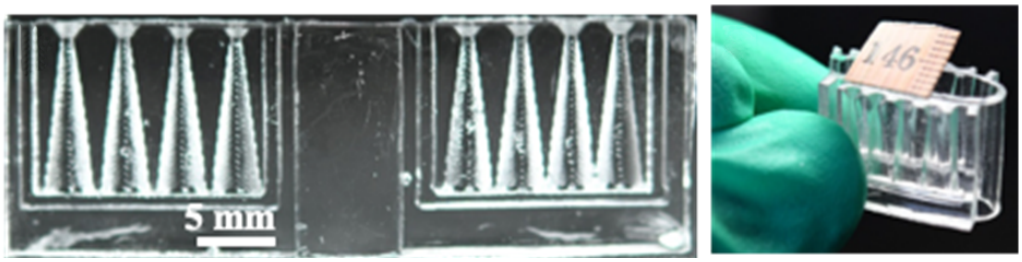

Figure C.4: Foldable MFCs for root analysis, published by Song *et al.* [296]. **A)** shows the PDMS-cast of the chip that will be bonded to two different glass slides. The central area that will later form the hinge by not being bonded to a glass slide can be spotted well. **B)** A finished MFC. If another PDMS-cast is bonded onto the same glass slide as the previous one, a long line of MFCs can be formed [296].

modules remained unbonded, serving as a flexible hinge. This configuration allowed for the creation of a long chain of mechanically connected but fluidically independent MFCs (see figure C.4). Each module accommodated four seeds. When folded, the setup allowed for space-efficient storage while maintaining uniform growth conditions for all seedlings. Once unfolded, individual root development could be examined separately. As a proof of concept, the authors germinated seedlings in the setup and studied the effects of drought stress and salt exposure on root growth [66].

In April 2020, Noirot-Gros *et al.* [73] introduced the root-microbe interaction chip, an MFC designed to study the interplay between plant growth and microbial colonization. The chip was capable of hosting six pre-germinated woody-plant seedlings of *Populus tremuloides* (aspen) for growth periods exceeding a month. To accommodate the relatively large roots, the growth channel was 100 µm high, 800 µm wide, and 36 mm long, which was significantly larger than typical root analysis microfluidic channels. The device, fabricated from a PDMS-cast bonded to a glass slide, featured two inlets for nutrient media and microbial inoculation. Analysis was performed using confocal laser scanning microscopy. As a proof of concept, the authors demonstrated that roots could be colonized by *Pseudomonas fluorescens* within the chip. They observed that biofilm formation in the device closely resembled colonization patterns seen in standard experimental setups, such as vertical plate assays [73].

Later that year, in October, Sun *et al.* [78] published findings on how channel width influences the growth behaviour of *A. thaliana* roots. Their study tested five different channel widths, with results summarized in figure C.5. The authors found that wider channels correlated with longer root growth over the same incubation period. Additionally, channel width affected root diameter: as the channel width increased up to 250 µm, root diameter also increased. However, in channels wider than 250 µm, root diameter began to decrease [78]. These findings highlight how the design of an MFC can itself influence the roots being studied, which must be considered when interpreting experimental results.

In September 2021, Singh *et al.* [71] published their work on tracking root hair growth in *A. thaliana* roots using a coverslip based microfluidic device (CMD). This chip was designed to accommodate three pre-germinated seedlings and track the lateral growth of root hairs with confocal microscopy. To achieve this, several 20 µm high and wide channels were positioned adjacent to the central channel, which housed the main root (250 µm wide × 100 µm high). The chip was perfused with nutritional and reactive media through these side channels, as illustrated in figure C.6. Due to this setup, the developing root hairs extended into the side channels, enabling individual growth analysis. The chip was fabricated from a PDMS-cast, which was bonded to a thin glass slide. The authors confirmed that root hair growth rates in the CMD were consistent with those determined using classical methods [71].

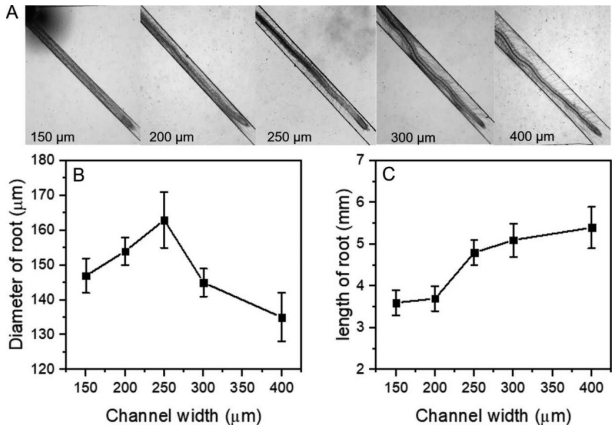

Figure C.5: A) Different channel widths can influence a root's growth behaviour, like the developing root-diameter or its growth within a certain amount of time. Sun *et al.* [78] showed this in their publication: For this, they manufactured the same microfluidic design five times, but with different channel widths (as displayed in the picture). **B)** Measured diameter of the developing root when cultivated in differently wide channels. **C)** Length of roots in channels of different widths after 7 d [78].

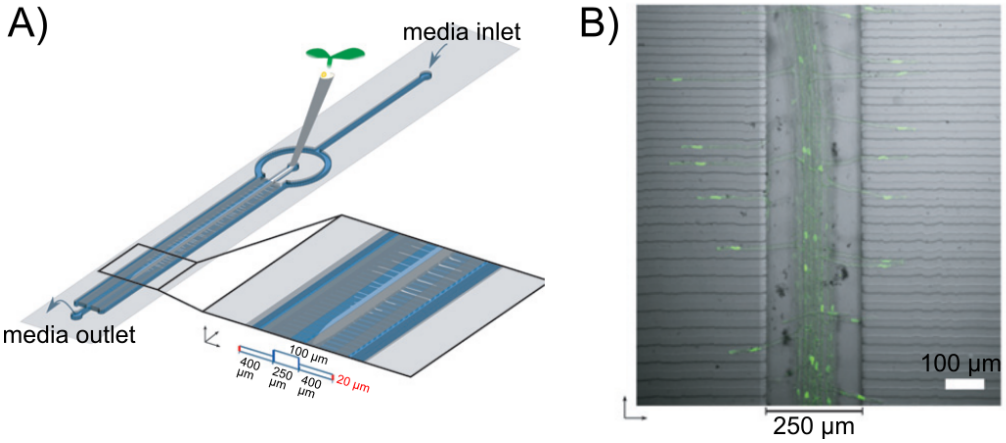

Figure C.6: A) Singh *et al.* [71] published their work on tracking the growth of root hairs in a CMD. **B)** Along the central channel for the main root, multiple channels with a width of 20 µm were located on both sides. Root hairs could grow into these small channels, allowing only one or two root hairs per channel and thus ensuring clear visibility of the individual root hair [71].

Aufrecht *et al.* [74] introduced their rhizosphere-on-a-chip platform in January 2022. They argued that conventional microfluidic root analysis chips, which analyse a single root in a straight channel, fail to account for the influence of soil structure on root behaviour. To address this, they designed a rhizosphere-on-a-chip platform that mimicked the porous media of Hawaiian sand particles. The shape and distribution of the sand particles were mapped into a 2D-image, and transferred onto a chrome mask, which was subsequently replicated in PDMS. The resulting channels between the "sand particles" were 300 µm deep and covered with a glass slide bonded via plasma treatment, as shown in figure C.7. Pre-germinated seedlings were transferred into the chip through a dedicated inlet using cut-off pipette tips. *Brachypodium distachyon* was chosen as the model plant due to its compact root system and its close relation to economically important grains such as wheat and oats. During the proof-of-concept tests, the seedlings grew for approximately a month within the chip, exhibiting similar developmental stages to those observed in standard setups. Microscopy and liquid micro-junction surface sampling probe mass spectrometry were used to analyse amino acid exudation from the roots [74].

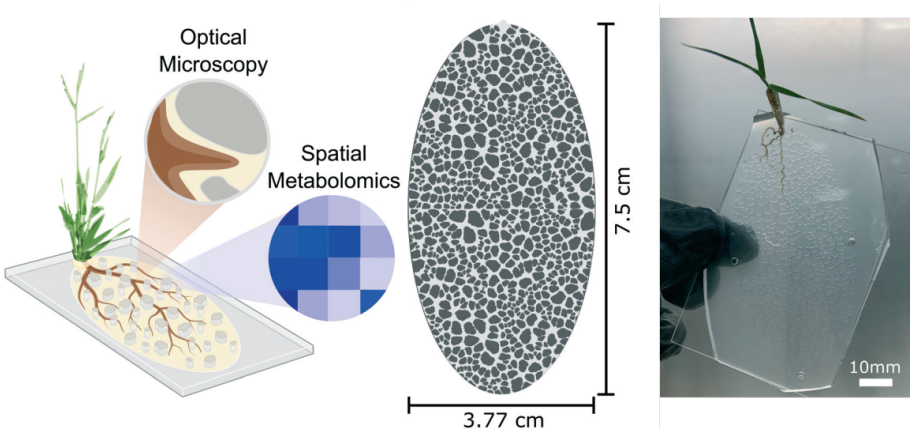

Figure C.7: Microfluidic setup to study the rhizosphere. The chip was presented by Aufrecht *et al.* [74]. The pattern of sand is created as a mould for PDMS using the process of soft lithography. This way, the root growth behaviour can be studied in a more varied environment [74].

The topic of rhizosphere research was further explored by Dai *et al.* [75] in May 2022. They combined conventional potted plant examination with a microfluidic approach. Pre-germinated rice seedlings (*O. sativa*) were cultivated in 300 g of soil per pot. Each pot was connected to an MFC, into which roots gradually extended through a pipe. The goal was to examine ROS generation in the rhizosphere soil using confocal scanning microscopy by measuring fluorescence triggered by ROS activity. The microfluidic setup was fabricated from PDMS and bonded using adhesive. However, the authors did not provide a detailed description of the MFC design. From the images provided in the publication, the structure appeared to consist of a perfused pillar array, similar to the design of Aufrecht *et al.* [74], but with a regularly structured pattern rather than a randomly distributed one. The authors demonstrated that ROS generation in the rhizosphere varied between light and dark conditions. They concluded that this ROS production resulted from the interaction between oxygen released by the root and extracellular electrons from microbial respiration [75].

In 2023, Allan *et al.* [67] expanded on the dual-flow RootChip concept introduced by Stanley *et al.* [64]. They developed an MFC for root analysis that not only used the laminar flow profile to expose each side of the root to different substances but also introduced the ability to reverse the flow direction. This bidirectional flow was enabled by splitting the final outlet into two separate openings, allowing the microfluidic setup to be perfused in either direction. Regardless of the flow direction, a dual-flow profile was maintained in the analysis channel due to laminar flow conditions at the appropriate flow rate. Figure C.8 illustrates this dual-flow RootChip. Like its predecessor, the MFC was manufactured from PDMS, with the channel structures sealed by plasma bonding a glass slide on top. For a proof of concept, the authors investigated the stress response to salinity (through NaCl application) and Ca_2^+ signalling (induced by drought stress created using polyethylene glycol) in fluorescent G-CaMP3 *A. thaliana* seedlings. Their experiments revealed distinct and complex signalling events that varied depending on the first point of contact with the substances [67].

Another study that built strongly on a previous publication was presented by Chai *et al.* [77] in June 2023. Based on the multi-chamber petaloid root-growth chip introduced by Chai *et al.* [65], they developed an MFC with an easily accessible design. Like its predecessor, the setup was PDMS-based. Around a central germination chamber, three drop-shaped growth chambers were arranged, each connected to the central chamber via channels. The cavities were 500 µm deep and cast from PDMS, which was then bonded onto a glass slide. This glass slide was sandwiched between two PMMA slabs, which were

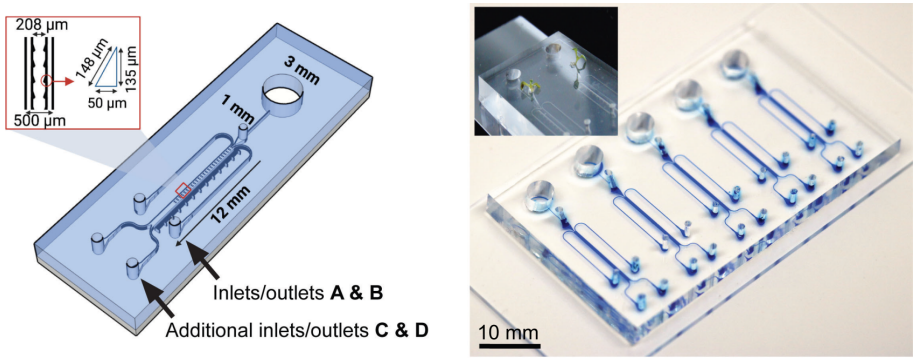

Figure C.8: Bidirectional dual-flow-RootChip presented by Allan *et al.* [297]. The chip can be perfused backwards and forwards each time, creating a two-face flow due to the laminar flow conditions. The picture shows the schematic sketch of the setup, as well as a finished chip, filled with blue-dyed epoxy for better visibility of the channels [67].

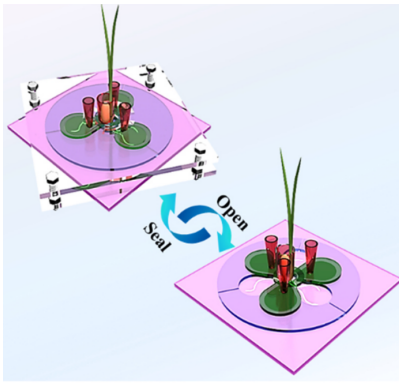

Figure C.9: Schematic illustration of an easy to open MFC for root analysis. The setup was published by Chai *et al.* [77] and is based on the PRGM-Chip-chip presented by Chai *et al.* [65] in 2019. Three petaloid shaped root analysis chambers are organised around a central germination chamber. Two PMMA-slabs sandwich the actual MFC. This chip is comprised of a PDMS-cast containing the analysis chambers bonded onto a glass slide. If the PMMA-slabs are turned, 30° the openings of the upper slab line up with the root growth chambers and the roots can be accessed for sampling and further inspection [77].

screwed together to form a clamp. The PMMA slabs contained drop-shaped openings corresponding to the growth chambers. By rotating the slabs, the root chambers could either be fully enclosed or exposed for sample collection. Figure C.9 illustrates this concept. The central germination chamber was designed to be large enough to hold an *O. sativa* seed without damaging it when the PMMA slabs were applied or rotated. As a proof of concept, the authors collected root tip samples to assess localised physical damage. They found that this type of damage did not accelerate root tip regeneration. Additionally, they analysed collected root samples for ROS content and solute composition, such as sugars [77].

In October 2023, Kamat *et al.* [79] published their work on integrating sensors for measuring nitrate and phosphate levels into an MFC for root analysis. The chip was manufactured from a PDMS-cast bonded onto a glass slide. However, the paper did not provide details on the channel structures, seedling introduction, or cultivation measures. Instead, it focused on the fabrication of the sensors, which were screen-printed onto the glass slide. The printing process involved placing a stencil onto the glass, depositing and drying a layer of silver/silver chloride (Ag/AgCl), followed by a layer of carbon graphene (Gr). The sensors were then activated using electrochemical methods described in detail in the publication. Once activated, they were connected to a monitoring system that collected real-time data on root growth and analysed nutrient concentrations ranging from 1 mmol

to 1000 mmol. For a proof of concept, the authors cultivated ten legume seeds (*Crimson Red Clover*) within the microfluidic setup and compared them to a control group of ten conventionally grown seeds. They found the nitrate and phosphate sensors to be highly precise, with detection accuracies of 99 % and 95 %, respectively [79]. Although the paper did not detail the channel structures for root analysis, it demonstrated a promising research direction for Root Chips by integrating sensors into microfluidic setups for real-time access to growth-related data. Therefore, it was included in this summary of Root Chip research.

This concludes the chronological overview of publications on plant root analysis in MFCs. A summary of key aspects relevant to the development of the RC in this thesis (see chapter 4 for details), focusing on setup design and manufacturing processes in plant root research, is provided in section 2.2.

D Further influential publications for LTW

As introduced in appendix A.3.3, the range of lasers available for laser welding was highly limited about ten to fifteen years ago. Only in the past decade have laser sources with wavelength spectra suitable for the direct welding of polymers without absorbers become commercially available. As a result, much of the research on laser transmission welding (LTW) has focused either on polymers other than PC or on processes involving absorbers. Consequently, the following two subsections will address both aspects: absorber-free laser transmission welding of polymers other than PC (appendix D.1) and absorber-based LTW of polymers, including but not limited to PC (appendix D.2).

D.1 Absorber-free LTW of other materials

While some studies on absorber-free laser transmission welding offer general insights, such as the influence of fixing unit material selection, others explore broader research areas, including the initial investigations into biopolymer weldability. The following paragraphs present the available publications in chronological order.

In 2011, Devrient, Frick and Schmidt [216] presented a proof-of-concept study demonstrating absorber-free laser transmission welding using PP and subsequently PMMA as welding partners. The process was based on a GaAs semiconductor laser with a characteristic wavelength of $\lambda = 937\,\text{nm}$. But, this wavelength falls outside the intrinsic absorption bands of polymers and the aim was to establish an absorber-free process. Thus a complex approach involving convective cooling of the upper welding partner, short focal lengths of the laser focusing lens, adjusted feed speed, and precise control of the focal set plane outside and below the interface of the welding partners was necessary. The experimental findings were supported by an FEM model based on the developing temperature field during welding. Ultimately, both PP and PMMA were successfully welded in this proof-of-concept study [216].

Subsequent research on absorber-free welding has focused on lasers with higher characteristic wavelengths, typically between 1660 nm and 1940 nm. These lasers align well with the absorption properties of common thermoplastics, which exhibit high but not excessive energy absorption within the range of $\lambda = 1.6\,\mu\text{m} - 2.1\,\mu\text{m}$ [136], [298].

Ruotsalainen, Laakso and Kujanpää [200] presented the application of quasi-simultaneous welding (QSW) for absorber-free laser transmission welding of thermoplastic polyamides using a thulium fibre laser ($\lambda = 1940\,\text{nm}$). Additionally, the authors introduced a beam offsetting technique to achieve a wider and consequently stronger weld seam. This method involved placing multiple small beam passes adjacent to one another. To evaluate the process, different line distances (0.05 mm, 0.1 mm, and 0.2 mm), laser powers (66 W–96 W), movement directions (back-and-forth vs. unidirectional), and weld widths (1 mm and 0.5 mm) were tested. While movement direction had no significant effect on weld seam properties, closely spaced passes allowed for reduced power usage and resulted in a flatter heat-affected zone (HAZ) compared to welds of similar width produced using the standard QSW irradiation strategy. This approach was identified as promising for welding thinner samples [200].

The absorber-free laser weldability of biopolymers was investigated by Brosda *et al.* [299] in 2018. The study focused on PLA, Bio-PE, and Bio-PET, which were welded using a diode laser with a characteristic wavelength of 1685 nm. A polymer is classified as a biopolymer if it is biodegradable and/or consists of at least 20 % renewable raw materials. The tested materials, sourced from different manufacturers, were still under development at the time of study. All three biopolymers were weldable, and their achieved weld strengths were within the typical range for their respective bulk materials. However, the tested PLA

exhibited significant micro gas bubble formation even at lower energy inputs. The authors concluded that further research should focus on newly developed biopolymers, as available variants evolve rapidly [299].

In 2020, Nguyen *et al.* [201] explored the absorber-free laser weldability of semi-crystalline PP using a thulium fibre laser ($\lambda = 1940\,\text{nm}$) and a QSW irradiation strategy. In appendix A.3.3, it was previously discussed that semi-crystalline polymers are more challenging to weld due to their internal reflection, which limits the maximum weldable material thickness, as well as their sudden structural collapse once T_G is exceeded (see appendix A.3.2 for further details). The study by Nguyen *et al.* [201] followed a three-step approach. First, beam propagation in PP was simulated to provide insight into the behaviour of laser light scattering in a semi-crystalline material. Second, an FEM-based thermal simulation was conducted to identify suitable weld parameters for this complex material. Finally, experimental weld tests were performed and compared to the thermal model results. The study found that the predicted weld seam height was consistently overestimated in all QSW irradiated tests, with a near-constant offset of approximately 16.6 %. Similarly, the predicted seam width was overestimated by 52.2 %. The authors attributed these discrepancies to two simplifications in the analytical models: the assumption that scattering properties remain unchanged under increasing temperatures, which neglects the influence of melting crystalline structures, and the assumption of homogeneous material properties, whereas local crystallinity in experimental samples depends on manufacturing conditions [201].

Previous research suggested that the material used for the clamping device securing the welding partners during welding influences the process. Brosda *et al.* [98] investigated this effect using a diode laser ($\lambda = 1660\,\text{nm}$) to weld 12 µm thick PET to 90 µm thick PE under a contour welding irradiation strategy. However, the HAZ was not analysed in this study, and no further details on welding behaviour of unevenly thick thin foils were provided. Consequently, this publication is not included in 2.5.2 but is discussed here as it contributes to the general understanding of absorber-free LTW. The study found that the industry standard for the upper part of the fixing unit is quartz white glass plates. For the lower fixing unit, five materials – brass, copper, stainless steel, aluminium, and glass – were tested. The authors attributed differences in welding performance to the reflective and heat-conducting properties of these materials. However, they were unable to isolate the effects of heat conduction from reflection due to the experimental setup. The study found that when highly reflective materials such as aluminium or copper were used as the base fixing material, the best welding results were achieved at the highest weld velocity (12 mm/s). The authors postulated that a significant portion of the incoming radiation was reflected by the base fixture, passing through the welding partners a second time and generating additional heat [98].

This concludes the overview of publications on absorber-free LTW applied to polymers other than PC. The approach used for bonding the cover film to the RC is detailed in 4.4.3.6

D.2 Absorber-based LTW of polymers

Before suitable lasers in the range of 1600 nm to 2100 nm became widely available, making absorber-free LTW a feasible option, polymers were welded using absorbers. The fundamentals of this approach have already been discussed in appendix A.3.3. However, absorber-based laser welding remains an area of active research, particularly for the challenging-to-weld polymer PC. Therefore, an overview of this topic follows, beginning with the introduction of the Transmission Welding by an Incremental Scanning Technique

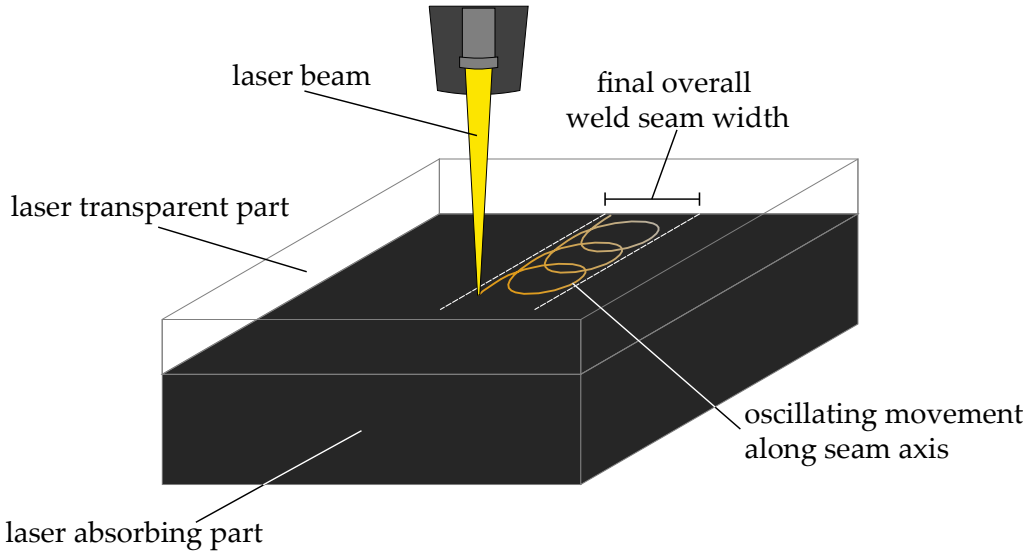

Figure D.1: The TWIST® irradiation strategy is a specialised form of the beam wobbling approach, where the final weld seam width is achieved by repeatedly overlaying geometrical patterns, resulting in a weld that exceeds the original laser beam width. Adapted after [202], [207].

(TWIST®) irradiation strategy using Carbon Black (cb) in 2007 and concluding with a recent study on underwater LTW of PC in 2024.

To enhance heating in the weld seam and promote intermolecular diffusion, the TWIST® strategy was developed and introduced by Boglea, Olowinsky and Gillner [300] in 2007. This method incrementally irradiates the weld seam along meandering, zigzag, or other geometrical paths within the seam's boundaries, as visualised in figure D.1 [207], [300]. In 2010, Boglea, Olowinksy and Gilner [301] conducted further experiments, applying this method to welding PP doped with 0.5-wt% cb. The TWIST® irradiation strategy enables precise control over temperature distribution in the weld seam, allowing defined heating and cooling areas within its boundaries by adjusting oscillation geometries. Additionally, it provides flexibility in tailoring weld seam width [207], [300], [301].

Despite its advancements, a key challenge of the TWIST® strategy remains the optimisation of contradicting performance factors – such as laser power, pulse frequency, scanning speed, wobble width, and wobble frequency – to produce high-quality bonds. The quality is often assessed in terms of weld seam width and lap shear strength. To address this, Kumar *et al.* [302] applied Machine Learning to develop a two-step optimisation model. First, an artificial neural network was trained to establish relationships between performance parameters and output characteristics. Then, two optimisation algorithms were applied to determine the optimal parameter sets. Among them, Non-dominated Sorted Genetic Algorithm II outperformed the alternative optimiser, offering a range of Pareto-optimal solutions rather than a single optimum, though it required a longer convergence time. The simulated results were validated through weld tests, leading the authors to conclude that combining artificial neural network with an optimiser is a reliable approach for optimising parameter sets for the TWIST® strategy [302].

In 2017, Acherjee [303] expanded on his prior research with a study focused specifically on absorber-based LTW of PC – a crucial step in understanding the current state of the art in welding this material. Using the Design-expert® software, the authors identified an optimal combination of weld seam width (2.65 mm) and weld strength (61.61 N/mm). Their model predicted that this combination could be achieved by welding at a speed of 12.27 mm/s from a stand-off distance of 31.73 mm, using a laser power of 20 W, and

applying a clamping pressure of 2.83 MPa. The study used 4 mm thick PC sheets – one natural and one doped with 0.1-wt% cb – welded with a diode laser ($\lambda = 809$ nm) [303]. While the findings provide valuable insight into process parameters, the proposed weld seam width would be unsuitable for microfluidic applications.

Not all absorber-based LTW approaches rely on absorbers that visibly colour the recipient material. In 2019, Mamuschkin, Aden and Olowinsky [304] investigated the use of the absorbing dye Lumogen® 788 (BASF SE, Ludwigshafen, Germany) for welding PC. As discussed in appendix A.3.3, absorbing dyes provide an alternative to conventional pigments. The authors used 0.04-wt% Lumogen® 788 to optimise transmittance and absorption properties with an adjustable laser beam source. To achieve a pre-defined wide HAZ, they analysed heat generation via absorption and thermal conduction, considering the effects of laser wavelength (varied between 850 nm and 884 nm) and scanning velocity (varied between 1 mm/s and 5 mm/s). Keeping the laser power constant at 0.75 W, they found that HAZ width decreased with lower absorption coefficients and higher welding velocities. Their simulation and experimental data indicated that the optical penetration depth – linked to the absorption coefficient – must exceed both the Rayleigh length of the laser beam and the sample thickness. The authors suggested that their findings could be extended to absorber-free LTW of PC by employing a laser with a characteristic wavelength above 1600 nm [304].

In recent years, new metal-based absorbers have been explored for welding dissimilar materials, such as polyarylsulfone (PASF) to PC. In 2023, Yu, Zhang and Wang [208] examined residual stress distribution during welding of 2 mm thick PASF and PC, analysing stress progression along the weld path and across the seam's thickness and width. Their simulations revealed a strong correlation between stress patterns and temperature distribution. This research was followed up in 2024 by Yu *et al.* [305], who investigated the effect of line energy (2 J/mm to 8 J/mm) on weld quality in PASF–PC joints using magnesium zinc alloy as absorbers. They found that seam width increased with higher line energy, but weld strength peaked at 4.67 J/mm. At this energy level, the generated heat was close to PASF's melting temperature (327.5 °C), minimising polymer decomposition while allowing sufficient interdiffusion, thus reducing bubble formation in the weld seam [305].

A different metal-based absorber approach was presented in 2023 by Kumar Goyal, Yadav and Kant [306], who investigated electrolytic iron powder (EIP) as an absorber between two 2 mm thick PC sheets. The lower welding partner was coated with EIP in the target weld area and joined using a fibre laser ($\lambda = 1080$ nm). Their analysis revealed that smaller bubbles enhanced lap shear strength, whereas larger bubbles weakened the joint due to void formation and degraded material in the weld seam. The authors concluded that EIP is a promising absorber material, though further parameter optimisation is required [306].

Appendix

E Initial layout of membrane and woven fabric: Technical drawings

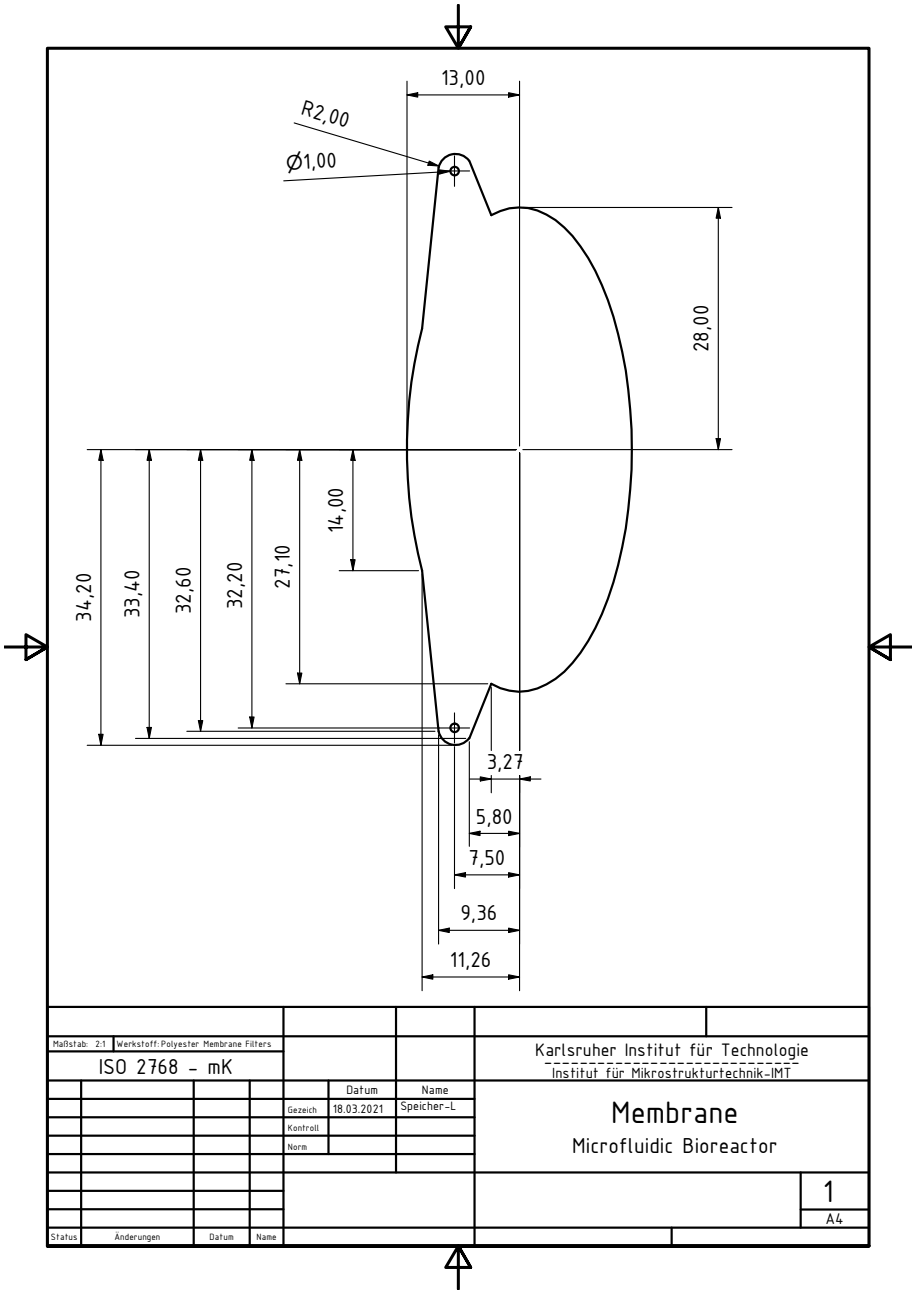

Figure E.1: Technical drawing of the membrane layout used in the initial design of the MBR.

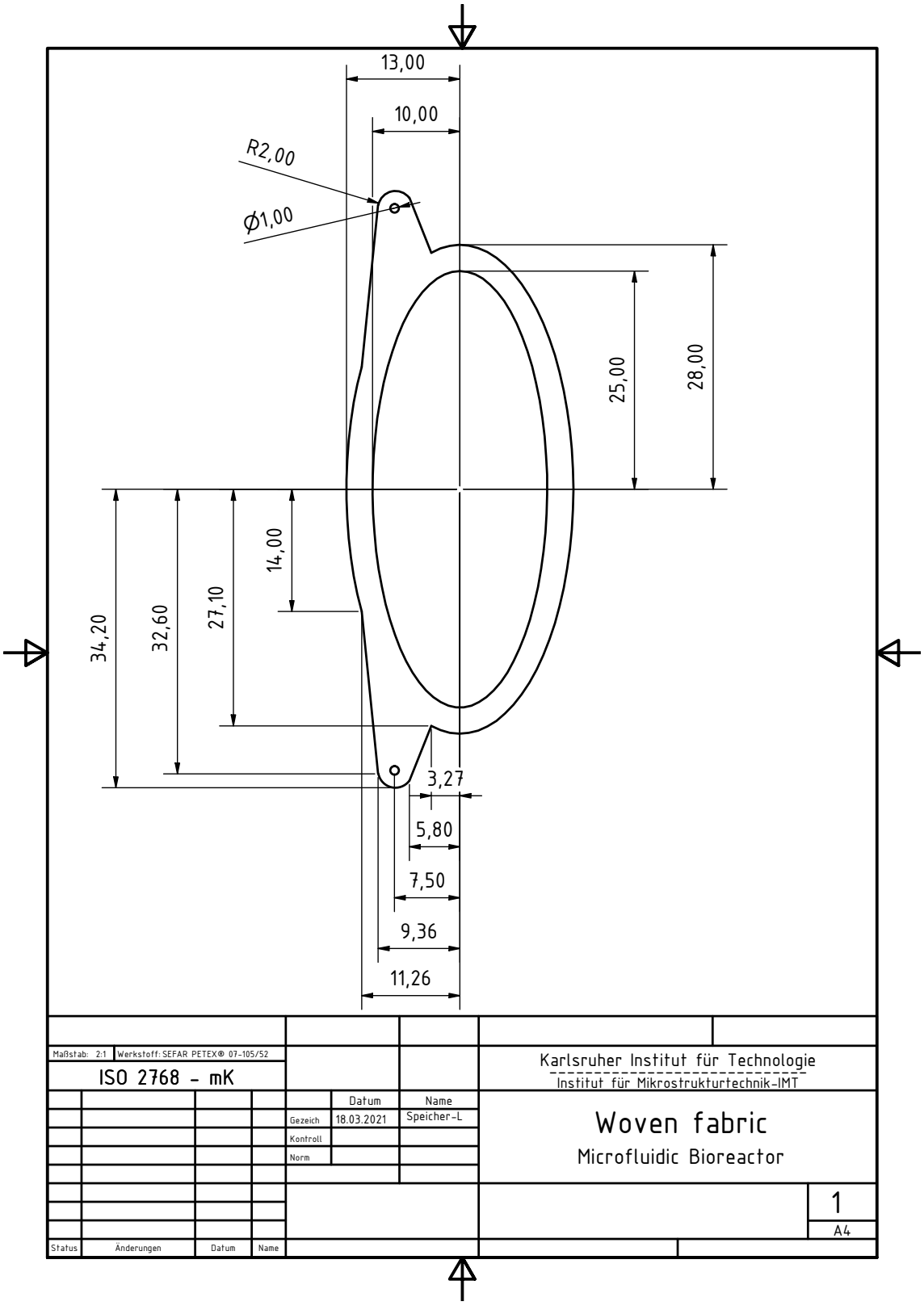

Figure E.2: Technical drawing of the woven fabric cutout used to shield the membrane in the MBR from too much wear during the ultrasonic welding process.

F Initial Microfluidic Bioreactor: Technical drawings

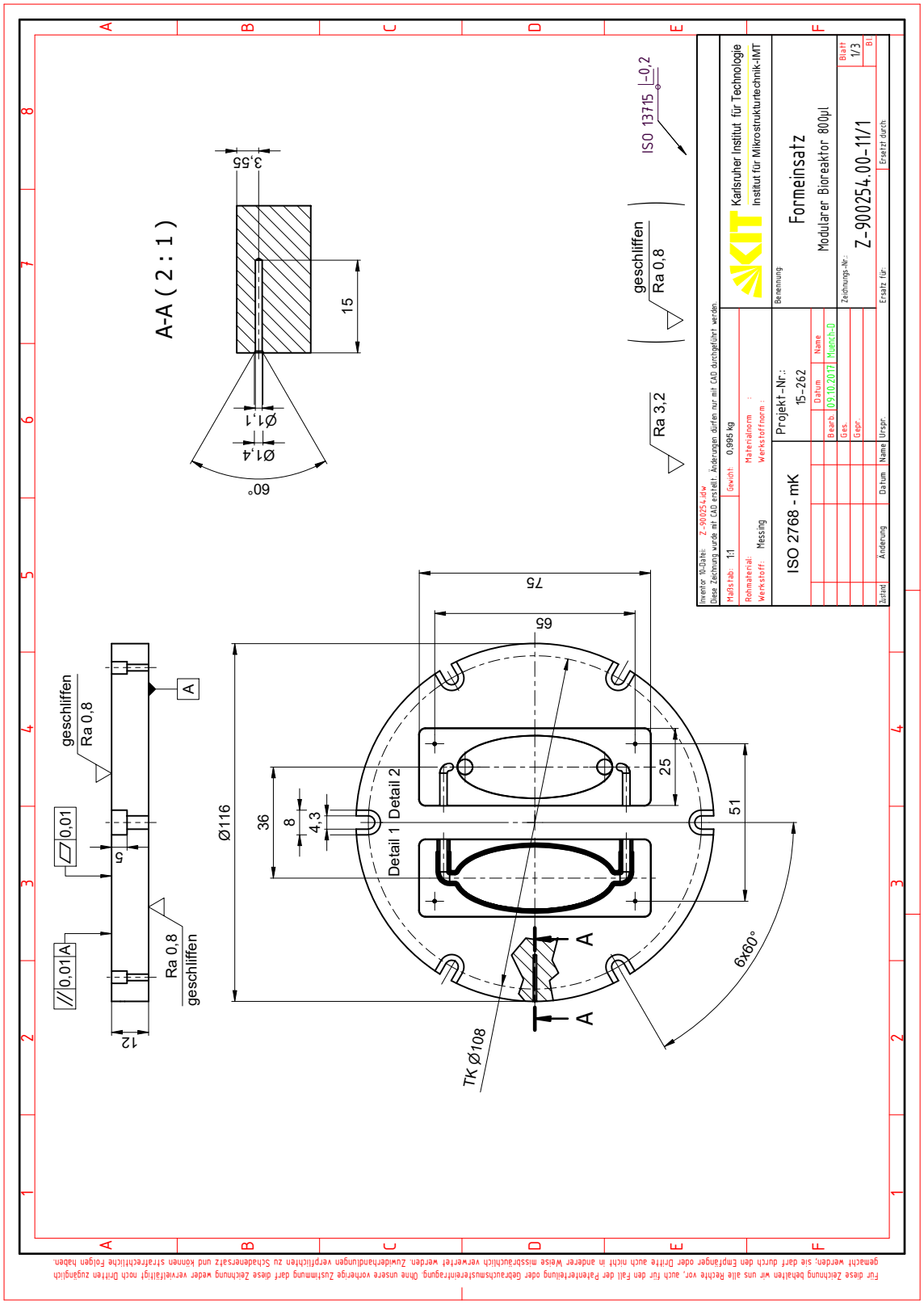

Figure F.1: Technical drawing of the MBR hot embossing mould. Adapted from [14]

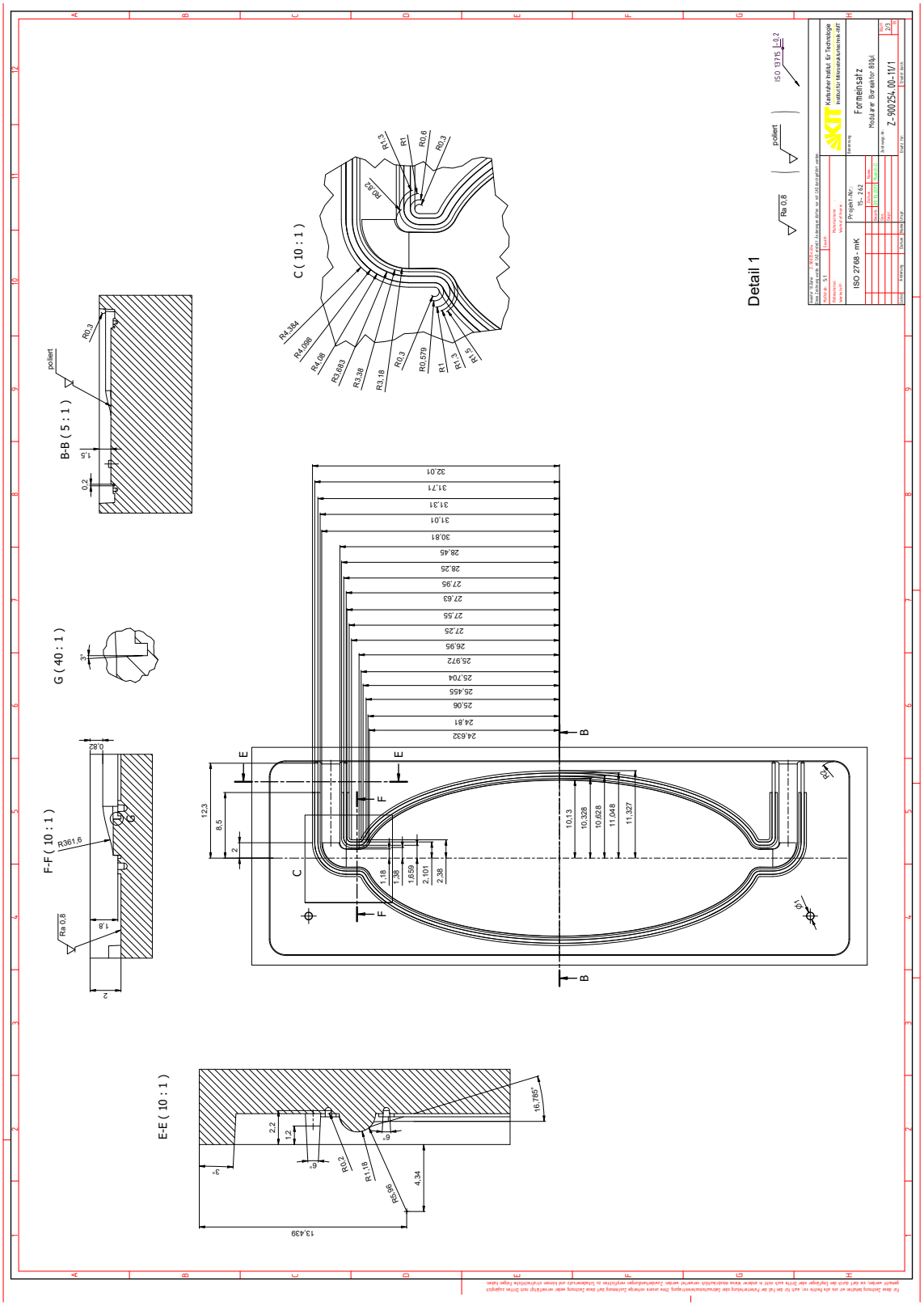

Figure F.2: Technical drawing of the MBR hot embossing mould. Details of the lower chip half. Adapted from [14]

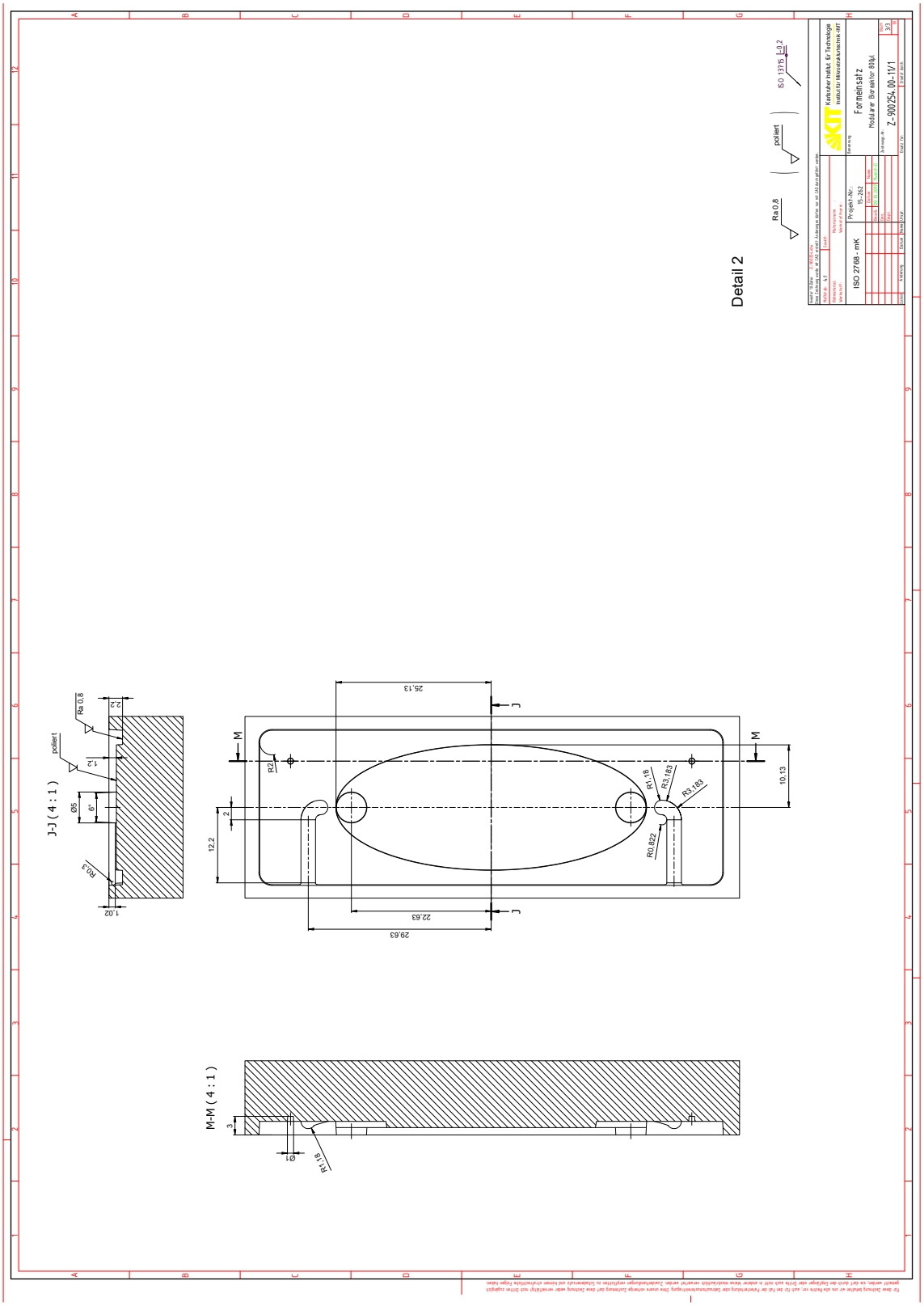

Figure F.3: Technical drawing of the MBR hot embossing mould. Details of the upper chip half. Adapted from [14]

G Redesigned Microfluidic Bioreactor: Technical drawings

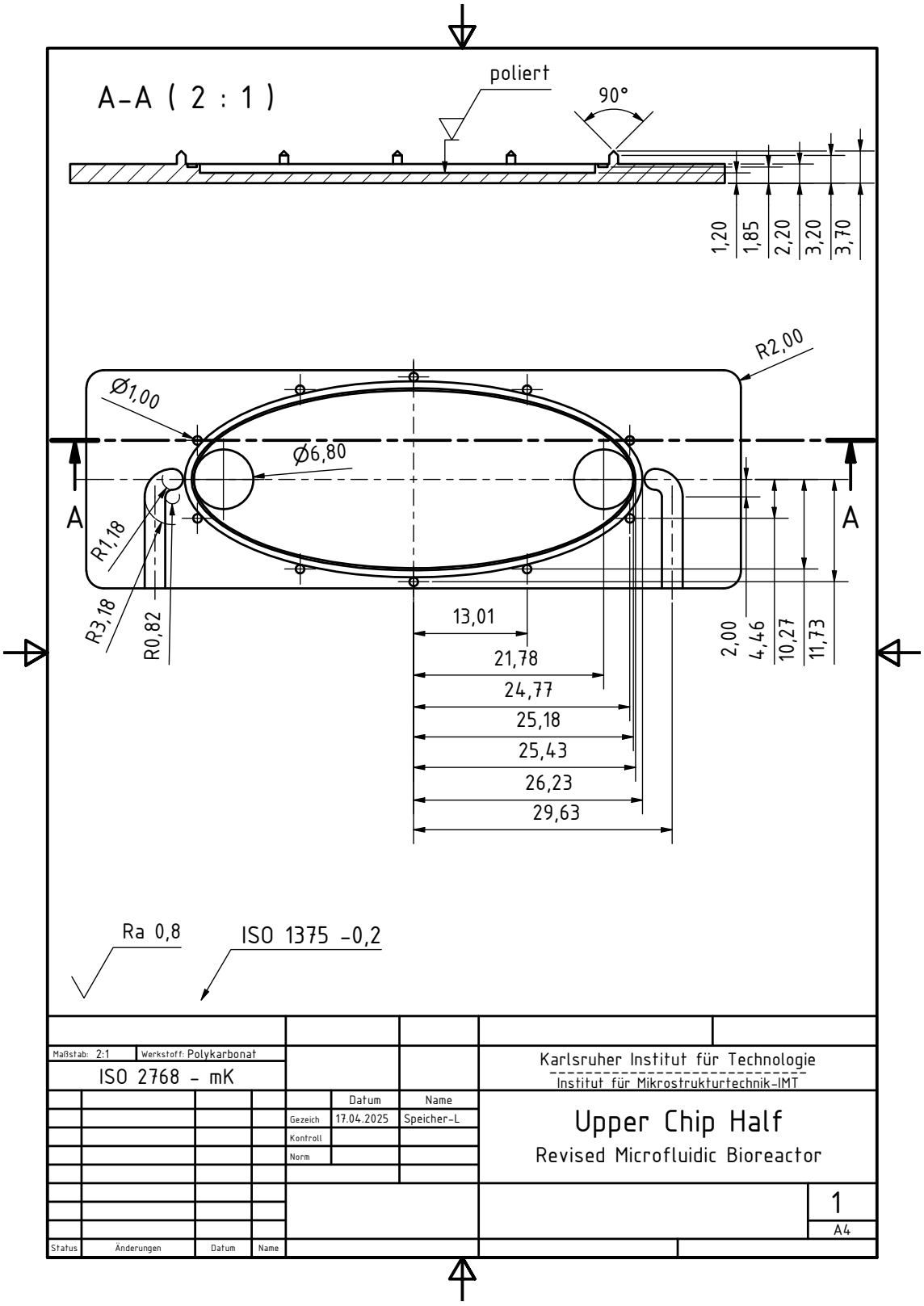

Figure G.1: Technical drawing of the upper chip half of the redesigned MBR.

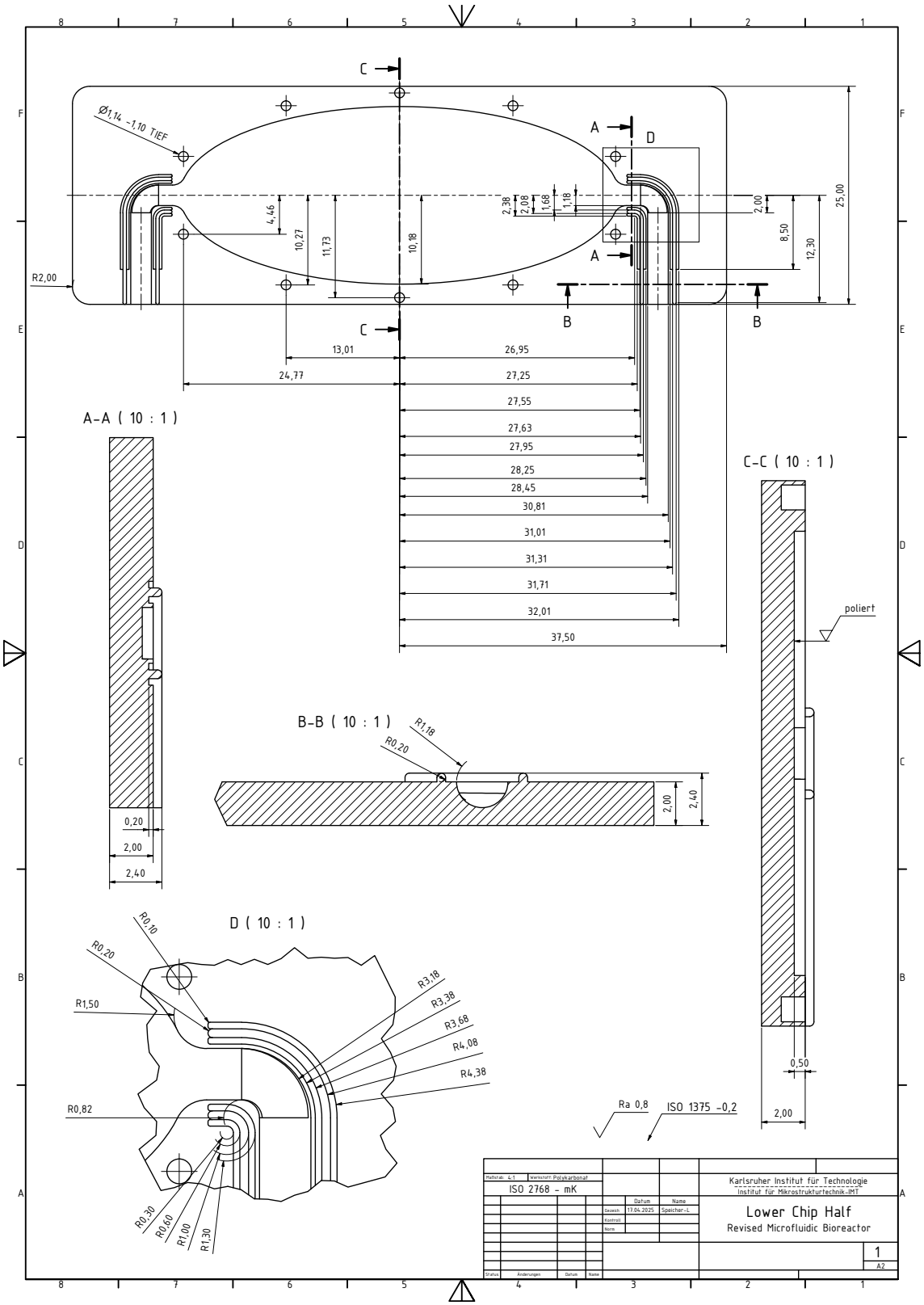

Figure G.2: Technical drawing of the lower chip half of the redesigned MBR.

H Layout of membrane for pillar-and-groove MBR: Technical drawing

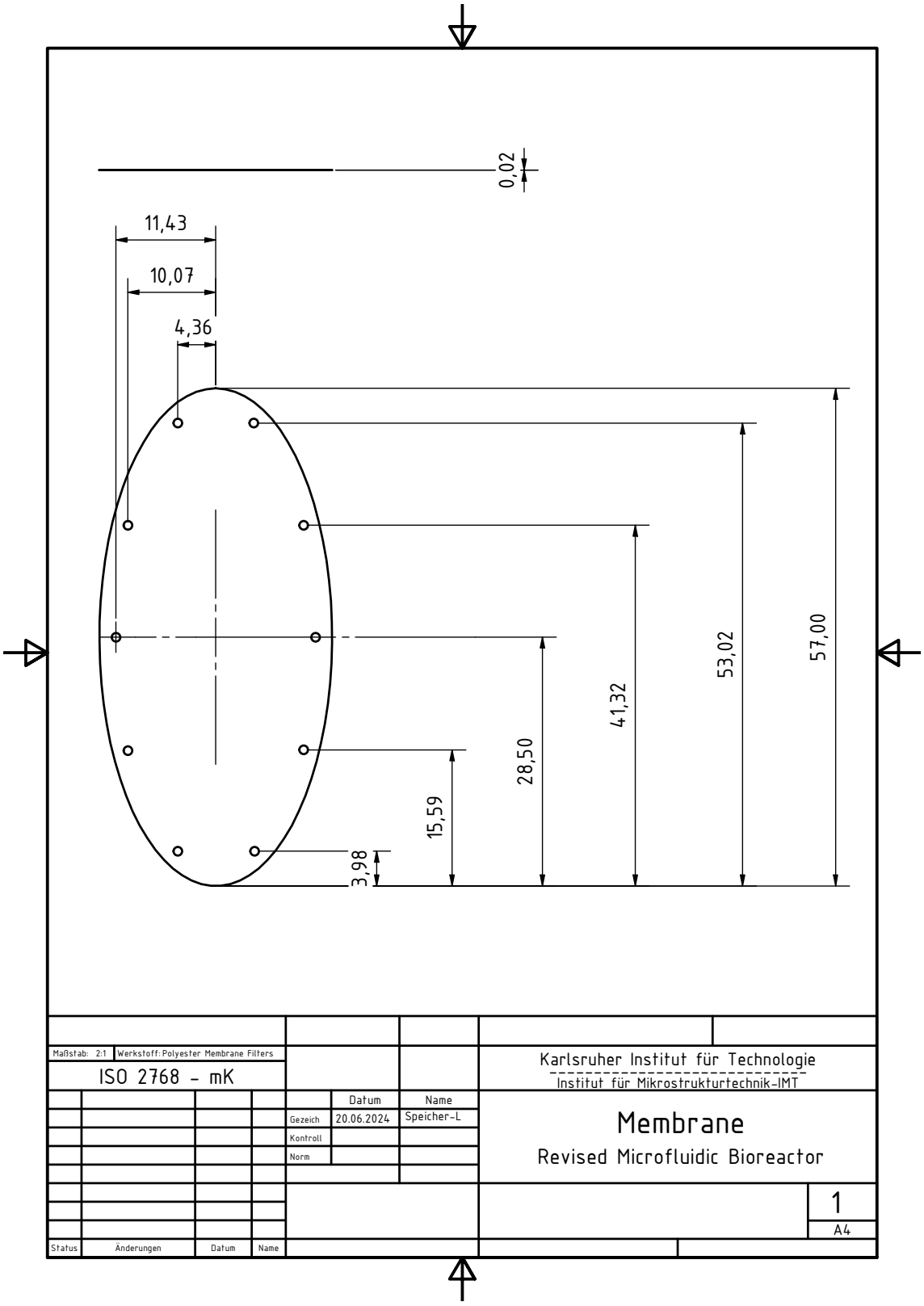

Figure H.1: Technical drawing of the membrane layout used for the revised design of the MBR. The openings for the pillars are positioned so that the membrane is put under initial stress.

I 9-Channel Root Chip: Technical drawing

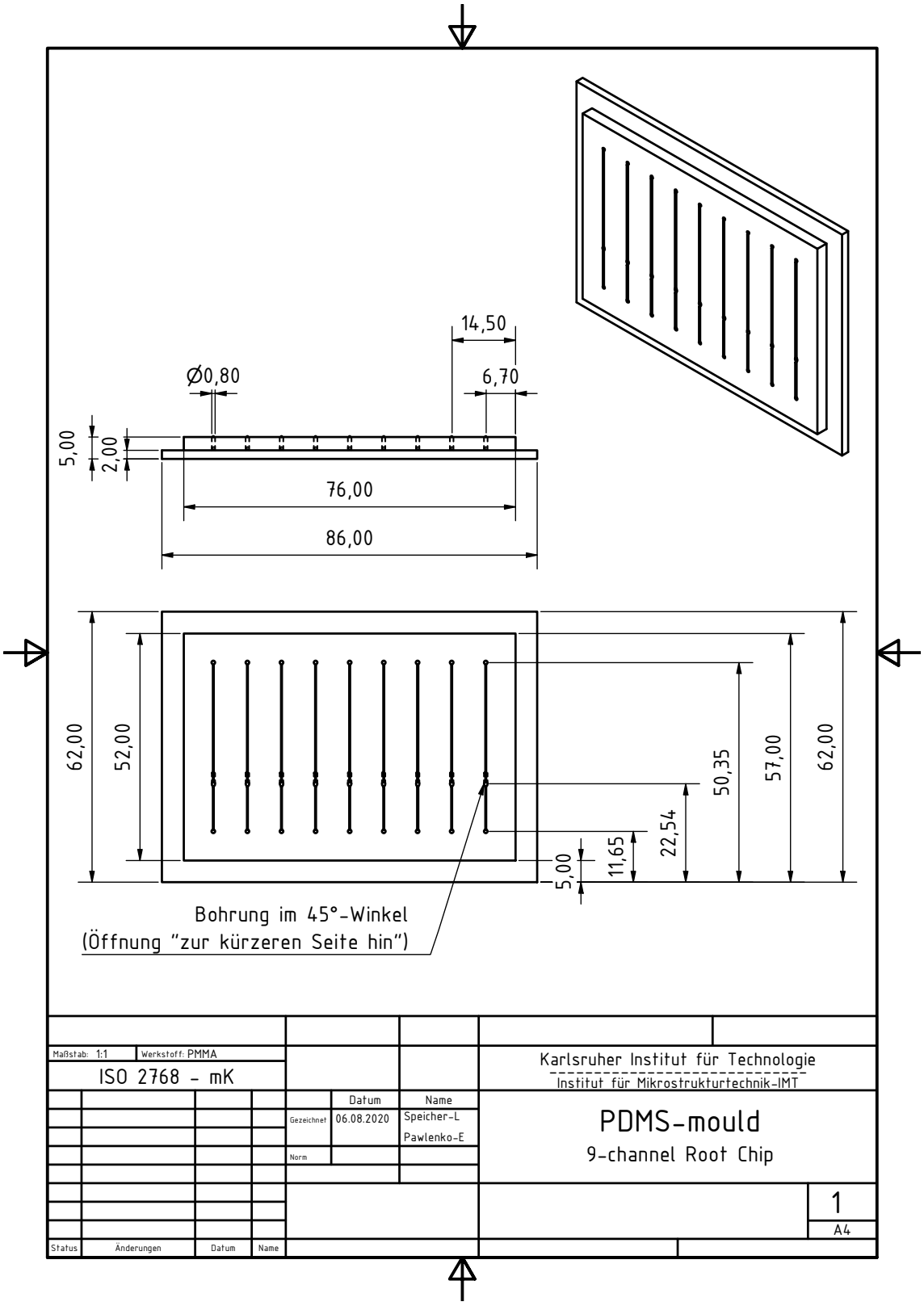

Figure I.1: Technical drawing of the PDMS-mould for creating the 9-channel RC.

J PC RC upper chip half: Technical drawing

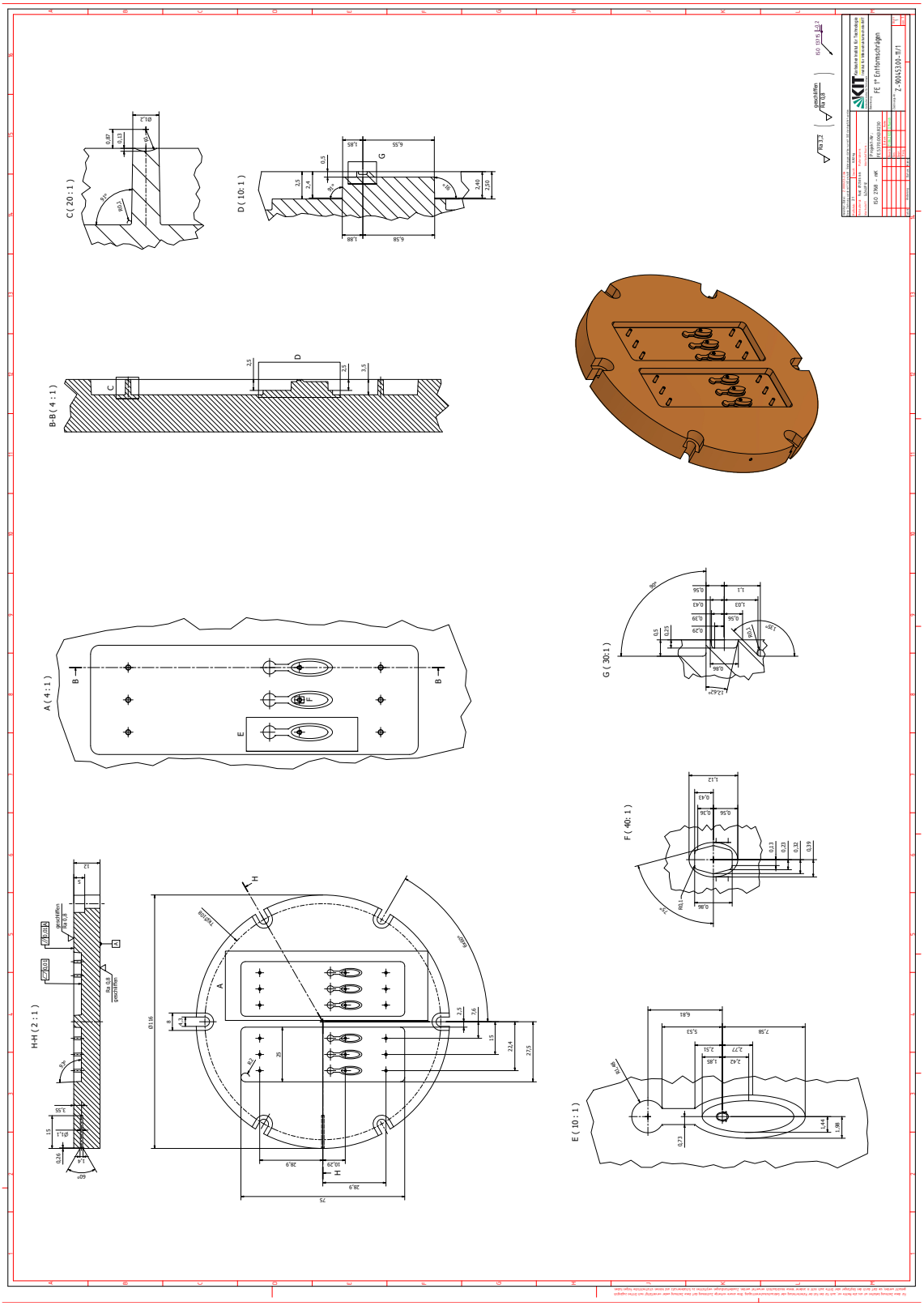

Figure J.1: Technical drawing of the hot embossing mould for creating the upper chip half of the PC RC. The inlets for the transfer tips containing the pre-germinated seedlings are formed into this chip half.

K PC RC lower chip half: Technical drawing

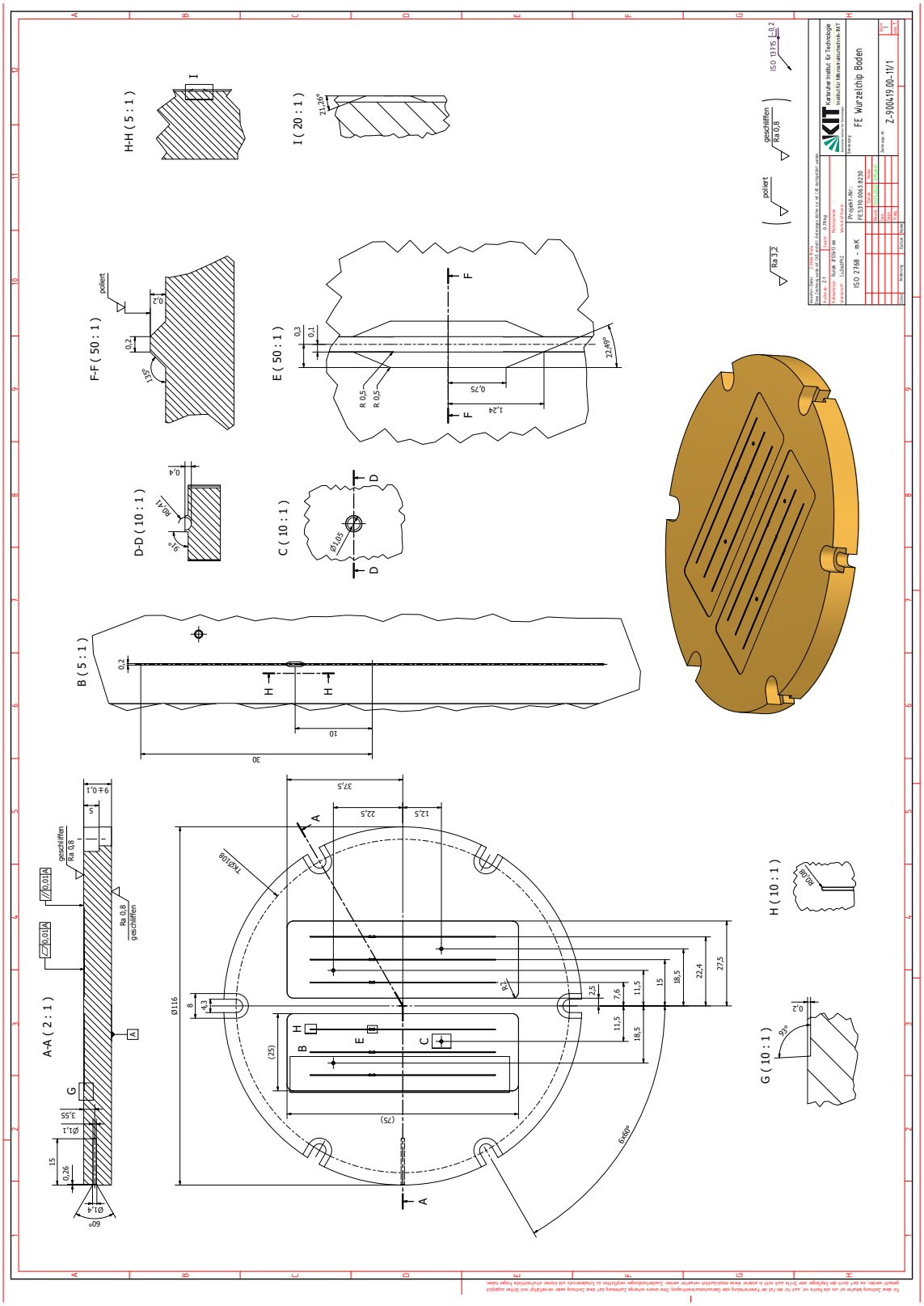

Figure K.1: Technical drawing of the HE-mould for thermoforming the lower chip half of the PC RC containing the channel structure of the analysis channel.

L Preparation and recording of LTW cross-sections

To assess the seam quality of the laser-welded stacks, cross-sections of the seams were prepared at the Materialography Laboratory of the Institute for Applied Materials – Materials Science and Engineering (IAM-WK), KIT, Karlsruhe, Germany. After laser welding, a 3.5 cm long segment was cut from the fabricated chip using a circular saw. The sections were embedded in Epoclear (Schmitz Metallographie GmbH, Herzogenrath, Germany), prepared according to the manufacturer's instructions with a mixing ratio of 100 g resin to 55 g hardener. Following overnight curing, the specimens were demoulded, deburred, and levelled.

Subsequently, the samples were mounted in a central force holder accommodating up to six specimens simultaneously. Sanding was performed according to the parameters listed in table L.1. The central force was set to 60 N, the head speed to 120 rpm, and the base speed to 60 rpm, operating in concordant rotation. Between sanding rounds, the specimens were briefly rinsed under clean water while remaining in the holder.

Sanding with	Time	Head speed	Grain size
Wet sanding sandpaper	2 × 1 min	120 rpm	320 grit and water
Wet sanding sandpaper	3 × 1 min	120 rpm	600 grit and water
Wet sanding sandpaper	5 × 1 min	120 rpm	1000 grit and water
Wet sanding sandpaper	8 × 1 min	120 rpm	2500 grit and water

Table L.1: Sanding parameters for preparing LTW samples. All steps were performed on a Buehler Automet 300 (Buehler Ltd., Leinfelden-Echterdingen, Germany) under central force at 60 N and 60 rpm platen speed. Sandpaper: WS Flex 18C, 320 grit, 600 grit, 1000 grit, 2500 grit, Hermes Schleifmittel GmbH, Hamburg, Germany.

After sanding, the samples were removed from the central force holder and mounted individually in a single-specimen holder. Polishing was conducted for 5 min per step, with the base plate rotating at 150 rpm and the head plate at 60 rpm in counter-rotation. The applied single-specimen force was 10 N. Table L.2 summarises the polishing cloths, diamond suspensions, and lubricants used. Between polishing steps, the specimens were taken out of the holder, rinsed, and placed in an ultrasonic bath filled with isopropanol. After the final polishing step, they were dried using compressed air.

Polishing with	Time	Head speed	Grain size
MD-SAT polishing cloth	5 min	150 rpm	6 µm diamond suspension
MD-DUR polishing cloth	5 min	150 rpm	3 µm diamond suspension
MD-DAC polishing cloth	5 min	150 rpm	1 µm diamond suspension

Table L.2: Polishing parameters for preparing LTW samples. All steps were performed on a Buehler Automet 300 (Buehler Ltd., Leinfelden-Echterdingen, Germany) under single specimen force at 10 N and at a platen speed of 60 rpm. Monocrystalline diamond suspensions (50 cts/L, Schmitz Metallographie GmbH, Herzogenrath, Germany) and oil-based lubricant coolTec III (Schmitz Metallographie GmbH, Herzogenrath, Germany) were applied throughout. Polishing cloths were supplied by Struers GmbH, Willich, Germany.

The prepared cross-sections were then examined using a Keyence VHX-7000 microscope (Keyence Deutschland GmbH, Frankfurt a.M., Germany) under polarised light.

List of Figures

List of Tables

Publications

In progress

[A1] **L. M. Speicher**, K. Chau-Nguyen, L. Supp, R. Ahrens, A. E. Guber, J. G. Korvink and D. Mager, *Directly fixed and sealed ultra-thin membrane enables an autoclavable two-chamber bioreactor with selective permeability and optical access.*

Journal Articles & Book Chapters

[A2] G. Dupouy, G. Singh, **L. M. Schmidt-Speicher**, E. Hoffmann, S. Baudrey, R. Ahrens, A. E. Guber, M. Ryckelynck, E. Herzog, M.-E. Chabouté and A. Berr, "Microfluidics to Follow Spatiotemporal Dynamics at the Nucleo-Cytoplasmic Interface During Plant Root Growth", in *Methods for Plant Nucleus and Chromatin Studies*, C. Baroux and C. Tatout, Eds., vol. 2873, New York, NY: Springer US, 2025, pp. 223–245, doi: 10.1007/978-1-0716-4228-3_13.

[A3] N. Hering, A.-C. Schmit, E. Herzog, L.-T. Corbin, **L. Schmidt-Speicher**, R. Ahrens, M.-L. Fauconnier and P. Nick, "Spearmint targets microtubules by (-)–carvone", *Horticulture Research*, vol. 11, no. 7, Art. no. 151, Jul. 2024, doi: 10.1093/hr/uhae151.

[A4] **L. M. Schmidt-Speicher** and K. Länge, "Microfluidic integration for electrochemical biosensor applications", *Current Opinion in Electrochemistry*, vol. 29, Art. no. 100755, Oct. 2021, doi: 10.1016/j.coelec.2021.100755.

[A5] **L. M. Schmidt-Speicher**, T. Mellert, A. C. Hurtado Rivera, K. Länge, R. Ahrens and A. E. Guber, "Rapid prototyping of moulds for PDMS-based microfluidic chips", *Current Directions in Biomedical Engineering*, vol. 7, no. 2, pp. 255–259, Oct. 2021, doi: 10.1515/cdbme-2021-2065.

[A6] T. Finkbeiner, C. Manz, M. L. Raorane, C. Metzger, **L. Schmidt-Speicher**, N. Shen, R. Ahrens, J. Maisch, P. Nick and A. E. Guber, "A modular microfluidic bioreactor to investigate plant cell–cell interactions", *Protoplasma*, vol. 259, no. 1, pp. 173–186, May 2021, doi: 10.1007/s00709-021-01650-0.

Conference Contributions & Reports

[A7] **L. M. Speicher**, C. Metzger, R. Ahrens, D. Mager, A. E. Guber and J. G. Korvink, "Wrinkle-free bonding of thin membranes in a microfluidic bioreactor", in *MikroSystemTechnik Kongress 2023*, (Dresden, Deutschland, 23rd–25th Oct. 2023), VDE Verlag, 2023, pp. 233–236, isbn: 978-3-80076204-0.

[A8] **L. M. Schmidt-Speicher**, C. Metzger, F. Kinn, B. Bailer and R. Ahrens, "Connection of ph-1 SMA HP5-sensor to microfluidic bioreactor", PreSens, Regensburg, Germany, Tech. Rep., May 2022.

[A9] P. W. Doll, **L. Schmidt-Speicher**, A. Bacher, A. Muslija, R. Ahrens and A. E. Guber, "Modifikation eines Cryo-basierten Reaktiven Ionenätzprozesses zur Herstellung von bioinspirierten Nanokonusstrukturen", in *MikroSystemTechnik Kongress 2021*, (Ludwigsburg, Deutschland, 8th–10th Nov. 2021), VDE Verlag, 2021, isbn: 978-3-8007-5656-8.

[A10] **L. M. Schmidt-Speicher**, L. Supp, C. Metzger, R. Ahrens, P. Nick and A. E. Guber, "Development of a modular microfluidic bioreactor to further research the inter-cellular communication of plant cells and pathogens", in *MikroSystemTechnik Kongress 2021*, (Ludwigsburg, Deutschland, 8th–10th Nov. 2021), VDE Verlag, 2021, pp. 543–547, isbn: 978-3-8007-5656-8.

Supervised Theses

[B1] Y. Peiffer, "Optimierung eines mikrofluidischen Wurzelchips: Ansätze für eine flexible Fluidzuführung sowie für die Serienfertigung", Master's Thesis, Karlsruhe Institute of Technology, Karlsruhe, Germany, Dec. 2021.

[B2] L. Supp, "Untersuchung und Optimierung des Strömungsverhaltens innerhalb eines mikrofluidischen Bioreaktors zur Kultivierung von Pflanzenzellen", Master's Thesis, Karlsruhe Institute of Technology, Karlsruhe, Germany, Dec. 2021.

[B3] B. Bailer, "Konstruktiver Anschluss von Sensoren an einen mikrofluidischen Bioreaktor sowie deren Testung auf Eignung für die online-Ermittlung der entsprechenden Parameters", Master's Thesis, Karlsruhe Institute of Technology, Karlsruhe, Germany, Apr. 2021.

[B4] T. Mellert, "Additive Fertigung und Untersuchung eines Formeinsatzes für PDMS basierte Mikrofluidikchips", Master's Thesis, Karlsruhe Institute of Technology, Karlsruhe, Germany, Mar. 2021.

[B5] E. Pawlenko, "Optimierung eines mikrofluidischen Chips zur Untersuchung des Wurzelwachstums und Ermittlung der industriellen Fertigungsmöglichkeiten durch eine Unternehmensstudie", Master's Thesis, Karlsruhe Institute of Technology, Karlsruhe, Germany, Nov. 2020.

Classes

- BioMEMS IV lecture series – Mikrosystemtechnik für Life-Sciences und Medizin:
  - WS 2020/21: 2 lectures
  - SS 2021: 3 lectures
  - WS 2021/22: 3 lectures
- Praktikum zur Vorlesung "Grundlagen der Mikrosystemtechnik"
  - WS 2019/20
  - SS 2020
  - WS 2020/21
  - SS 2021
  - WS 2021/22

Bibliography

[1] T. Frische, S. Egerer, S. Matezki, C. Pickl and J. Wogram, "5-Point programme for sustainable plant protection", *Environmental Sciences Europe*, vol. 30, no. 8, pp. 1–17, Mar. 2018, doi: 10.1186/s12302-018-0136-2.

[2] S. Fleischer, "Nachhaltigkeit im Weinbau", in *Chefsache Nachhaltigkeit: Praxisbeispiele aus Unternehmen*, P. Buchenau, M. Geßner, C. Geßner and A. Kölle, Eds., Wiesbaden: Springer Gabler, 2016, pp. 101–110, isbn: 978-3-658-11071-0.

[3] B. O. Olivares Campos, M. Araya-Alman and E. E. Marys, Eds., *Sustainable Crop Plants Protection: Implications for Pest and Disease Control*. Basel: MDPI - Multidisciplinary Digital Publishing Institute, 2023, isbn: 978-3-0365-9150-6.

[4] S. Del Duca, S. Mocali, F. Vitali *et al.*, "Impacts of soil management and sustainable plant protection strategies on soil biodiversity in a Sangiovese vineyard", *Land*, vol. 13, no. 5, Art. no. 599, Apr. 2024, doi: 10.3390/land13050599.

[5] H. Molisch, "Der Einfluss einer Pflanze auf die Andere, Allelopathie", *Nature*, vol. 141, no. 3568, pp. 493–493, Mar. 1938, doi: 10.1038/141493a0.

[6] U. Sonnewald, "Allelophysiologie", in *Strasburger - Lehrbuch der Pflanzenwissenschaften*, Berlin, Heidelberg: Springer Berlin Heidelberg, 13th May 2021, pp. 615–645, doi: 10.1007/978-3-662-61943-8_16.

[7] J. S. Bale, J. C. Van Lenteren and F. Bigler, "Biological control and sustainable food production", *Philosophical Transactions of the Royal Society B: Biological Sciences*, vol. 363, no. 1492, pp. 761–776, Sep. 2007, doi: 10.1098/rstb.2007.2182.

[8] S. Madlhophe, U. V. Ogugua, F. N. Makhubu and S. Figlan, "Use of biological control agents for managing fungal pathogens in Solanaceae crops: Progress and future perspectives – a review", *Discover Applied Sciences*, vol. 7, no. 1, Art. no. 83, Jan. 2025, doi: 10.1007/s42452-025-06500-9.

[9] Y. C. Colmenarez and C. Vasquez, "Benefits associated with the implementation of biological control programmes in Latin America", *BioControl*, vol. 69, no. 3, pp. 303–320, May 2024, doi: 10.1007/s10526-024-10260-7.

[10] Å. Lankinen, J. Witzell, K. Aleklett *et al.*, "Challenges and opportunities for increasing the use of low-risk plant protection products in sustainable production. A review", *Agronomy for Sustainable Development*, vol. 44, no. 2, Art. no. 21, Apr. 2024, doi: 10.1007/s13593-024-00957-5.

[11] V. Halleux, "Sustainable use of plant protection products", European Parliament, Briefing PE 739.218, Nov. 2023, Art. no. 12, [Online]. Available: https://www.europarl.europa.eu/RegData/etudes/BRIE/2022/739218/EPRS_BRI(2022)739218_EN.pdf (Accessed: 14/05/2025).

[12] A. Berlin, H. N. Källström, A. Lindgren and Å. Olson, "Scientific evidence for sustainable plant disease protection strategies for the main arable crops in Sweden. A systematic map protocol", *Environmental Evidence*, vol. 7, no. 1, Art. no. 31, Dec. 2018, doi: 10.1186/s13750-018-0141-3.

[13] K. Kreppenhofer, "Modular biomicrofluidics: Mikrofluidikchips im Baukastensystem für Anwendungen aus der Zellbiologie", Dissertation, Karlsruher Institut für Technologie, Karlsruhe, 2013, doi: 10.5445/KSP/1000035104.

[14] T. Finkbeiner, "Entwicklung eines mikrofluidischen Bioreaktors für die Kultivierung von Pflanzenzellen", Ph.D. dissertation, Karlsruher Institut für Technologie (KIT), Karlsruhe, Jul. 2019, doi: 10.5445/IR/1000096929.

[15] J.-M. Ko, J. Ju, S. Lee and H.-C. Cha, "Tobacco protoplast culture in a polydimethylsiloxane-based microfluidic channel", *Protoplasma*, vol. 227, no. 2–4, pp. 237–240, May 2006, doi: 10.1007/s00709-005-0142-2.

[16] M. Held, C. Edwards and D. V. Nicolau, "Examining the behaviour of fungal cells in microconfined mazelike structures", in *Imaging, Manipulation, and Analysis of Biomolecules, Cells, and Tissues VI*, D. L. Farkas, D. V. Nicolau and R. C. Leif, Eds., San Jose, CA, Feb. 2008, Art. no. 68590U, doi: 10.1117/12.759453.

[17] Y. Cao, J. Yang, Z. Q. Yin *et al.*, "Study of high-throughput cell electrofusion in a microelectrode-array chip", *Microfluidics and Nanofluidics*, vol. 5, no. 5, pp. 669–675, Apr. 2008, doi: 10.1007/s10404-008-0289-1.

[18] A. K. Yetisen, L. Jiang, J. R. Cooper, Y. Qin, R. Palanivelu and Y. Zohar, "A microsystem-based assay for studying pollen tube guidance in plant reproduction", *Journal of Micromechanics and Microengineering*, vol. 21, no. 5, Art. no. 054018, Apr. 2011, doi: 10.1088/0960-1317/21/5/054018.

[19] N. Hu, J. Yang, Z.-Q. Yin *et al.*, "A high-throughput dielectrophoresis-based cell electrofusion microfluidic device", *ELECTROPHORESIS*, vol. 32, no. 18, pp. 2488–2495, Aug. 2011, doi: 10.1002/elps.201100082.

[20] H. Wu, W. Liu, Q. Tu *et al.*, "Culture and chemical-induced fusion of tobacco mesophyll protoplasts in a microfluidic device", *Microfluidics and Nanofluidics*, vol. 10, no. 4, pp. 867–876, Apr. 2011, doi: 10.1007/s10404-010-0720-2.

[21] C. G. Agudelo, A. Sanati, M. Ghanbari, M. Packirisamy and A. Geitmann, "A microfluidic platform for the investigation of elongation growth in pollen tubes", *Journal of Micromechanics and Microengineering*, vol. 22, no. 11, Art. no. 115009, Sep. 2012, doi: 10.1088/0960-1317/22/11/115009.

[22] B. Zaban, W. Liu, X. Jiang and P. Nick, "Plant cells use auxin efflux to explore geometry", *Scientific Reports*, vol. 4, no. 1, Art. no. 5852, Jul. 2014, doi: 10.1038/srep05852.

[23] Z. Yu, C. R. Boehm, J. M. Hibberd *et al.*, "Droplet-based microfluidic analysis and screening of single plant cells", *PLOS One*, vol. 13, no. 5, Art. no. 0196810, May 2018, doi: 10.1371/journal.pone.0196810.

[24] M. Held, O. Kašpar, C. Edwards and D. V. Nicolau, "Intracellular mechanisms of fungal space searching in microenvironments", *Proceedings of the National Academy of Sciences*, vol. 116, no. 27, pp. 13 543–13 552, Jul. 2019, doi: 10.1073/pnas.1816423116.

[25] K. Sakai, F. Charlot, T. Le Saux *et al.*, "Design of a comprehensive microfluidic and microscopic toolbox for the ultra-wide spatio-temporal study of plant protoplasts development and physiology", *Plant Methods*, vol. 15, no. 1, Art. no. 79, Jul. 2019, doi: 10.1186/s13007-019-0459-z.

[26] E. Kozgunova and G. Goshima, "A versatile microfluidic device for highly inclined thin illumination microscopy in the moss Physcomitrella patens", *Scientific Reports*, vol. 9, no. 1, Art. no. 15182, Oct. 2019, doi: 10.1038/s41598-019-51624-9.

[27] Z. Han, L. Chen, S. Zhang, J. Wang and X. Duan, "Label-Free and Simultaneous Mechanical and Electrical Characterization of Single Plant Cells Using Microfluidic Impedance Flow Cytometry", *Analytical Chemistry*, vol. 92, no. 21, pp. 14 568–14 575, Sep. 2020, doi: 10.1021/acs.analchem.0c02854.

[28] L. Chen, Z. Han, X. Fan, S. Zhang, J. Wang and X. Duan, "An impedance-coupled microfluidic device for single-cell analysis of primary cell wall regeneration", *Biosensors and Bioelectronics*, vol. 165, Art. no. 112374, Oct. 2020, doi: 10.1016/j.bios.2020.112374.

[29] K. Shimizu, Y. Kawakatsu, K.-I. Kurotani *et al.*, "Development of microfluidic chip for entrapping tobacco BY-2 cells", *PLOS One*, vol. 17, no. 4, Art. no. 0266982, Apr. 2022, doi: 10.1371/journal.pone.0266982.

[30] M. Chandrasekar, J. L. Collins, S. Habibi and R. G. Ong, "Microfluidic reactor designed for time-lapsed imaging of pretreatment and enzymatic hydrolysis of lignocellulosic biomass", *Bioresource Technology*, vol. 393, Art. no. 129989, Feb. 2024, doi: 10.1016/j.biortech.2023.129989.

[31] M.-S. Hung, Y.-M. Zhao, K. O. Okeyo and O. Kurosawa, "One-to-one fusion of plant protoplasts by using electrofusion based on electric field constriction", *BioNanoScience*, vol. 14, no. 4, pp. 4520–4531, Feb. 2024, doi: 10.1007/s12668-024-01331-1.

[32] N. A. Dudukovic, E. J. Fong, H. B. Gemeda *et al.*, "Cellular fluidics", *Nature*, vol. 595, no. 7865, pp. 58–65, Jun. 2021, doi: 10.1038/s41586-021-03603-2.

[33] Y. Zhu, P. D. Piehowski, R. Zhao *et al.*, "Nanodroplet processing platform for deep and quantitative proteome profiling of 10–100 mammalian cells", *Nature Communications*, vol. 9, no. 1, Art. no. 882, Feb. 2018, doi: 10.1038/s41467-018-03367-w.

[34] Y. Liang, Y. Zhu, M. Dou *et al.*, "Spatially Resolved Proteome Profiling of <200 Cells from Tomato Fruit Pericarp by Integrating Laser-Capture Microdissection with Nanodroplet Sample Preparation", *Analytical Chemistry*, vol. 90, no. 18, pp. 11 106–11 114, Aug. 2018, doi: 10.1021/acs.analchem.8b03005.

[35] Y. Zhu, M. Dou, P. D. Piehowski *et al.*, "Spatially Resolved Proteome Mapping of Laser Capture Microdissected Tissue with Automated Sample Transfer to Nanodroplets", *Molecular & Cellular Proteomics*, vol. 17, no. 9, pp. 1864–1874, Jun. 2018, doi: 10.1074/mcp.TIR118.000686.

[36] V. K. Balasubramanian, S. O. Purvine, Y. Liang *et al.*, "Cell-Type-Specific Proteomics Analysis of a Small Number of Plant Cells by Integrating Laser Capture Microdissection with a Nanodroplet Sample Processing Platform", *Current Protocols*, vol. 1, no. 5, e153, May 2021, doi: 10.1002/cpz1.153.

[37] C. Luo, R. Wightman, E. Meyerowitz and S. K. Smoukov, "A 3-dimensional fibre scaffold as an investigative tool for studying the morphogenesis of isolated plant cells", *BMC Plant Biology*, vol. 15, no. 1, Art. no. 211, Aug. 2015, doi: 10.1186/s12870-015-0581-7.

[38] J. Maisch, K. Kreppenhofer, S. Büchler *et al.*, "Time-resolved NMR metabolomics of plant cells based on a microfluidic chip", *Journal of Plant Physiology*, vol. 200, pp. 28–34, Aug. 2016, doi: 10.1016/j.jplph.2016.06.004.

[39] J. Comtet, K. H. Jensen, R. Turgeon, A. D. Stroock and A. E. Hosoi, "Passive phloem loading and long-distance transport in a synthetic tree-on-a-chip", *Nature Plants*, vol. 3, no. 4, Art. no. 17032, Mar. 2017, doi: 10.1038/nplants.2017.32.

[40] N. Shamsudhin, H. B. Atakan, N. Laubli *et al.*, "Probing the micromechanics of the fastest growing plant cell – The pollen tube", in *2016 38th Annual International Conference of the IEEE Engineering in Medicine and Biology Society (EMBC)*, Orlando, FL, USA: IEEE, Aug. 2016, pp. 461–464, doi: 10.1109/EMBC.2016.7590739.

[41] K.-I. Kurotani, Y. Kawakatsu, M. Kikkawa *et al.*, "Analysis of plasmodesmata permeability using cultured tobacco BY-2 cells entrapped in microfluidic chips", *Journal of Plant Research*, vol. 135, no. 5, pp. 693–701, Jul. 2022, doi: 10.1007/s10265-022-01406-8.

[42] S. Zhang, T. Zhang, S. Wang, Z. Han, X. Duan and J. Wang, "Phenotyping of single plant cells on a microfluidic cytometry platform with fluorescent, mechanical, and electrical modules", *The Analyst*, vol. 149, no. 17, pp. 4436–4442, Jul. 2024, doi: 10.1039/D4AN00682H.

[43] A. Sanati Nezhad, M. Naghavi, M. Packirisamy, R. Bhat and A. Geitmann, "Quantification of cellular penetrative forces using lab-on-a-chip technology and finite element modeling", *Proceedings of the National Academy of Sciences*, vol. 110, no. 20, pp. 8093–8098, May 2013, doi: 10.1073/pnas.1221677110.

[44] C. Hu, G. Munglani, H. Vogler *et al.*, "Characterization of size-dependent mechanical properties of tip-growing cells using a lab-on-chip device", *Lab on a Chip*, vol. 17, no. 1, pp. 82–90, Nov. 2016, doi: 10.1039/C6LC01145D.

[45] D. E. Sadava, D. M. Hillis, H. C. Heller and S. D. Hacker, *Purves Biologie*, J. Markl, Ed., 10th ed. Berlin, Heidelberg: Springer Spektrum, Jan. 2019, isbn: 978-3-662-58171-1.

[46] W. Nultsch, *Allgemeine Botanik: Glossarium mit 803 Stichworten*, 12th ed. Stuttgart, New York: Georg Thieme Verlag, 2012, isbn: 978-3-13-383312-7.

[47] W. Reißer, F.-M. Dux, M. Möschke and M. Hofmeister, *Pflanzenanatomischer Grundkurs: Module für die differenzierte Gestaltung*, 2nd ed. Berlin, Heidelberg: Springer Berlin Heidelberg, 2019, isbn: 978-3-662-58719-5.

[48] C. Metzger, "Ecosystem on a chip: Understanding communication between plant and fungus", Ph.D. dissertation, Karlsruher Institut für Technologie (KIT), Karlsruhe, Jan. 2023, doi: 10.5445/IR/1000161004.

[49] S. Trachsel, S. M. Kaeppler, K. M. Brown and J. P. Lynch, "Shovelomics: High throughput phenotyping of maize (zea mays l.) root architecture in the field", *Plant and Soil*, vol. 341, pp. 75–87, Nov. 2010, doi: 10.1007/s11104-010-0623-8.

[50] E. S. McLamore and D. M. Porterfield, "Noninvasive tools for measuring metabolism and biophysical analyte transport at the root-rhizosphere interface: Self-referencing electrochemical and optical sensors", in *Plant roots: the hidden half*, A. Eshel and T. Beeckman, Eds., 4th ed., Boca Raton, FL: CRC Press, Apr. 2013, Art. no. 43, pp. 770–787, doi: 10.1201/b14550-54.

[51] B. Rewald and J. E. Ephrath, "Minirhizotron techniques", in *Plant roots: the hidden half*, A. Eshel and T. Beeckman, Eds., 4th ed., Boca Raton, FL: CRC Press, Apr. 2013, Art. no. 42, pp. 754–769, doi: 10.1201/b14550-53.

[52] K. Nagel, *GrowScreen-Rhizo 3*, Forschungszentrum Jülich GmbH, Ed., 2024, [Online]. Available: https://www.fz-juelich.de/de/ibg/ibg-2/expertise/technologie-prozessentwicklung/growscreen-rhizo-3 (Accessed: 23/09/2024).

[53] R. Rellán-Álvarez, G. Lobet, H. Lindner *et al.*, "GLO-Roots: An imaging platform enabling multidimensional characterization of soil-grown root systems", *eLife*, vol. 4, Art. no. 07597, Aug. 2015, doi: 10.7554/eLife.07597.

[54] T. Selzner, J. Horn, M. Landl *et al.*, "3D U-Net segmentation improves root system reconstruction from 3d mri images in automated and manual virtual reality work flows", *Plant Phenomics*, vol. 5, Art. no. 76, Jan. 2023, doi: 10.34133/plantphenomics.0076.

[55] D. Van Dusschoten, R. Metzner, J. Kochs *et al.*, "Quantitative 3D analysis of plant roots growing in soil using magnetic resonance imaging", *Plant Physiology*, vol. 170, no. 3, pp. 1176–1188, Mar. 2016, doi: 10.1104/pp.15.01388.

[56] R. Metzner, A. Eggert, D. Van Dusschoten *et al.*, "Direct comparison of MRI and X-ray CT technologies for 3D imaging of root systems in soil: Potential and challenges for root trait quantification", *Plant Methods*, vol. 11, no. 1, Art. no. 17, 2015, doi: 10.1186/s13007-015-0060-z.

[57] P. S. Dittrich and A. Manz, "Lab-on-a-chip: Microfluidics in drug discovery", *Nature Reviews Drug Discovery*, vol. 5, no. 3, pp. 210–218, Mar. 2006, doi: 10.1038/nrd1985.

[58] P. Abgrall and A.-M. Gué, "Lab-on-chip technologies: Making a microfluidic network and coupling it into a complete microsystem – a review", *Journal of Micromechanics and Microengineering*, vol. 17, no. 5, Art. no. R15, May 2007, doi: 10.1088/0960-1317/17/5/R01.

[59] G. Grossmann, W.-J. Guo, D. W. Ehrhardt *et al.*, "The rootchip: An integrated microfluidic chip for plant science", *The Plant Cell*, vol. 12, pp. 4234–4240, 2011, doi: 10.1105/tpc.111.092577.

[60] W. Busch, B. T. Moore, B. Martsberger *et al.*, "A microfluidic device and computational platform for high-throughput live imaging of gene expression", *Nature Methods*, vol. 9, no. 11, pp. 1101–1106, Nov. 2012, doi: 10.1038/nmeth.2185.

[61] H. Jiang, Z. Xu, M. R. Aluru and L. Dong, "Plant chip for high-throughput phenotyping of arabidopsis", *Lab on a Chip*, vol. 14, pp. 1281–1293, 2014, doi: 10.1039/C3LC51326B.

[62] H. Massalha, E. Korenblum, S. Malitsky, O. H. Shapiro and A. Aharoni, "Live imaging of root-bacteria interactions in a microfluidics setup", *PNAS*, vol. 114, pp. 4549–4554, Apr. 2017, doi: 10.1073/pnas.1618584114.

[63] Y.-H. Park, N. Lee, G. Choi and J.-K. Park, "Plant array chip for the germination and growth screening of Arabidopsis thaliana", *Lab on a Chip*, vol. 17, no. 18, pp. 3071–3077, Aug. 2017, doi: 10.1039/C7LC00463J.

[64] C. E. Stanley, J. Shrivastava, R. Brugman, E. Heinzelmann, D. van Swaay and G. Grossmann, "Dual-flow-rootchip reveals local adaptations of roots towards environmental asymmetry at the physiological and genetic levels", *New Phytologist*, vol. 217, pp. 1357–1369, 2018, doi: 10.1111/nph.14887.

[65] H. H. Chai, F. Chen, S. J. Zhang *et al.*, "Multi-chamber petaloid root-growth chip for the non-destructive study of the development and physiology of the fibrous root system of oryza sativa", *Royal Society of Chemistry*, vol. 19, pp. 2383–2393, Jun. 2019, doi: 10.1039/C9LC00396G.

[66] Z. X. Song, H. H. Chai, F. Chen, L. Yu and C. Fang, "A foldable chip array for the continuous investigation of seed germination and the subsequent root development of seedlings", *Micromachines*, vol. 10, no. 12, Art. no. 884, Dec. 2019, doi: 10.3390/mi10120884.

[67] C. Allan, A. Tayagui, R. Hornung, V. Nock and C.-N. Meisrimler, "A dual-flow rootchip enables quantification of bi-directional calcium signaling in primary roots", *Frontiers in Plant Science*, vol. 13, Art. no. 1040117, Jan. 2023, doi: 10.3389/fpls.2022.1040117.

[68] M. Meier, E. M. Lucchetta and R. F. Ismagilov, "Chemical stimulation of the arabidopsis thaliana root using multi-laminar flow on a microfluidic chip", *Lab on a Chip*, vol. 10, no. 16, pp. 2147–2153, Jun. 2010, doi: 10.1039/c004629a.

[69] A. Parashar and S. Pandey, "Plant-in-chip: Microfluidic system for studying root growth and pathogenic interactions in arabidopsis", *Applied Physics Letters*, vol. 98, no. 26, Art. no. 263703, Jun. 2011, doi: 10.1063/1.3604788.

[70] J. A. Aufrecht, J. M. Ryan, S. Hasim *et al.*, "Imaging the root hair morphology of arabidopsis seedlings in a two-layer microfluidic platform", *Journal of Visualized Experiments*, no. 126, Art. no. 55971, Aug. 2017, doi: 10.3791/55971.

[71] G. Singh, D. Pereira, S. Baudrey *et al.*, "Real-time tracking of root hair nucleus morphodynamics using a microfluidic approach", *The Plant Journal*, vol. 108, no. 2, pp. 303–313, Sep. 2021, doi: 10.1111/tpj.15511.

[72] D. E. W. Patabadige, L. J. Millet, J. A. Aufrecht *et al.*, "Label-free time- and space-resolved exometabolite sampling of growing plant roots through nanoporous interfaces", *Scientific Reports*, vol. 9, no. 1, Art. no. 10272, Jul. 2019, doi: 10.1038/s41598-019-46538-5.

[73] M.-F. Noirot-Gros, S. V. Shinde, C. Akins *et al.*, "Functional Imaging of Microbial Interactions With Tree Roots Using a Microfluidics Setup", *Frontiers in Plant Science*, vol. 11, Art. no. 408, Apr. 2020, doi: 10.3389/fpls.2020.00408.

[74] J. Aufrecht, M. Khalid, C. L. Walton, K. Tate, J. F. Cahill and S. T. Retterer, "Hotspots of root-exuded amino acids are created within a rhizosphere-on-a-chip", *Lab on a Chip*, vol. 22, no. 5, pp. 954–963, Jan. 2022, doi: 10.1039/D1LC00705J.

[75] H. Dai, B. Wu, B. Chen, B. Ma and C. Chu, "Diel fluctuation of extracellular reactive oxygen species production in the rhizosphere of rice", *Environmental Science & Technology*, vol. 56, no. 12, pp. 9075–9082, May 2022, doi: 10.1021/acs.est.2c00005.

[76] R. Walczak, B. Kawa and K. Adamski, "Inkjet 3D printed microfluidic device for growing seed root and stalk mechanical characterization", *Sensors and Actuators A: Physical*, vol. 297, Art. no. 111557, Aug. 2019, doi: 10.1016/j.sna.2019.111557.

[77] H. Chai, F. Chen, K. Ning, W. Sun and L. Yu, "An easy-to-open multi-chamber device to study the molecular changes behind the plant root microscale phenotypic variations", *Sensors and Actuators B: Chemical*, vol. 392, Art. no. 134107, Jun. 2023, doi: 10.1016/j.snb.2023.134107.

[78] L. Sun, L. Liu, X. Lin *et al.*, "Microfluidic devices for monitoring the root morphology of arabidopsis thaliana in situ", *Analytical Sciences*, vol. 37, no. 4, pp. 605–611, Oct. 2020, doi: 10.2116/analsci.20P281.

[79] V. Kamat, L. Burton, V. Venkadesh, K. Jayachandran and S. Bhansali, "Enabling smart agriculture through sensor-integrated microfluidic chip to monitor nutrient uptake in plants", *ECS Sensors Plus*, vol. 2, no. 4, Art. no. 043201, Oct. 2023, doi: 10.1149/2754-2726/ad024e.

[80] E. Pawlenko, "Optimierung eines mikrofluidischen Chips zur Untersuchung des Wurzelwachstums und Ermittlung der industriellen Fertigungsmöglichkeiten durch eine Unternehmensstudie", Master's Thesis, Karlsruhe Institute of Technology, Karlsruhe, Germany, Nov. 2020.

[81] M. Focke, D. Kosse, C. Müller, H. Reinecke, R. Zengerle and F. von Stetten, "Lab-on-a-foil: Microfluidics on thin and flexible films", *Lab on a chip*, vol. 10, no. 11, pp. 1365–1386, 2010, doi: 10.1039/c001195a.

[82] A. A. Espinoza Orías and J. E. Renaud, "An optimization study of the ultrasonic welding of thin film polymers", in *Volume 1: 30th Design Automation Conference*, ASMEDC, 2004, pp. 75–84, doi: 10.1115/DETC2004-57082.

[83] E. Tsiangou, S. Teixeira de Freitas, I. F. Villegas and R. Benedictus, "Ultrasonic welding of epoxy- to polyetheretherketone- based composites: Investigation on the material of the energy director and the thickness of the coupling layer", *Journal of Composite Materials*, vol. 54, no. 22, pp. 3081–3098, 2020, doi: 10.1177/0021998320910207.

[84] D. Dobrotă and S. V. Lazăr, "Ultrasonic welding of pbt-gf30 (70% polybutylene terephthalate + 30% fiber glass) and expanded polytetrafluoroethylene (e-ptfe)", *Polymers*, vol. 13, no. 2, Art. no. 298, 2021, doi: 10.3390/polym13020298.

[85] A. Korycki, F. Carassus, C. Garnier, F. Chabert and T. Djilali, "Effect of energy director thickness on thermal diffusion and joint quality during ultrasonic welding of cf/peek composites", in *Material Forming 26th International ESAFORM Conference on Material Forming (ESAFORM 2023)*, L. Madej, M. Sitko and K. Perzynski, Eds., ser. Materials Research Proceedings, vol. 28, Millersville, PA, USA: Materials Research Forum LLC, 2023, pp. 1819–1828, doi: 10.21741/9781644902479-197.

[86] M. Brosda, P. Nguyen, A. Olowinsky and A. Gillner, "Analysis of the interaction process during lasertransmission welding of multilayer polymer films with adapted laser wavelength by numerical simulation and thermography", *Journal of Laser Applications*, vol. 32, no. 2, 2020, doi: 10.2351/7.0000113.

[87] N. Tang, Y. Li, J. Ge *et al.*, "Ultrathin cellulose voronoi-nanonet membranes enable high-flux and energy-saving water purification", *ACS applied materials & interfaces*, vol. 12, no. 28, pp. 31 852–31 862, 2020, doi: 10.1021/acsami.0c08504.

[88] R. Shah. "To seam or not to seam: Polyzen creates a robust seam in rf welding of ultra-thin films", Polyzen, Inc. (2012), [Online]. Available: https://www.polyzen.com/2012/04/25/seam-not-seam-polyzen-creates-robust-seam-rf-welding-ultra-thin-films/ (Accessed: 08/01/2024).

[89] Q. Li, Z. Mu, M. Luo, A. Huang and S. Pang, "Laser spot micro-welding of ultra-thin steel sheet", *Micromachines*, vol. 12, no. 3, Art. no. 342, 2021, doi: 10.3390/mi12030342.

[90] J. de Jong, R. G. H. Lammertink and M. Wessling, "Membranes and microfluidics: A review", *Lab on a chip*, vol. 6, no. 9, pp. 1125–1139, 2006, doi: 10.1039/B603275C.

[91] J. Qiu, G. Zhang, E. Sakai, W. Liu and L. Zang, "Thermal welding by the third phase between polymers: A review for ultrasonic weld technology developments", *Polymers*, vol. 12, no. 4, Art. no. 759, 2020, doi: 10.3390/polym12040759.

[92] T. B. Scheffler and A. J. Leao, "Fabrication of polymer film heat transfer elements for energy efficient multi-effect distillation", *Desalination*, vol. 222, no. 1–3, pp. 696–710, 2008, doi: 10.1016/j.desal.2007.02.076.

[93] S. Iwasiro, A. Watanabe, Y. Onozuka, M. Minai, H. Nishimura and S. Takeuchi, "Development and estimation of brain tumor cells culture flask with acoustic window film for ultrasound exposure", *Japanese Journal of Applied Physics*, vol. 53, no. 7S, Art. no. 07KF12, 2014, doi: 10.7567/JJAP.53.07KF12.

[94] D. Dahlstrand, *How to solve common ultrasonic welding problems: Understand and address the likely origins of welding problems to keep production on track.* Gardner Business Media Inc., Ed., Cincinnati, Ohio, USA, 2017, [Online]. Available: https://www.ptonline.com/articles/how-to-solve-common-ultrasonic-welding-problems (Accessed: 17/01/2024).

[95] Dukane Intelligent Assembly Solutions, *Guide to ultrasonic plastics assembly*, Dukane Intelligent Assembly Solutions, Ed., St. Charles, IL, USA, Aug. 2011, [Online]. Available: https://documents.dukane.com/DesignGuides/Guide%20To%20US%20Plastic%20Assembly.pdf (Accessed: 17/01/2024).

[96] W. A. Beck, M. Huang, J. Ketterl and T. Hughes, "IR laser welding of thin polymer films as a fabrication method for polymer mems", in *Saratov Fall Meeting 2002: Laser Physics and Photonics, Spectroscopy, and Molecular Modeling III; Coherent Optics of Ordered and Random Media III*, D. A. Zimnyakov, V. L. Derbov, L. A. Melnikov and L. M. Babkov, Eds., ser. SPIE Proceedings, vol. 1, Bellingham, WA, USA: SPIE, 2002, pp. 167–178, doi: 10.1117/12.518600.

[97] C. Hopmann, W. Michaeli, H. Greif and L. Wolters, *Technologie der Kunststoffe: Lern- und Arbeitsbuch für die Aus- und Weiterbildung*, 4th ed. München: Carl Hanser Verlag, 2015, isbn: 978-3-446-44233-7.

[98] M. Brosda, N.-P. Nguyen, A. Olowinksy and A. Gillner, "Investigations on the influence of beam shaping in lasertransmission welding of multi-layer polymer films with wavelength-adapted diode laser beam sources", in *Advanced Joining Processes*, ser. Springer eBook Collection, L. F. M. Da Silva, P. A. F. Martins and M. S. El-Zein, Eds., Singapore: Springer Singapore and Imprint Springer, 2020, pp. 91–100, doi: 10.1007/978-981-15-2957-3_7.

[99] N. Brown, D. Kerr, M. R. Jackson and R. M. Parkin, "Laser welding of thin polymer films to container substrates for aseptic packaging", *Optics & Laser Technology*, vol. 32, no. 2, pp. 139–146, 2000, doi: 10.1016/S0030-3992(00)00033-5.

[100] T. Klotzbuecher, M. Letschert, T. Braune, K.-S. Drese and T. Doll, "Diode laser welding for packaging of transparent micro-structured polymer chips", in *Laser-based Micropackaging*, F. G. Bachmann, W. Hoving, Y. Lu and K. Washio, Eds., ser. SPIE Proceedings, SPIE, 2006, doi: 10.1117/12.649248.

[101] N. Pagano, G. Campana, M. Fiorini and R. Morelli, "Laser transmission welding of polylactide to aluminium thin films for applications in the food-packaging industry", *Optics & Laser Technology*, no. 91, pp. 80–84, 2017, doi: 10.1016/j.optlastec.2016.12.014.

[102] X. Jiang, S. Chandrasekar and C. Wang, "A laser microwelding method for assembly of polymer based microfluidic devices", *Optics and Lasers in Engineering*, no. 66, pp. 98–104, 2015, doi: 10.1016/j.optlaseng.2014.08.014.

[103] H. Liu, Y. Jiang, W. Tan, G. Chen, W. Liu and X. Wang, "The study of laser transmission joining PA66 and PVC with large compatibility difference", *Journal of Manufacturing Processes*, no. 26, pp. 252–261, 2017, doi: 10.1016/j.jmapro.2017.02.024.

[104] T. Boeltken, A. Wunsch, T. Gietzelt, P. Pfeifer and R. Dittmeyer, "Ultra-compact microstructured methane steam reformer with integrated palladium membrane for on-site production of pure hydrogen: Experimental demonstration", no. 41, pp. 18 058–18 068, 2014, doi: 10.5445/IR/110100686.

[105] A. P. Hoult and M. Burrell, "The effect of diode laser wavelength on the clearweld™ welding process", in *ICALEO 2002 – 21st International Congress on Applications of Laser and Electro-Optics*, Scottsdale, Arizona, USA: Laser Institute of America, 2002, Art. no. 584221, doi: 10.2351/1.5065751.

[106] N.-P. Nguyen, "Laserdurchstrahlschweißen von transparenten Kunststoffen mit Thulium-Faserlaserstrahlung: Laser transmission welding of transparent plastics with thulium fibre laser radiation", Ph.D. dissertation, RWTH Aachen, Aachen, May 2023, isbn: 978-3-98555-172-9.

[107] N.-P. Nguyen, M. Brosda, A. Olowinksy and A. Gilner, "Absorber-free quasi-simultaneous laser welding for microfluidic applications", *Journal of Laser Micro/Nanoengineering*, no. 14, pp. 255–261, 2019, doi: 10.2961/jlmn.2019.03.0009.

[108] V. Mamuschkin, A. Olowinsky, K. van der Straeten and C. Engelmann, "Laser transmission welding of absorber-free thermoplastics using dynamic beam superposition", in *Conference Proceedings of SPIE*, F. Dorsch, Ed., San Francisco, California, United States: SPIE, Mar. 2015, Art. no. 93560Y, doi: 10.1117/12.2079691.

[109] V. Mamuschkin, C. Engelmann and A. Olowinsky, "Improvement of energy deposition in absorber-free laser welding through quasi-simultaneous irradiation", *Physics Procedia*, vol. 83, pp. 472–482, 2016, doi: 10.1016/j.phpro.2016.08.049.

[110] D. Kumar Goyal and R. Kant, "Mechanical and morphological analysis of laser transmission welded dissimilar plastics using metal absorber", *Optics & Laser Technology*, vol. 170, p. 110 238, 20th Oct. 2023, doi: 10.1016/j.optlastec.2023.110238.

[111] Covestro Deutschland AG, *Makrolon*, Feb. 2018, [Online]. Available: https://solutions.covestro.com/en/brands/makrolon (Accessed: 01/08/2025).

[112] G. Fedder, "Optimierung der Fertigung eines mikrofluidischen Bioreaktors", Master's thesis, Karlsruhe Institute of Technology, Karlsruhe, Germany, Feb. 2020.

[113] L. Supp, "Untersuchung und Optimierung des Strömungsverhaltens innerhalb eines mikrofluidischen Bioreaktors zur Kultivierung von Pflanzenzellen", Master's Thesis, Karlsruhe Institute of Technology, Karlsruhe, Germany, Dec. 2021.

[114] H.-J. Kretzschmar and W. Wagner, "D2.1 Thermophysikalische Stoffwerte von Wasser", in *VDI-Wärmeatlas*, Berlin, Heidelberg: Springer Berlin Heidelberg, 2019, pp. 201–218, doi: 10.1007/978-3-662-52989-8_12.

[115] J. Crank, *The mathematics of diffusion*, 2nd ed. Oxford: Univ. Pr, 2011, isbn: 978-0-19-853411-2.

[116] J. H. Spurk and N. Aksel, *Strömungslehre: Einführung in die Theorie der Strömungen*, 9th ed. Berlin, Heidelberg: Springer Berlin Heidelberg, 2019, isbn: 978-3-662-58763-8.

[117] Y. Song, X. Zhao, Q. Tian and H. Liang, "Fundamental concepts and physics in microfluidics", in *Microfluidics: fundamentals, devices and applications*, Weinheim: Wiley-VCH, 2018, pp. 19–111, doi: 10.1002/9783527800643.ch2.

[118] R. B. Bird, W. E. Stewart and E. N. Lightfoot, *Transport phenomena*, 2nd ed. New York: Wiley, 2007, isbn: 978-0-470-11539-8.

[119] COMSOL AB, *COMSOL Multiphysics® v. 6.3*, COMSOL AB, Stockholm, Sweden, 2024.

[120] F. Schlegel and COMSOL Group, *Understanding stabilization methods*, May 2014, [Online]. Available: https://www.comsol.com/blogs/understanding-stabilization-methods (Accessed: 14/04/2025).

[121] J. Bear, *Modeling Phenomena of Flow and Transport in Porous Media* (Theory and Applications of Transport in Porous Media). Cham: Springer International Publishing, 2018, vol. 31, isbn: 978-3-319-72825-4.

[122] D. G. Roddeman, J. Drukker, C. W. J. Oomens and J. D. Janssen, "The wrinkling of thin membranes: Part I–theory", *Journal of Applied Mechanics: Transactions ASME*, vol. 54, pp. 884–887, 1987, doi: 10.1115/1.3173133.

[123] J. D. G. Jones and J. L. Dangl, "The plant immune system", *Nature*, vol. 444, no. 7117, pp. 323–329, 2006, doi: 10.1038/nature05286.

[124] D. Lecourieux, R. Ranjeva and A. Pugin, "Calcium in plant defence-signalling pathways", *The New Phytologist*, vol. 171, no. 2, pp. 249–269, 2006, doi: 10.1111/j.1469-8137.2006.01777.x.

[125] V. Demidchik, S. Shabala, S. Isayenkov, T. A. Cuin and I. Pottosin, "Calcium transport across plant membranes: Mechanisms and functions", *The New Phytologist*, vol. 220, no. 1, pp. 49–69, 2018, doi: 10.1111/nph.15266.

[126] A.-C. Schmit, personal communication, May 2020.

[127] A.-C. Schmit, personal communication, Jul. 2020.

[128] A.-C. Schmit, personal communication, Feb. 2020.

[129] T. Mellert, "Additive Fertigung und Untersuchung eines Formeinsatzes für PDMS basierte Mikrofluidikchips", Master's Thesis, Karlsruhe Institute of Technology, Karlsruhe, Germany, Mar. 2021.

[130] L. M. Schmidt-Speicher, T. Mellert, A. C. Hurtado Rivera, K. Länge, R. Ahrens and A. E. Guber, "Rapid prototyping of moulds for PDMS-based microfluidic chips", *Current Directions in Biomedical Engineering*, vol. 7, no. 2, pp. 255–259, Oct. 2021, doi: 10.1515/cdbme-2021-2065.

[131] W. Kaiser, *Kunststoffchemie für Ingenieure: Von der Synthese bis zur Anwendung*, 6th ed. München: Hanser, 2024, isbn: 978-3-446-47807-7.

[132] A.-C. Schmit, personal communication, 27th May 2021.

[133] A.-C. Schmit, personal communication, 23rd Apr. 2021.

[134] Y. Peiffer, "Optimierung eines mikrofluidischen Wurzelchips: Ansätze für eine flexible Fluidzuführung sowie für die Serienfertigung", Master's Thesis, Karlsruhe Institute of Technology, Karlsruhe, Germany, Dec. 2021.

[135] C.-C. Hong, J.-W. Choi and C. H. Ahn, "A novel in-plane passive microfluidic mixer with modified Tesla structures", *Lab on a Chip*, vol. 4, no. 2, Art. no. 109, 2004, doi: 10.1039/b305892a.

[136] V. Mamuschkin, A. Haeusler, C. Engelmann, A. Olowinsky and H. Aehling, "Enabling pyrometry in absorber-free lasertransmission welding through pulsed irradiation", *Journal of Laser Applications*, vol. 29, no. 2, Art. no. 022409, May 2017, doi: 10.2351/1.4983515.

[137] S. Nemoto, "Waist shift of a Gaussian beam by plane dielectric interfaces", *Applied Optics*, vol. 27, no. 9, Art. no. 1833, May 1988, doi: 10.1364/AO.27.001833.

[138] W. M. Steen and J. Mazumder, *Laser material processing*, 4th ed. London New York: Springer, 2010, isbn: 978-1-84996-062-5.

[139] H. Potente, *Fügen von Kunststoffen: Grundlagen, Verfahren, Anwendung ; mit 31 Tabellen*. München and Wien: Hanser, 2004, isbn: 978-3-446-22755-2.

[140] T. Finkbeiner, C. Manz, M. L. Raorane *et al.*, "A modular microfluidic bioreactor to investigate plant cell–cell interactions", *Protoplasma*, vol. 259, no. 1, pp. 173–186, May 2021, doi: 10.1007/s00709-021-01650-0.

[141] N. Hering, A.-C. Schmit, E. Herzog *et al.*, "Spearmint targets microtubules by (-)–carvone", *Horticulture Research*, vol. 11, no. 7, Art. no. 151, Jul. 2024, doi: 10.1093/hr/uhae151.

[142] T. F. S. Inc., *Polycarbonate (PC) Labware*, Oct. 2024, [Online]. Available: https://www.thermofisher.com/de/de/home/life-science/lab-plasticware-supplies/plastic-material-selection/polycarbonate-pc-labware.html (Accessed: 25/10/2024).

[143] AdvanTech Plastics, LLC, *Polycarbonate: The 'clear' choice for medical devices*, Feb. 2021, [Online]. Available: https://advantechplastics.com/blog/polycarbonate-the-clear-choice-for-medical-devices/ (Accessed: 25/10/2024).

[144] P. F. W. Simon and A. Fahmi, *Polymere - Chemie und Strukturen: Herstellung, Charakterisierung und Werkstoffe*. Weinheim: Wiley-VCH Verlag GmbH & Co. KGaA, 2020, isbn: 978-3-527-33462-9.

[145] M. Kübler, A. Müller and H. Schürmann, "Kunststoffe", in *Dubbel Taschenbuch für den Maschinenbau 1: Grundlagen und Tabellen*, ser. DUBBEL - Taschenbuch für den Maschinenbau, 26th ed., vol. 1, Berlin, Heidelberg: Springer Berlin / Heidelberg, 2020, pp. 625–671, doi: 10.1007/978-3-662-59711-8_32.

[146] R. J. Young and P. A. Lovell, *Introduction to polymers*, 3rd ed. Boca Raton: CRC press, 2011, isbn: 978-0-8493-3929-5.

[147] M. Worgull, *Hot embossing: Theory and Technology of Microreplication* (Micro and Nano Technologies). Oxford, UK: William Andrew Publishing, 2009, vol. 7, isbn: 978-0-8155-1579-1.

[148] The Dow Chemical Company, *Processing DOWSIL™ addition cure gels and elastomers*, The Dow Chemical Company, Ed., 2019, [Online]. Available: https://www.dow.com/documents/en-us/mark-prod-info/11/11-11/11-1132-01-processing-dowsil-addition-cure-gel-elastomer.pdf (Accessed: 06/08/2025).

[149] E. Berthier, E. W. K. Young and D. Beebe, "Engineers are from PDMS-land, biologists are from polystyrenia", *Lab on a chip*, vol. 12, no. 7, pp. 1224–1237, 2012, doi: 10.1039/c2lc20982a.

[150] E. Biffi, Ed., *Microfluidic and Compartmentalized Platforms for Neurobiological Research* (SpringerLink Bücher). New York, NY: Humana Press, 2015, vol. 103, isbn: 978-1-4939-2510-0.

[151] P. Occhetta, E. Biffi and M. Rasponi, "A reliable reversible bonding method for perfused microfluidic devices", in *Microfluidic and Compartmentalized Platforms for Neurobiological Research*, ser. SpringerLink Bücher, E. Biffi, Ed., New York, NY: Humana Press, 2015, isbn: 978-1-4939-2510-0.

[152] The Dow Chemical Company, *Sylgard™184 silicone elastomer: Technical data sheet*, 2017, [Online]. Available: https://www.dow.com/en-us/document-viewer.html?docPath=/content/dam/dcc/documents/en-us/productdatasheet/11/11-31/11-3184-sylgard-184-elastomer.pdf (Accessed: 12/07/2022).

[153] G. M. Whitesides, "The origins and the future of microfluidics", *Nature*, vol. 442, no. 7101, pp. 368–373, 2006, doi: 10.1038/nature05058.

[154] J. C. McDonald and G. M. Whitesides, "Poly(dimethylsiloxane) as a material for fabricating microfluidic devices", *Accounts of chemical research*, vol. 35, no. 7, pp. 491–499, 2002, doi: 10.1021/ar010110q.

[155] D. C. Duffy, J. C. McDonald, O. J. Schueller and G. M. Whitesides, "Rapid prototyping of microfluidic systems in poly(dimethylsiloxane)", *Analytical chemistry*, vol. 70, no. 23, pp. 4974–4984, 1998, doi: 10.1021/ac980656z.

[156] M. A. Eddings, M. A. Johnson and B. K. Gale, "Determining the optimal PDMS–PDMS bonding technique for microfluidic devices", *Journal of Micromechanics and Microengineering*, vol. 18, no. 6, Art. no. 067001, 2008, doi: 10.1088/0960-1317/18/6/067001.

[157] B. M. Brewer, D. J. Webb and D. Li, "The fabrication of microfluidic platforms with pneumatically/hydraulically controlled PDMS valves and their use in neurobiological research", in *Microfluidic and Compartmentalized Platforms for Neurobiological Research*, ser. SpringerLink Bücher, E. Biffi, Ed., New York, NY: Humana Press, 2015, pp. 3–24, doi: 10.1007/978-1-4939-2510-0_1.

[158] Yeong-Eun Yoo, "Micro/nano fabrication for fluidic devices", in *Engineering of Micro/Nano Biosystems*, ser. Springer eBooks Engineering, G. Barbillon, A. Bosseboeuf, K. Chun, R. Ferrigno and O. Français, Eds., Singapore: Springer, 2020, pp. 90–104, isbn: 978-981-13-6549-2.

[159] A. Kalpattu, "Pdms shrinkage", University of Pennsylvania, Tech. Rep., 10th Aug. 2017, doi: 20.500.14332/45861.

[160] R. Filion, A. St-Georges-Robillard, H. Chaudoir *et al.*, "Mass fabrication of PDMS microfluidic devices by injection molding and applications in sensitive 3D spheroid and explant culture", en, *Scientific Reports*, vol. 15, no. 1, p. 33 218, Sep. 2025, ISSN: 2045-2322, doi: 10.1038/s41598-025-16863-z.

[161] B. Arnold, *Werkstofftechnik für Wirtschaftsingenieure*, 2nd ed. Berlin, Heidelberg: Springer Berlin Heidelberg, 2017, isbn: 978-3-662-54548-5.

[162] P. Kurzweil, *Chemie: Grundlagen, technische Anwendungen, Rohstoffe, Analytik und Experimente*, 12th ed. Wiesbaden: Springer Vieweg, 2023, isbn: 978-3-658-41568-6.

[163] P. Eyerer, *Polymer Engineering 1: Einführung, Synthese, Eigenschaften*, 2nd ed. Berlin, Heidelberg: Springer Berlin Heidelberg, 2020, isbn: 978-3-662-59837-5.

[164] A. Risse, *Fertigungsverfahren der Mechatronik, Feinwerk- und Präzisionsgerätetechnik*. Wiesbaden: Vieweg+Teubner Verlag, 2012, isbn: 978-3-8348-8312-4.

[165] E. Uhlmann, "Werkzeugmaschinen für die Mikroproduktion", in *Dubbel Taschenbuch für den Maschinenbau 2: Anwendungen*, ser. DUBBEL - Taschenbuch für den Maschinenbau, 26th ed., vol. 2, Berlin, Heidelberg: Springer Berlin Heidelberg, 2020, pp. 1219–1227, doi: 10.1007/978-3-662-59713-2_52.

[166] W. Böge and L. Barfels, "Zerspantechnik", in *Handbuch Maschinenbau: Grundlagen und Anwendungen der Maschinenbau-Technik*, ser. Springer eBook Collection, 24th ed., Wiesbaden: Springer Vieweg, 2021, pp. 1189–1229, doi: 10.1007/978-3-658-30273-3.

[167] J. Dietrich and A. Richter, *Praxis der Zerspantechnik: Verfahren, Prozesse, Werkzeuge* (Springer eBook Collection), 13th ed. Wiesbaden: Springer Vieweg, 2020, isbn: 978-3-658-30967-1.

[168] E. Paucksch, S. Holsten, M. Linß and F. Tikal, *Zerspantechnik: Prozesse, Werkzeuge, Technologien* (SpringerLink Bücher), 12th ed. Wiesbaden: Vieweg+Teubner, 2008, isbn: 978-3-8348-9494-6.

[169] H. K. Tönshoff and B. Denkena, *Spanen: Grundlagen* (Engineering online library), 3rd ed. Berlin [u.a.]: Springer, 2011, isbn: 978-3-642-19772-7.

[170] A. Kalweit, C. Paul, S. Peters and R. Wallbaum, "KUN Kunststoffe", in *Handbuch für Technisches Produktdesign: Material und Fertigung, Entscheidungsgrundlagen für Designer und Ingenieure*, ser. VDI-Buch, Berlin, Heidelberg: Springer Berlin Heidelberg, 2012, pp. 61–113, doi: 10.1007/978-3-642-38891-0_37.

[171] W. Menz, J. Mohr and O. Paul, *Mikrosystemtechnik für Ingenieure*, 3rd ed. Weinheim: Wiley-VCH, 2012, isbn: 978-3-527-66346-0, [Online]. Available: http://nbn-resolving.org/urn:nbn:de:bsz:31-epflicht-1110610.

[172] A. Rieße, *Fertigungsverfahren der Mechatronik, Feinwerk- und Präzisionsgerätetechnik: Mit 25 Tabellen*. Wiesbaden: Springer Vieweg, 2012, isbn: 978-3-8348-1519-4.

[173] J. Schroers, Q. Pham and A. Desai, "Thermoplastic forming of bulk metallic glass – a technology for mems and microstructure fabrication", *Journal of Microelectromechanical Systems*, vol. 16, no. 2, pp. 240–247, 2007, doi: 10.1109/JMEMS.0007.892889.

[174] A. Kolew, *Heißprägen von Verbundfolien für mikrofluidische Anwendungen*. Karlsruhe: KIT Scientific Publishing, 2012, isbn: 978-3-86644-888-9.

[175] M. A. Unger, H. P. Chou, T. Thorsen, A. Scherer and S. R. Quake, "Monolithic microfabricated valves and pumps by multilayer soft lithography", *Science (New York, N.Y.)*, vol. 288, no. 5463, pp. 113–116, 2000, doi: 10.1126/science.288.5463.113.

[176] S. Satyanarayana, R. N. Karnik and A. Majumdar, "Stamp-and-stick room-temperature bonding technique for microdevices", *Journal of Microelectromechanical Systems*, vol. 14, no. 2, pp. 392–399, 2005, doi: 10.1109/JMEMS.2004.839334.

[177] B. Samel, M. K. Chowdhury and G. Stemme, "The fabrication of microfluidic structures by means of full-wafer adhesive bonding using a poly(dimethylsiloxane) catalyst", *Journal of Micromechanics and Microengineering*, vol. 17, no. 8, pp. 1710–1714, 2007, doi: 10.1088/0960-1317/17/8/038.

[178] K. Haubert, T. Drier and D. Beebe, "PDMS bonding by means of a portable, low-cost corona system", *Lab on a chip*, vol. 6, no. 12, pp. 1548–1549, 2006, doi: 10.1039/b610567j.

[179] D. A. Grewell, A. Benatar and J. B. Park, "Ultrasonic welding", in *Plastics and composites welding handbook*, D. A. Grewell, A. Benatar and J. B. Park, Eds., München: Carl Hanser Verlag, 2003, pp. 141–188, isbn: 978-1-56990-313-1.

[180] E. Haberstroh and R. Lützeler, "Ultraschallschweißen von Kunststoffen", in *Montage hybrider Mikrosysteme*, ser. SpringerLink Bücher, U. Dilthey and A. Brandenburg, Eds., Berlin, Heidelberg: Springer Berlin Heidelberg, 2005, isbn: 978-3-540-27536-7, [Online]. Available: https://link.springer.com/chapter/10.1007/3-540-27536-3_12 (Accessed: 06/10/2022).

[181] W. Lehfeldt, *Ultraschall: kurz und bündig: Physikalische Grundlagen und Anwendungen* (Kamprath-Reihe). Würzburg: Vogel-Verlag, 1973, isbn: 978-3-8023-0060-8.

[182] F. C. Campbell, *Joining: Understanding the Basics*. Materials Park: A S M International, 2011, isbn: 978-1-61503-848-0, [Online]. Available: https://ebookcentral.proquest.com/lib/kxp/detail.action?docID=3002458 (Accessed: 06/10/2022).

[183] M. Heilig, B. Baudrit, H. Leicht, C. Pommer, T. Hochrein and M. Bastian, *Schweißen von lasergesinterten Kunststoffbauteilen aus PA12: Heizelementschweißen und Ultraschallschweißen* (SKZ - Forschung und Entwicklung), SKZ - Das Kunststoff-Zentrum, Ed. Aachen, DE: Shaker Verlag, 2018, isbn: 978-3-8440-5949-6.

[184] W. Strohfuß, "Ultraschallschweißen", in *Handbuch Kunststoff-Verbindungstechnik*, G. W. Ehrenstein, Ed., München: Carl Hanser Verlag, 2004, pp. 257–279, isbn: 978-3-446-22668-5.

[185] U. Dilthey and A. Brandenburg, Eds., *Montage hybrider Mikrosysteme: Handhabungs- und Fügetechniken für die Klein- und Mittelserienfertigung* (SpringerLink Bücher). Berlin, Heidelberg: Springer Berlin Heidelberg, 2005, isbn: 978-3-540-27536-7.

[186] J. Rotheiser, *Joining of plastics: Handbook for designers and engineers*, 3rd ed. Cincinnati, Ohio and Munich: Hanser, 2009, isbn: 978-1-56990-445-9.

[187] G. Müller and M. Möser, Eds., *Ultraschall in Medizin und Technik* (Fachwissen Technische Akustik). Berlin, Heidelberg: Springer Vieweg, 2017, isbn: 978-3-662-55442-5.

[188] A. Gillner, *Laser in der Kunststofftechnik*. Heidelberg München Landsberg Frechen Hamburg: Hüthig, 2009, isbn: 978-3-7785-4003-9.

[189] H. Hügel and T. Graf, *Laser in der Fertigung: Strahlquellen, Systeme, Fertigungsverfahren* (Studium), 2nd ed. Wiesbaden: Vieweg + Teubner, 2009, isbn: 978-3-8351-0005-3.

[190] J. Korte and M. Welz, "Laserstrahlschweißen", in *Handbuch Kunststoff-Verbindungstechnik*, G. W. Ehrenstein, Ed., München: Carl Hanser Verlag, 2004, pp. 232–256, isbn: 978-3-446-22668-5.

[191] A. Gillner, E. Haberstroh, W. Michaeli and R. Poprawe, "Laserstrahlmikroschweißen", in *Montage hybrider Mikrosysteme: Handhabungs- und Fügetechniken für die Klein- und Mittelserienfertigung*, ser. SpringerLink Bücher, U. Dilthey and A. Brandenburg, Eds., Berlin, Heidelberg: Springer Berlin Heidelberg, 2005, pp. 103–122, doi: 10.1007/3-540-27536-3_10.

[192] G. Hoffmann, *CO2-Laser Kohlendioxidlaser*, Feb. 2024, [Online]. Available: https://www.schneidforum.de/schneidwissen/laserschneiden/co2-laser/ (Accessed: 30/06/2024).

[193] U. Dilthey, Ed., *Schweißtechnische Fertigungsverfahren 1: Schweiß- und Schneidtechnologien*, 3rd ed. Berlin Heidelberg: Springer, 2006, isbn: 978-3-540-21673-5.

[194] R. Klein, *Laser welding of plastics*. Weinheim: Wiley-VCH, 2012, isbn: 978-3-527-40972-3.

[195] B. G. Wybourne and W. F. Meggers, "Spectroscopic properties of rare earths", *Physics Today*, vol. 18, no. 9, pp. 70–72, Jan. 1965, doi: 10.1063/1.3047727.

[196] P. Forster, "Thulium: Holmium-Co-Doped Fiber Lasers: Power scaling and long-wavelength emission", Ph.D. dissertation, Karlsruher Institut für Technologie (KIT), Karlsruhe, DE, 2024, doi: 10.5445/IR/1000169153.

[197] D. C. Hanna, R. M. Percival, I. R. Perry, R. G. Smart, P. J. M. Suni and A. C. Tropper, "Continuous-wave oscillation of a monomode Thulium-Doped Silica Fiber Laser", in *OSA proceedings on tunable solid state lasers: proceedings of the OSA topical meeting, May 1 – 3, 1989, North Falmouth, Cape Cod, Massachusetts*, Optical Society of America and M. L. Shand, Eds., ser. OSA Proceedings Series, Washington, DC: Optical Society of America, 1989, pp. 350–353, isbn: 978-1-55752-111-8.

[198] D. A. Grewell, "Infrared and laser welding", in *Plastics and composites welding handbook*, D. A. Grewell, A. Benatar and J. B. Park, Eds., München: Carl Hanser Verlag, 2003, pp. 271–311, isbn: 978-1-56990-313-1.

[199] T. Kramer, A. M. Olowinsky and F. Durand, "Shadow – a new welding technique", in *Photon Processing in Microelectronics and Photonics*, K. Sugioka, M. C. Gower, J. R. F. Haglund *et al.*, Eds., ser. SPIE Proceedings, vol. 4637, SPIE, 2002, pp. 545–554, doi: 10.1117/12.470664.

[200] S. Ruotsalainen, P. Laakso and V. Kujanpää, "Laser welding of transparent polymers by using quasi-simultaneous beam off-setting scanning technique", *Physics Procedia*, vol. 78, pp. 272–284, 2015, doi: 10.1016/j.phpro.2015.11.038.

[201] N.-P. Nguyen, S. Behrens, M. Brosda, A. Olowinsky and A. Gillner, "Laser transmission welding of absorber-free semi-crystalline polypropylene by using a quasi-simultaneous irradiation strategy", *Welding in the World*, vol. 64, no. 7, pp. 1227–1235, 2020, doi: 10.1007/s40194-020-00913-3.

[202] *Laserstrahlschweißen thermoplastischer Kunststoffe*, Richtlinie, Düsseldorf, Jan. 2014.

[203] P. J. Bates, T. B. Okoro and M. Chen, "Thermal degradation of PC and PA6 during lasertransmission welding", *Welding in the World*, vol. 59, no. 3, pp. 381–390, 2015, doi: 10.1007/s40194-014-0209-9.

[204] J. B. Park and D. A. Grewell, "Guidelines for process selection", in *Plastics and composites welding handbook*, D. A. Grewell, A. Benatar and J. B. Park, Eds., München: Carl Hanser Verlag, Jan. 2003, pp. 335–360, doi: 10.1007/978-1-4939-2113-3_13.

[205] U. A. Russek, "Prozesstechnische Aspekte des Laserdurchstrahlschweißens von Thermoplasten", Ph.D. dissertation, RWTH Aachen, Aachen, 2006, isbn: 978-3-8322-5267-0.

[206] E. Ghorbel, G. Casalino and S. Abed, "Laser diode transmission welding of polypropylene: Geometrical and microstructure characterisation of weld", *Materials & Design*, vol. 30, no. 7, pp. 2745–2751, Aug. 2009, doi: 10.1016/j.matdes.2008.10.027.

[207] A. Boglea, "Laser transmission welding of thermoplastics using local laser beam modulation", Ph.D. dissertation, RWTH Aachen, Aachen, 2013, isbn: 978-3-8440-2081-6.

[208] X. Yu, J. Zhang and C. Wang, "The numerical simulation of welding residual stress of dissimilar transparent thermoplastics with MZA powder absorbent", *Journal of Material Science and Technology Research*, vol. 10, pp. 108–116, Dec. 2023, doi: 10.31875/2410-4701.2023.10.12.

[209] S. Kreimeier Sooriyapiragasam and C. Hopmann, "Modeling of the heating process during the lasertransmission welding of thermoplastics and calculation of the resulting stress distribution", *Welding in the World*, vol. 60, no. 4, pp. 777–791, Jul. 2016, doi: 10.1007/s40194-016-0330-z.

[210] C. Hopmann, S. Bölle and S. Kreimeier, "Modeling of the thermally induced residual stresses during lasertransmission welding of thermoplastics", *Welding in the World*, vol. 63, no. 5, pp. 1417–1429, Sep. 2019, doi: 10.1007/s40194-019-00770-9.

[211] P. Lakemeyer, "Entwicklung und Analyse neuartiger Verfahrensvarianten zum quasisimultanen Laserdurchstrahlschweißen unter Berücksichtigung der Temperaturentwicklung", Ph.D. dissertation, Universität Paderborn, Aachen, 2018, isbn: 978-3-8440-6252-6.

[212] A. J. Boehm, A. Glaser and K. Muellen, "The Quaterrylimides - Highly efficient NIR absorbers for plastics", in *Annual Technical Conference - ANTEC, Conference Proceedings*, ser. ANTEC 2003: Conference Proceedings, vol. 3, Nashville, TE, USA: Society of Plastics Engineers, Jan. 2003, pp. 3687–3691.

[213] R. Klein and R. Wissemborski, "Marking and welding in one operation", *Kunststoffe international*, vol. 1, no. 2011, pp. 16–19, 2011.

[214] S. Polster, "Laserdurchstrahlschweißen transparenter Polymerbauteile", Ph.D. dissertation, Alexander-Universität Erlangen-Nürnberg, Bamberg, 2009, doi: 10.25593/978-3-87525-294-1.

[215] I. Jumpertz, E. Krampe and E. Wintermantel, "Kunststoffverarbeitung für die Medizintechnik", in *Medizintechnik: Life Science Engineering ; Interdisziplinarität, Biokompatibilität, Technologien, Implantate, Diagnostik, Werkstoffe, Zertifizierung, Business*, 5th ed., Berlin Heidelberg: Springer, 2009, pp. 551–556, doi: 10.1007/978-3-540-93936-8_25.

[216] M. Devrient, T. Frick and M. Schmidt, "Laser transmission welding of optical transparent thermoplastics", *Physics Procedia*, vol. 12, pp. 157–165, 2011, doi: 10.1016/j.phpro.2011.03.020.

[217] I. Jones, "Laser welding for plastic components", *Assembly Automation*, vol. 22, no. 2, pp. 129–135, Jun. 2002, doi: 10.1108/01445150210697429.

[218] H.-W. Heldt and B. Piechulla, *Pflanzenbiochemie*, 5th ed. Berlin: Springer Spektrum, Jan. 2015, isbn: 978-3-662-44398-9.

[219] L. Taiz and E. Zeiger, *Physiologie der Pflanzen* (Spektrum-Lehrbuch). Heidelberg Berlin: Spektrum Akad. Verl, 2000, isbn: 978-3-8274-0538-8.

[220] K. Esau, R. F. Evert and S. E. Eichhorn, *Esaus Pflanzenanatomie: Meristeme, Zellen und Gewebe der Pflanzen: ihre Struktur, Funktion und Entwicklung*. Berlin: de Gruyter, 2009, isbn: 978-3-11-020592-3.

[221] U. Lüttge, M. Kluge and G. Thiel, *Botanik: Die umfassende Biologie der Pflanzen* (Wiley-VCH-Lehrbuchkollektion). Germany: Wiley-VCH, Jan. 2014, vol. 1, isbn: 978-3-527-68287-4, [Online]. Available: http://onlinelibrary.wiley.com/book/10.1002/3527682872.

[222] P. Schopfer and A. Brennicke, *Pflanzenphysiologie*, 7th ed. Berlin, Heidelberg: Springer Berlin Heidelberg, 2016, isbn: 978-3-662-49879-8.

[223] A. Wijerathna-Yapa and J. Hiti-Bandaralage, "Tissue culture–A sustainable approach to explore plant stresses", *Life*, vol. 13, no. 3, Art. no. 780, Mar. 2023, doi: 10.3390/life13030780.

[224] Y. Zhang, J. Xu, R. Li, Y. Ge, Y. Li and R. Li, "Plants' response to abiotic stress: Mechanisms and strategies", *International Journal of Molecular Sciences*, vol. 24, no. 13, Art. no. 10915, Jun. 2023, doi: 10.3390/ijms241310915.

[225] T. E. Juenger and P. E. Verslues, "Time for a drought experiment: Do you know your plants" water status?", *The Plant Cell*, vol. 35, no. 1, pp. 10–23, Jan. 2023, doi: 10.1093/plcell/koac324.

[226] A. Füzy, R. Kovács, I. Cseresnyés *et al.*, "Selection of plant physiological parameters to detect stress effects in pot experiments using principal component analysis", *Acta Physiologiae Plantarum*, vol. 41, no. 5, Art. no. 56, Mar. 2019, doi: 10.1007/s11738-019-2842-9.

[227] H. Claeys, S. Van Landeghem, M. Dubois, K. Maleux and D. Inzé, "What is stress? Dose-response effects in commonly used in vitro stress assays", *Plant Physiology*, vol. 165, no. 2, pp. 519–527, Apr. 2014, doi: 10.1104/pp.113.234641.

[228] P. Nick, R. Fischer, D. Gradl *et al.*, Eds., *Modellorganismen*. Berlin, Heidelberg: Springer Berlin Heidelberg, 2019, isbn: 978-3-662-54868-4.

[229] G. Wanner, *Mikroskopisch-botanisches Praktikum*, 2nd ed. Stuttgart New York: Georg Thieme Verlag, 2010, isbn: 978-3-13-149962-2.

[230] B. Kost, "Bau und Feinbau der Zelle", in *Lehrbuch der Pflanzenwissenschaften*, 37th ed., Berlin: Springer Spektrum, Jan. 2014, pp. 3–69, doi: 10.1007/978-3-642-54435-4_1.

[231] W. Braune, A. Leman and H. Taubert, *Pflanzenanatomisches Praktikum I: Zur Einführung in die Anatomie der Vegetationsorgane der Samenpflanzen*, 9th ed. Heidelberg: Spektrum Akademischer Verlag, 2009, isbn: 978-3-8274-2290-3.

[232] W. Menke, *Die Struktur der Chloroplasten. Zum Mechanismus der Photosynthese* (Arbeitsgemeinschaft für Forschung des Landes Nordrhein-Westfalen Ser v.171). Wiesbaden: VS Verlag fur Sozialwissenschaften GmbH, 1967, isbn: 978-3-663-00332-8.

[233] E. Martinoia and R. Ratajczak, "Transport of organic molecules across the tonoplast", in *Advances in Botanical Research*, vol. 25, Elsevier, 1997, pp. 365–400, doi: 10.1016/S0065-2296(08)60158-5.

[234] H. Walter and K. Kreeb, "Die Pflanzenzelle als osmotisches System", in *Die Hydratation und Hydratur des Protoplasmas der Pflanzen und ihre Öko-Physiologische Bedeutung*, ser. Protoplasmatologia, Handbuch der Protoplasmaforschung 2 / C / 6, Vienna: Springer, 1970, doi: 10.1007/978-3-7091-5742-8.

[235] T. Dingermann, W. Kreis, K. Nieber, H. Rimpler and I. Zündorf, Eds., *Reinhard Pharmazeutische Biologie: Grundlagen für Studium und Praxis*, 8th ed. Stuttgart: Wissenschaftliche Verlagsgesellschaft Stuttgart, 2016, isbn: 978-3-8047-3546-0.

[236] R. Kollmann and I. Dörr, "Strukturelle Grundlagen des zwischenzelligen Stoffaustausches", *Berichte der Deutschen Botanischen Gesellschaft*, vol. 82, no. 5-6, pp. 415–425, Oct. 1969, doi: 10.1111/j.1438-8677.1969.tb02277.x.

[237] U. Kück and G. Wolff, *Botanisches Grundpraktikum*, 3rd ed. Berlin: Springer Spektrum, Jan. 2014, isbn: 978-3-642-53705-9.

[238] J. W. Deacon, *Fungal biology*, 4th ed. Malden, MA: Blackwell Pub, 2006, isbn: 978-1-4051-3066-0.

[239] M. P. Greaves and J. F. Darbyshire, "The ultrastructure of the mucilaginous layer on plant roots", *Soil Biology and Biochemistry*, vol. 4, no. 4, pp. 443–449, Nov. 1972, doi: 10.1016/0038-0717(72)90059-4.

[240] P. H. Raven, R. F. Evert and S. E. Eichhorn, *Biology of plants*, 7th ed. New York, NY: W.H. Freeman, 2005, isbn: 978-0-7167-1007-3.

[241] W. Schweers and F. H. Meyer, "Einfluß der Mykorrhiza auf den Transport von Assimilaten in die Wurzel", *Berichte der Deutschen Botanischen Gesellschaft*, vol. 83, no. 3–4, pp. 109–119, Dec. 1970, doi: 10.1111/j.1438-8677.1970.tb02328.x.

[242] G. Trolldenier, "Die Ökophysiologie der Wurzeln und der Rhizosphäre", *Biologie in unserer Zeit*, vol. 25, no. 2, pp. 120–129, Apr. 1995, doi: 10.1002/biuz.19950250213.

[243] F. Bouché, *Arabidopsis - root cell types*, 2017, doi: 10.6084/m9.figshare.4688752.v1.

[244] B. Kost, "Interaktionen von Zellen im Entwicklungsgeschehen", in *Lehrbuch der Pflanzenwissenschaften*, 37th ed., Berlin: Springer Spektrum, Jan. 2014, pp. 273–280, doi: 10.1007/978-3-642-54435-4_15.

[245] J. W. Kadereit, "Stammesgeschichte und Systematik der Bakterien, Archaeen, „Pilze", Pflanzen und anderer photoautotropher Eukaryoten", in *Strasburger - Lehrbuch der Pflanzenwissenschaften*, Berlin, Heidelberg: Springer Berlin Heidelberg, 2021, pp. 699–900, doi: 10.1007/978-3-662-61943-8_19.

[246] T. Nagata, Y. Nemoto and S. Hasezawa, "Tobacco BY-2 cell line as the "HeLa" cell in the cell biology of higher plants", in *International review of cytology: a survey of cell biology: Volume 132*, ser. International review of cytology 132, London: Elsevier, 1992, pp. 1–30, doi: 10.1016/S0074-7696(08)62452-3.

[247] T. Nagata, "When I encountered tobacco BY-2 cells!", in *Tobacco BY-2 Cells*, ser. Biotechnology in Agriculture and Forestry, vol. 53, Berlin, Heidelberg: Springer Berlin Heidelberg, 2004, pp. 1–6, doi: 10.1007/978-3-662-10572-6_1.

[248] K. Kato, T. Matsumoto, A. Koiwai *et al.*, "Liquid suspension culture of tobacco cells.", in *Fermentation Technology Today: Proceedings of the IVth International Fermentation Symposium, March 19-25, 1972, Kyoto, Japan*, Kyoto, Japan: Society of Fermentation Technology, Japan, 1972, pp. 698–695, [Online]. Available: https://books.google.de/books?id=eUVupOgdvn0C.

[249] T. Nagata, "Hidden history of the tobacco BY-2 cell line", *Journal of Plant Research*, vol. 136, no. 6, pp. 781–786, Aug. 2023, doi: 10.1007/s10265-023-01490-4.

[250] T. Nagata, S. Hasezawa, D. Inzé, T. Nagata, H. Lörz and J. M. Widholm, Eds., *Tobacco BY-2 Cells* (Biotechnology in Agriculture and Forestry). Berlin, Heidelberg: Springer Berlin Heidelberg, 2004, vol. 53, isbn: 978-3-662-10572-6.

[251] P. Nick, "Arabidopsis thaliana (Ackerschmalwand)", in *Modellorganismen*, Berlin, Heidelberg: Springer Berlin Heidelberg, 2019, pp. 117–149, doi: 10.1007/978-3-662-54868-4_5.

[252] R. Sivasubramanian, N. Mukhi and J. Kaur, "Arabidopsis thaliana: A model for plant research", in *Plant Biology and Biotechnology: Volume II: Plant Genomics and Biotechnology*, New Delhi: Springer India, 2015, pp. 1–26, doi: 10.1007/978-81-322-2283-5_1.

[253] P. W. Crous, B. Slippers, M. J. Wingfield *et al.*, "Phylogenetic lineages in the Botryosphaeriaceae", *Studies in Mycology*, vol. 55, pp. 235–253, May 2006, doi: 10.3114/sim.55.1.235.

[254] A. Carlucci, F. Cibelli, F. Lops and M. L. Raimondo, "Characterization of Botryosphaeriaceae species as causal agents of trunk diseases on grapevines", *Plant Disease*, vol. 99, no. 12, pp. 1678–1688, Dec. 2015, doi: 10.1094/PDIS-03-15-0286-RE.

[255] B. Slippers and M. J. Wingfield, "Botryosphaeriaceae as endophytes and latent pathogens of woody plants: Diversity, ecology and impact", *Fungal Biology Reviews*, vol. 21, no. 2-3, pp. 90–106, May 2007, doi: 10.1016/j.fbr.2007.06.002.

[256] I. M. Khattab, J. Fischer, A. Kaźmierczak, E. Thines and P. Nick, "Ferulic acid is a putative surrender signal to stimulate programmed cell death in grapevines after infection with *Neofusicoccum parvum*", *Plant, Cell & Environment*, vol. 46, no. 1, pp. 339–358, Dec. 2022, doi: 10.1111/pce.14468.

[257] E. Prichard and R. Lawn, *Measurement of pH*. Royal Society of Chemistry, Jan. 2003, isbn: 978-0-85404-473-3.

[258] A. Steinegger, O. S. Wolfbeis and S. M. Borisov, "Optical sensing and imaging of pH values: Spectroscopies, materials, and applications", *Chemical Reviews*, vol. 120, no. 22, pp. 12 357–12 489, Nov. 2020, doi: 10.1021/acs.chemrev.0c00451.

[259] J. Janata, "Do optical sensors really measure pH?", *Analytical Chemistry*, vol. 59, no. 9, pp. 1351–1356, May 1987, doi: 10.1021/ac00136a019.

[260] S. P. L. Sørensen, "Enzymstudien II: Über die Messung und die Bedeutung der Wasserstoffionenkonzentration bei enzymatischen Prozessen", *Biochemische Zeitschrift*, vol. 21, pp. 131–304, May 1909.

[261] K. T. V. Grattan, Z. Mouaziz and A. W. Palmer, "Dual wavelength optical fibre sensor for ph measurement", *Biosensors*, vol. 3, no. 1, pp. 17–25, Jan. 1987, doi: 10.1016/0265-928X(87)80010-X.

[262] M. A. Hanson, X. Ge, Y. Kostov, K. A. Brorson, A. R. Moreira and G. Rao, "Comparisons of optical pH and dissolved oxygen sensors with traditional electrochemical probes during mammalian cell culture", *Biotechnology and Bioengineering*, vol. 97, no. 4, pp. 833–841, Jul. 2007, doi: 10.1002/bit.21320.

[263] D. Westover, R. Seitz and B. K. Lavine, "Synthesis and evaluation of nitrated poly(4-hydroxystyrene) microspheres for pH sensing", *Microchemical Journal*, vol. 74, no. 2, pp. 121–129, Apr. 2003, doi: 10.1016/S0026-265X(02)00178-9.

[264] N. Opitz and D. W. Lübbers, "New fluorescence photometrical techniques for simultaneous and continuous measurements of ionic strength and hydrogen ion activities", *Sensors and Actuators*, vol. 4, pp. 473–479, Jan. 1983, doi: 10.1016/0250-6874(83)85059-8.

[265] T. Nguyen, K. P. McNamara and Z. Rosenzweig, "Optochemical sensing by immobilizing fluorophore-encapsulating liposomes in sol–gel thin films", *Analytica Chimica Acta*, vol. 400, no. 1-3, pp. 45–54, Nov. 1999, doi: 10.1016/S0003-2670(99)00607-8.

[266] J. K. Tusa and H. He, "Critical care analyzer with fluorescent optical chemosensors for blood analytes", *Journal of Materials Chemistry*, vol. 15, no. 27-28, Art. no. 2640, May 2005, doi: 10.1039/b503172a.

[267] R. J. Meier, L. H. Fischer, O. S. Wolfbeis and M. Schäferling, "Referenced luminescent sensing and imaging with digital color cameras: A comparative study", *Sensors and Actuators B: Chemical*, vol. 177, pp. 500–506, Feb. 2013, doi: 10.1016/j.snb.2012.11.041.

[268] J. R. Lakowicz, *Principles of fluorescence spectroscopy*, Third edition, corrected at 4. printing. New York, NY: Springer, Sep. 2006, isbn: 978-0-387-31278-1.

[269] X.-D. Wang and O. S. Wolfbeis, "Optical methods for sensing and imaging oxygen: Materials, spectroscopies and applications", *Chemical Society Reviews*, vol. 43, no. 10, pp. 3666–3761, Mar. 2014, doi: 10.1039/C4CS00039K.

[270] M. Tomasulo, I. Yildiz and F. M. Raymo, "pH-sensitive quantum dots", *The Journal of Physical Chemistry B*, vol. 110, no. 9, pp. 3853–3855, Feb. 2006, doi: 10.1021/jp060185h.

[271] I. Klimant, C. Huber, G. Liebsch, G. Neurauter, A. Stangelmayer and O. S. Wolfbeis, "Dual lifetime referencing (DLR) – a new scheme for converting fluorescence intensity into a frequency-domain or time-domain information", in *New trends in fluorescence spectroscopy: applications to chemical and life sciences*, ser. Springer Series on Fluorescence Methods and Applications, Berlin, DE; Heidelberg, DE: Springer, May 2001, pp. 257–274, doi: 10.1007/978-3-642-56853-4_13.

[272] X.-d. Wang, R. J. Meier and O. S. Wolfbeis, "A Fluorophore-Doped Polymer Nanomaterial for Referenced Imaging of pH and Temperature with Sub-Micrometer Resolution", *Advanced Functional Materials*, vol. 22, no. 20, pp. 4202–4207, Oct. 2012, doi: 10.1002/adfm.201200813.

[273] G. Liebsch, I. Klimant, C. Krause and O. S. Wolfbeis, "Fluorescent imaging of pH with optical sensors using time domain dual lifetime referencing", *Analytical Chemistry*, vol. 73, no. 17, pp. 4354–4363, Jul. 2001, doi: 10.1021/ac0100852.

[274] K. Krumova and G. Cosa, "Chapter 1. Overview of reactive oxygen species", in *Comprehensive Series in Photochemical & Photobiological Sciences*, vol. 1, Cambridge: Royal Society of Chemistry, Jan. 2016, pp. 1–21, doi: 10.1039/9781782622208-00001.

[275] J. F. Woolley, J. Stanicka and T. G. Cotter, "Recent advances in reactive oxygen species measurement in biological systems", *Trends in Biochemical Sciences*, vol. 38, no. 11, pp. 556–565, Nov. 2013, doi: 10.1016/j.tibs.2013.08.009.

[276] M. Manna, V. M. M. Achary and M. K. Reddy, "ROS signaling and its role in plants", in *Sensory Biology of Plants*, Singapore: Springer Singapore, Nov. 2019, pp. 361–388, doi: 10.1007/978-981-13-8922-1_14.

[277] A. Wojtala, M. Bonora, D. Malinska, P. Pinton, J. Duszynski and M. R. Wieckowski, "Methods to monitor ROS production by fluorescence microscopy and fluorometry", in *Conceptual background and bioenergetic/mitochondrial aspects of oncometabolism*, ser. Methods in enzymology, vol. 542, Amsterdam Boston: Elsevier Academic Press, 2014, pp. 243–262, isbn: 978-0-12-416618-9, [Online]. Available: https://www.sciencedirect.com/bookseries/methods-in-enzymology/vol/542/suppl/C.

[278] K. K. Griendling, R. M. Touyz, J. L. Zweier *et al.*, "Measurement of reactive oxygen species, reactive nitrogen species, and redox-dependent signaling in the cardiovascular system: A scientific statement from the American Heart Association", *Circulation Research*, vol. 119, no. 5, pp. 39–75, Jul. 2016, doi: 10.1161/RES.0000000000000110.

[279] S. F. Moussavi-Harami, K. M. Mladinich, E. K. Sackmann *et al.*, "Microfluidic device for simultaneous analysis of neutrophil extracellular traps and production of reactive oxygen species", *Integrative Biology*, vol. 8, no. 2, pp. 243–252, Jan. 2016, doi: 10.1039/C5IB00225G.

[280] N. Kwon, D. Kim, K. M. K. Swamy and J. Yoon, "Metal-coordinated fluorescent and luminescent probes for reactive oxygen species (ROS) and reactive nitrogen species (RNS)", *Coordination Chemistry Reviews*, vol. 427, Art. no. 213581, Jan. 2021, doi: 10.1016/j.ccr.2020.213581.

[281] L.-T. Cheah, Y.-H. Dou, A.-M. L. Seymour *et al.*, "Microfluidic perfusion system for maintaining viable heart tissue with real-time electrochemical monitoring of reactive oxygen species", *Lab on a Chip*, vol. 10, no. 20, Art. no. 2720, Aug. 2010, doi: 10.1039/c004910g.

[282] Y. Li, C. Sella, F. Lemaître, M. Guille-Collignon, C. Amatore and L. Thouin, "Downstream simultaneous electrochemical detection of primary reactive oxygen and nitrogen species released by cell populations in an integrated microfluidic device", *Analytical Chemistry*, vol. 90, no. 15, pp. 9386–9394, Jul. 2018, doi: 10.1021/acs.analchem.8b02039.

[283] S. Zhao, G. Zang, Y. Zhang *et al.*, "Recent advances of electrochemical sensors for detecting and monitoring ROS/RNS", *Biosensors and Bioelectronics*, vol. 179, Art. no. 113052, May 2021, doi: 10.1016/j.bios.2021.113052.

[284] P. K. Chand, M. R. Davey, J. B. Power and E. C. Cocking, "An improved procedure for protoplast fusion using polyethylene glycol", *Journal of Plant Physiology*, vol. 133, no. 4, pp. 480–485, Mar. 1988, doi: 10.1016/S0176-1617(88)80041-5.

[285] Q. Guan, Y. Guo, Y. Wei, F. Meng and Z. Zhang, "Regeneration of somatic hybrids of ginger via chemical protoplast fusion", *Plant Cell, Tissue and Organ Culture (PCTOC)*, vol. 102, no. 3, pp. 279–284, Sep. 2010, doi: 10.1007/s11240-010-9730-8.

[286] C. G. Agudelo, A. Sanati Nezhad, M. Ghanbari, M. Naghavi, M. Packirisamy and A. Geitmann, "TipChip: A modular, MEMS-based platform for experimentation and phenotyping of tip-growing cells", *The Plant Journal*, vol. 73, no. 6, pp. 1057–1068, Mar. 2013, doi: 10.1111/tpj.12093.

[287] A. Sanati Nezhad, M. Ghanbari, C. G. Agudelo *et al.*, "Optimization of flow assisted entrapment of pollen grains in a microfluidic platform for tip growth analysis", *Biomedical Microdevices*, vol. 16, no. 1, pp. 23–33, Sep. 2013, doi: 10.1007/s10544-013-9802-8.

[288] S. Tyanova, T. Temu and J. Cox, "The MaxQuant computational platform for mass spectrometry-based shotgun proteomics", *Nature Protocols*, vol. 11, no. 12, pp. 2301–2319, Oct. 2016, doi: 10.1038/nprot.2016.136.

[289] X. Dai, S. Zhang, S. Liu *et al.*, "Functional characterization and phenotyping of protoplasts on a microfluidics-based flow cytometry", *Biosensors*, vol. 12, no. 9, Art. no. 688, Aug. 2022, doi: 10.3390/bios12090688.

[290] B. Techaumnat, K. Tsuda, O. Kurosawa, G. Murat, H. Oana and M. Washizu, "High-yield electrofusion of biological cells based on field tailoring by microfabricated structures", *IET Nanobiotechnology*, vol. 2, no. 4, pp. 93–99, Dec. 2008, doi: 10.1049/iet-nbt:20080008.

[291] Y. Kimura, M. Gel, B. Techaumnat *et al.*, "A novel cell manipulation device for cytoplasmic transplantation", in *2008 International Symposium on Micro-NanoMechatronics and Human Science*, Nagoya, Japan: IEEE, Nov. 2008, pp. 196–201, doi: 10.1109/MHS.2008.4752449.

[292] M. Washizu, "Electrostatic bio-manipulation for the modification of cellular functions", *Journal of Physics: Conference Series*, vol. 418, Art. no. 012137, Mar. 2013, doi: 10.1088/1742-6596/418/1/012137.

[293] M. Okanojo, K. O. Okeyo, H. Hanzawa *et al.*, "Nuclear transplantation between allogeneic cells through topological reconnection of plasma membrane in a microfluidic system", *Biomicrofluidics*, vol. 13, no. 3, Art. no. 034115, Jun. 2019, doi: 10.1063/1.5098829.

[294] M. Gel, Y. Kimura, O. Kurosawa, H. Oana, H. Kotera and M. Washizu, "Dielectrophoretic cell trapping and parallel one-to-one fusion based on field constriction created by a micro-orifice array", *Biomicrofluidics*, vol. 4, no. 2, Art. no. 022808, Jun. 2010, doi: 10.1063/1.3422544.

[295] G. Grossmann, M. Meier, H. N. Cartwright *et al.*, "Time-lapse fluorescence imaging of Arabidopsis root growth with rapid manipulation of the root environment using the rootchip", *Journal of Visualized Experiments*, no. 65, Art. no. e4290, Jul. 2012, doi: 10.3791/4290.

[296] K.-Y. Song, H. Zhang, W.-J. Zhang and A. Teixeira, "Enhancement of the surface free energy of PDMS for reversible and leakage-free bonding of PDMS–PS microfluidic cell-culture systems", *Microfluidics and Nanofluidics*, vol. 22, no. 11, Art. no. 135, 2018, doi: 10.1007/s10404-018-2152-3.

[297] C. Allan, B. Elliot, V. Nock and C.-N. Meisrimler, "Bi-directional dual-flow-rootchip for physiological analysis of plant primary roots under asymmetric perfusion of stress treatments", *BIO-PROTOCOL*, vol. 13, no. 15, Art. no. e4764, Aug. 2023, doi: 10.21769/BioProtoc.4764.

[298] Z. Chen, Z. Wu, S. Lu, G. Zhang and H. Yan, "A new laser welding method of two transparent plastic parts based on reflector assisted method", *Journal of Materials Research and Technology*, vol. 24, pp. 5309–5320, Apr. 2023, doi: 10.1016/j.jmrt.2023.04.108.

[299] M. Brosda, P. Nguyen, A. Olowinsky and A. Gillner, "Laserwelding of biopolymers", *Procedia CIRP*, vol. 74, pp. 548–552, 2018, doi: 10.1016/j.procir.2018.08.116.

[300] A. Boglea, A. Olowinsky and A. Gillner, "Twist – a new method for the microwelding of polymers with fibre lasers", in *2007 ICALEO*, ser. LIA pub, Orlando, Fla.: Laser Institute of America, 2007, Art. no. M601, doi: 10.2351/1.5061144.

[301] A. Boglea, A. Olowinksy and A. Gilner, "Extending the limits of laser polymer welding using advanced irradiation strategies", *Journal of Laser Micro/Nanoengineering*, vol. 5, no. 2, pp. 138–144, Jun. 2010, doi: 10.2961/jlmn.2010.02.0008.

[302] D. Kumar, S. Ganguly, B. Acherjee and A. S. Kuar, "Performance evaluation of TWIST Welding using machine learning assisted evolutionary algorithms", *Arabian Journal for Science and Engineering*, vol. 49, no. 2, pp. 2411–2441, Sep. 2023, doi: 10.1007/s13369-023-08238-1.

[303] B. Acherjee, "Selection of optimal parameters for lasertransmission welding of polycarbonate using desirability function analysis", *Materials Today: Proceedings*, vol. 4, no. 8, pp. 7161–7170, Oct. 2017, doi: 10.1016/j.matpr.2017.07.042.

[304] V. Mamuschkin, M. Aden and A. Olowinsky, "Investigations on the interplay between focusing and absorption in absorber-free lasertransmission welding of plastics", *Lasers in Manufacturing and Materials Processing*, vol. 6, no. 2, pp. 113–125, Mar. 2019, doi: 10.1007/s40516-019-00083-1.

[305] X. Yu, C. Ni, H. Qiao, Y. Chen, Y. Liu and C. Wang, "The effects of laser line energy on welding strength of PASF/PC using magnesium zinc alloy powders as absorbents in lasertransmission welding", *Optics & Laser Technology*, vol. 174, Art. no. 110702, Feb. 2024, doi: 10.1016/j.optlastec.2024.110702.

[306] D. Kumar Goyal, R. Yadav and R. Kant, "Laser transmission welding of polycarbonate sheets using electrolytic iron powder absorber", *Optics & Laser Technology*, vol. 161, Art. no. 109165, Jun. 2023, doi: 10.1016/j.optlastec.2023.109165.